INFORMATION TO USERS

While the most advanced technology has been used to photograph and reproduce this manuscript, the quality of the reproduction is heavily dependent upon the quality of the material submitted. For example:

- Manuscript pages may have indistinct print. In such cases, the best available copy has been filmed.
- Manuscripts may not always be complete. In such cases, a note will indicate that it is not possible to obtain missing pages.
- Copyrighted material may have been removed from the manuscript. In such cases, a note will indicate the deletion.

Oversize materials (e.g., maps, drawings, and charts) are photographed by sectioning the original, beginning at the upper left-hand corner and continuing from left to right in equal sections with small overlaps. Each oversize page is also filmed as one exposure and is available, for an additional charge, as a standard 35mm slide or as a 17"x 23" black and white photographic print.

Most photographs reproduce acceptably on positive microfilm or microfiche but lack the clarity on xerographic copies made from the microfilm. For an additional charge, 35mm slides of 6"x 9" black and white photographic prints are available for any photographs or illustrations that cannot be reproduced satisfactorily by xerography.

Tsitouras, Christos D.

EXPERIMENTAL STUDY OF THREE-DIMENSIONAL TURBULENT JET-SOLID BOUNDARY INTERACTION

City University of New York PH.D. 1987

PLEASE NOTE:

In all cases this material has been filmed in the best possible way from the available copy. Problems encountered with this document have been identified here with a check mark __✓__.

1. Glossy photographs or pages _____
2. Colored illustrations, paper or print _____
3. Photographs with dark background _____
4. Illustrations are poor copy _____
5. Pages with black marks, not original copy _____
6. Print shows through as there is text on both sides of page _____
7. Indistinct, broken or small print on several pages ✓
8. Print exceeds margin requirements _____
9. Tightly bound copy with print lost in spine _____
10. Computer printout pages with indistinct print _____
11. Page(s) _____ lacking when material received, and not available from school or author.
12. Page(s) _____ seem to be missing in numbering only as text follows.
13. Two pages numbered _____. Text follows.
14. Curling and wrinkled pages _____
15. Dissertation contains pages with print at a slant, filmed as received _____
16. Other _____

_____

_____

University
Microfilms
International

EXPERIMENTAL STUDY OF THREE-DIMENSIONAL TURBULENT JET-SOLID BOUNDARY INTERACTION

by

CHRISTOS D. TSITOURAS

A dissertation submitted to the Graduate Faculty in Engineering in partial fulfillment of the requirements for the degree of Doctor of Philosophy, The City University of New York.

1987

This manuscript has been read and accepted for the Graduate Faculty in Engineering in satisfaction of the dissertation requirement for the Degree of Doctor of Philosophy.

3/3/87

Date

Chair of Examining Committee

3/3/87

Date

Executive Officer

Prof. Yiannis Andreopoulos

Prof. Peter Ganatos

Prof. Robert Pfeffer

Prof. Rishi Raj

Supervisory Committee

The City University of New York

ABSTRACT

A comprehensive experimental study was carried out to investigate jet-boundary interaction of blocked three-dimensional turbulent air jets discharging offset from and parallel to a solid boundary. The study was undertaken to establish the general flow and thermal characteristics associated with this configuration. Attention was focused on surface pressure distribution, jet trajectory and velocity and temperature distributions. Three outlets of aspect ratio, 0.1, 0.25 and 0.44, as well as the two-dimensional case (e = 0) were investigated at offset distances ranging from 0 (wall jet) to ∞ (free jet). The discharge Reynolds number ranged from 26,000 to 55,000. Flow visualization, employing smoke and oil/lampblack techniques, was used to determine gross jet spread behavior as well as the reattachment location.

Mapping of surface pressure revealed a complex two-dimensional pattern of sub-ambient and above ambient pressure distribution. Comparisons between three-dimensional and two-dimensional jets showed similarities as well as significant differences. Similarities at asymptotic conditions associated with the discharge aspect ratio e and offset distance h were examined. For $eh \ll 1$, the behavior of three-dimensional jets was found to approach that of two-dimensional slot jets. The influence of the offset surface on flow and thermal characteristics increased as h was decreased. Maximum velocity and temperature decays were shown to be similar to those of free jets in upstream regions and to approach wall jet decay further downstream.

ACKNOWLEDGEMENTS

I would like to thank my mentor, Herbert Kayser Professor Latif M. Jiji, since his guidance and valued suggestions served to clarify many aspects of the problem and greatly contributed to the completion of the project. His ready assistance in securing financial support and smoothing over many of the academic rough spots is gratefully acknowledged.

Appreciation is also extended to Professors Rishi Raj and Yiannis Andreopoulos, who made themselves available for numerous helpful discussions and suggestions. I am also grateful to Dr. Birinchi Hazarika and Mr. Rakesh Bhargava for making available to me some of the equipment belonging to "CCNY Turbomachinery Laboratory."

Finally, I wish to acknowledge the faithful support that my wife, Lena, and my family have given me throughout my years of study. Last but not least I would like to thank my brother, Panayiotis, who, having assumed at his own initiative the role of my deceased father, undertook the task of providing me with both financial and psychological support throughout this venture.

TABLE OF CONTENTS

LIST OF FIGURES

Page No.

NOMENCLATURE

A^*	:	discharge area	$= d^* \cdot \ell^*$
C_p	:	surface pressure coefficient	$= (P_s^* - P_\infty^*)/\frac{1}{2}\rho_o^* U_o^{*2}$
C_{pc}	:	centerline surface pressure coefficient	
C_{pcmax}	:	maximum surface pressure coefficient along centerline	
d^*	:	discharge height	
e	:	discharge aspect ratio	$= d^*/\ell^*$
h^*	:	discharge offset distance	
h	:	dimensionless discharge offset distance	$= h^*/d^*$
H^*	:	modified discharge offset distance	$= h^* + \frac{1}{2}d^*$
H	:	dimensionless modified discharge offset distance	$= H^*/d^*$
ℓ^*	:	discharge width	
L^*	:	channel length	
P_s^*	:	surface pressure	
P_∞^*	:	ambient pressure	
R_{e_o}	:	discharge Reynolds number	$= U_o^* d^*/\nu_o^*$
T^*	:	temperature	
T_c^*	:	centerplane temperature	
T_{max}^*	:	local maximum temperature	
T_{cmax}^*	:	centerplane local maximum temperature	
T_o^*	:	discharge temperature	
T_∞^*	:	ambient temperature	
U^*	:	velocity	
U	:	dimensionless velocity	$= U^*/U_o^*$

U^*_c : centerplane velocity

U_c : dimensionless centerplane velocity $= U^*_c/U^*_o$

U^*_o : discharge maximum velocity

U^*_{max} : local maximum velocity

$U_{/max}$: dimensionless velocity based on local maximum $= U^*/U^*_{max}$

$U_{c/max}$: dimensionless centerplane velocity based on local maximum $= U^*_c/U^*_{max}$

U^*_{cmax} : centerplane local maximum velocity

U_{cmax} : dimensionless centerplane local maximum velocity $= U^*_{cmax}/U^*_o$

$\bar{U}^*$: velocity vector

$\bar{U}^*_o$: maximum discharge velocity vector

u^*, v^*, w^* : velocity components

u, v, w : dimensionless velocity components $= u^*/U^*_o, v^*/U^*_o, w^*/U^*_o$

x^*, y^*, z^* : coordinate system

x, y, z : dimensionless coordinate system $= x^*/d^*, y^*/d^*, z^*/d^*$

x^*_a : axial distance corresponding to maximum C_{p_c}

x_a : dimensionless axial distance corresponding to maximum $C_{p_c} = x^*_a/d^*$

x^*_r : reattachment distance

x_r : dimensionless reattachment distance $= x^*_r/d^*$

Y^* : modified vertical coordinate $= y^* - H^*$

Y : dimensionless modified vertical coordinate $= Y^*/d^*$

$Y^*_{1/2}$: velocity halfwidth in y-direction

$Y_{1/2}$: dimensionless velocity halfwidth in y-direction $= Y^*_{1/2}/d^*$

$Y^*_{T1/2}$: thermal halfwidth in y-direction

$Y_{T1/2}$: dimensionless thermal halfwidth in y-direction $= Y^*_{T1/2}/d^*$

$Z^*_{1/2}$: velocity halfwidth in z-direction

$Z^*_{T1/2}$: thermal halfwidth in z-direction

Θ : dimensionless temperature $= (T^* - T_\infty^*)/(T_o^* - T_\infty^*)$

Θ_c : dimensionless centerplane temperature $= (T_c^* - T_\infty^*)/(T_o^* - T_\infty^*)$

$\Theta_{/max}$: dimensionless temperature based on local maximum

$= (T^* - T_\infty^*)/(T_{max}^* - T_\infty^*)$

$\Theta_{c/max}$: dimensionless centerplane temperatured based on local maximum

$= (T_c^* - T_\infty^*)/(T_{max}^* - T_\infty^*)$

Θ_{cmax} : dimensionless centerplace local maximum temperature

$= (T_{cmax}^* - T_\infty^*)/(T_{max}^* - T_\infty^*)$

ν_o^* : kinematic viscosity at discharge

ρ_o^* : density at discharge

θ : yaw angle

φ : pitch angle

Subscripts

∞ : ambient

1/2 : halfwidth

a : location corresponding to maximum C_{p_c}

c : centerplane (z = 0)

o : discharge

max : maximum

r : reattachment

s : surface

T : thermal

Superscripts

*	:	dimensional quantity

I. INTRODUCTION

1. Background

The study of turbulent jets has long been of interest because of its extensive use in engineering applications. Generally, jets have applications in film cooling, combustion, sewage disposal, fluid and heat dissipation from power generation, turbo-jet thrust reverser and the directional nozzle controlling the lateral thrust of the STOL aircraft, etc. Greater interest in heated turbulent jets has recently developed due to increased concern over thermal pollution from power plants.

Three types of jet-boundary interaction problems are commonly encountered: (i) wall jet, in which the fluid is discharged at the boundary, (ii) impinging jet, where the discharge is aimed towards the boundary, and (iii) offset jet, in which the fluid is discharged at some distance from the boundary and eventualy attaches to it due to the lateral pressure forces. Clearly, the wall and free jets may be considered as limiting cases of the offset jet (Figure 1).

Two basic configurations are associated with the discharge planes (Figure 2). In one arrangement, known as a "blocked jet," the fluid is discharged through an outlet in a plate normal to the surface. The presence of such a plate prevents axial entrainment of secondary flow at the discharge plane. In another arrangement, known as "ventilated jet," no vertical plate is placed at the discharge outlet and consequently axial entrainment of secondary flow takes place.

The case of a heated submerged jet in the vicinity of a solid boundary is of special interest because of its application to thermal discharges from power

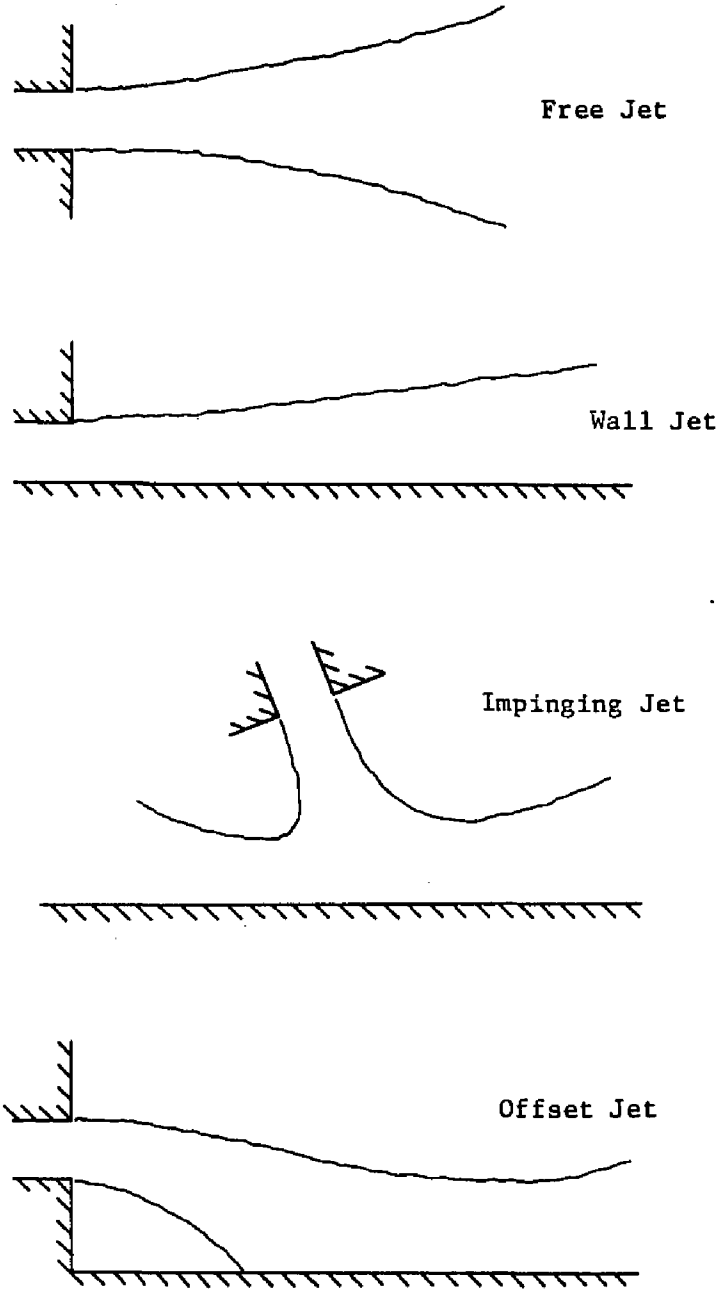

Figure 1. Illustration of various jet flow configurations.

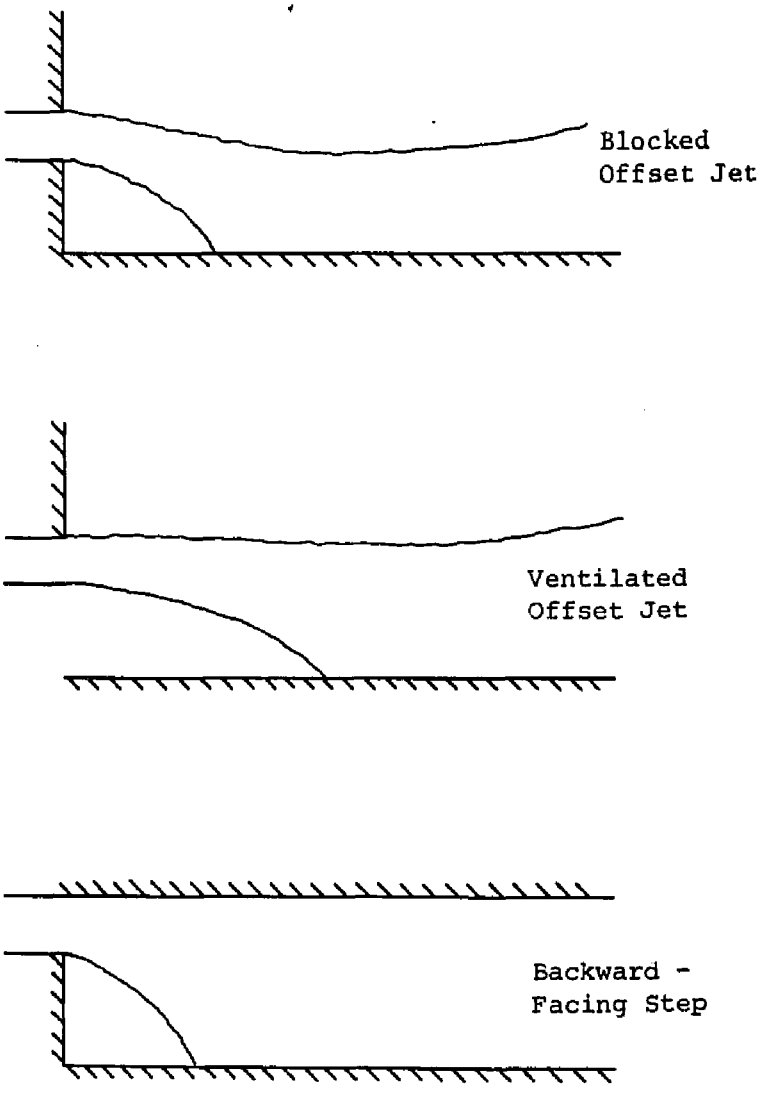

Figure 2. Illustration of various offset jet configurations.

plants near the bottom of rivers and lakes. The subsequent interaction with the solid surface may significantly alter plume behavior. Furthermore, pressure and shearing forces by the floor-bound jet give rise to scouring and bed erosion resulting in structural problems at the discharge area.

Jet-boundary interaction occurs when a discharge outlet is located in the vicinity of a solid boundary. As the jet discharges from the outlet the surrouncing fluid is entrained due to the turbulent mixing and the static pressure on the wall becomes less than that of the surrounding field. As a consequence the jet curves towards the solid boundary and eventually attaches to it (Figure 3).

The following three regions, which apply in the two-dimensional model, also appear in the three-dimensional offset jet case: (i) the pre-attachment region, which is the region prior to the jet attachment with the solid wall and where pressures are generally lower than hydrostatic levels, (ii) the impingement region, located past the jet attachment, and (iii) the wall jet type region, which is the zone where the jet undergoes turbulent diffusion analogous to that of a wall jet (Figure 4).

2. Objectives

The present study deals with a detailed experimental investigation of the characteristics of flow and temperature fields of steady, incompressible, blocked, three-dimensional, turbulent, air jet-boundary interaction. The jet is discharged from rectangular outlets near a plane surface (Figure 3). The free stream velocity is assumed to be zero. The surface pressure as well as the mean velocity and temperature fields are examined, taking into consideration the

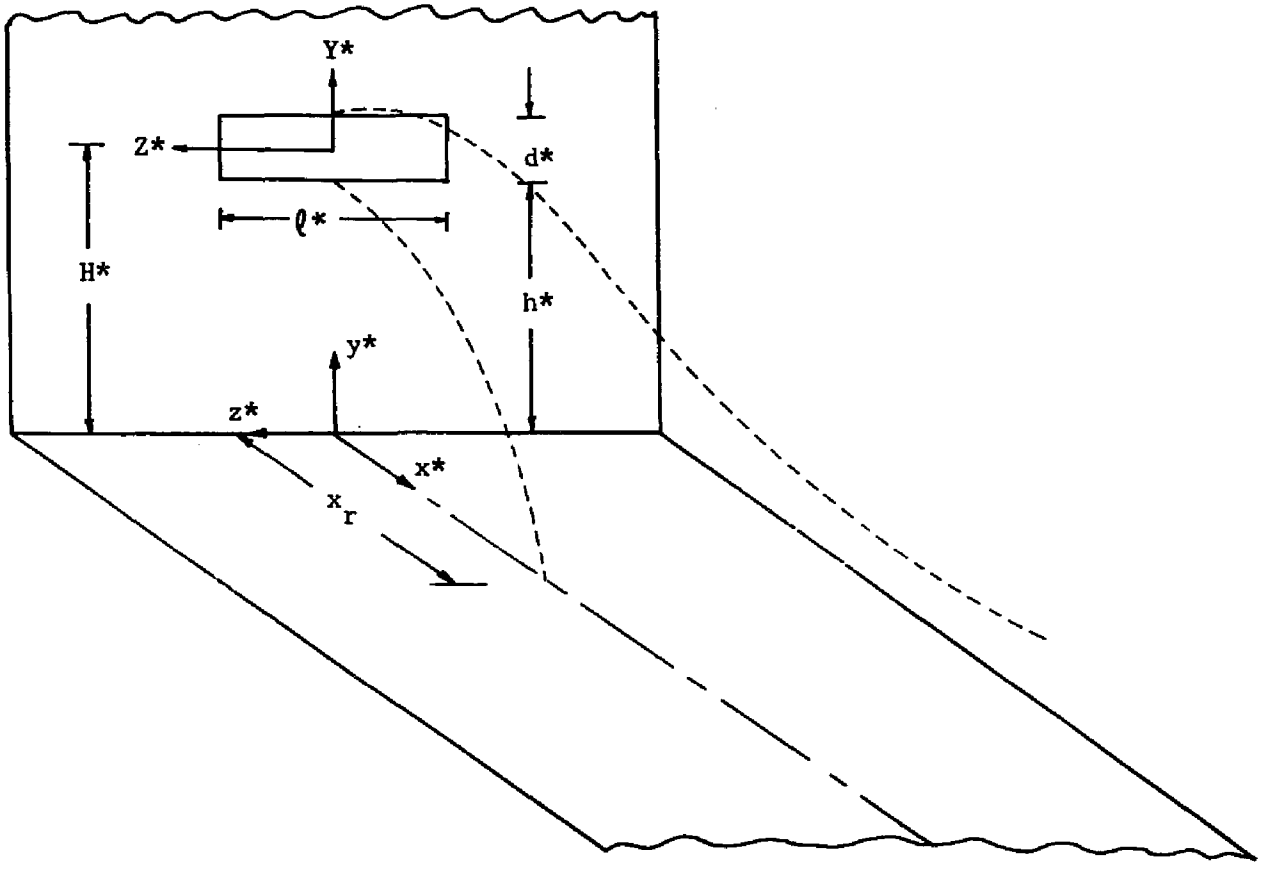

Figure 3. Schematic of three-dimensional blocked offset jet.

general flowfield structure and the effects of offset distance, discharge aspect ratio and Reynolds number. In addition, the experimental investigation includes flow visualization -- using smoke and oil/lampblack techniques -- in order to provide an overall view of the entire flowfield in this complex three-dimensional jet-boundary interaction problem.

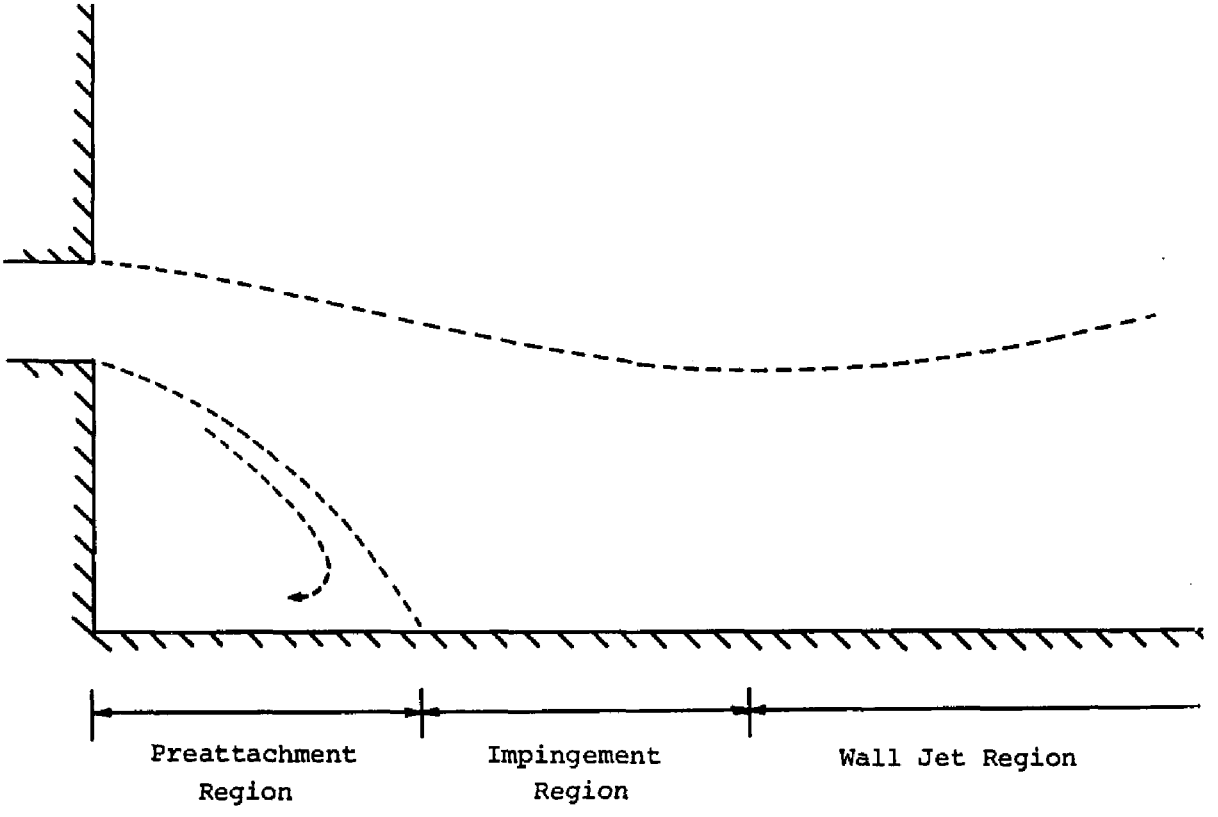

Figure 4. Schematic of two-dimensional blocked offset jet.

II. LITERATURE SURVEY

The problem of three-dimensional heated turbulent offset jets has not been previously investigated. The only published work on the corresponding case of isothermal offset jets appeared in 1974. However the limiting cases of three-dimensional wall and free jets, as well as other related configurations, have received more attention.

This chapter presents a review of the various types of jet problems, whose study leads to a better understanding of the turbulent rectangular offset jet problem. The mechanism of entrainment and its two basic hypotheses are also discussed.

1. Three-Dimensional Offset Jets

The only experimental and theoretical study of the three-dimensional jet flow in the vicinity of a solid boundary was presented by Sacks, John and Marks,[1] who examined the case of a long slender discharge. Their experimental work showed that for such discharge configurations the velocity distribution in the near field could be approximated by the velocity distribution of the two-dimensional free jet. They reported that the pre-attachment interaction region between the jet and the boundary surface exhibits totally different characteristics than that of the two-dimensional offset jet. For the present type of three-dimensional geometry this region is dominated by a significant crossflow from the sides, in contrast to the two-dimensional case where a reverse flow-vortex is formed. This entrainment from the sides of the jet inhibits the jet from bending towards the boundary. Assuming that the crossflow in the sides of the jet due to

entrainment is perpendicular to the direction of the jet flow, Sacks et al. were able to model the influence of the horizontal boundary on the jet. Jet displacement was obtained from a dynamical equation based on the pressure difference across the jet. Flow visualization through the use of smoke injection and cotton streamers did not demonstrate the presence of a recirculation pattern for the three-dimensional offset jet even at the limit of a very low aspect ratio. Therefore, the three-dimensional offset jet flows discharging from low aspect ratio channels and having negligible but finite offset distance are expected to exhibit different behavior than the three-dimensional wall jet and the two-dimensional offset jet flows.

2. Two-Dimensional Offset Jet (Blocked)

Studies concerning flow characteristics of two-dimensional, incompressible, turbulent offset jets were carried out by Sawyer,[2, 3] Bourque and Newman,[4] Bourque[5] and Rajaratnam and Subramanya.[6] These studies concentrated on the pre-attachment region and attempted to predict the recirculation pressure, the jet's curvature as it bends towards the horizontal boundary, the pre-attachment length, the flow behavior and the entrainment mechanism of the curved pre-attached jet. Simplifying assumptions regarding the flow were made in order to obtain analytical expressions. The validity of these results were questioned and model modifications were made by Hoch and Jiji[7, 8] to provide a more complete description of the two-dimensional offset jet-boundary interaction problem.

Three distinct regions characterize the two-dimensional jet discharging parallel to and offset from a solid boundary:[7] (i) the pre-attached free jet region,

(ii) the impingement region, and (iii) the plane wall jet region (Figure 4). In the first region, reduced entrainment below the jet results in a low pressure region between the jet and the boundary causing the jet to bend towards the boundary and eventually be attached to it. In this region pressures are generally lower than hydrostatic levels. As the jet approaches the boundary, pressure levels within the jet increase, causing the jet to decelerate, eventually reaching a maximum value in the neighborhood of the reattachment location. By attaching to the boundary a recirculation region is set up which is bounded by the discharge plane, the solid boundary and the dividing or reattaching streamline. Fluid entrained by the jet from the recirculation region is returned to it resulting in no net mass exchange. The recirculation produces a well-mixed region resulting in a nearly uniform cavity temperature. The fluid above the dividing streamline is accelerated along the boundary following jet reattachment due to the jet's positive pressure. In the second or impingement region, the pressure decreases, eventually reaching hydrostatic levels, and the acceleration ceases. In the third region the jet undergoes turbulent diffusion analogous to that of a classical wall jet.

Sawyer,[2] using a control volume approach together with the constant radius of curvature assumption, obtained a solution for the reattachment location as a function of discharge offset distance using a single value for the spread parameter. He also found that the velocity profiles of the jet, as it curved towards the boundary, exhibited no obvious asymmetry. In a later study, Sawyer[3] modified the earlier analysis to include the different entrainment rate effects. Pressure variations in the vicinity of reattachment were included in the conservation of the horizontal momentum. With the use of the first order mixing length model, the curved jet velocity profiles were found to be nearly sym-

metrical, not differing significantly from their free jet counterpart. The spread rate and total entrainment were found to be nearly independent of the jet curvature. The model predicted the reattachment location to occur close to the maximum surface pressure position along the horizontal boundary. This was in agreement with experimental observations.

In their theoretical formulation, Bourque and Newman[4] assumed: (a) constant discharge velocity, cavity pressure and radius of curvature, (b) similar velocity distribution and entrainment in the pre-attachment region to that of the free jet, (c) the horizontal forces due to shear stress at the boundary to be negligible in comparison to those due to the jet momentum in the vicinity of reattachment, and (d) entrainment to occur normal to the flow. They observed experimentally that the reattachment location corresponds to the position of maximum surface pressure only when the angle at which the jet approaches the horizontal boundary is close to right angle. This occurs at large offset distance to discharge height ratios. For small ratios it corresponded more closely to the position at which the surface pressure changed sign. The surface pressure coefficient was found to initially decrease with axial distance, then rapidly increase, becoming positive immediately preceding pre-attachment. The flow was found to become independent of offset ratio for values of 40 or larger.

In a later model, Bourque[5] relaxed the constant radius of curvature restriction by assuming a sinusoidal shape for the reattachment streamline and jet centerline. The pressure difference across the jet was considered to increase uniformly up to the location of reattachment, corresponding to the increasing curvature. This new model was found to accurately predict the reattachment location for any offset distance when the same constant value for the spread

parameter, as previously determined,[4] was used.

Rajaratnam and Subramanya[6] were the first investigators who presented a study on the various flow regions of the turbulent two-dimensional offset jet. These were specified as the free jet region, the impingement zone and the plane wall jet region. This study examined the flow field for small offset distance to discharge height ratios ($1 < h < 6$). Using dimensional analysis, they showed that for large Reynolds numbers the pre-attachment distance to discharge height ratio is solely a function of the offset ratio. Pressure distribution in the recirculation region and surface pressure along the boundary confirmed earlier findings. They found the reattachment location to coincide with the position at which the maximum surface pressure occurred. They also observed that for small offset ratios the decay of maximum axial velocity can be approximated by the classical wall jet, while for larger ratios the decay is initially more rapid, as expected for free-type behavior, followed by a slight recovery in the impingement region, and approaching plane wall jet behavior further downstream. They therefore considered the reattached wall jet velocity field to be composed of two parts: (i) the characteristic decay region, which is dependent on the offset ratio, and (ii) the classical wall jet decay region in which all jets exhibit the same decay rate.

An observation based on the experimental data of Rajaratnam and Subramanya[6] appears in the paper by Daggett.[9] He observed that when the values of axial velocity were adjusted by shifting the axis to a suitable mean virtual origin, the resultant self-similar axial velocity profiles were found to agree with classical free jet theory. This justified the use of free jet profiles for the axial velocity component tangent to the curved jet centerline in the pre-

attachment region.

Hoch and Jiji[7] presented an integral formulation of the two-dimensional jet-boundary interaction problem, which includes the effect of free stream motion and offset parameter, and deals with the near and far fields of the jet. The jet entrainment assumption has been modified for the offset jet. In addition, the classical jet-integral solution has been extended so as to account for variations of pressure in both the pre-attachment and impingement regions. They assumed a sinusoidal variation for the radius of curvature and free jet velocity distribution in the pre-attachment region. The jet spread and maximum centerline velocity decay were taken to be different from that of the free jet.

A typical photograph of the flow pattern in the recirculation region, using smoke injection, showing the position of the dividing streamline confirms their assumption that the maximum surface pressure occurs at the end of the pre-attachment region. For low free stream to jet discharge velocity ratios, the maximum axial velocity decay for the pre-attachment and impingement regions was approximately that of a jet with zero free stream ratio, although for larger ratios the velocity decays were displaced successively upwards. The analytical velocity distribution differed significantly from that of the two-dimensional free jet. The presence of a free stream flow was seen to delay the reattachment and to decrease the maximum surface pressure for a given offset distance.

A theoretical and experimental investigation of the temperature field of a heated two-dimensional, non-buoyant, turbulent jet discharging parallel to and offset from an adiabatic boundary was presented by Hoch and Jiji.[8] The model was based on an integral formulation of the basic conservation laws and takes

into consideration the effects of free stream motion and jet offset distance. They assumed Gaussian velocity profiles in the pre-attachment and free jet regions, a 1/7 power law in the velocity boundary layer, an asymmetrical Gaussian temperature profile in the pre-attachment region and a Gaussian-type temperature profile, which satisfies the adiabatic wall boundary condition, in the impingement and wall jet regions. The vertical temperature and velocity halfwidths were observed to grow linearly following reattachment. The uniformity of temperature in the recirculation region was substantiated experimentally. Free stream velocity was found to have a minor effect on the maximum axial temperature decay. Variations in the offset ratio were found to have noticeable influence on the maximum axial temperature decay in the pre-attachment region, diminishing progressively downstream.

Parameswaran and Alpay[10] obtained experimental data on flow characteristics of two-dimensional offset jets and compared them with those of a plane wall jet. The reattachment location and the center of the vortex in the cavity were determined experimentally and corresponding laws were formulated. The vortex center distance to the reattachment distance ratio remained nearly constant. The reattachment distance to the offset distance ratio appeared to approach an asymptotic value. The maximum velocity decay followed the same type of exponential law as in the case of plane wall jets. The shear stress distribution on the horizontal boundary exhibited some similarity in shape beyond reattachment. The peak value of shear stress found to be decreased as the offset ratio was increased.

An experimental study of a radial turbulent jet attaching to an offset disc plate appears in Tanaka and Tanaka.[11] The effects of diameter, height of the

nozzle and offset distance on the flow pattern were investigated. An oil-film flow visualization technique was applied. The flow characteristics in the recirculation region were found to be governed solely by the offset ratio and to have a different tendency as the offset ratio reaches the value of 6. The pre-attachment distance of the radial offset jet was found larger than that of plane offset jet.

Kumada, Mabucki and Oyakawa[12] studied the velocity field and heat transfer characteristics of plane turbulent offset jets using analogy to mass transfer. The reattachment distance, the averaged static pressure in the cavity and the virtual origin of the reattached wall jet show a different tendency as the offset ratio reaches the value of 6.5. Moreover, the velocity profiles and the local surface friction coefficient confirmed the wall jet flowfield characteristics downstream of reattachment. They also obtained relations for the maximum Sherwood number, the averaged Sherwood number in the cavity and the local Sherwood number of the reattached wall jet.

3. Two-Dimensional Ventilated Jets

The flow characteristics of a two-dimensional, ventilated, turbulent jet discharge parallel to and at some height above a solid boundary were presented by Murai et al.,[13] Marsters,[14] El-Taher[15] and Shibl and Shaalan.[16] The "ventilated" jet is characterized by the existence of a gap between the jet and the boundary, and a secondary flow is entrained through the gap, preventing the formation of a closed recirculation region (see Figure 2). The jet initially behaves as a free jet but eventually bends and attaches to the surface. The central streamline is observed to bend at some distance past attachment, though

the curvature is not due to a "Coanda" effect below the jet, as in the case of a blocked offset jet. Mass entrainment below the jet is analogous to that observed in free jet flow.

Based on the location of the central streamline, Murai et al.[13] observed three distinct regions following free jet impingement: (i) the initial region where the central streamline, or velocity boundary, remains constant, (ii) the transient region in which the thickness decreases and (iii) the wall jet region where the central streamline continues to approach the boundary and eventually rises further downstream. For small offset ratios, the maximum axial velocity decay is about that predicted for the two-dimensional wall jet, while for offset ratios greater than 0.5 the decay is more rapid, equal to that of the free jet until the end of the transient region. However, the rate decreases downstream and eventually approaches that of the traditional wall jet. Their numerical solution predicted that the location of maximum axial velocity was significantly decreased with increasing diffusivity, so that the wall shear stress was seen to be the governing factor in the bending of the central streamline towards the boundary. Furthermore, the greater the diffusivity, the wider the spread was. When a suitable wall shear stress correction factor was employed, reasonable agreement between the analytical solution and experimental results for the jet spread, boundary layer growth and velocity decay was observed.

In the experimental study by Marsters,[14] the wall boundary layer growth found to be typical of the behavior of unventilated wall jets and the location of maximum surface pressure was directly proportional to the offset distance. It was concluded that the mixing effect of the primary jet results in a transfer of momentum to the secondary stream and hence this device operates as an ejector

or thrust augmentor. The overall thrust augmentation is reduced by the wall shear stress.

The effect of wall curvature on the mean velocity field, as well as the turbulence characteristics of ventilated wall jets were investigated by El-Taher[15] and by Shibl and Shaalan.[16] The following conclusions were drawn from these studies: (i) the entrainment rate through the gap increases and the reattachment location moves closer to the outlet as the wall curvature increases, (ii) the wall curvature has a negligible effect on the flowfield in the positive and negative pressure gradient zones, (iii) the similarity of mean velocity profiles in the outer layer of the constant pressure zone is not affected by the wall curvature, whereas the similarity curve in the inner layer appears to change slightly with increasing curvature, and (iv) the increase in $\sqrt{v'^2}$ due to wall curvature is much larger than the corresponding increase in $\sqrt{u'^2}$.

An experimental study of the heat transfer characteristics of a ventilated jet attaching to a plane wall and its comparison with the case of a "blocked" offset jet was presented by Marsters, Howkins and Kortschak.[17] Examinations of the wall temperature excess or fluid temperature distribution indicated that the effectiveness of a ventilated jet is decreased as the gap is increased. Also, the temperature excess in the blocked jet is generally greater than that of ventilated flow.

4. Backward Facing Steps

Heat transfer and fluid dynamic measurements behind a backward-facing step were presented by Vogel, Eaton and Adams.[18] The heat transfer coefficient

was seen to follow the gross features of the flow, showing the secondary recirculation vortex and attaining its maximum value at the reattachment location. The differences between the heat transfer behavior and the mean skin friction were seen to be the result of the sublayer influence which tended to dominate heat transfer behavior. This influence was explained by the fluctuating skin friction which closely followed the behavior of the Stanton number.

5. Three-Dimensional Free Jets

There exists an abundance of experimental and theoretical studies in the literature concerning the three-dimensional free jet in which the mean flowfield characteristics, the overall turbulence structure and various alternative mechanics describing the observed behavior are discussed.

Sforza, Steiger and Trentacoste[19] were among the first investigators who carried out experimental and theoretical studies concerning turbulent three-dimensional free jets. They observed that the flowfield of a jet issuing from a rectangular slot is characterized by three distinct regions: (i) the potential core region, (ii) the characteristic decay region, and (iii) the axisymmetric decay region. An implicit finite difference analysis, which depicts the mean streamwise flow with reasonable accuracy, was presented. Experimental flow field characteristics were also included.

The experimental work by Trentacoste and Sforza[20] on rectangular free jets provided considerable information regarding flow field characteristics. They included many detailed remarks about axis velocity decays, the three flow regions, velocity profile similarity, approach to axisymmetry, mass entrainment,

momentum conservation and velocity irregularities. Mass entrainment was found to be dependent on Reynolds number when it exceeded the value of 2.5×10^4. The centerline velocity decay in the characteristic decay region was reported to be inversely proportional to the axial coordinate raised to a power. Values of this power were given for many outlets with different aspect ratios.

Quinn, Pollard and Marsters[21, 22] measured mean velocities and turbulence quantities using hot-wire anemometry in the two central planes of a free jet of air issuing into still air surroundings. The mean axial velocity decay along the jet centerline was found to consist of four regions: (i) a potential core region, (ii) a typical decay region, (iii) a transition region, and (iv) a final decay region. The mean axial velocity profiles in the plane of the outlet major axis were characterized by off-center peaks within the typical decay region. The turbulence kinetic energy and shear stress profiles did not show any signs of self-preservation within the examined range, $x \leq 100$.

A great deal of information concerning the physical structure of the flowfield was contained in the experimental work by Marsters and Fotheringham[23] where surface and contour plots were presented. The mean velocity contour plots were shown the growths of the jet and the corresponding halfwidths, as well as the "rotation of the major axis." This phenomenon is the shift of the axis containing the larger halfwidth from the spanwise to the vertical direction and corresponds to the location where the halfwidth crossover is seen to occur. They found that two length scales -- vertical and spanwise -- were necessary for scaling the flowfield to enable certain characteristics to manifest themselves, which were not apparent when a single length scale was used.

In addition, the presence of off-axis velocity peaks in the spanwise direction was found to characterize low aspect ratio rectangular jets. Eventually the shearing stresses diffuse the vorticity, and self-similar Gaussian profiles were ensued. A characteristic feature of the saddling was that it occurred in the direction containing the major axis. Their proposed explanation of the saddling phenomenon was that it is the result of the rolling up of vortex sheets shed from the edge of the three-dimensional outlet.

Trentacoste and Sforza[24] have observed these velocity irregularities in the flowfields of three-dimensional free jets, wall jets and wakes exiting from short though smoothly converging orifices, but did not find this feature present in the flowfields from axisymmetric and square discharges and from wakes having eccentricity near unity.

Marsters[25] has presented an hypothesis to account for the spanwise velocity irregularities observed in free turbulent shear flows discharging from rectangular outlets. The proposed mechanism was based on a centrally located high pressure region which could drive secondary flows that could move high velocity fluid from the central one to the outer ends of the flowfield. The presence of strong vorticity interactions and important secondary flow effects were considered responsible for the formation of saddle-based profiles and unequal spanwise and vertical spreading rates. Also, it has been observed that the peaks appear to merge at the same region that transition from characteristic decay gives way to axisymmetric decay, and that intense turbulence activity was present at the ends of the jet.

In the numerical model for three-dimensional, turbulent, free jets formulated by McGuirk and Rodi,[26] the introduction of secondary motions in the plane of the jet cross-section was necessary in order to describe the inversion of major and minor axes of the jet. A vena contracta effect was evident and the halfwidths in the direction of the long axis were actually decreased initially whereas the minor axis halfwidth grew; further downstream they were seen to cross over (major axis rotation) after which they both continued to grow, but at slightly different rates, tending to approach each other as the jet tended to axisymmetry. Measurements were shown that the displacement of the maximum velocity some way from the center-plane (spanwise axial velocity irregularities) was much more pronounced for the jet out of a sharp-edged outlet. The present turbulence model was incapable of predicting these experimentally observed irregularities. Two possible causes were mentioned here: (i) the axial pressure gradient which was ignored may not be negligible where there is significant lateral motion, and this may act to accelerate or decelerate some regions of the flow relative to others, and (ii) the existence of other secondary flows superimposed upon those due to the discharge conditions, which may act to convect high momentum fluid from the central portions of the jet out towards the edges and thus create the saddle-shape.

The presence of the halfwidth crossover and the spanwise axial velocity irregularities have been explained by Sforza to be the result of a system of closed vortex rings produced by the orifice edge. Experimentally, a system of closed vortex rings was found to produce an axial component of vorticity in the direction of jet flow thus generating a secondary motion along a cross-section normal to the flow. The vortex sheets generated at the discharge continuously roll up to form a system of closed vortex rings. The influence of this large scale

system on the overall jet structure must be accurately accounted for when modeling the three-dimensional flowfields.

The mean flowfield and turbulent intensities of airjets, issuing from rectangular slots having different geometries and aspect ratios were measured using hot-wire anemometers by Sfeir.[27] Turbulence measurements were found to be consistent with the mean flow and showed a similar departure from the behavior of a two-dimensional jet. The turbulence intensity along the centerline did not remain constant for any appreciable length, and stayed well below intensity levels usually measured in two-dimensional jets.

The mean velocity and temperature profiles of heated three-dimensional turbulent free jets have been investigated by Sforza and Stasi[28] and Sfeir.[29] The geometries employed in the two studies were significantly different though the qualitative results were similar. The velocity and temperature flowfields were found to be divided in three distinct regions respectively referred to as the potential core, the characteristic decay region and the axisymmetric decay region. These regions were not exactly the same for temperature as for velocity, the former being shifted somewhat upstream of the latter. Measurements shown in these studies have indicated that the nature of the discharge flow conditions play a large role in the development of the near field jet characteristics. The thermal halfwidths observed by Sforza were found to be greater than the velocity halfwidths. This is apparently indicative of the more rapid mixing of heat compared to mixing of momentum. The phenomena of rotation of axes and thermal halfwidth cross-over were also observed for the heated free jet. Contours of constant mass flux showed the shift in major axis from the spanwise to vertical directions and the approach to elliptical contour in the axisymmetric decay zone.

Jiji and Moghadam[30] presented analytical solutions and experimental data for buoyant three-dimensional turbulent free jets discharged horizontally from rectangular outlets into a quiescent fluid. Attention was focused on the mean and thermal characteristics of the jet, such as centerline velocity and temperature decays and jet trajectories. The theoretical model was based on integral formulation of the conservation laws using the entrainment concept for closure. Assumed velocity and temperature profiles, appropriate to the various regions of the jet, were used to generate sets of simultaneous ordinary differential equations which were solved numerically. Experimental data using four aspect ratios were obtained at various Froude numbers and were in reasonable agreement with the theoretical solutions.

6. Three-Dimensional Wall Jets

The behavior of wall jets in the outer layer above the boundary layer is very similar to that of the corresponding free jet flow but generally different mechanisms operate in the two flows because of the influence of the wall boundary. Nevertheless, the observation of three distinct regions for both the velocity and temperature decays, the general nature of the halfwidth growth, the appearance of spanwise velocity irregularities in slender jets and the general similarity in behavior of velocity and temperature fields are common to both free and wall jet flows of turbulent incompressible fluid discharging from moderate to low aspect ratio channels. Therefore, many of the characteristics and the parameters which are important in the characterization of wall bounded shear flows can be obtained by studying the properties found for the free jet case.

Sforza[31] and Sforza and Herbst[32] experimentally examined the flowfield characteristics of three-dimensional wall jets. They found three regions, analogous to the flowfield structure originally observed in free jets.[19] These regions were distinguished by different rates of decay of the maximum velocity. The decay rate in the near field was found to depend on the aspect ratio, whereas far downstream it was the same with that of a radial wall jet. For low aspect ratios decay rates seemed to be similar to those corresponding to two-dimensional wall jets, although some spanwise irregularities were evident in the measured velocity profiles.

The effects of a curved and flat wall surface on the flow development of an axisymmetric jet exhausting into a moving stream were investigated by Catalano, Morton and Humphris.[33, 34] The curved wall (flap) was found to have a very large effect on both the mean velocity and the turbulent velocity components of the flowfield. The potential core region was found to break up more rapidly for flow over a flap. Measurements of the velocity in the vertical direction over the surface of a flap indicated that the flow seems to be revolving or rolling up as it spreads out over the curved wall.

A significant alteration in the large scale structure of turbulent wall jets results from a modification of flowfield geometry. Evidence of this exists in the isocorrelation contours of the wall vs. flap jet flows of Morton, Catalano and Humphris.[35]

The growth rates of the length scales for wall jets having an aspect ratio near unity (issuing from circular, square, triangular, elliptic and rectangular outlets) were studied by Rajaratnam and Pani.[36, 37] They found that a linear

relation for each of the vertical and spanwise directions was suitable for correlating the halfwidth growth of all examined geometries. They experimentally confirmed the predictions obtained from dimensional analysis of a linear variation of maximum centerline velocity and velocity halfwidth growth with the inverse of the axial distance from a suitable point source or the virtual origin.

Butterman, Jiji and Hoch[38] presented results of an experimental and theoretical investigation of the mean flow and thermal characteristics of wall jets issued from various rectangular channels parallel to an adiabatic wall. They measured the velocity and temperature fields for a turbulent air jet discharging into stagnant air. Data were obtained for axial velocity and temperature decays, as well as jet momentum and thermal spread rates. A simplified theoretical model in which buoyancy effects were neglected was reported. The model was based on integral formulation of the conversation of mass, momentum and energy. The entrainment concept was used to provide closure. Reasonable agreement between theoretical predictions and experimental data was obtained.

7. Mechanism of Entrainment

This part is concerned with the phenomenon of entrainment which is a feature of all free turbulent shear flows. The very rapid spreading of wakes and jets, as compared with their laminar counterparts, is ascribed to the mechanism of entrainment whereby the non-turbulent ambient fluid becomes turbulent. Two basic hypotheses have been suggested: (i) viscous diffusion of vorticity at the smallest scales of the turbulence and (ii) large scale mixing that engulf volumes of fluid in bulk. The second one appears to be the more favorable, since the

viscous diffusion mechanism is inconsistent with the observed self-preserving development of many flows.

The nature and origin of the structure of fully sheared turbulence as it appears in different flows are discussed in Townsend.[39] He also suggests how the entrainment mechanism conforms to the wide range of entrainment rates prescribed by the structural similarity and the energy balance. It was found that the interface between turbulent and non-turbulent fluid advances into the ambient fluid probably by small-scale motions, but the rate of entrainment depends on continuous deformation and folding of the interface. The small-scale erosion of the ambient fluid is really the last stage of the entrainment by folding and engulfing by the large-scale motion of the interface. The differences in entrainment rates between flows are attributed to the relative durations of the active and quiescent periods and to the magnitude of the entrainment rate during the active periods.

In the study by Paizis and Schwarz,[40] it is accepted that the ambient irrotational fluid acquires vorticity by viscous diffusion and this vorticity is amplified by the rate of strain field. A certain portion of the fluid drawn towards the turbulent flow remains irrotational and is dragged along the turbulent interface. A rigorous definition of the entrainment rate of turbulent flows has been proposed as the mean of the instantaneous rate of increase of turbulent fluid with the downstream distance. The reason for this alternative definition to the conventional one -- which has the form of the product of a characteristic velocity scale with the growth rate of a characteristic length scale -- was the fact that the conventional definition is meaningless for flows that are not self-preserving and crude for self-preserving flows. Estimates of

entrainment rate were made for the two-dimensional jet, round jet, two-dimensional wake and turbulent boundary layer.

The technical note by Bevilaqua and Lykoudis[41] was prepared to outline their reasons for rejecting the small-scale mechanism hypothesis. Some experimental evidence for the existence of large-scale mixing jets which overlap and engulf large volumes of fluid at a time was also described. The superlayer (or surface layer) hypothesis, introduced by Corrsin and Kistler,[42] suggested that the interface is a thin fluid layer in which the turbulence is diffused by viscosity. From a critical re-examination of the assumptions and implications of the superlayer hypothesis, they have concluded that entrainment is a process that more nearly resembles a folding of the turbulent and non-turbulent fluids by the rotation of the large eddies.

The large structure of the turbulent/non-turbulent interface is believed by Bremhorst and Harch[43] to be the significant factor in the entrainment process. Their measurement showed that the entrainment and entrainment rate of a fully pulsed air jet are considerably higher than for a steady jet. Based on the assumption that entrainment in this type of jets is principally due to the intrinsic turbulence component, they concluded from autocorrelations of the intrinsic turbulence of fully pulsed jets that the size of the interface indentations is significantly larger than for steady jets. A direct consequence of this behavior is the much larger entrainment of irrotational exterior fluid in fully pulsed jets.

III. EXPERIMENTAL APPARATUS AND TECHNIQUES

A schematic drawing of the experimental set-up is presented in Figure 5. Ambient air is supplied to a 1 HP centrifugal blower. The air passes through a piping system, an orifice plate and two flow regulating valves. For the case of heated jets, a bypass channels the air through a 4.5 kW electric heater having a range of approximately 90° - 250° C. The flow rate through the system is determined from pressure drop measurement across the orifice. This flow rate is compared with that obtained from velocity measurements at the discharge.

The air is directed to a settling chamber housing the channel. A 6.35 cm thick piece of aluminum honeycomb sheeting (0.64 cm mesh spacing) marks the entranceway to the wooden settling chamber. The honeycomb sheet serves as a device to enhance the break up of large turbulent eddies and as a means of providing a more uniform incoming flow. The channel entrance has a contoured inlet to help direct and align the flow and is of sufficient length so as to eliminate any entrace effects. To provide fully developed velocity profiles at the discharge, all channels have a length to height ratio, L^*/d^*, greater than 50. The respective channels exhaust the air jet into the test section through rectangular openings in a 100 x 100 cm vertical wall. This wall forms a 90° corner with an adjustable horizontal adiabatic offset surface along which the jet flows. Both surfaces (vertical and horizontal) are wood covered with formica sheeting. The horizontal surface is 244 cm long and 122 cm wide, consisted of a 0.08 cm formica sheet laminated to 2.54 cm thick plywood, and the underside is covered with fiberglass foam sheeting insulation. The distance between the offset surface and the discharge can be adjusted by varying the elevation of the table.

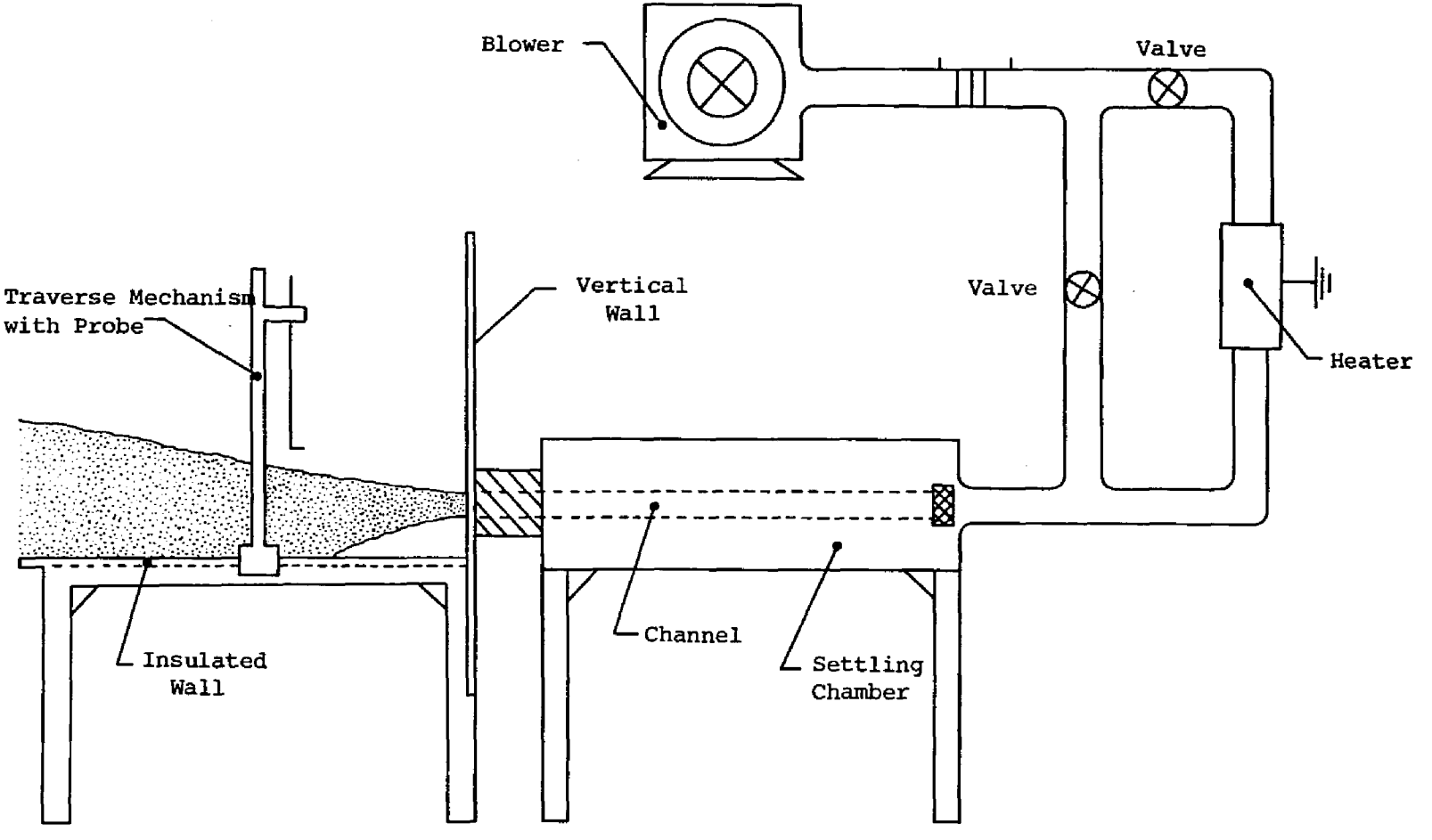

Figure 5. Experimental arrangement.

The experimental set-up is only partially enclosed to permit jet heat dissipation into a larger surrounding space while eliminating extraneous cross-currents. Four types of "United Sensor" probes were used: (i) a 0.05 cm boundary layer total head proble, (ii) a 0.16 cm Pitot-static pressure probe, (iii) a 0.32 cm copper-constantan combination Pitot-static and temperature probe, and (iv) a three-dimensional directional probe (five-holes probe). The various probes were calibrated in a low speed wind tunnel and were found to have coefficients between 0.998 and 1.002.

Surface pressure measurements were made on an especially designed plexiglass plate with pressure sensors connected to surface taps. A single row of 0.04 cm diameter holes were drilled through the 1.27 cm thick plexiglass horizontal plate along the axial direction, x^*. To map surface pressure in the z^*-direction, the plate was designed to move laterally. This arrangement eliminates the need for an excessive number of surface taps.

An alternate method of measuring surface pressure has been also tested. According to this method, measurements were made with pressure sensors connected to a disc probe (for details, see Appendix B). The data collected with this probe were found to be very inaccurate, especially in the wall jet type region.

A "Validyne CD15" carrier demodulator, a "Validyne DP15" pressure transducer and a "Disa 55D31" digital voltmeter were used to measure pressure differences (Figure 6). The transducer-demodulator set was calibrated before and after each series of experiments (for details, see Appendix D). The outputs of the temperature probe and that of the ambient thermocouple were connected to an "Omega Engineering 199" digital readout indicator (Figure 7).

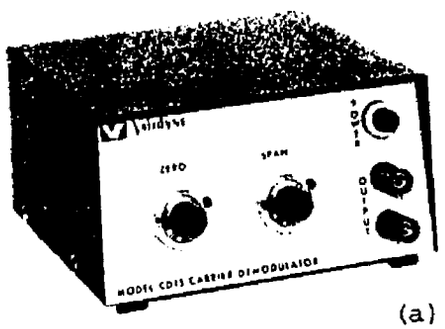

(a)

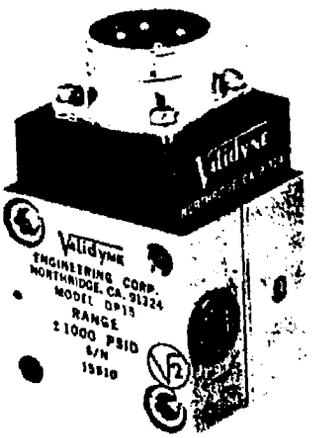

(b)

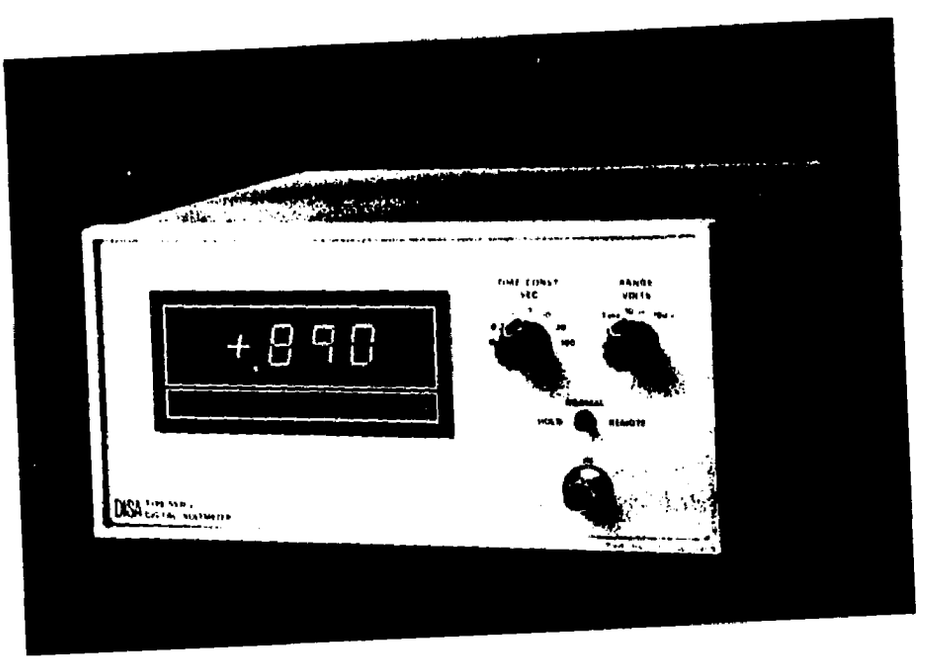

(c)

Figure 6. (a) Demodulator (b) Transducer (c) Voltmeter.

A traverse mechanism (Figure 8), on which a probe mount assembly was fastened, rides along guides in the longitudinal direction. Two 1/50 HP "Bodine" motors and "Minarik" motor drivers provide a traverse in both vertical and horizontal directions for a fixed longitudinal location along the table. The probe mount has a gear tooth assembly for rotation in the x-y and x-z planes and has the capability to hold two probes simultaneously (Figures 9 and 10).

The location of pressure and temperature probes in the jet field are determined using three orthogonal location scales appropriately mounted on the traversing mechanism system.

Three channel sizes were used: 0.95 x 9.64, 3.56 x 14.17 and 1.95 x 4.47, all measured in centimeters. These correspond to nominal aspect ratios, e = 0.1, 0.25 and 0.44, respectively. The average discharge axial velocity U_o^* was varied from approximately 18.3 to 48.2 m/sec. Corresponding discharge Reynolds numbers Re_o, based on channel height, d*, were well within the turbulent limit, ranging from 2.6×10^4 to 5.5×10^4.

The patterns of air flow adjacent to the offset surface were made visible by employing the oil/lampblack technique.[45] According to this technique, the offset surface is coated with a thin film of a lampblack and oil mixture and then exposed to the airflow. Under the action of the shear stresses exerted by the air on the surface, the mixture is caused to flow along the surface in the flow direction. The result is a streak pattern which reveals the path of the air as it passes over the surface. For the present experiments, a ten to one mixture (weight proportion of oil to lampblack) was found to give satisfactory results. The oil was a red manometer fluid.

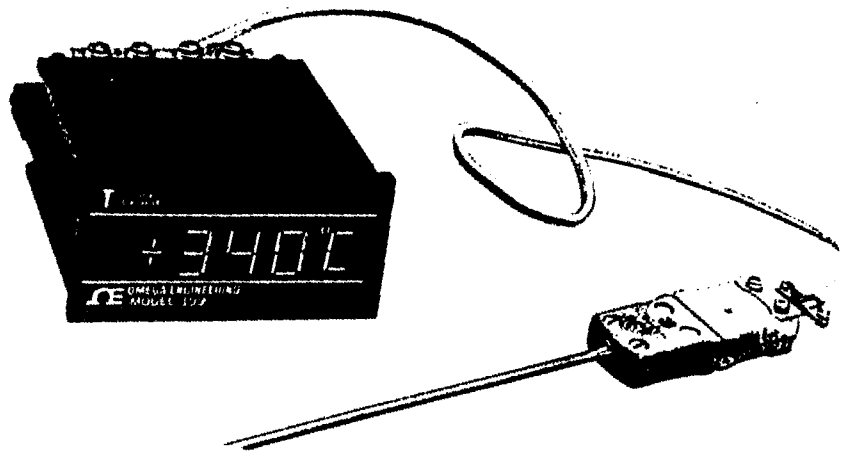

Figure 7. Temperature Indicator.

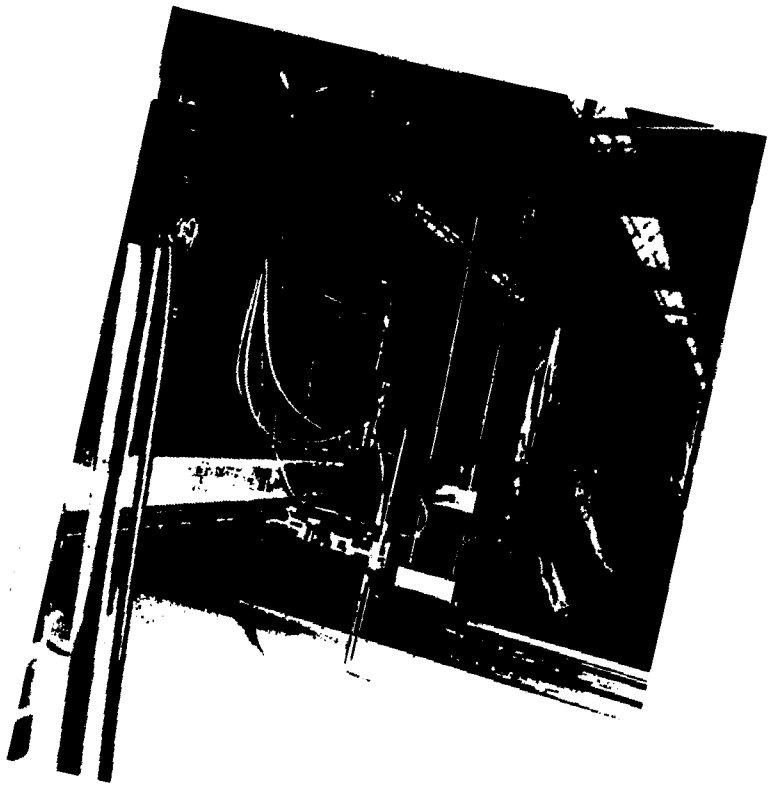

Figure 8. Traverse mechanism and probe mount assembly.

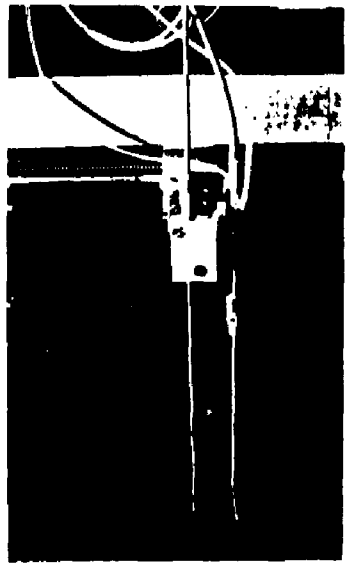

Figure 9. Probe mount assembly
(front view)

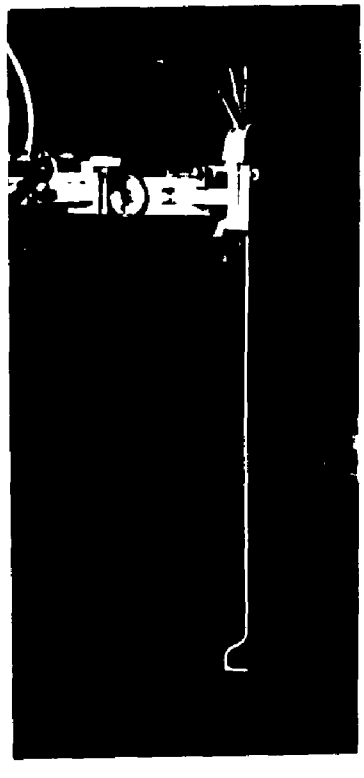

Figure 10. Probe mount assembly
(side view)

The overall picture of the entire flowfield was made visible by employing the smoke injection technique. A white smoke is produced at the blower's inlet by ignition of "Superior" smoke candles which last 60 or 30 seconds according to their size.

IV. RESULTS

The flow and thermal behavior of jet-boundary interaction may be described by specifying surface pressure distributions, spread rates, maximum velocity and temperature decay rates, and vertical and spanwise profiles. This study investigates the mean flowfield and temperature characteristics of rectangular offset jets having various aspect ratios and at various offset distances from a horizontal surface.

1. Surface Pressure

Extensive data were obtained on the surface pressure distribution, $P_s^*(x^*, z^*)$, at different discharge Reynolds number Re_o, aspect ratio e and offset distance h. In all tests the nominal air temperature at the discharge was approximately 40^oC and the ambient temperature 31^oC. The effect of discharge Reynolds Re_o on the pressure coefficient C_p along the wall centerline is shown in Figure 11 for an aspect ratio e = 0.44 and an offset distance h = 0.61. The general features of C_{p_c} for the three Reynolds numbers considered (Re_o = 26,300; 39,100; 55,400) are similar. Although little change in pressure is observed as Re_o is increased from 26,300 to 39,100, pressure peaks are found to amplify significantly at Re_o = 55,400. However, at this Reynolds number considerable fluctuations in surface pressure were recorded in the region of $4 < x < 13$.

Sudden expansion near the discharge and entrainment of the surrounding fluid due to the turbulent mixing results in sub-ambient pressure on the wall

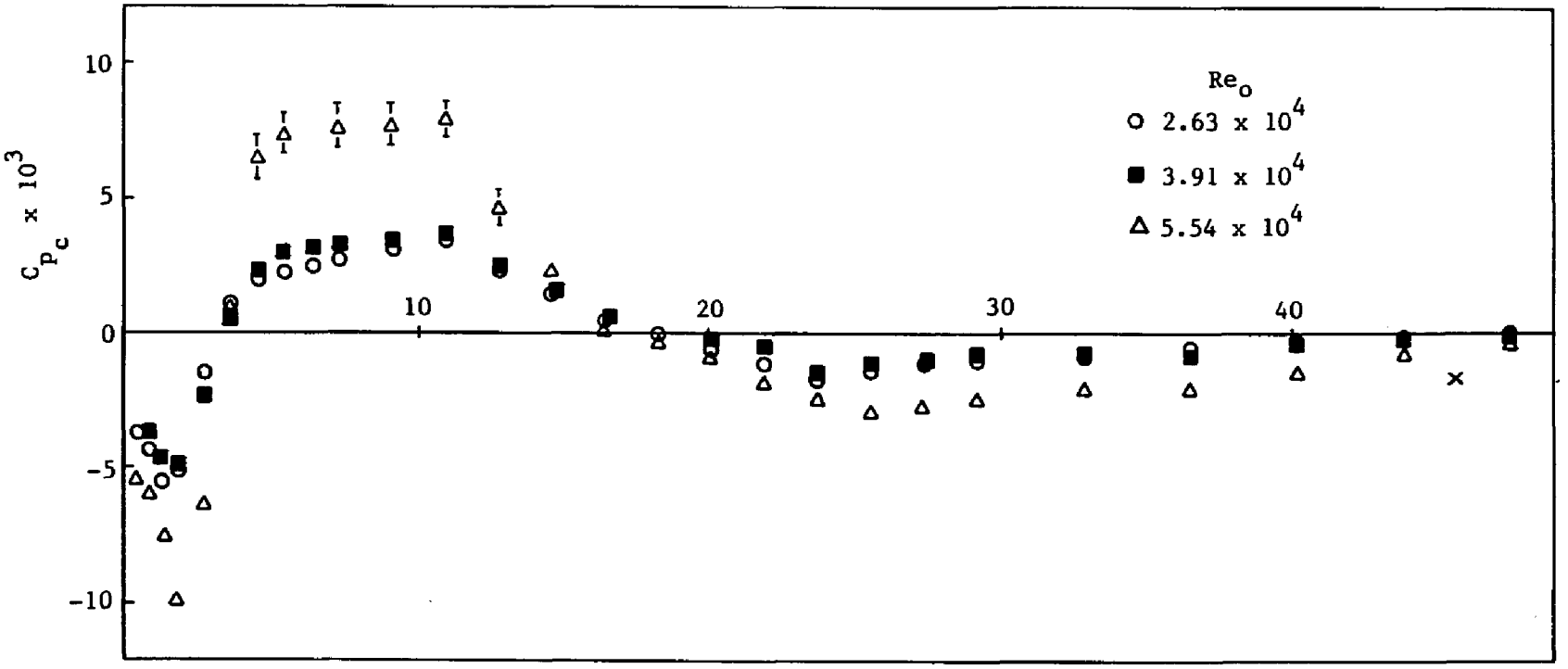

Figure 11. Effect of discharge Reynolds number on axial surface pressure distribution (e=0.44, h=0.61, z=0)(Table B3).

causing the jet to bend towards the surface and giving negative values for C_p as shown in Figures 11-16. This behavior is also characteristic of two-dimensional offset jets (Figure 17) and is known as the Coanda effect.[4, 6, 7, 10, 12] As the jet approaches the horizontal surface, it decelerates resulting in an increase in C_p which becomes positive close to the reattachment position $x = x_r$ where the jet impinges on the surface. Beyond the reattachment position, C_p reaches a maximum positive value with the jet remaining attached to the surface and eventually behaving as a wall jet (reattached wall jet). Correspondingly, the pressure coefficient drops reaching negative values before increasing and asymptotically vanishing further downstream. This second region of sub-ambient pressure is caused by jet expansion and curvature over the thickening surface boundary layer in the reattached wall jet. Although the peaking of C_p and its subsequent drop have been observed in two-dimensional jets,[4, 6, 7, 10, 12, 43] negative values downstream of x_r have not been previously reported. Careful examination of published surface pressure data shows that several investigators[4, 7, 10, 43] terminated pressure measurements where they first reached ambient level downstream of reattachment position x_r. Those who extended surface pressure measurements further downstream[6, 12] observed that the pressure remains at ambient level. Similarly, studies on ventilated two-dimensional offset jets[13-16] showed that once surface pressure drops to ambient level downstream of x_r, it remains constant at the ambient value. However, Marsters[14] recorded a small negative pressure at a single location downstream of x_r for $h = 6.75$ only. This slight local shift to negative pressure coefficient gives the appearance of data scatter, rather than an indication of a trend in surface pressure, which may explain why it was not discussed or commented on. El-Taher[15] and Shibl and Shaalan[16] examined the effect of surface curvature on surface pressure distribution. They found that for convex surfaces wall pressure

drops below ambient level downstream of x_r and remains negative. This negative pressure decreases as the radius of curvature is increased.

Comparisons of surface pressure distributions with velocity vectors mappings and flow visualization pictures indicate that the reattachment location corresponds more closely to the position at which the pressure coefficient changed sign, rather than the position of maximum surface pressure observed in two-dimensional jets with large offset ratio case.[4]

The negative-positive-negative feature of surface pressure coefficient at the wall centerline (x, 0, 0) was found to characterize three-dimensional offset jets at various values of aspect ratio e and offset distance h, as shown in Figures 11-16. This behavior persists at lateral distances z within the channel halfwidth, i.e., z less than 1/2e, as shown in Figure 12. For a discharge with aspect ratio e = 0.25, the outlet extends to z = 2 in the lateral direction. Figures 12 and 14 suggest that, for e = 0.25, z = 2 appears to be the approximate limit for the negative-positive-negative behavior of surface pressure. At z greater than 2, the peaks are attenuated in magnitude and no negative pressure develops downstream of the reattachment position. It is interesting to note that the maximum peaks do not occur at the centerline (z = 0). Figures 12 and 13 show that the first two peaks along x are more pronounced at z = 1 than z = 0. The complex two-dimensional surface pressure distribution is illustrated in Figure 14 where isopressure curves are mapped.

Tests were carried out for various outlets to examine the effect of discharge aspect ratio on surface pressure. Figure 15 shows surface pressure distribution along the wall centerline for e = 0, 0.1, 0.25 and 0.44. To reveal the

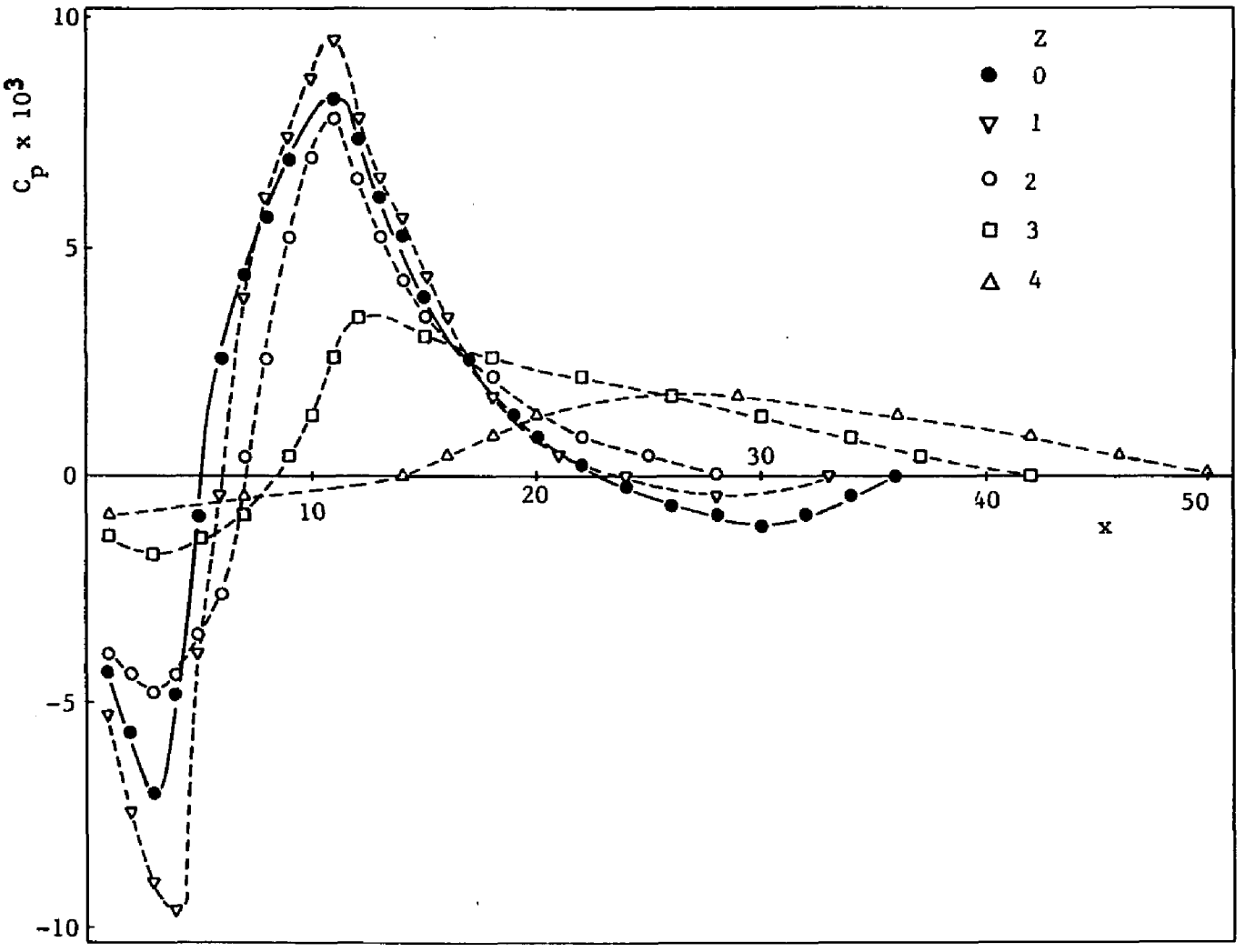

Figure 12. Effect of lateral distance on axial surface pressure distribution (e=0.25 , h=1 , $Re_o=3.9x10^4$) (Table B1)

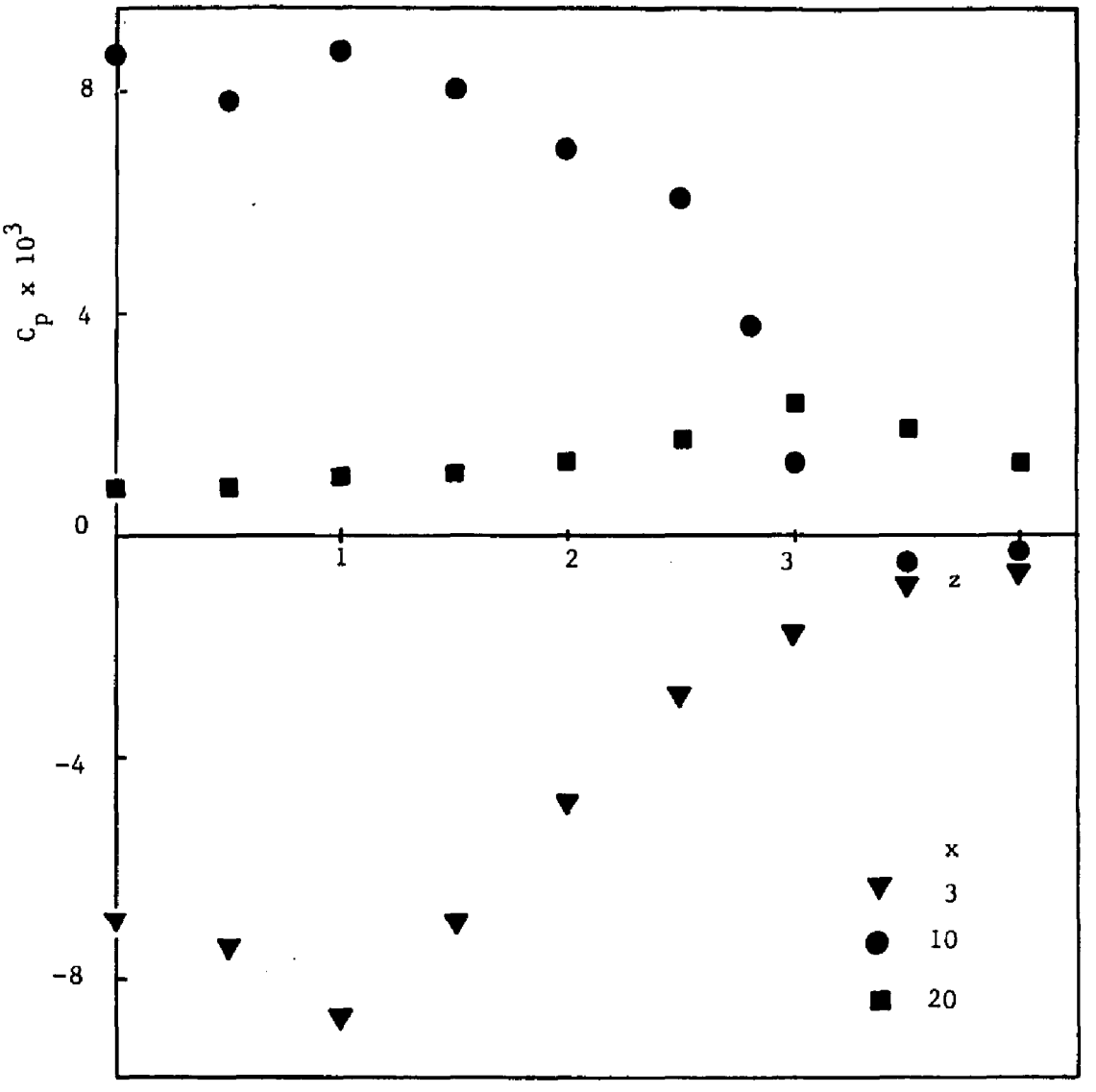

Figure 13. Effect of axial distance on lateral surface pressure distribution (e=0.25 , h=1 , Re_o=3.9x10^4)(Table B2)

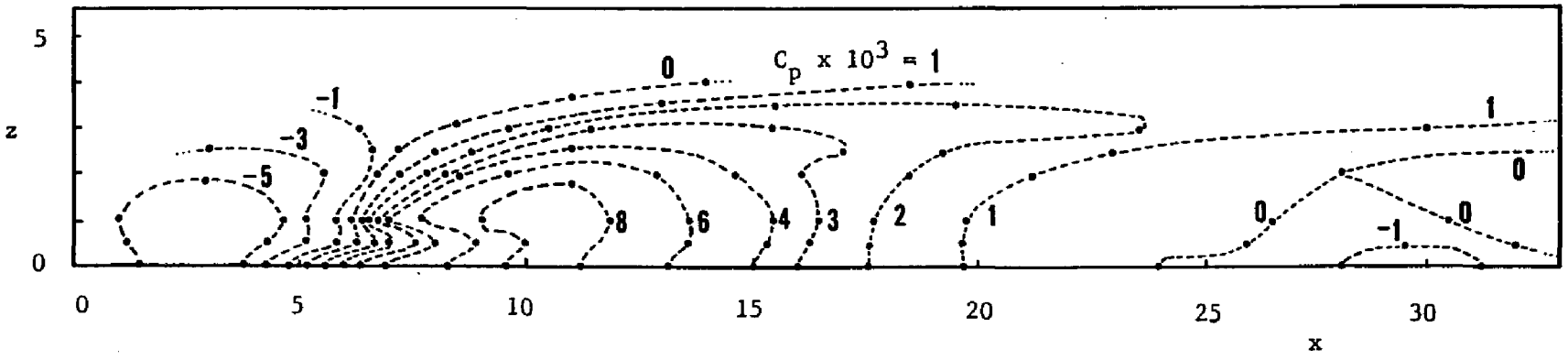

Figure 14. Dimensionless surface isopressure map (e=0.25 , h=1 , Re_o=3.9x10^4) (Table B1)

details of pressure behavior downstream of the reattachment points, the pressure coefficient scale is magnified for x greater than 12. The negative pressure peaks just downstream of the discharge and the positive peaks after the reattachment are enhanced as the aspect ratio e is decreased. These peaks reach their maximum level for e = 0, which corresponds to a two-dimensional slot jet. This case represents a slot of infinite length having no lateral entrainment. Experimentally it is simulated by placing a vertical plate on each side of the outlet. The lower pressure peaks associated with three-dimensional outlets are attributed to lateral entrainment, which is absent in two-dimensional jets. This entrainment tends to relieve the pressure along the wall centerline resulting in lower pressure levels when compared to two-dimensional slot jets. Another consequence of lateral entrainment is the shifting upstream of pressure peaks as the aspect ratio is decreased, approaching its limit at e = 0.

Careful measurements of pressure distribution downstream of the reattachment location show that sub-ambient pressure readings were observed in this region for e = 0.1, 0.25 and 0.44 (Figure 15). The magnitude of pressure readings in this region is very small, typically $P_s^* - P_\infty^* \approx 0.08$ mm water and therefore it can be mistakenly considered zero unless a sensitive pressure recording instrument is used.

The axial surface pressure distribution along the wall centerline, C_{p_c}, corresponding to values of the offset distance h ranging from 0.35 to 2.9 is shown in Figure 16. The effect of h on centerline pressure is qualitatively similar to that of the aspect ratio e shown in Figure 15. Also a comparison with Figure 17, which represents distributions of the two-dimensional case (e = 0), shows a completely different behavior as the offset distance changes.

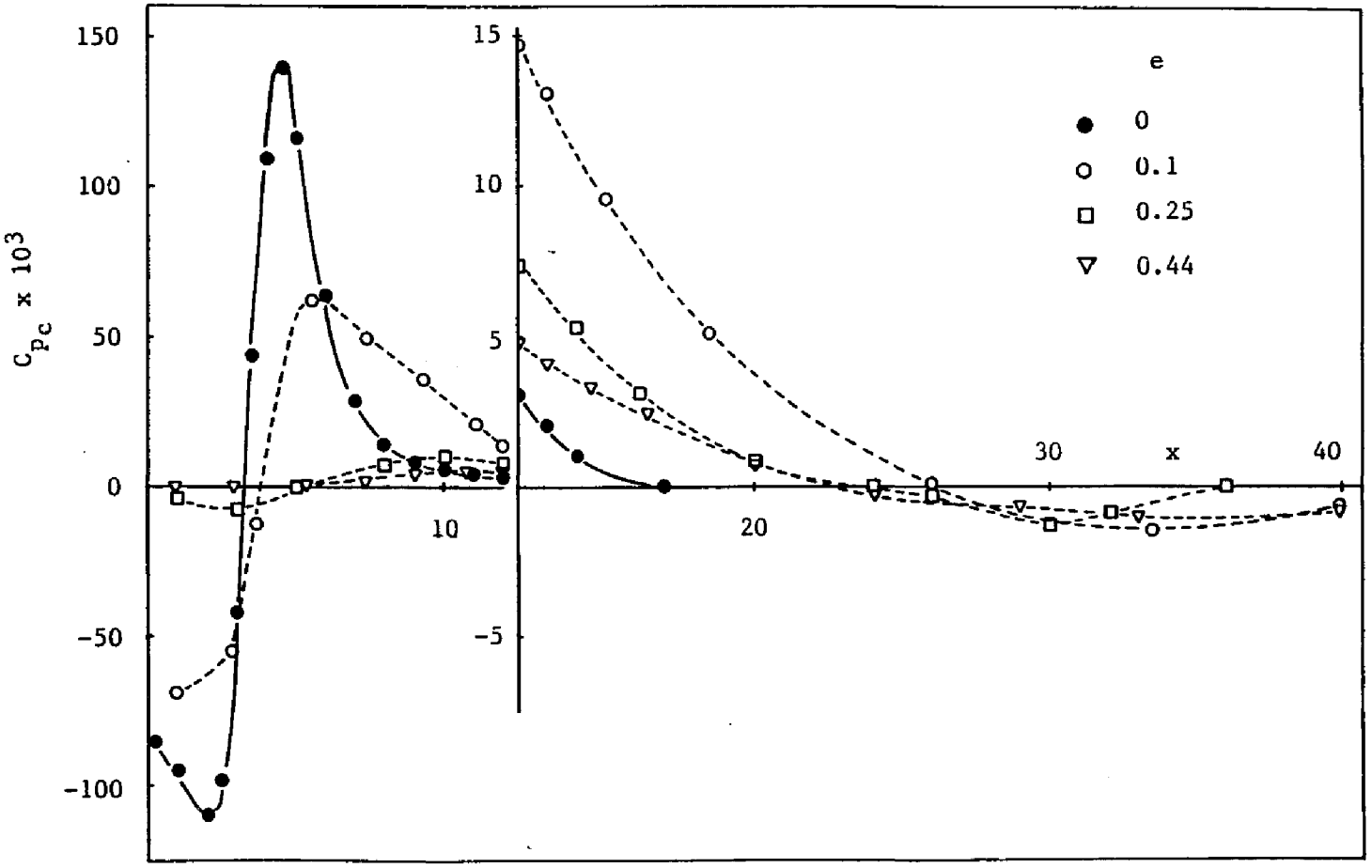

Figure 15. Effect of discharge aspect ratio on axial surface pressure distribution (h=1, z=0, Re_o=3.9x10^4) (Tables B4, B5 and B6)

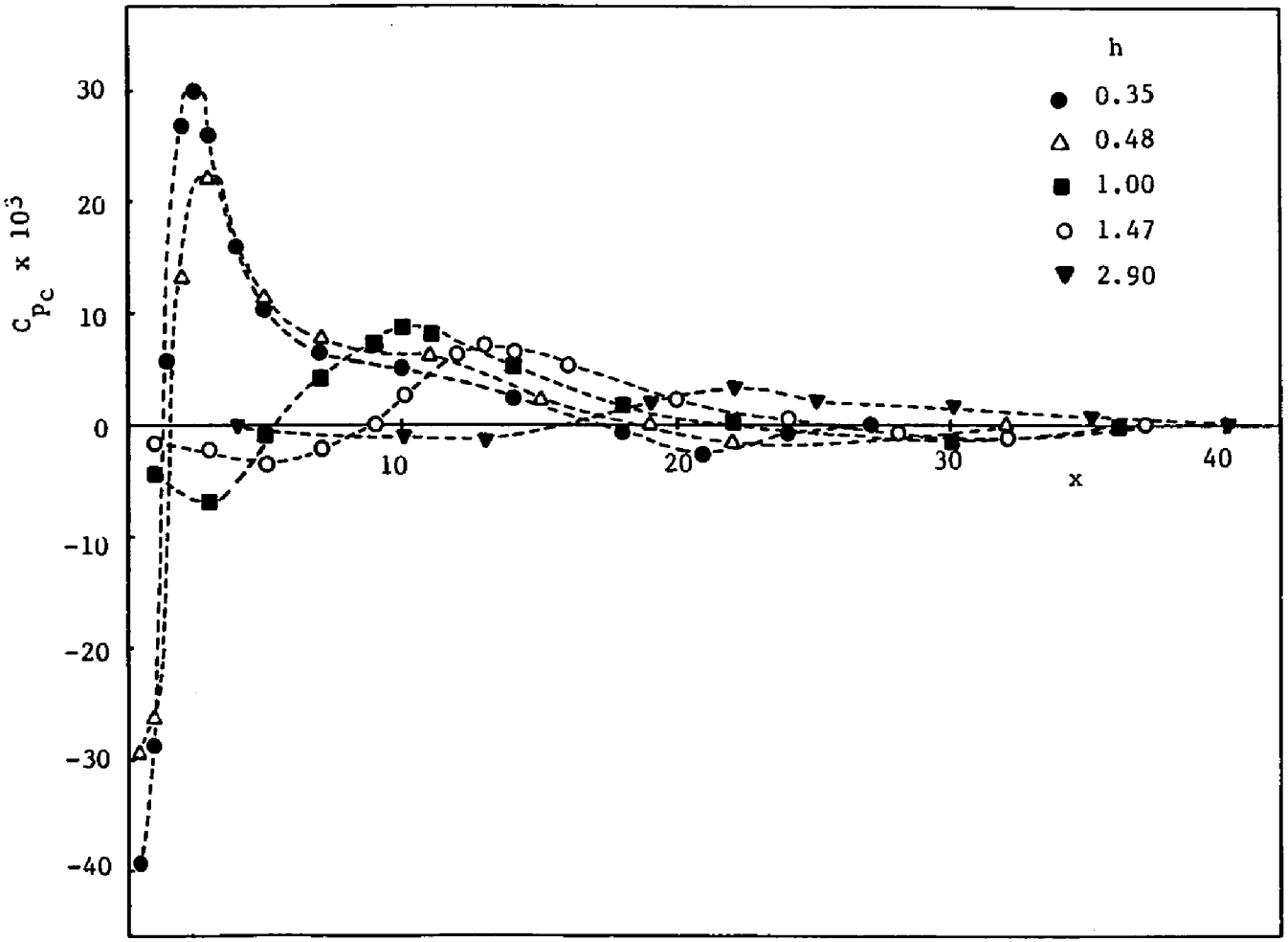

Figure 16. Effect of offset distance on axial surface pressure distribution (e=.25, z=0, Re_o=3.9x10^4) (Table B4)

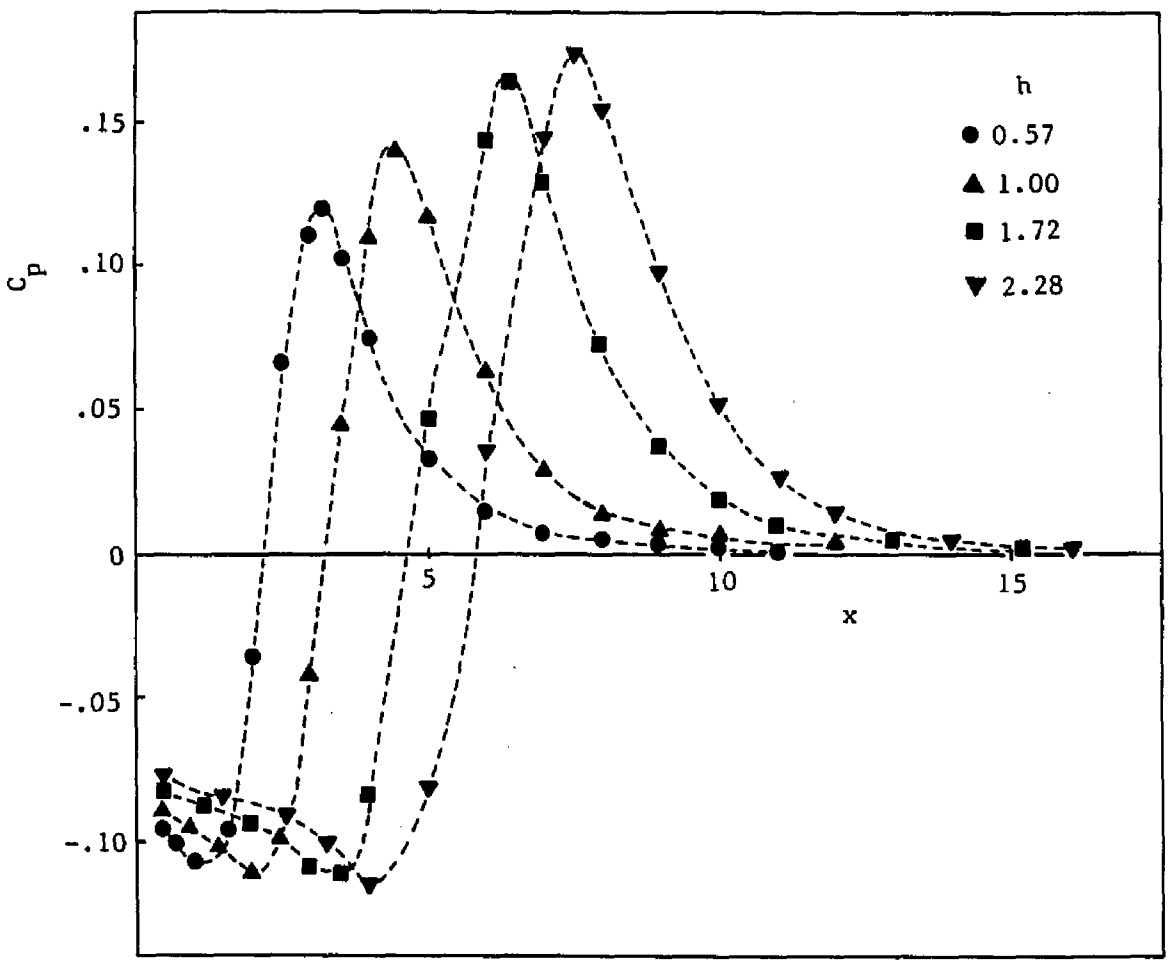

Figure 17. Effect of offset distance on axial surface pressure distribution for two-dimensional offset jet (Re_o= 3.9 x 10^4) (Table B6)

The maximum pressure coefficient $C_{p_c}max$ which occurs downstream of the reattachment is plotted against h in Figure 18. Data for three-dimensional jets with aspect ratios e = 0.1, 0.25 and 0.44 are compared with the limiting case of the two-dimensional slot jet (e = 0). Striking differences between the two configurations are observed. For three-dimensional jets $C_{p_c}max$ is significantly lower than that of two-dimensional slot jets. For example, at h = 0.5, $C_{p_c}max$ for e = 0.44 is an order of magnitude lower than the two-dimensional value and at h = 3 it is two orders of magnitude lower. Furthermore, a decrease in h brings about a decrease in $C_{p_c}max$ for two-dimensional jets while it causes an increase in $C_{p_c}max$ for three-dimensional jets.

The behavior of surface pressure for small values of h requires careful consideration. For small values of the dimensional offset distance h* compared to the discharge width ℓ^*, centerline surface pressure in the vicinity of the discharge should approach that of two-dimensional slot jets. Expressing this ratio in dimensionless form gives $h^*/\ell^* = eh$. Thus, two-dimensional behavior should be approached when h is very much less than 1/e. From this it follows that the larger the aspect ratio, the smaller h must be to obtain pressure values of two-dimensional jets. This is clearly shown in Figure 18 in which $C_{p_c}max$, which occurs in the vicinity of the discharge, is examined. For e = 0.1, $C_{p_c}max$ approaches its two-dimensional value at h approximately equal to 0.5. At this offset distance $C_{p_c}max$ for e = 0.44 is still an order of magnitude lower than the value corresponding to two-dimensional jets. However, decreasing h further brings the values of $C_{p_c}max$ asymptotically closer to their two-dimensional level. In the limiting case of a wall jet, h = 0, the pressure throughout the jet is essentially equal to ambient value and therefore $C_p = C_{p_c}max = 0$. Thus, at very small values of h (i.e., $h < 0.15$) the $C_{p_c}max$ curves for all aspect ratios should

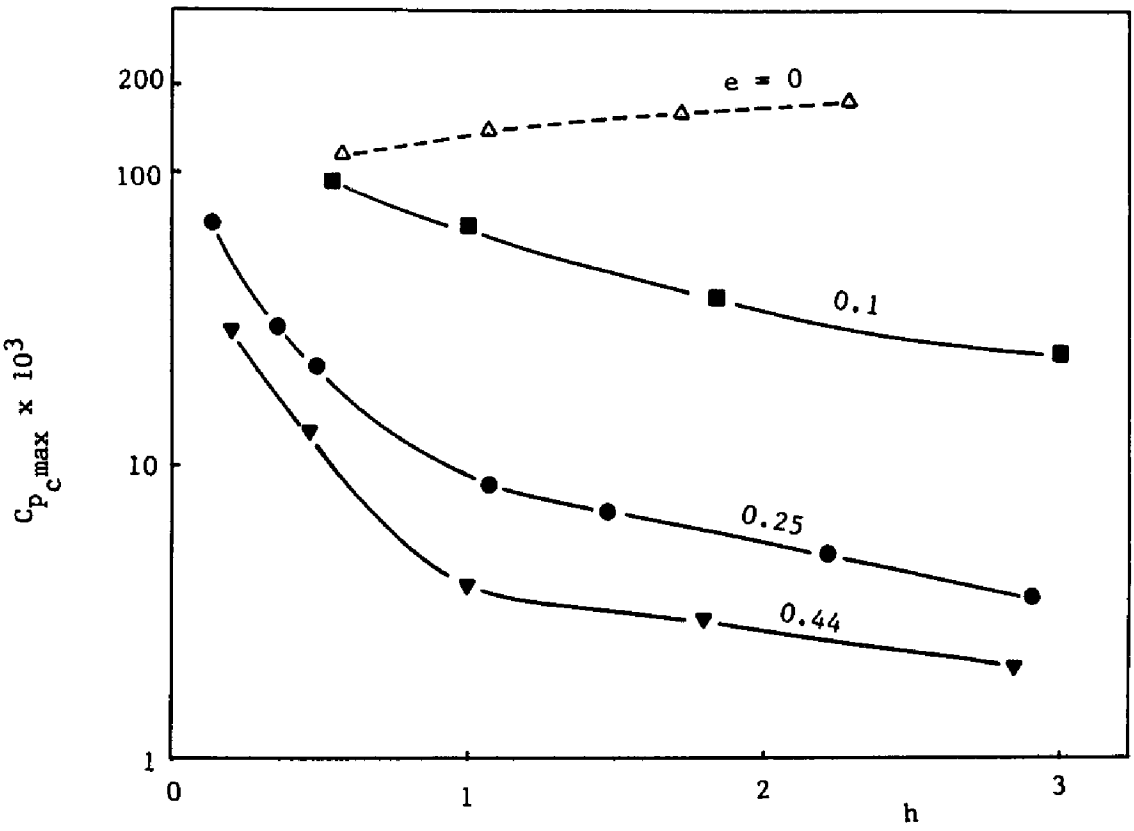

Figure 18. Effect of offset distance on the maximum surface pressure coefficient for two- and three-dimensional offset jets (z=0, Re_o= 3.9 x 10^4) (Table B7)

coalesce into a single curve along which $C_{pc}max$ decreases as h is decreased (two-dimensional behavior), vanishing at h = 0. It was not possible to verify this asymptotic behavior with the present experimental apparatus. To do so requires accurate positioning and measurement of small offset distances ($h^* < 0.2$ cm) and surface pressure measurements at several distances close to the outlet ($x_r^* < 1$ cm). Difficulties were encountered in attempting to examine surface pressure near the discharge for the limiting case of a wall jet (h = 0). It was found that a small mismatch between the discharge channel surface and the offset surface of the order of 0.05 cm produced significant non-zero surface pressure readings near the outlet.

The behavior of the reattachment position x_r is shown in Figures 19 and 20. The results of Kumada et al.[12], Parameswaran et al.[10] and Bourque et al.[4] for the limiting two-dimensional case are also shown. Agreement with the present results for e = 0 is good in the range of examined offset ratios. The variation of reattachment distance x_r with the offset ratio h, at various values of e, is given by the experimental lines (Figure 19):

$$x_r = 1.186 + 2.20\,h \qquad (e = 0)$$

$$x_r = -0.960 + 5.92\,h \qquad (e = 0.25)$$

$$x_r = -0.800 + 6.67\,h \qquad (e = 0.44)$$

It is shown that the reattachment distance in three-dimensional jets is significantly larger than that corresponding to the two-dimensional jet. This may be attributed to the fact that in the two-dimensional case the decrease in the wall pressure and the corresponding increase in the curvature of the jet are more pronounced than in three-dimensional jets.

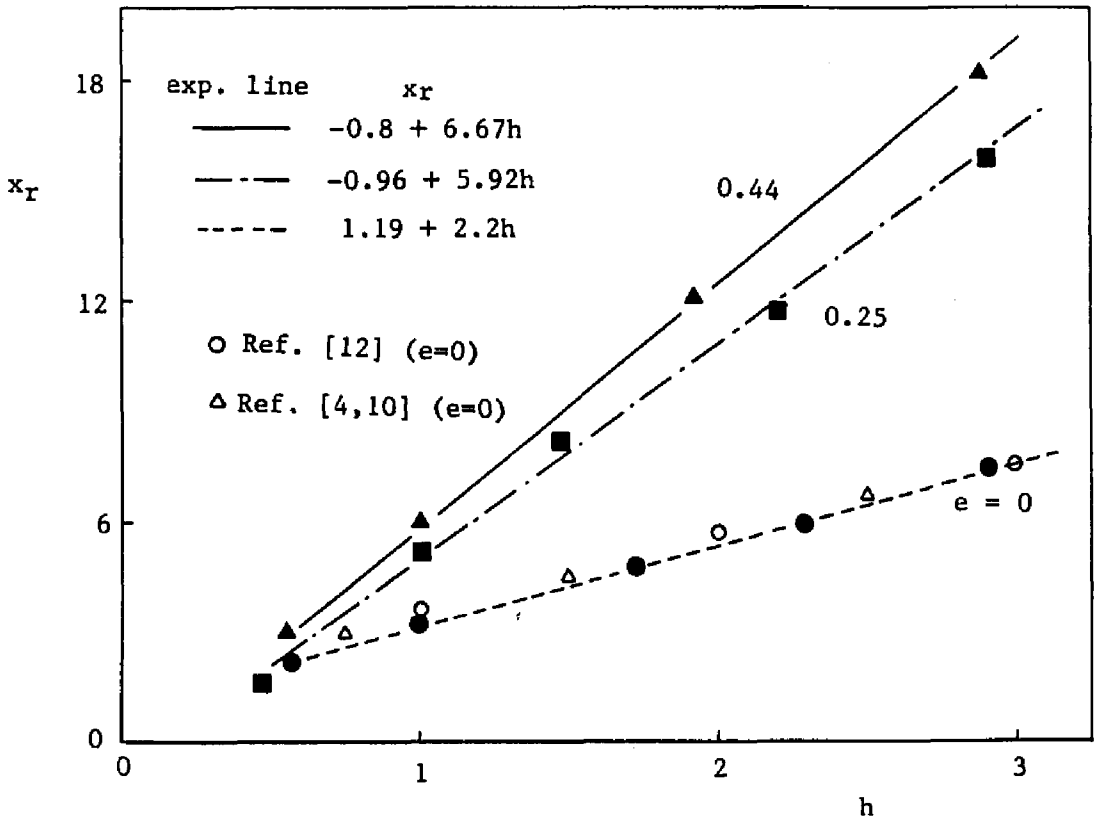

Figure 19. Variation of reattachment distance with offset distance for two- and three-dimensional offset jets (z=0, Re_o = 3.9 x 10^4) (Table B8)

The ratio x_r/h for $0.5 < h < 2.9$ indicates a significantly different behavior between the two- and three-dimensional jets (Figure 20). In the two-dimensional jet case (e = 0), x_r/h decreases and asymptotically approaches a value of 2.4 as h is increased. However, for three-dimensional jets (e = 0.25 and 0.44), x_r/h increases and reaches asymptotically the values of 5.5 and 6.5, respectively.

The variation of the axial distance corresponding to the maximum centerline surface pressure, x_a, with the offset ratio h is presented in Figure 21. From the plot it appears that the location of the positive surface pressure peak also shifts downstream with increasing offset distance and/or aspect ratio. It is also shown that x_a is independent of aspect ratio at $h \approx 0.55$ and is given by the value of 3.25.

The variations of the parameters $(C_{p_c max} \cdot x_r/h)$ and $(C_{p_c max} \cdot x_a/h)$ with respect to the offset distance h for the two- and three-dimensional cases are given in Figures 22 and 23, respectively. The tendency of the curves corresponding to three-dimensional jets (e = 0.25 and 0.44) to approach the behavior observed in the two-dimensional case (e = 0) for small values of offset distance can be seen in both figures. It is interesting to note that the $(C_{p_c max} \cdot x_r/h)$ parameter for the two-dimensional case is approximately independent of the offset distance and is given by the value of 0.44. Both parameters decrease as the aspect ratio increases.

2. Velocity Field

Velocity measurements at the outlet of several channels under different exit conditions showed that the discharge profiles tend to depart somewhat from

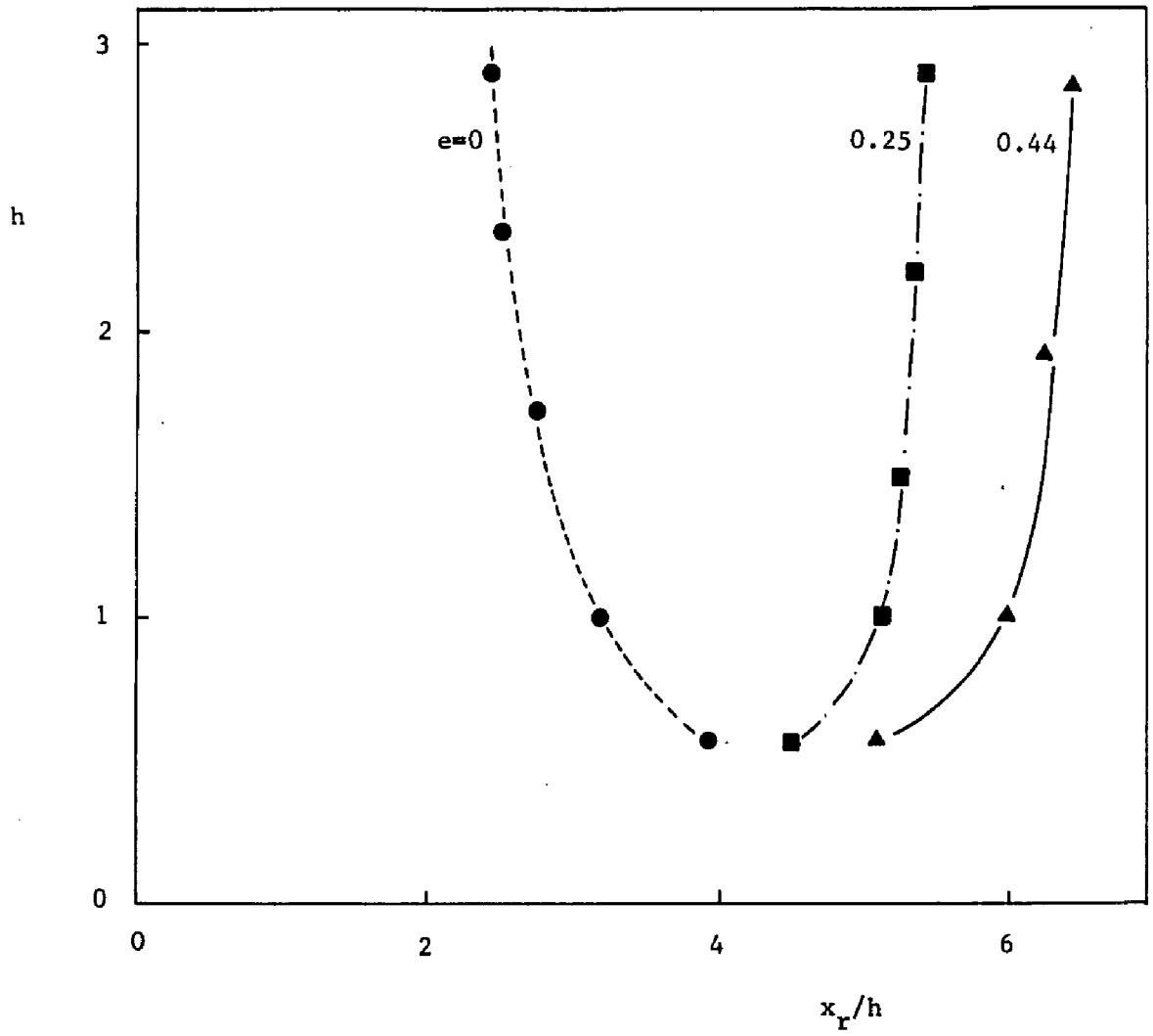

Figure 20. Variation of reattachment to offset distance ratio with offset distance for two- and three-dimensional offset jets (z = 0, $Re_o = 3.9 \times 10^4$)(Table B8)

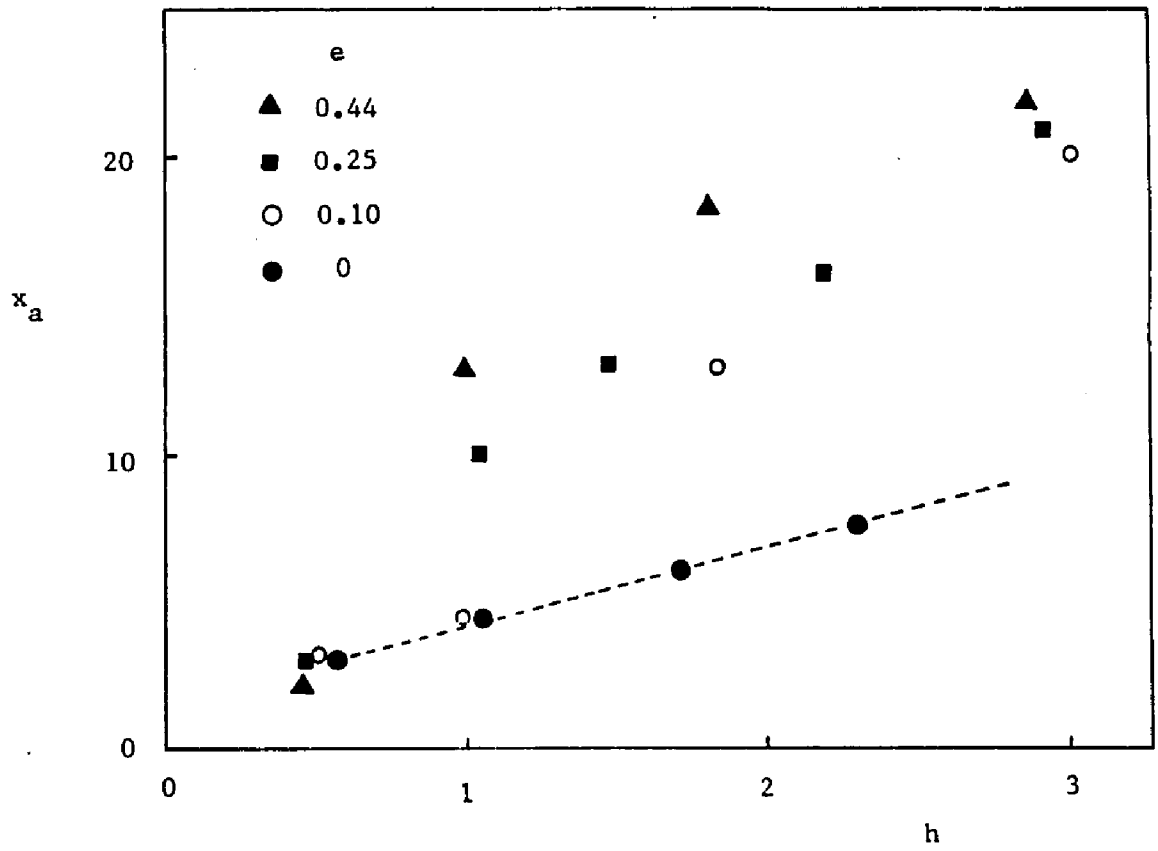

Figure 21. Variation of maximum C_p distance with offset distance for two- and three-dimensional offset jets ($z = 0$, $Re_o = 3.9 \times 10^4$)(Table B9)

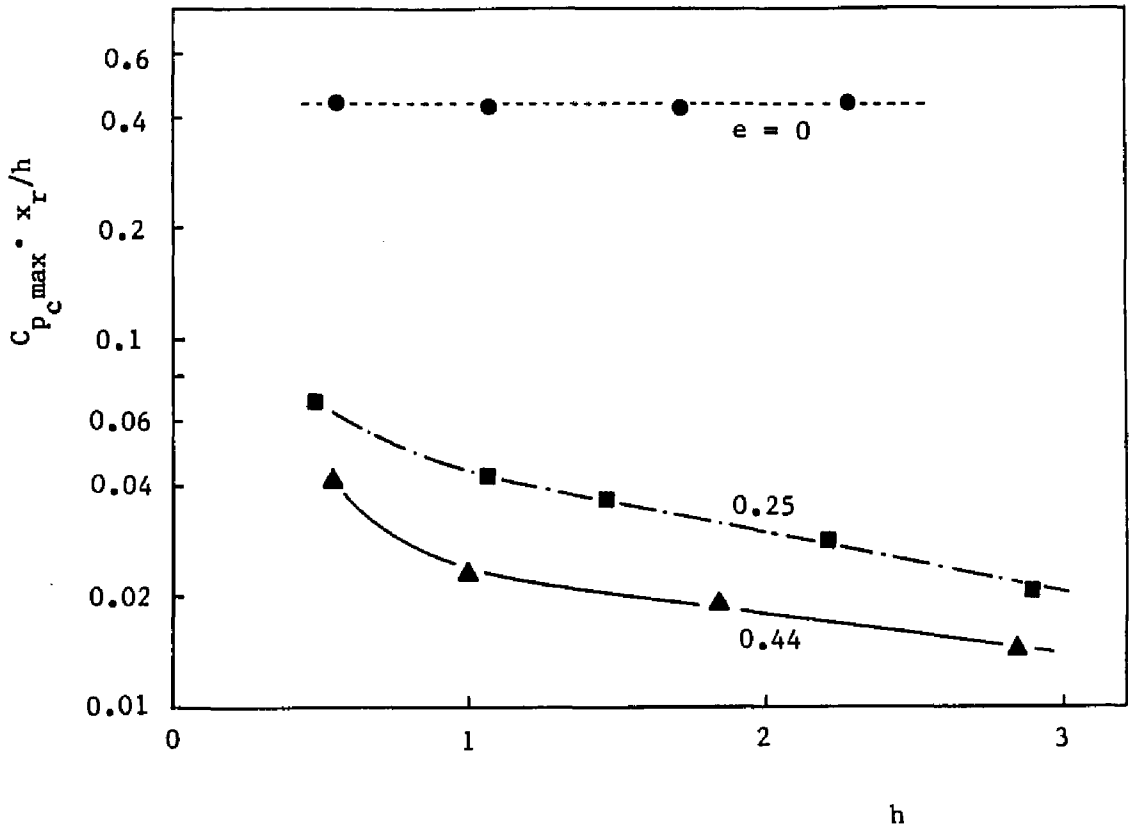

Figure 22. Variation of $C_{p_c max} \cdot x_r/h$ with offset distance for two- and three- dimensional offset jets (z=0 , $Re_o = 3.9 \times 10^4$) (Table B7 and B8)

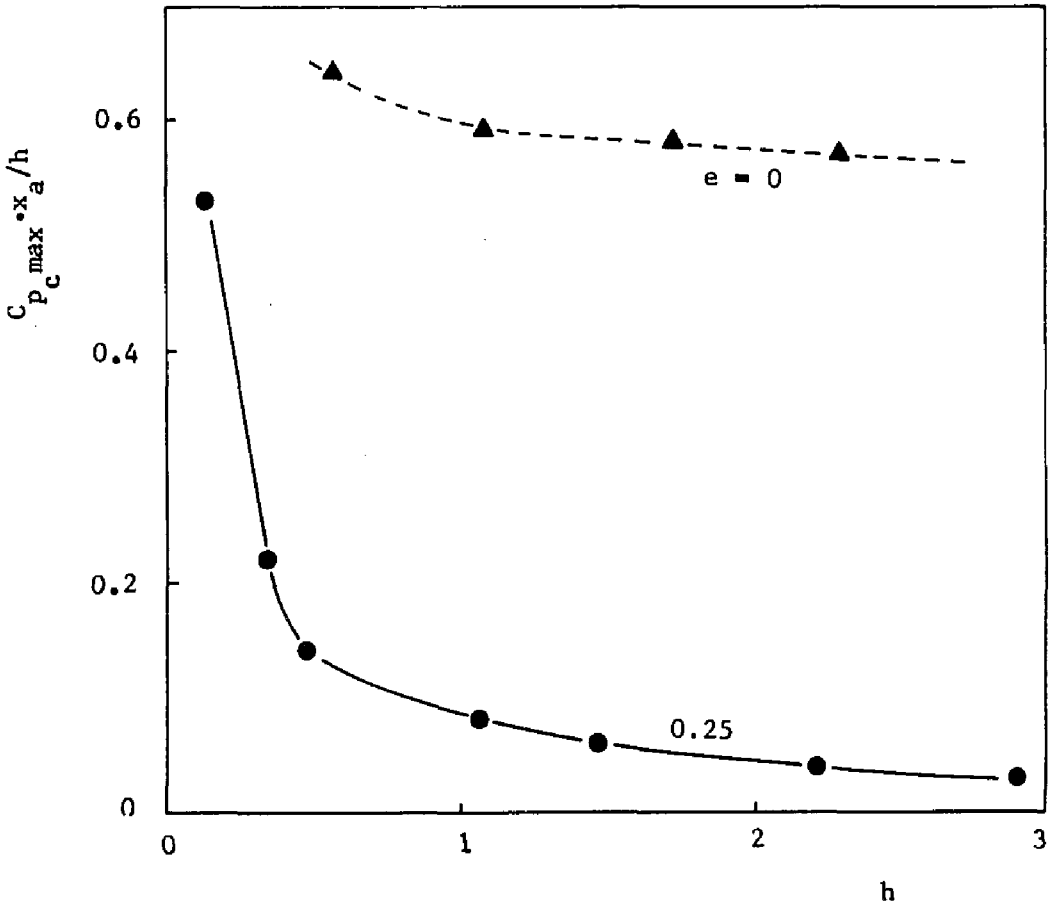

Figure 23. Variation of $C_{p_c max} \cdot x_a/h$ with offset distance for two- and three-dimensional offset jets (z = 0, $Re_o = 3.9 \times 10^4$) (Tables B7 and B9)

the top-hat shape. Figure 24 shows mean velocity profiles for two channels, e = 0.1 and e = 0.44, under typical flow conditions.

The development of the vertical profiles of velocity along the x-direction for a typical case (e = 0.44, h = 4.85) was examined at $z^* = 0$ and $z^* = 0.4\ell^*$ planes and is presented in Figures 25 and 26, respectively. The centerplane (z = 0) velocity distributions near the discharge (i.e., x = 5 and x = 10) show a behavior similar to that of free jets, whereas further downstream (i.e., $x \geq 25$) the profiles are significantly influenced by the offset surface.

Comparison between profiles examined at the same axial station (x = 25) but at different planes ($z^* = 0$, $z^* = 0.4\ell^*$) indicates that the influence of the offset surface on the velocity profiles is more pronounced in the central plane (z = 0) than elsewhere (z > 0). In addition, off-center velocity peaks are clearly evident at the profile corresponding to x = 5, $z^* = 0.4\ell^*$ station.

To reveal similarity of the profiles considered in Figure 25, an alternate form of nondimensionalization was used. In this alternate form, Figure 27, velocity and vertical distance become dimensionless with division by the local maximum velocity (U^*_{max}) and vertical halfwidths ($Y^*_{1/2}$ distance where velocity has decayed to half of its maximum value), respectively. Now, the general tendency towards a single similar profile is apparent for all data except for those in the vicinity of the offset surface. This single profile may be approximate by the following exponential equation,

$$U_{c/max} = \exp\left[-(0.8021\ Y/Y_{1/2})^2\right] \qquad \text{(for } Y/Y_{1/2} \geq -1.1\text{)}$$

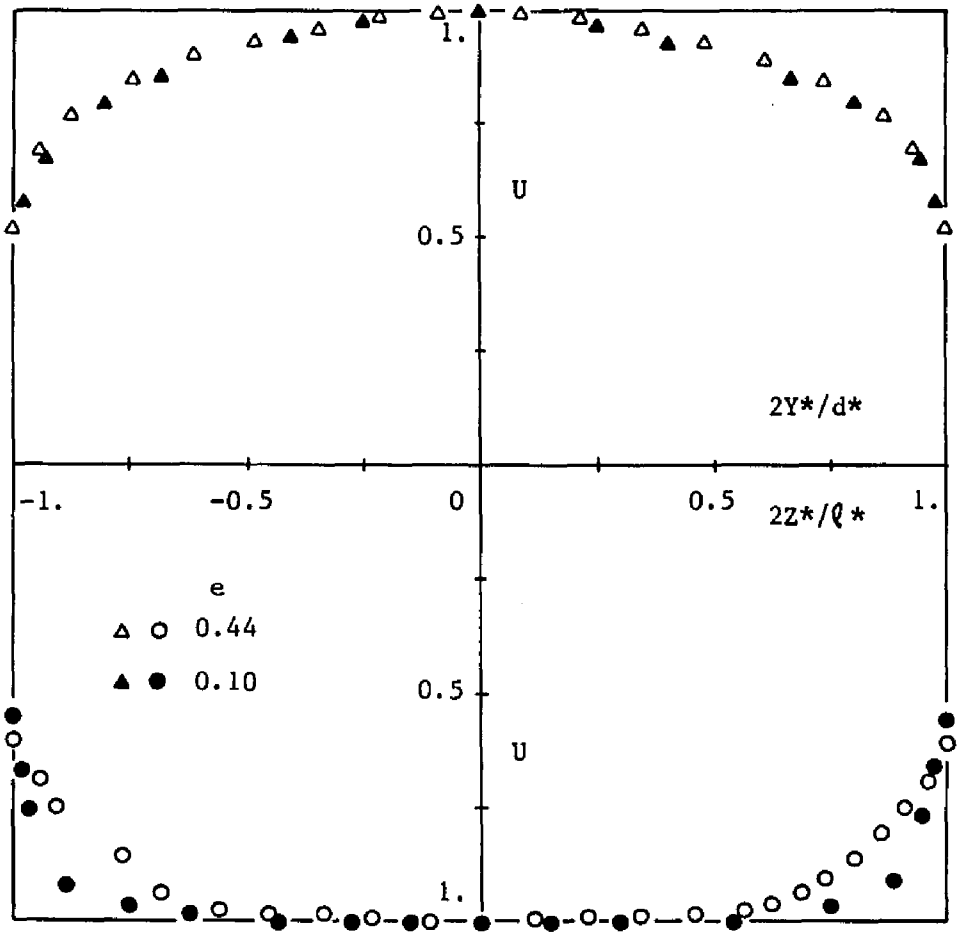

Figure 24. Discharge velocity profiles (Tables D1 and D2)

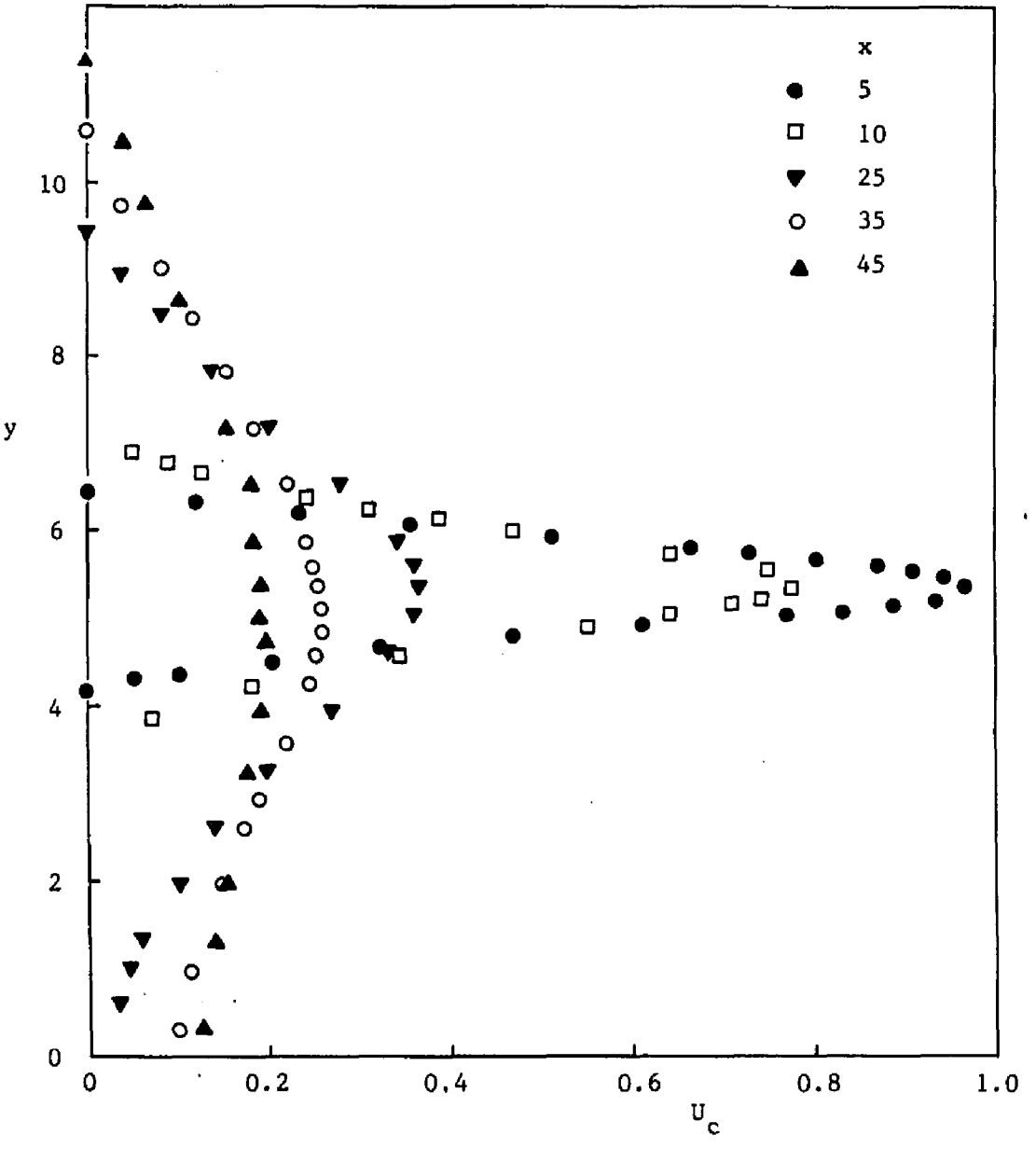

Figure 25. Vertical profiles of velocity (e = 0.44, h = 4.85, z = 0)(Table D3)

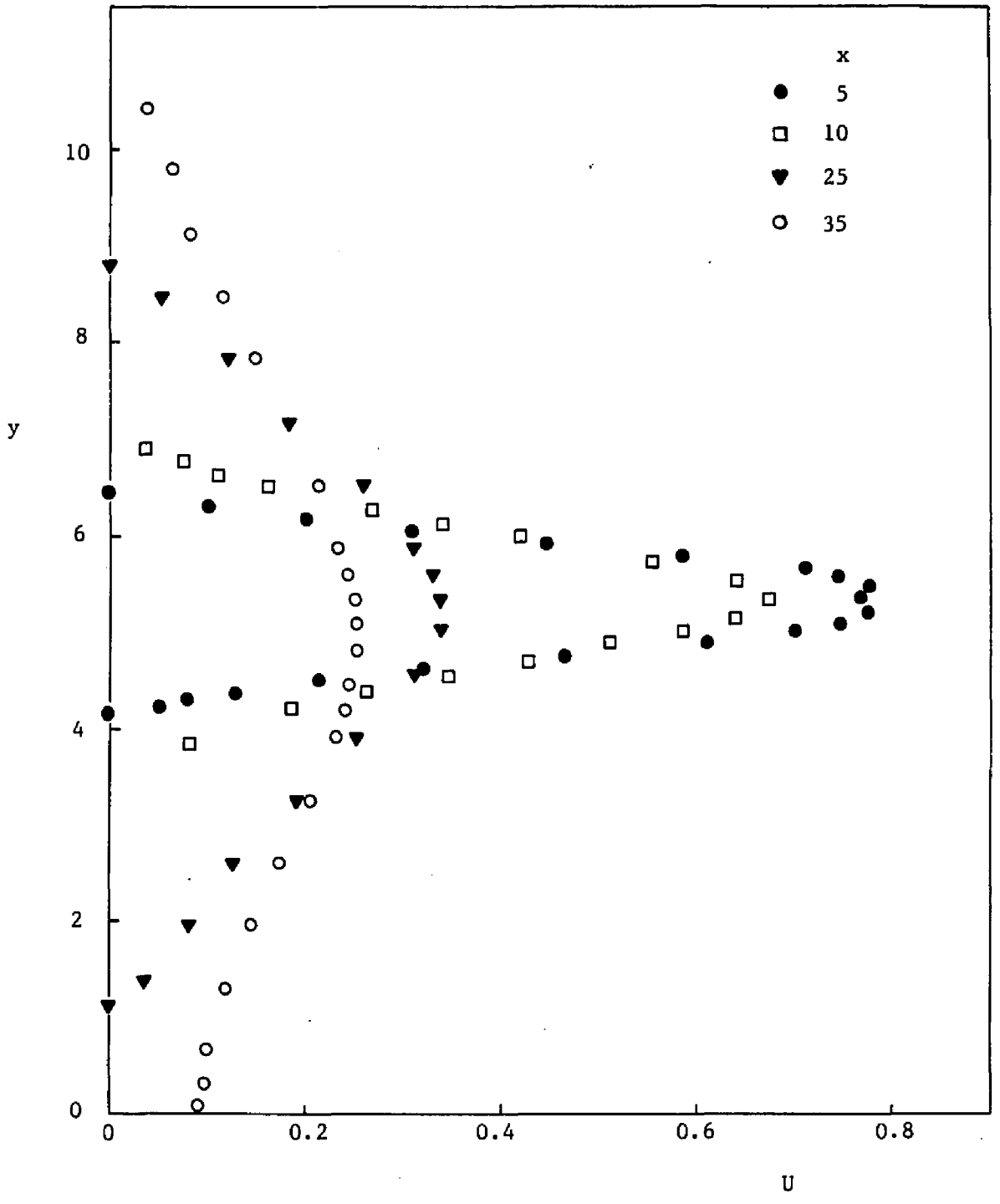

Figure 26. Vertical profiles of velocity (e=0.44, h=4.85, $z^*=0.4\ell^*$) (Table D4)

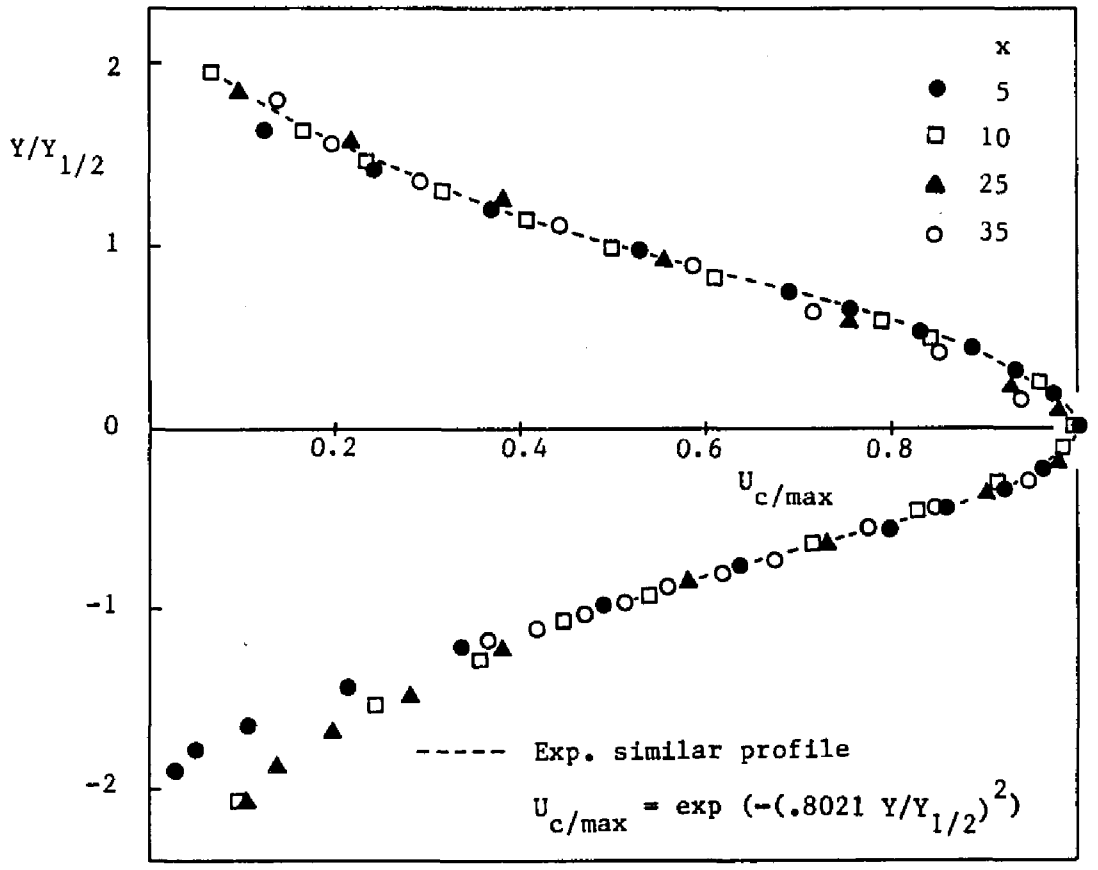

Figure 27. Vertical profiles of velocity in similarity form (e=0, h=4.85, z=0) (Table D3)

The development of the spanwise profiles of velocity along the x-direction was examined at y = 5.35 (horizontal centerplane) and y = 4.7 planes and is presented in Figures 28 and 29, respectively. The profiles in Figure 28 appear to be still developing with only a slight off-axis increase in velocity. The saddling effect observed by Sforza and Herbst[32] is present in the profile taken at x = 10 and y = 4.7 station of Figure 29. They note that secondary motions in the x-z plane may be a mechanism by which the observed off-center velocity peaks are formed. These peaks cannot be formed in the x-y plane as the pressure simply recovers quickly to the atmospheric value from low values on the jet centerline and as the vena-contracta in this plane is very close to the discharge area.

The development of the spanwise profiles of velocity along the y-direction was examined at x = 10 station and is presented in Figure 30. These profiles correspond to the horizontal centerplane (y = 5.35) and to two other symmetrical planes (y = 5.35 ± 0.65). The observed asymmetry between the two planes (upper and lower) is caused by the offset surface.

Some similarity of the spanwise profiles along the x-direction is evident in Figure 31. This figure represents an alternate form of presenting the data in Figure 28. According to this form, velocity and lateral distance are nondimensionalized with division by the local maximum velocity (U^*_{max}) and lateral halfwidths ($Z^*_{1/2}$), respectively. The shape exhibited at $x \gtrsim 25$ stations is seen to converge onto a single similar profile, which may be approximated by the equation:

$$U_{/max} = \exp\left[-(0.8756\, Z/Z_{1/2})^2\right] \qquad (\text{for } x \gtrsim 25)$$

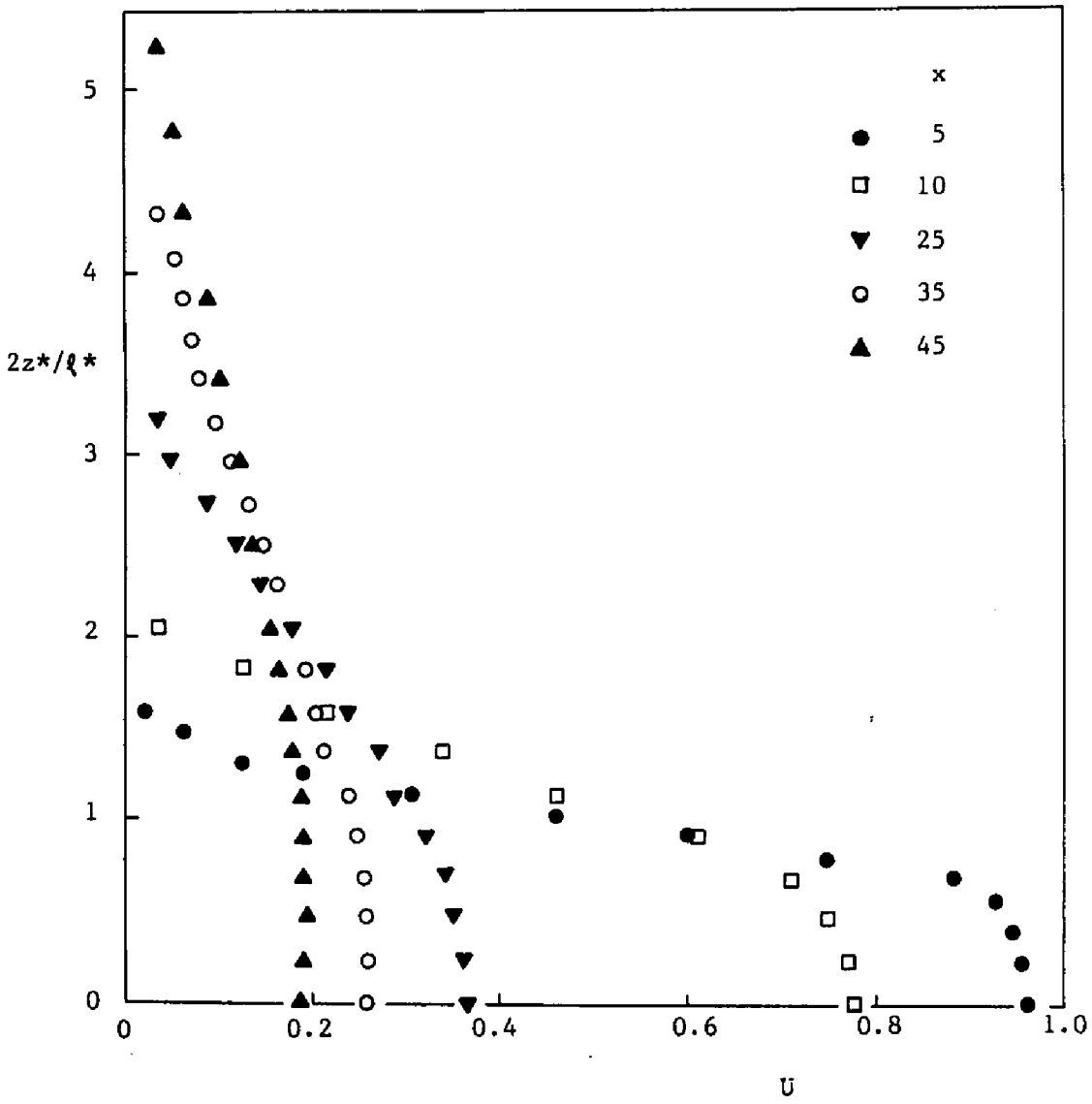

Figure 28. Spanwise profiles of velocity (e = 0.44, h = 4.85, y = 5.35)(Table D5)

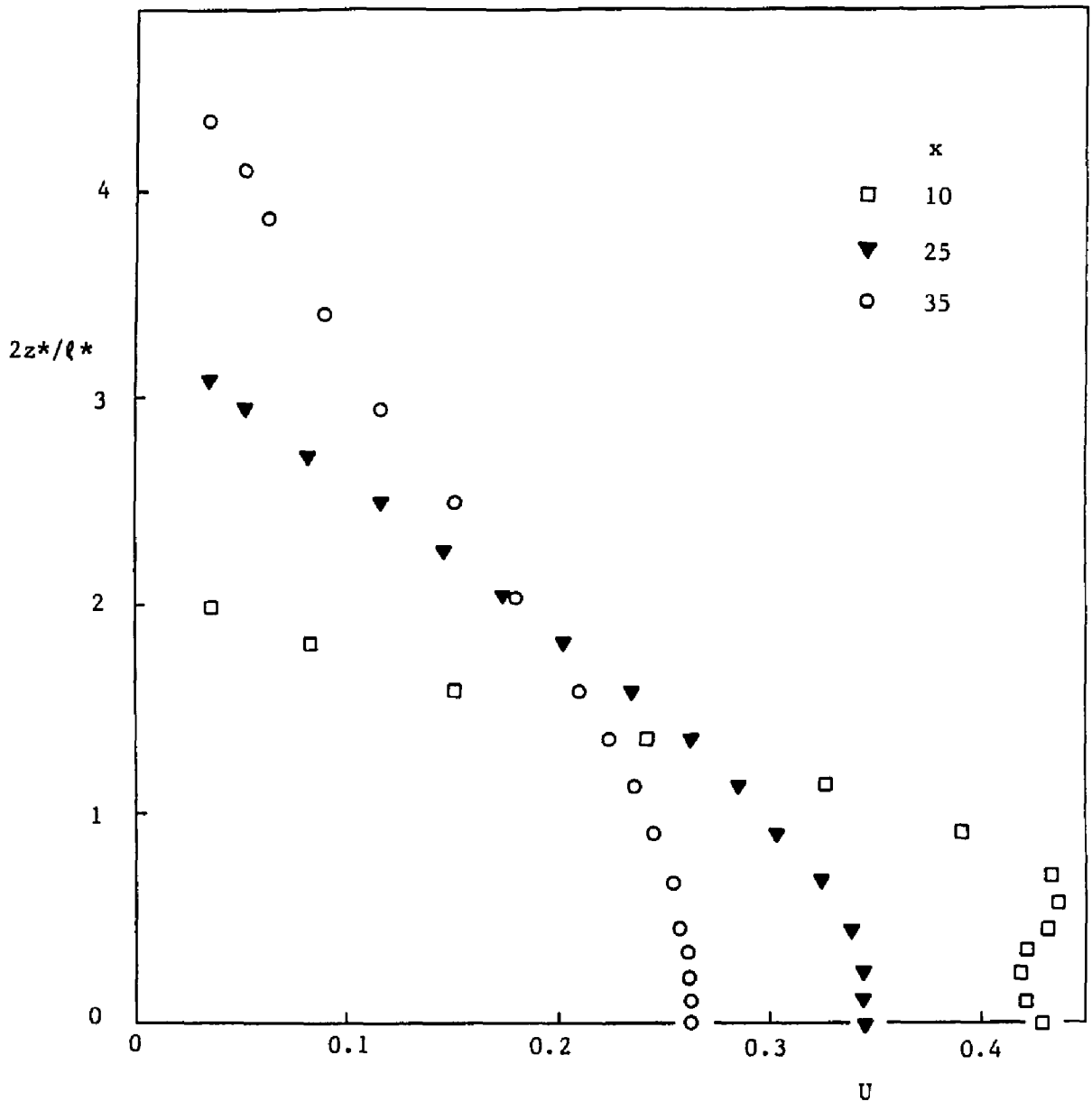

Figure 29. Spanwise profiles of velocity (e = 0.44, h = 4.85, y = 4.7)(Table D6)

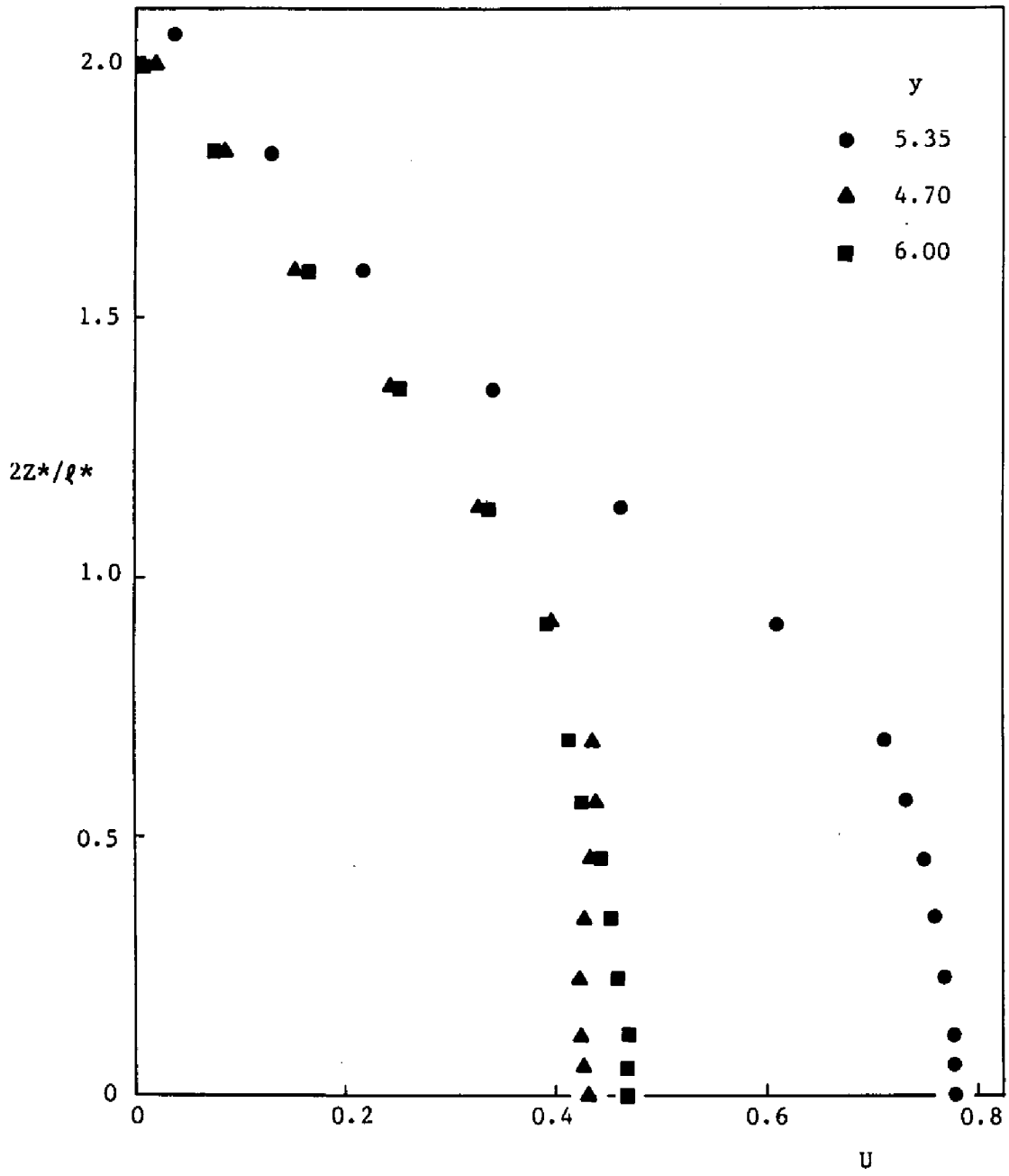

Figure 30. Spanwise profiles of velocity (e = 0.44, h = 4.85, x = 10)(Table D7)

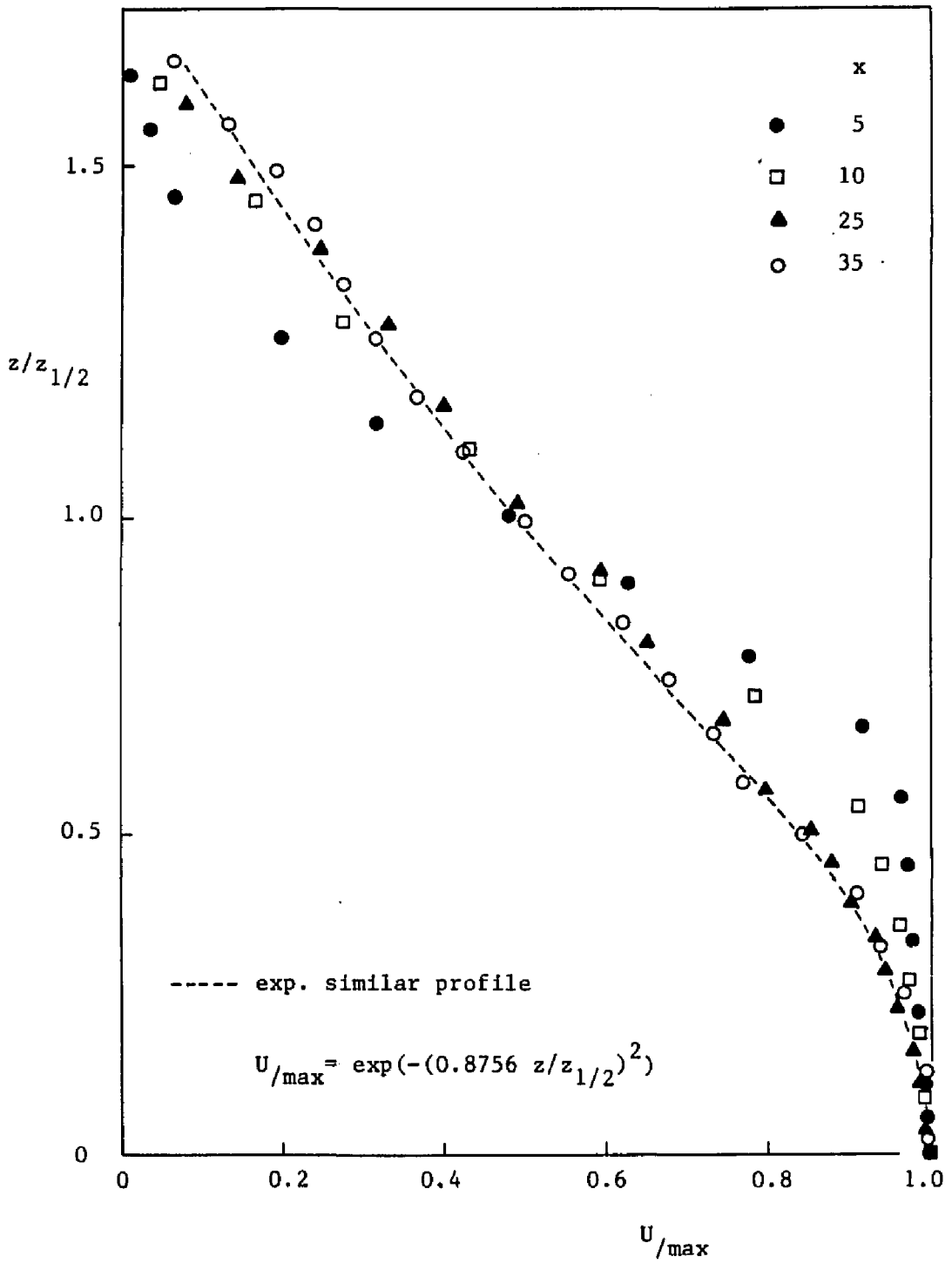

Figure 31. Spanwise profiles of velocity in similarity form (e=0.44, h=4.85, y=5,35) (Table D5)

The local effectiveness of a jet may be measured by the decay of the maximum velocity and temperature fields. In response to that, maximum velocity decays, as well as trajectories along the vertical centerplane (z = 0) and at various values of the discharge Reynolds number, Re_o, are shown in Figures 32 and 33, respectively. It is shown that decays and trajectories are approximately independent of Re_o. This is in agreement with the conclusion obtained in the study of two-dimensional offset jets.[46] The best fit curve which describes the maximum velocity decays for a typical case (e = 0.44, h = 1.85, z = 0) with various Re_o (i.e., 26,000, 38,000 and 50,000) was found to be given by the correlation equation:

$$U_{cmax} = 4.622\, x^{-0.779} \qquad (\text{for } x \geq 7.5)$$

The effect of the offset distance parameter, h, on velocity field was investigated in detail and the results are presented in Figures 34 through 40. In addition, comparisons of offset jets with the limiting cases of free ($h \to \infty$) and wall (h = 0) jets are included in this set of figures.

The development of the vertical centerplane (z = 0) profiles of velocity as h is changed ($4.85 \leq h \leq 1.07$) was examined at two axial stations (x = 10, x = 25) and is presented in Figures 34 and 35, respectively. For better understanding of the offset distance effect on velocity profiles, each of the above figures includes three different ways of plotting, depending on the definition of the vertical coordinate.

The tendency of velocity profiles to approach the wall jet profile behavior as the offset distance decreases is evident. Another observation is that profiles

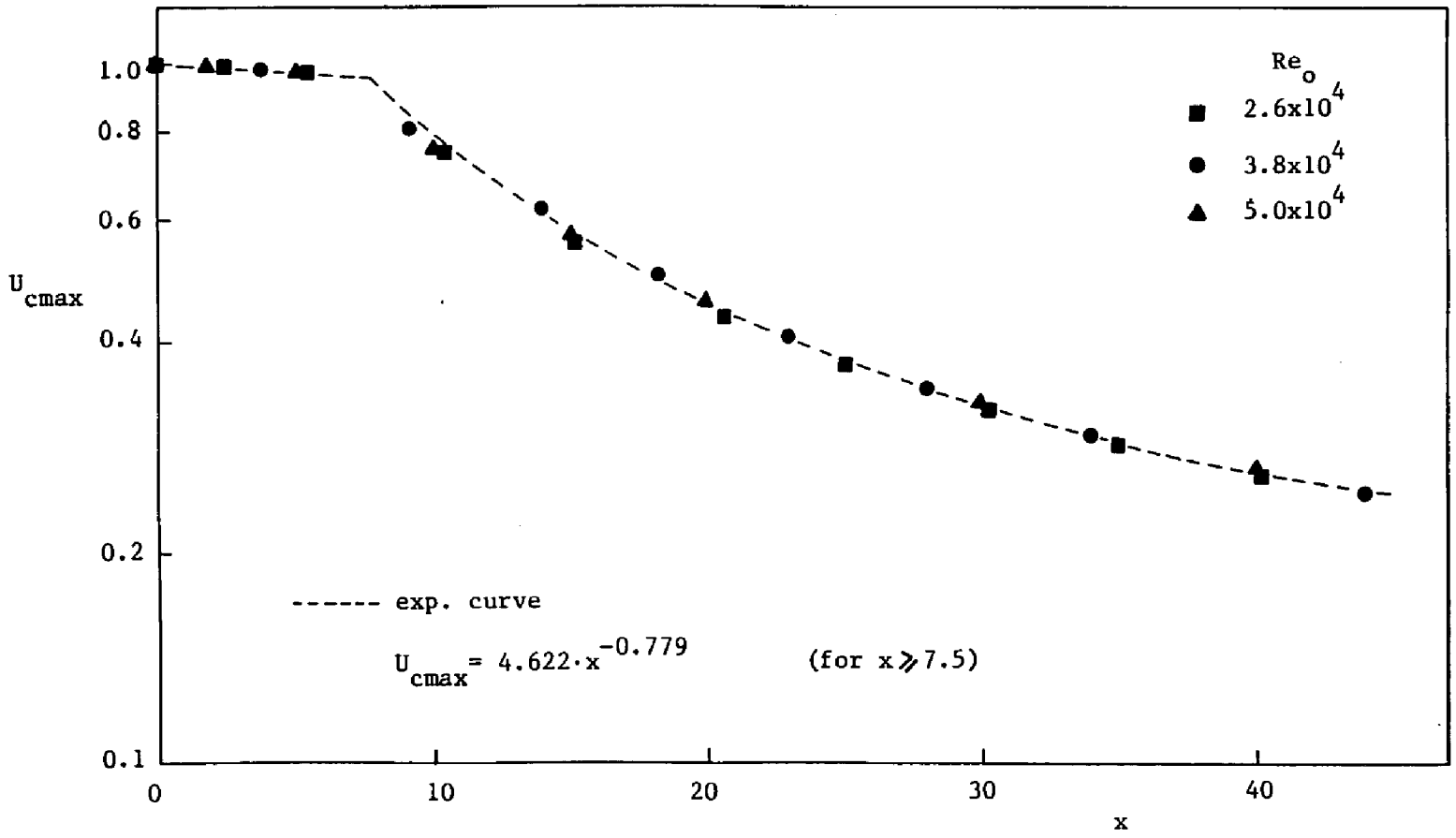

Figure 32. Maximum velocity decays (e=0.44 , h=1.85 , z=0) (Table D8)

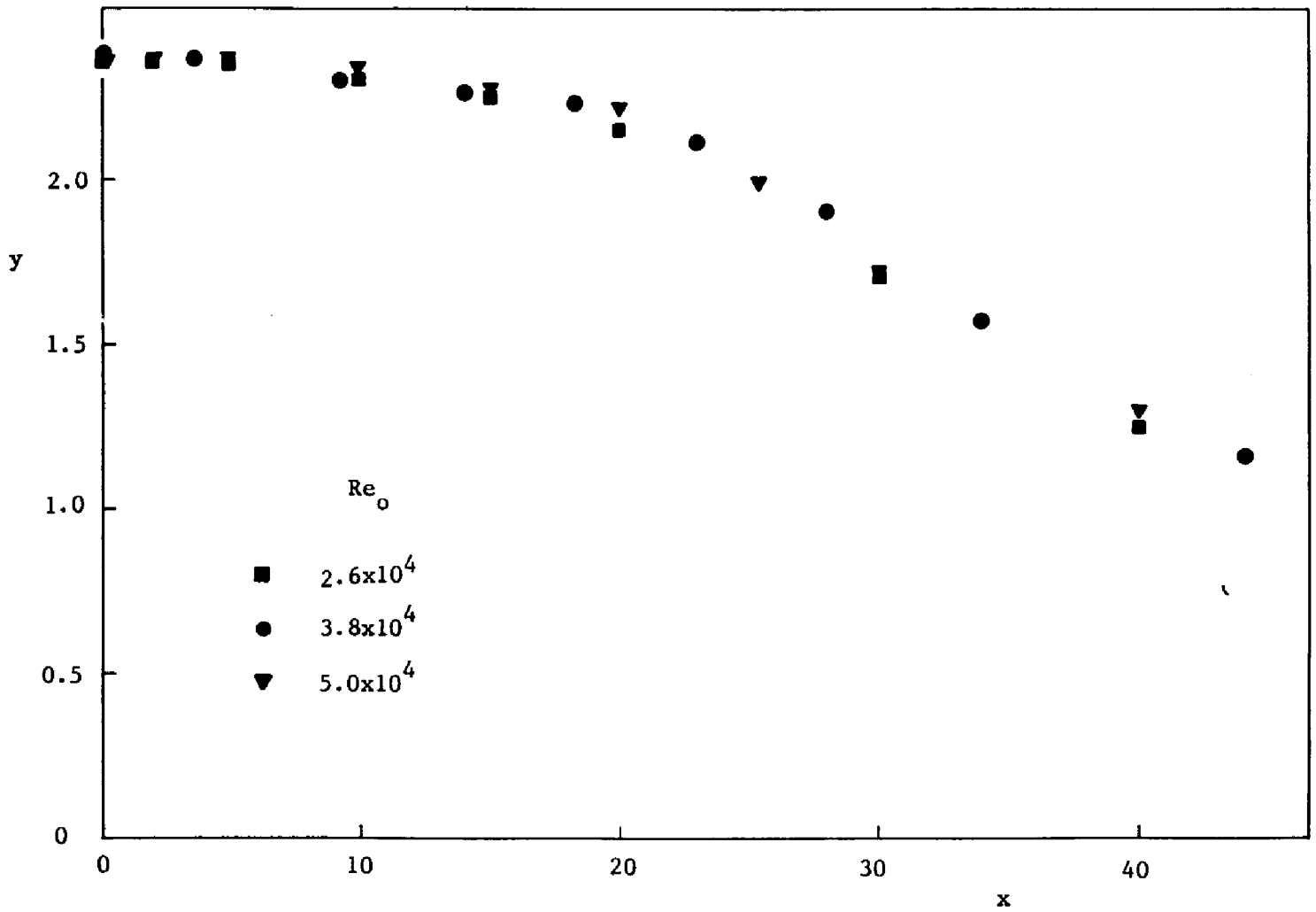

Figure 33. Trajectories (e=0.44 , h=1.85 , z=0)
(Table D8)

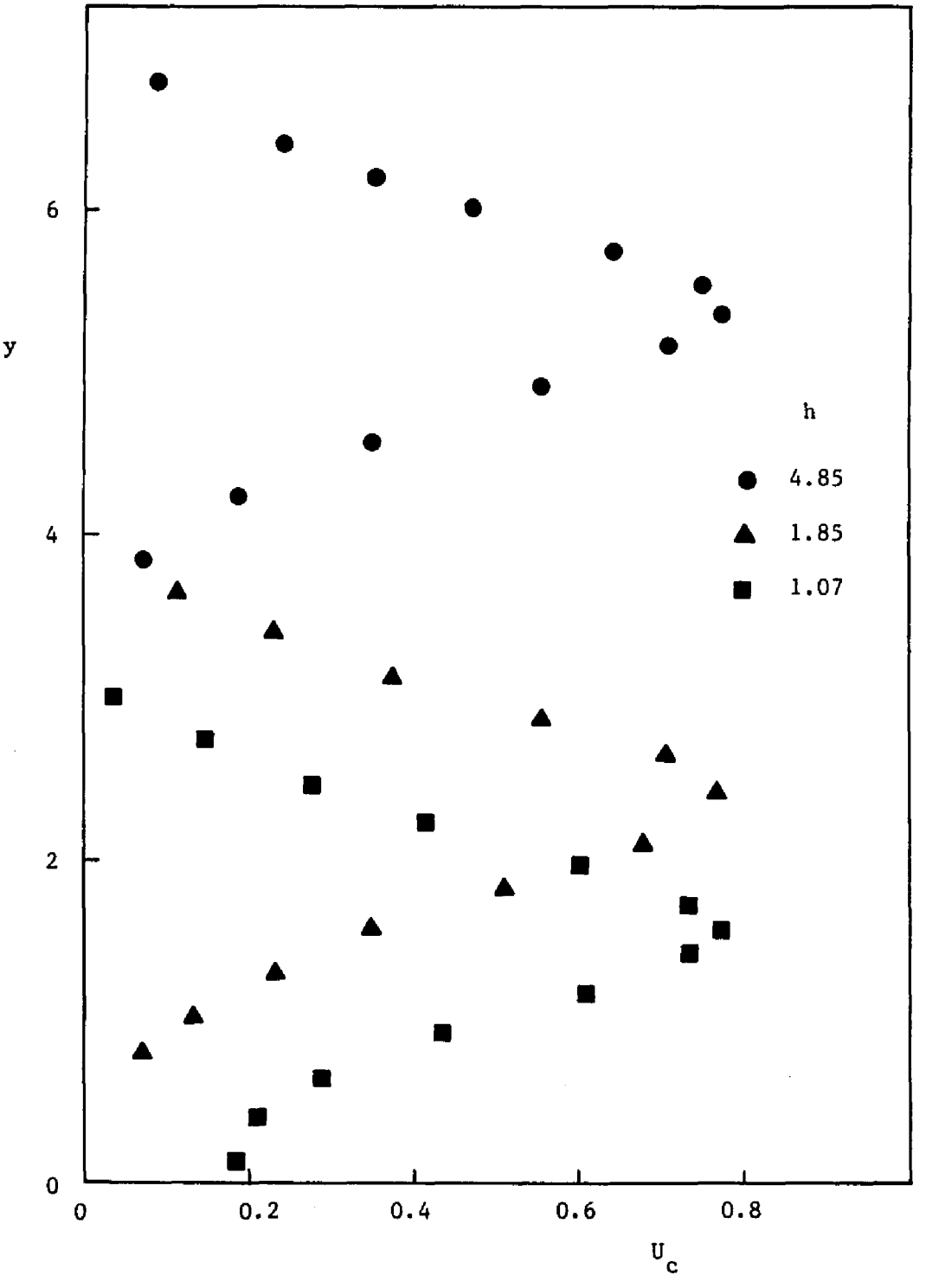

Figure 34.a. Vertical profiles of velocity (e=0.44 , x=10 , z=0) (Table D9)

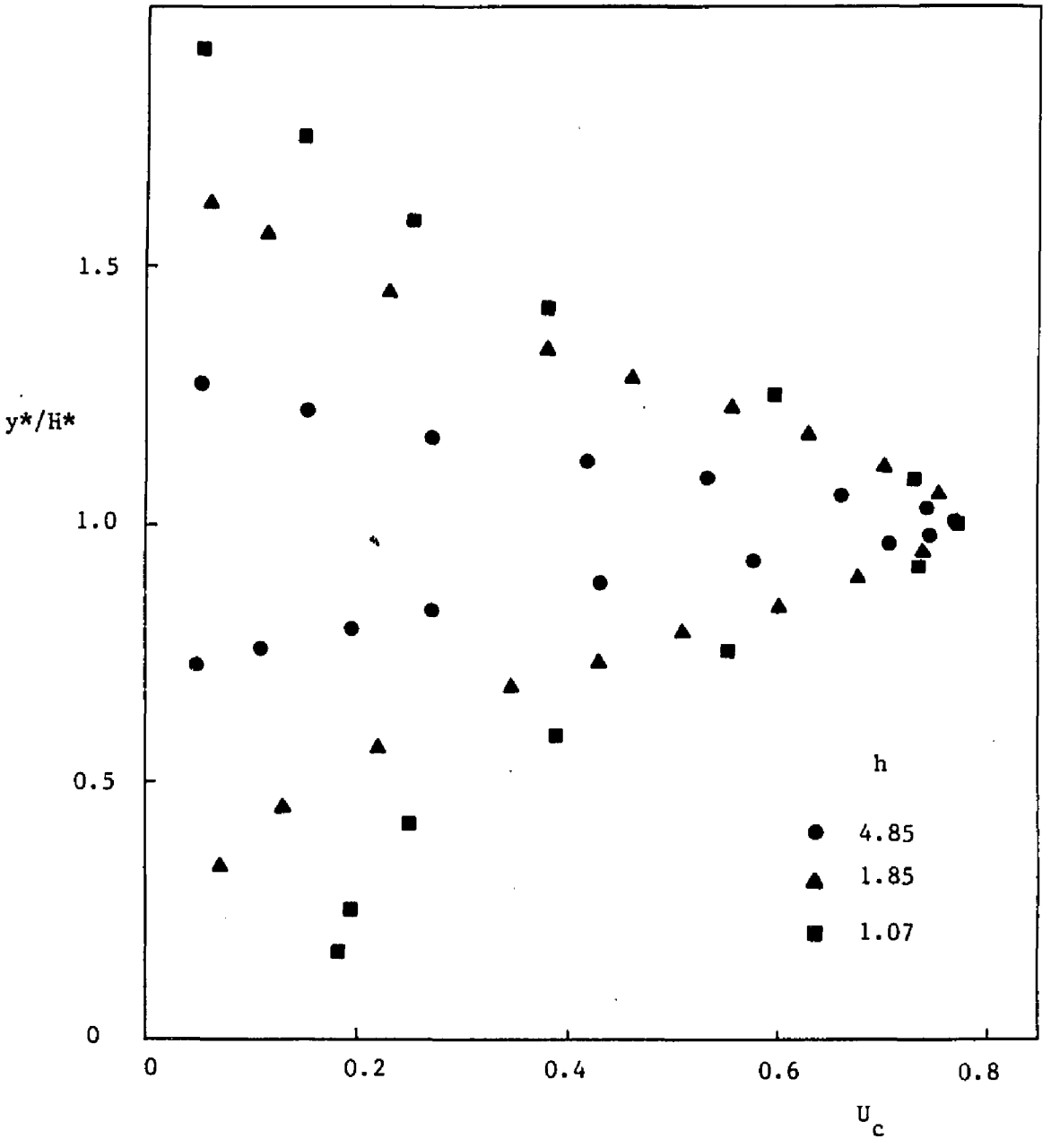

Figure 34.b. Vertical profiles of velocity (e=0.44 , x=10 , z=0) (Table D9)

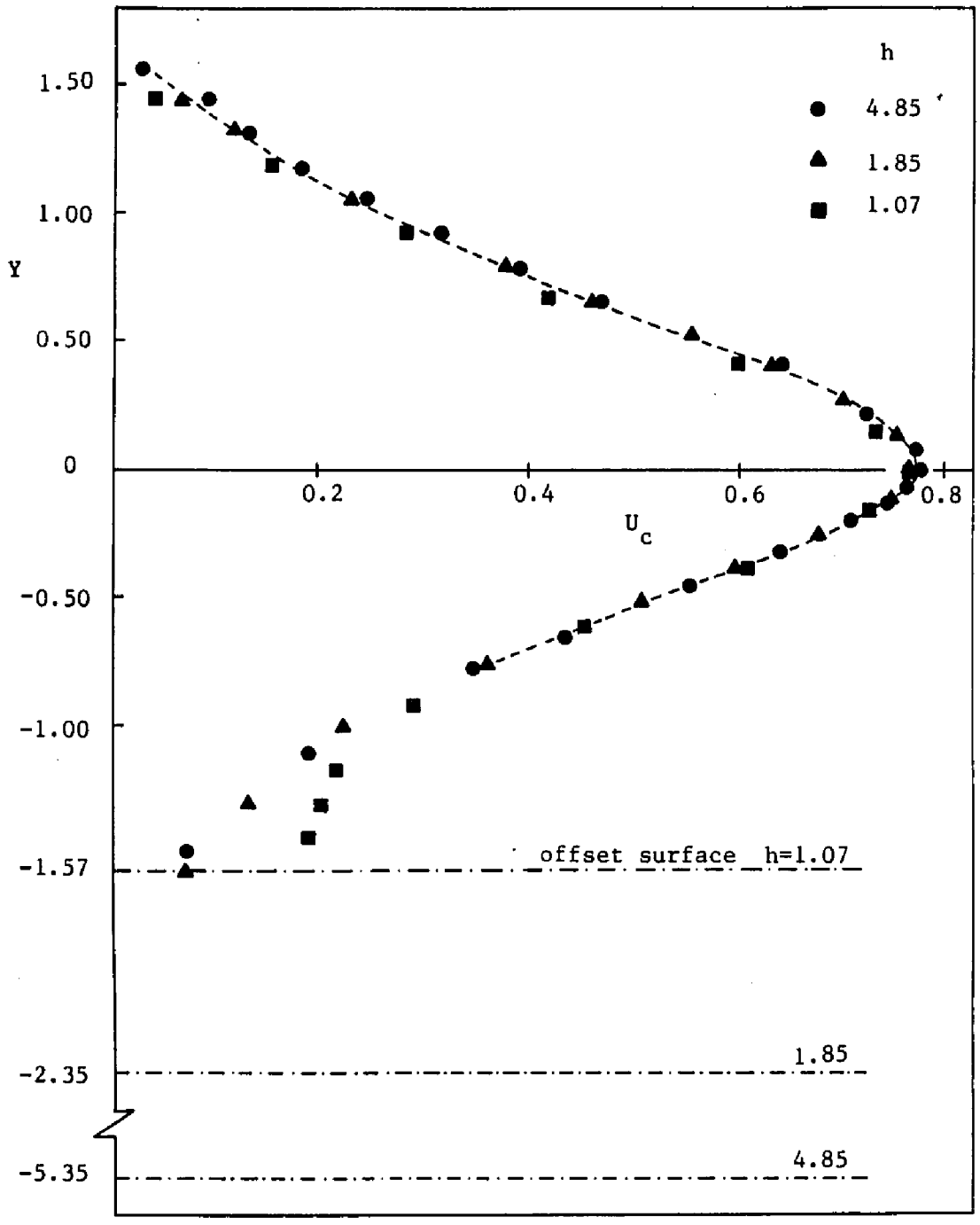

Figure 34.c. Vertical profiles of velocity (e=0.44 , x=10 , z=0) (Table D9)

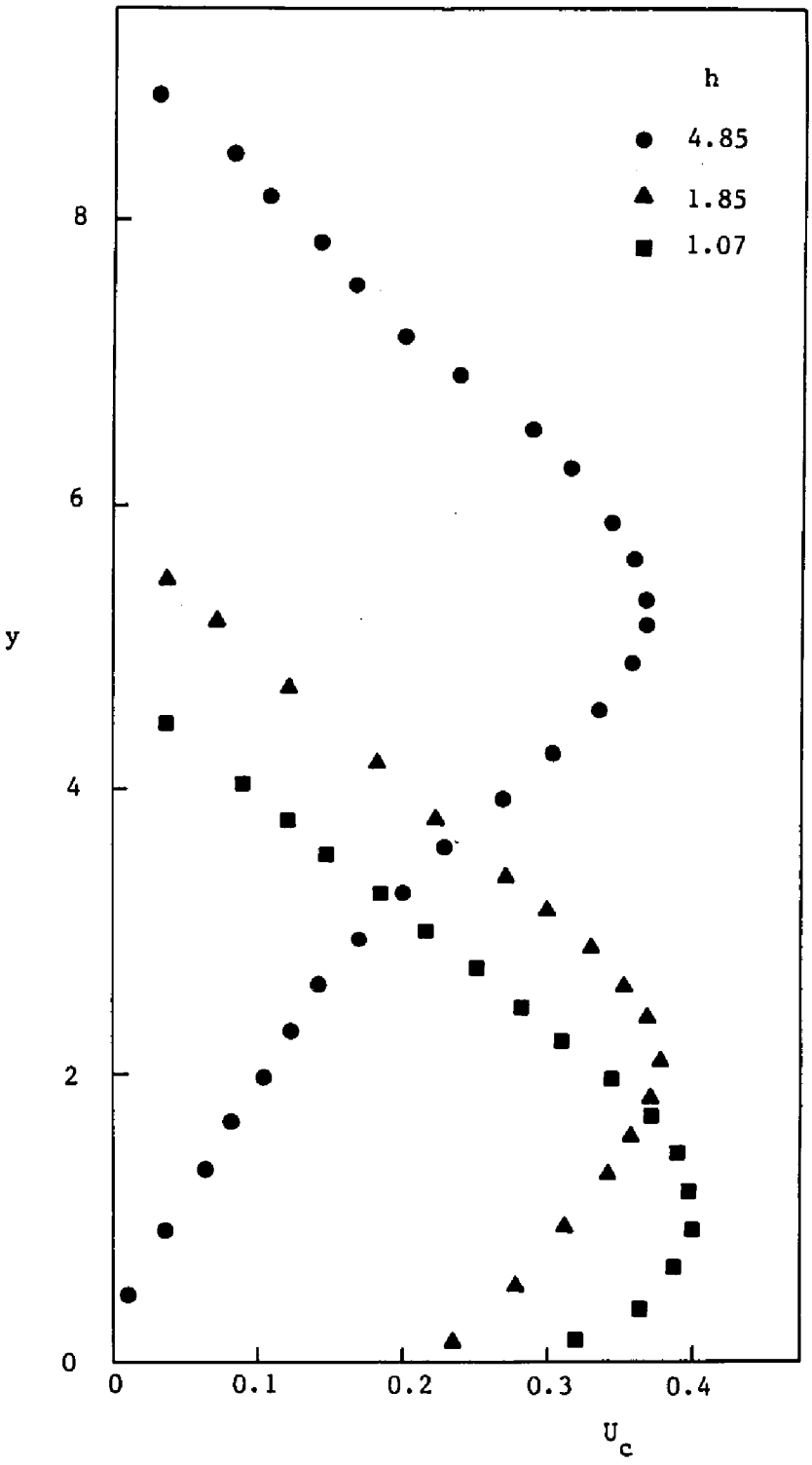

Figure 35.a. Vertical profiles of velocity
(e=0.44 , x=25 , z=0) (Table D 10)

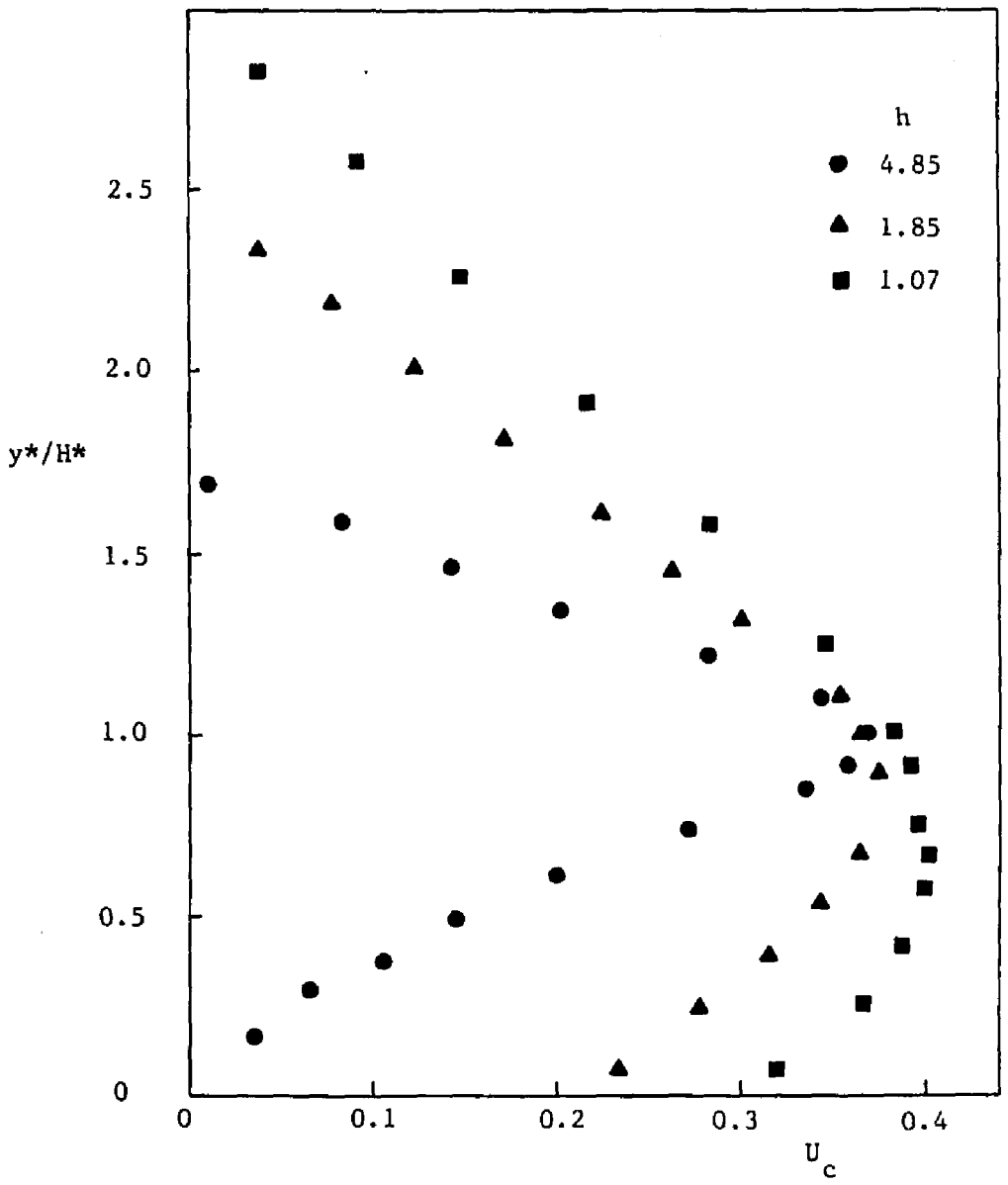

Figure 35.b. Vertical profiles of velocity (e=0.44 , x=25 , z=0) (Table D10)

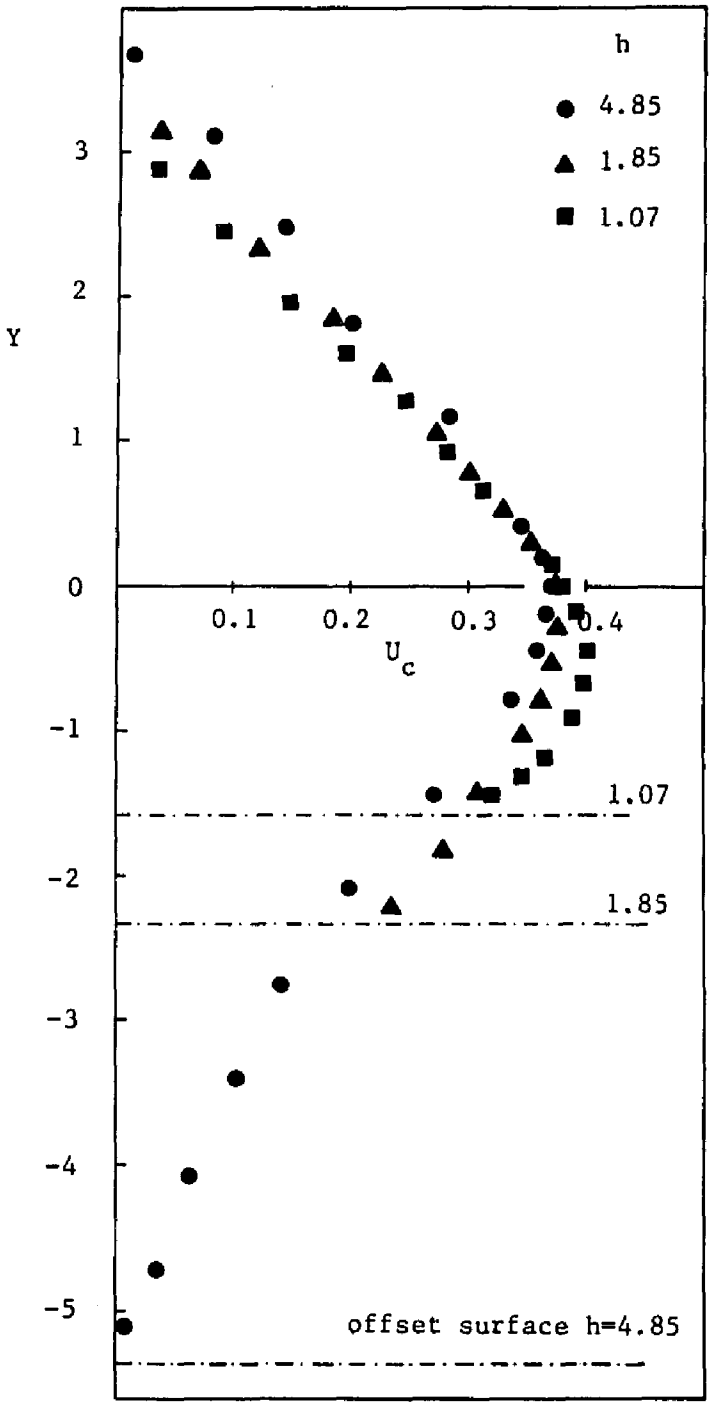

Figure 35.c. Vertical profiles of velocity (e=0.44, x=10 , z=0) (Table D10)

corresponding to upstream stations (i.e., x = 10) are independent of h in regions located away from the offset surface.

One of the most important characteristics to consider in the study of turbulent jet behavior is the jet's dilution capacity or its ability to spread into the surrounding fluid medium. Rather than measure the growth rate of the outer edge of the jet, its influence is usually measured in terms of the growth of the distance at which the velocity or temperature has decayed to half of its value at the respective centerline (halfwidths).

The growth of the velocity halfwidths in both directions (y and z) for various values of h (i.e., ∞ , 4.85, 1.85, 1.07, 0) are presented in Figures 36 and 37, respectively. The upper part of Figure 36 shows that offset jet vertical halfwidths are characterized by a tendency to approach wall jet behavior further downstream. The increasing influence of the offset surface on the velocity field as h is decreased is also verified by these vertical halfwidths plots.

The spanwise halfwidth growth ($2Z^*_{1/2}/\ell^*$), given in Figure 37, shows a behavior approximately similar to that of (i) free jet when h = 4.85 or h = 1.85, and (ii) wall jet when h = 1.07. The spanwise spread of jets was found to increase as h was decreased. As it was expected, all experimental data on halfwidths ($Y_{1/2}$, $2Z^*_{1/2}/\ell^*$) of various offset jets were found to be within the area bounded by the curves corresponding to the two limiting cases of free and wall jets.

The local effectiveness of the jets was measured by the decay of the maximum velocity along the vertical centerplane and is presented in Figure 38.

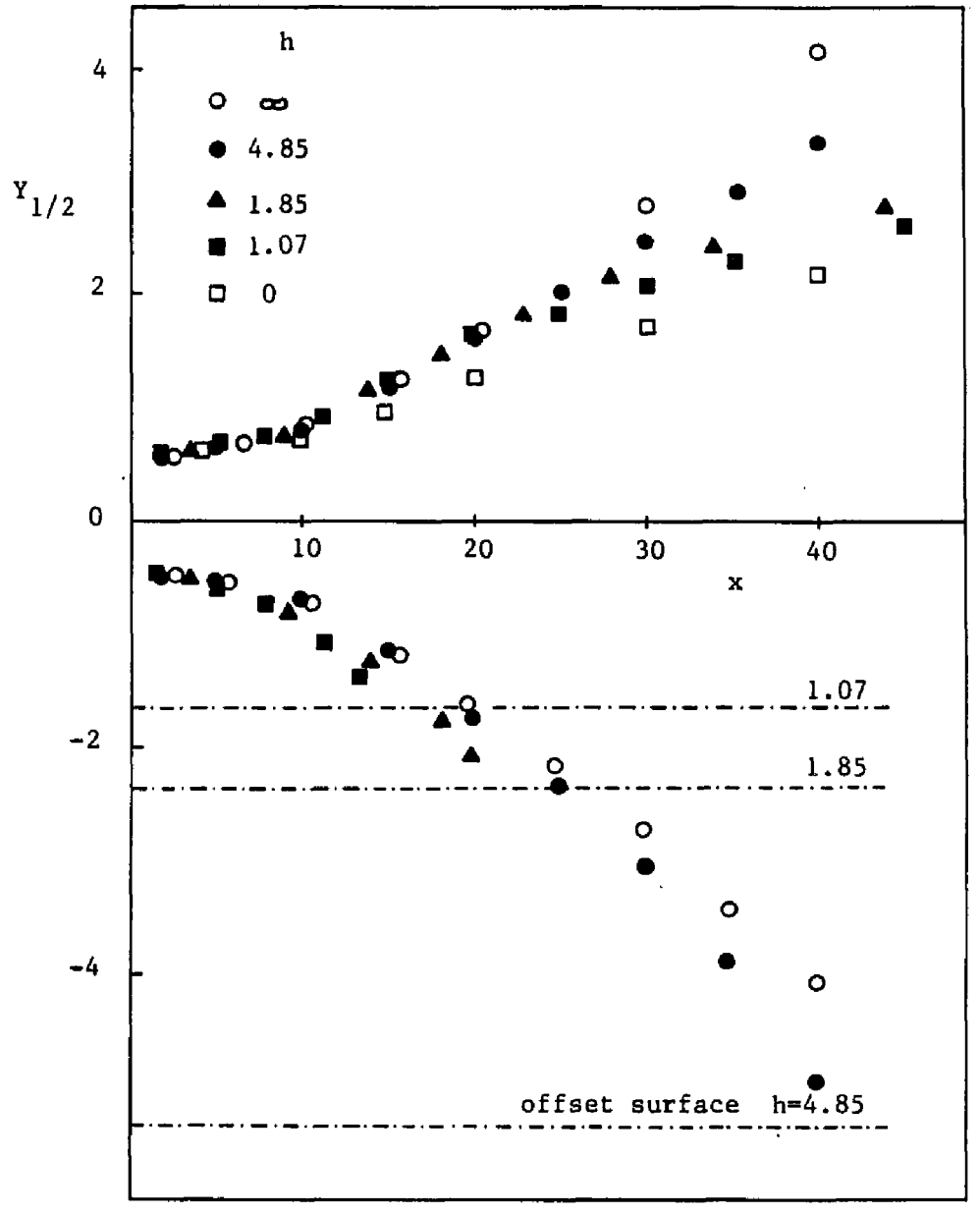

Figure 36. Vertical halfwidths of velocity (e=0.44 , z=0)
(Table D11)

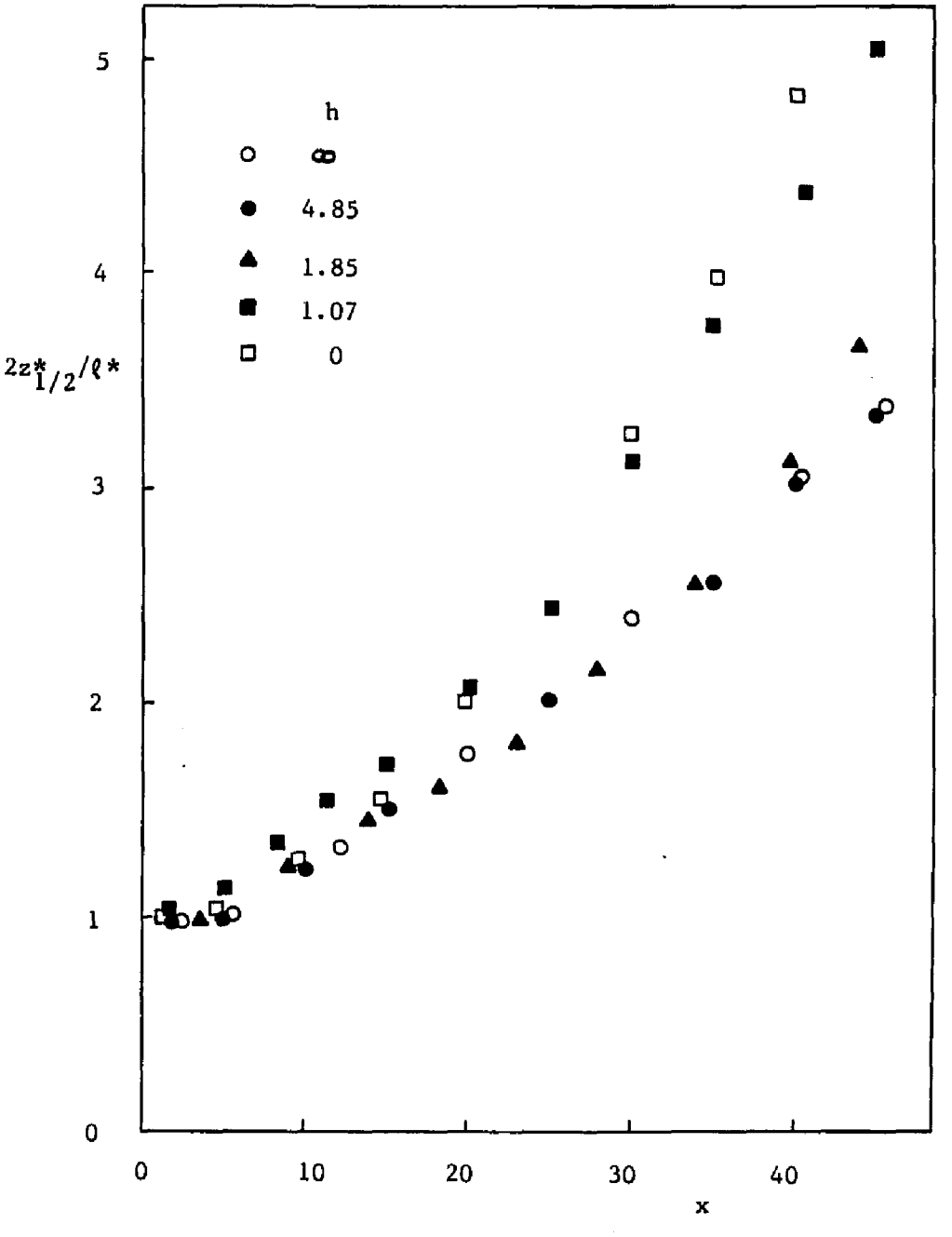

Figure 37. Spanwise halfwidths of velocity (e=0.44 ,y=h+1/2)

(Table D12)

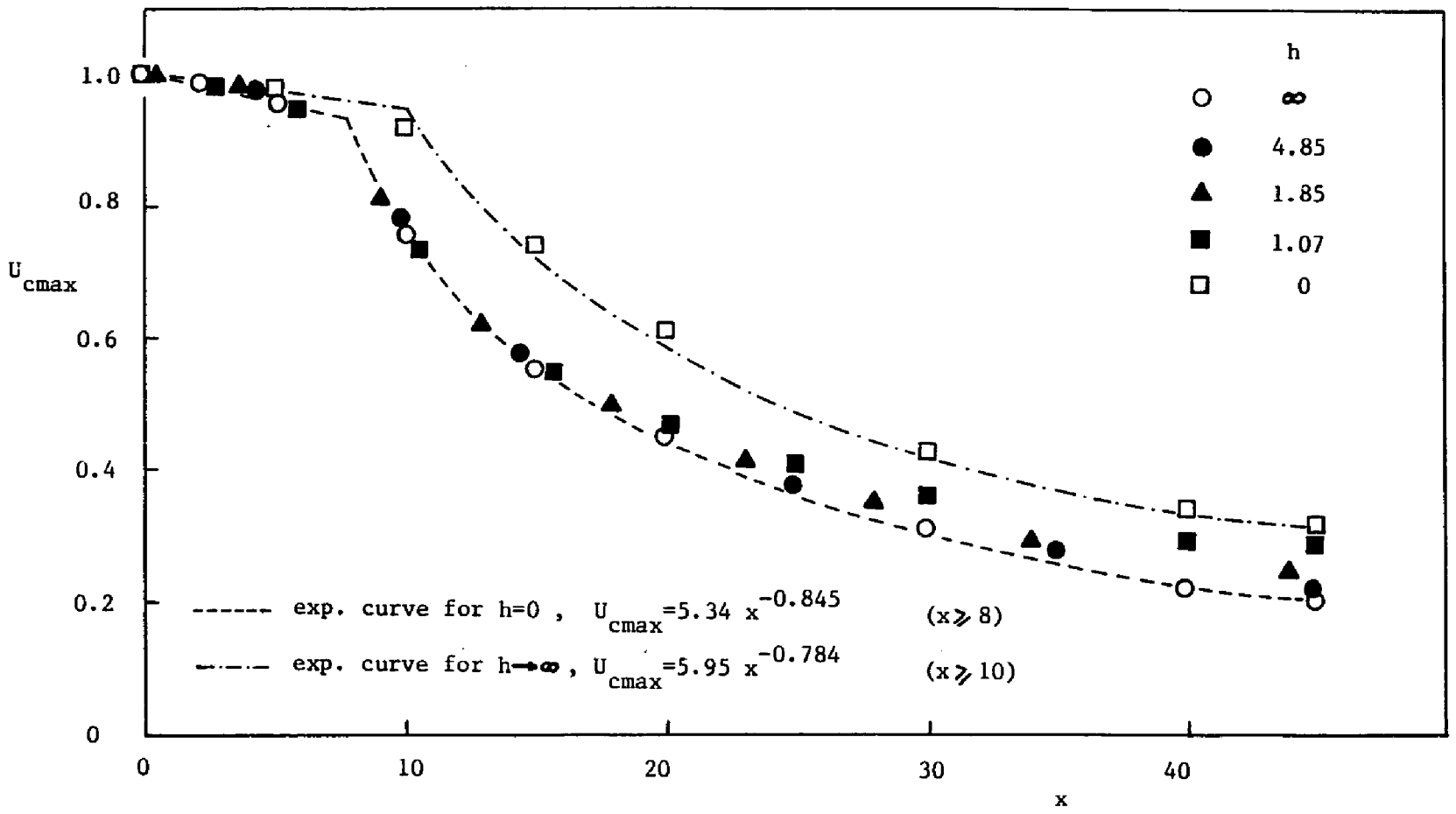

Figure 38. Maximum velocity decays (e=0.44 , z=0) (Table D13)

The offset jet decay was found to be approximately similar to that of the free jet in upstream regions ($x \leq 15$). On the other hand, it was found to approach the wall jet decay further downstream. The experimentally calculated velocity decay of free and wall jets was in agreement with those obtained by Butterman.[47] For the case of e = 0.44, the decay can be approximated by the empirical equations:

Wall jet: $U_{cmax} = 5.95\, x^{-0.784}$ (for $x \geq 10$)

Free jet: $U_{cmax} = 5.34\, x^{-0.845}$. (for $x \geq 8$)

Trajectories (position of maximum velocity along the vertical centerplane) for various values of h are presented in Figure 39. An alternate presentation is given in Figure 40, where y* was nondimensionalized with division by H* instead of d*. Both ways of presentation indicate that the bending of jet towards the offset surface becomes more pronounced as h is decreased.

The effect of the discharge geometry on the velocity field was investigated and is presented in Figures 41 through 50. Also, comparisons between three- and two-dimensional (e = 0) jets are included in this set of figures.

Velocity profiles in the y-direction of jets discharging from various aspect ratio channels (i.e., e = 0.44, e = 0.25, e = 0.1) are given in Figure 41. All profiles were examined for a typical case with h = 1.07, x = 10 and z = 0. These centerplane profiles show that their behavior approaches that of the two-dimensional jet as e is decreased. This is also evident in the next figure, 42, where the profile of e = 0.1 channel is examined at an upstream station (x =

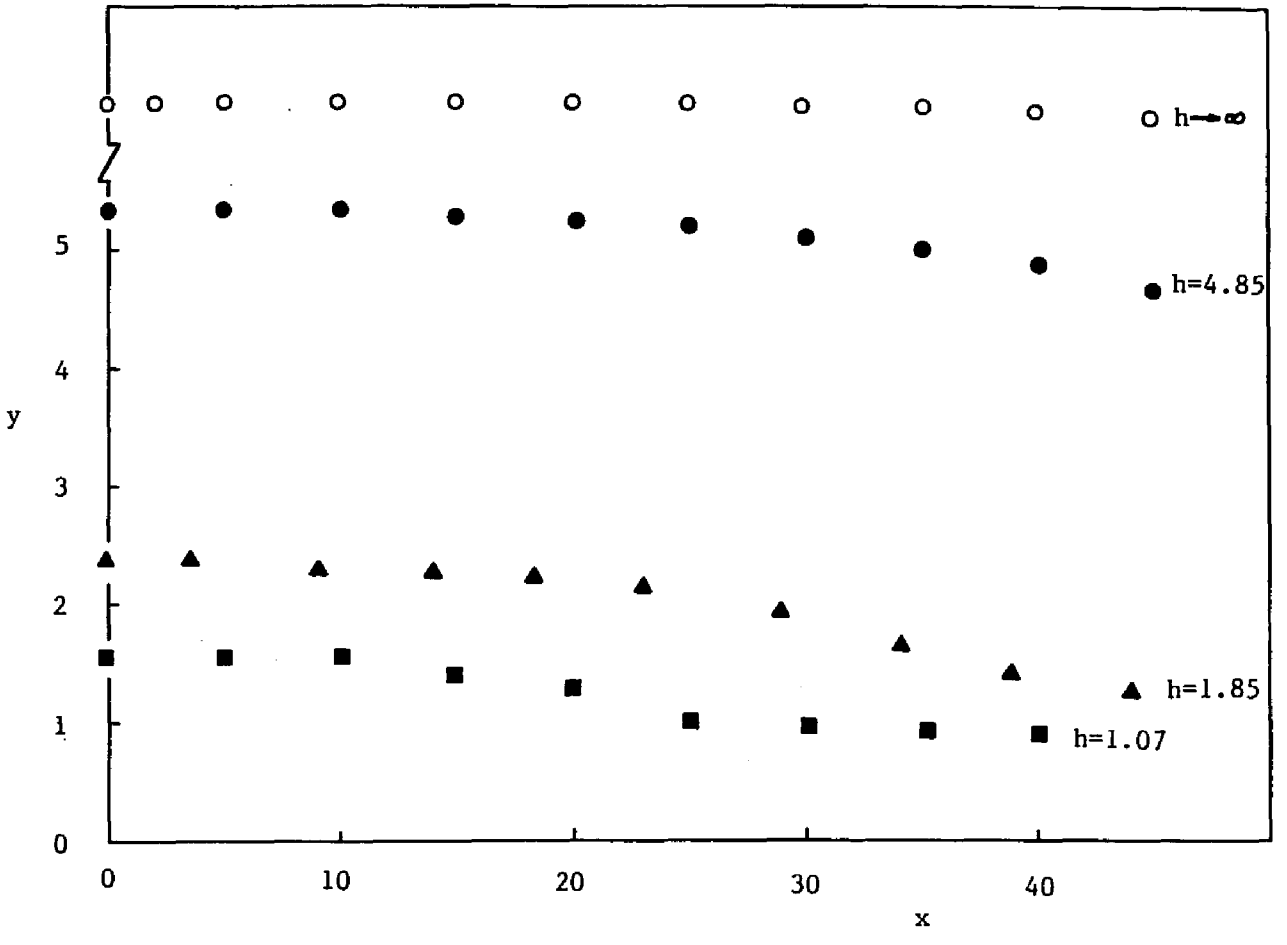

Figure 39. Jet trajectories (e=0.44 , z=0) (Table D13)

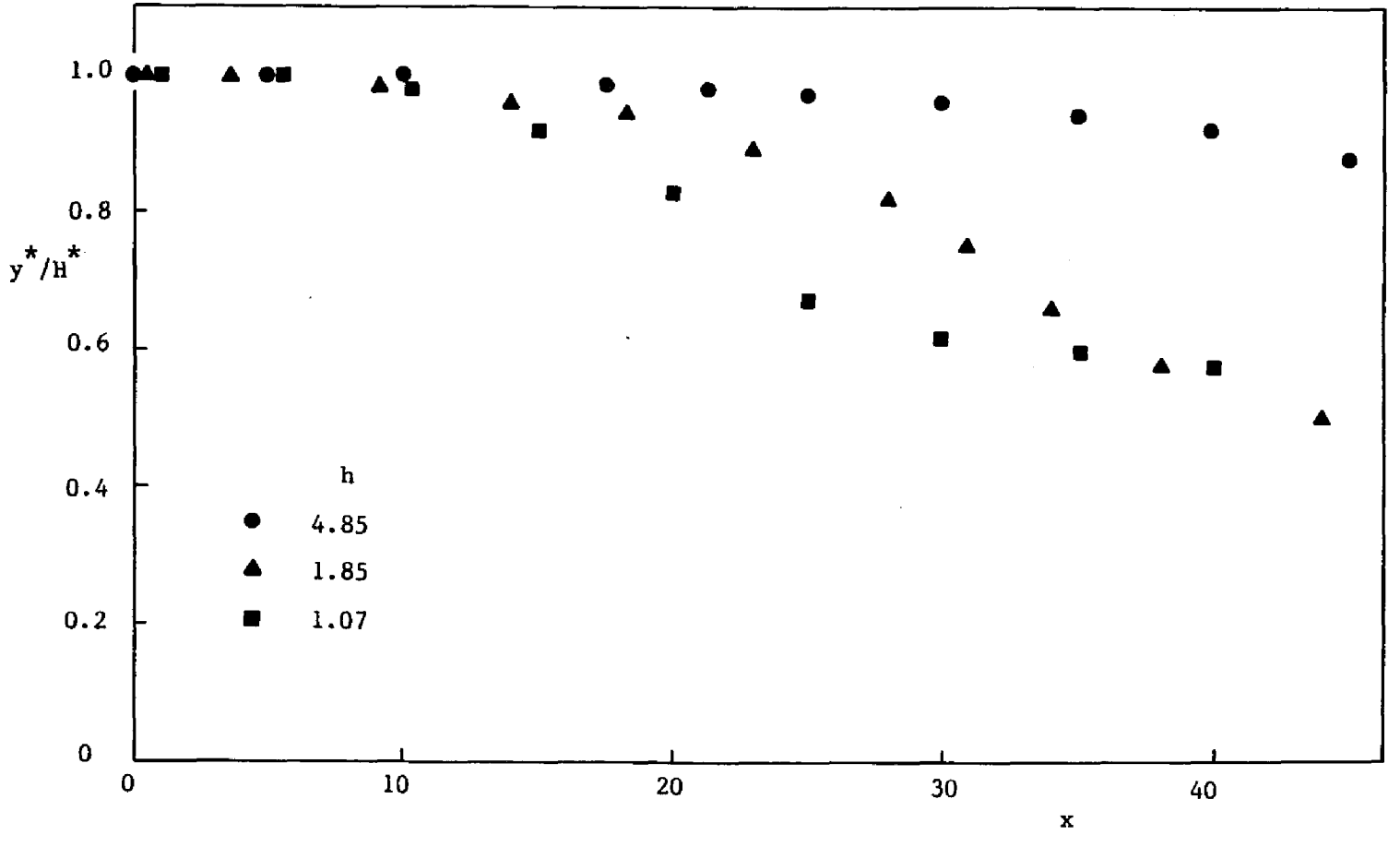

Figure 40. Jet trajectories (e=0.44 , z=0) (Table D13)

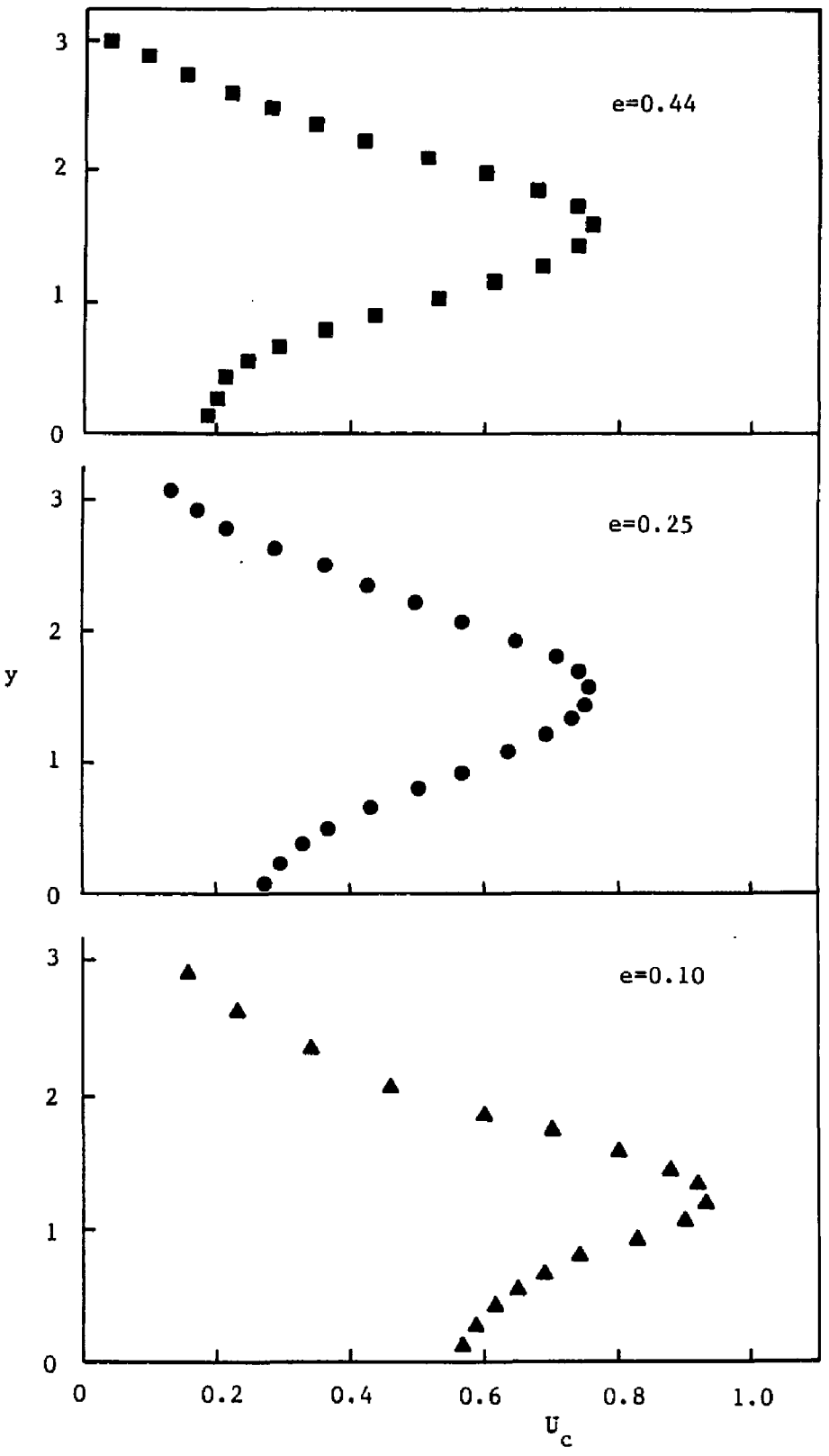

Figure 41. Vertical profiles of velocity (h=1.07 , x=10 , z=0) (Tables D9 and D14)

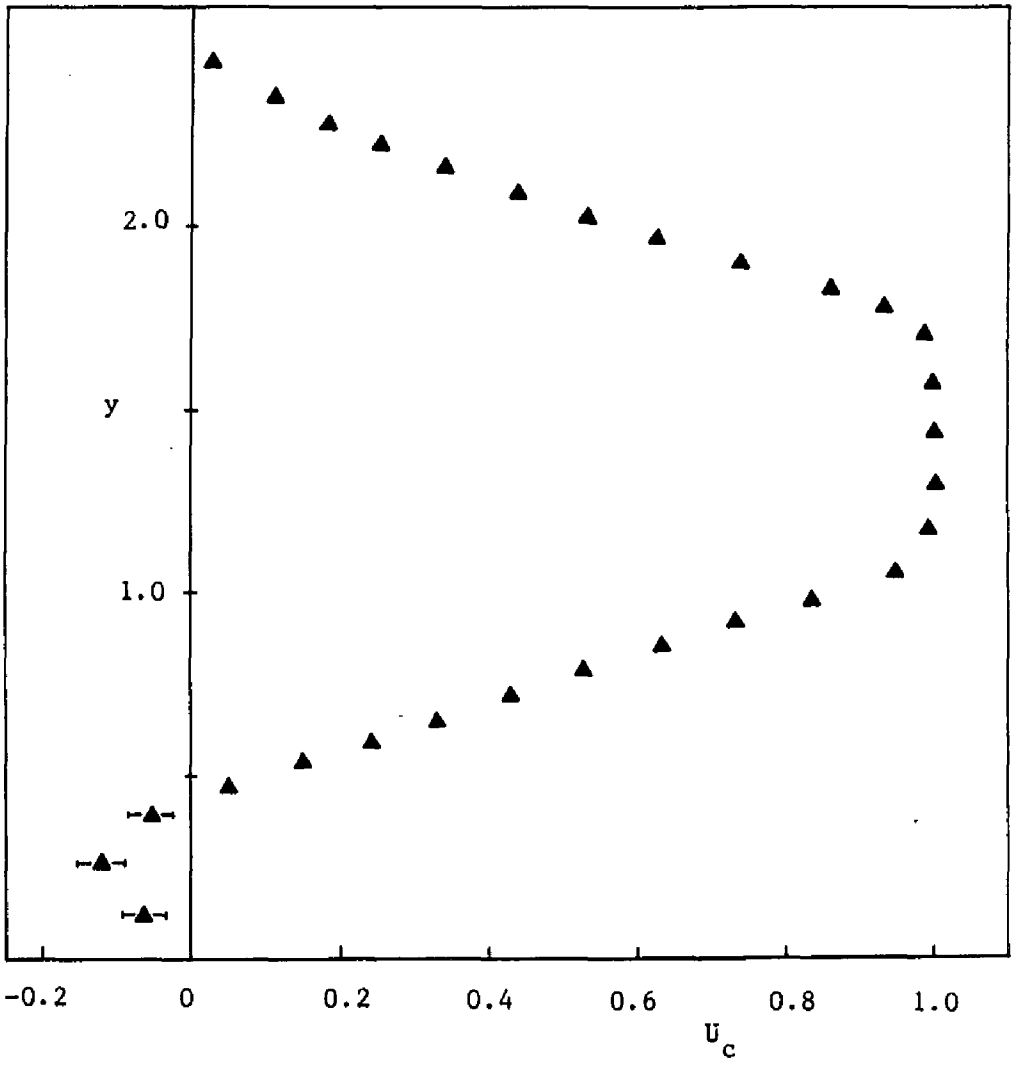

Figure 42. Vertical profile of velocity (e=0.10 , h=1.07 , x=3.55 , z=0) (Table D16)

3.55). In this case, a reversed flow appears in the vicinity of the offset surface. This phenomenon, as was mentioned earlier, constitutes a fundamental characteristic of the two-dimensional offset jet.

The previously discussed observations (Figures 41 and 42) are in agreement with the conclusion based on surface pressure data, namely that the three-dimensional offset jet behavior approaches that of two-dimensional jet when h is very much less than 1/e.

Velocity profiles in z-direction of jets discharging from e = 0.44 and e = 0.25 channels are presented in Figures 43. Both profiles were examined at a typical case with h = 1.07, x = 10 and y = 1.57. This figure shows an increase of the lateral spread and a tendency for uniform profiles as e is increased.

The dilution capacity of jets of various aspect ratios, having a constant h, appears in Figures 44 through 47. The growth of the velocity halfwidths in the y-direction ($Y_{1/2}$), Figure 44, shows the different flow patterns which characterize the two- and three-dimensional offset jets. The e = 0.1 jet begins to depart from the general three-dimensional behavior and moves towards the two-dimensional path. The velocity halfwidths in the z-direction ($2Z^*_{1/2}/\ell^*$), Figure 45, indicate the effect of e on the lateral spread.

Normalization of velocity halfwidths in both directions was achieved in Figures 46 and 47, where $Y^*_{1/2}$, $Z^*_{1/2}$ and x* were nondimensionalized with division by $\sqrt{A^*}$ (where $A^* = d^* \cdot \ell^*$). Now, it can be observed that the different aspect ratio vertical halfwidths lose their memory of the discharge geometry and follow an approximately similar behavior.

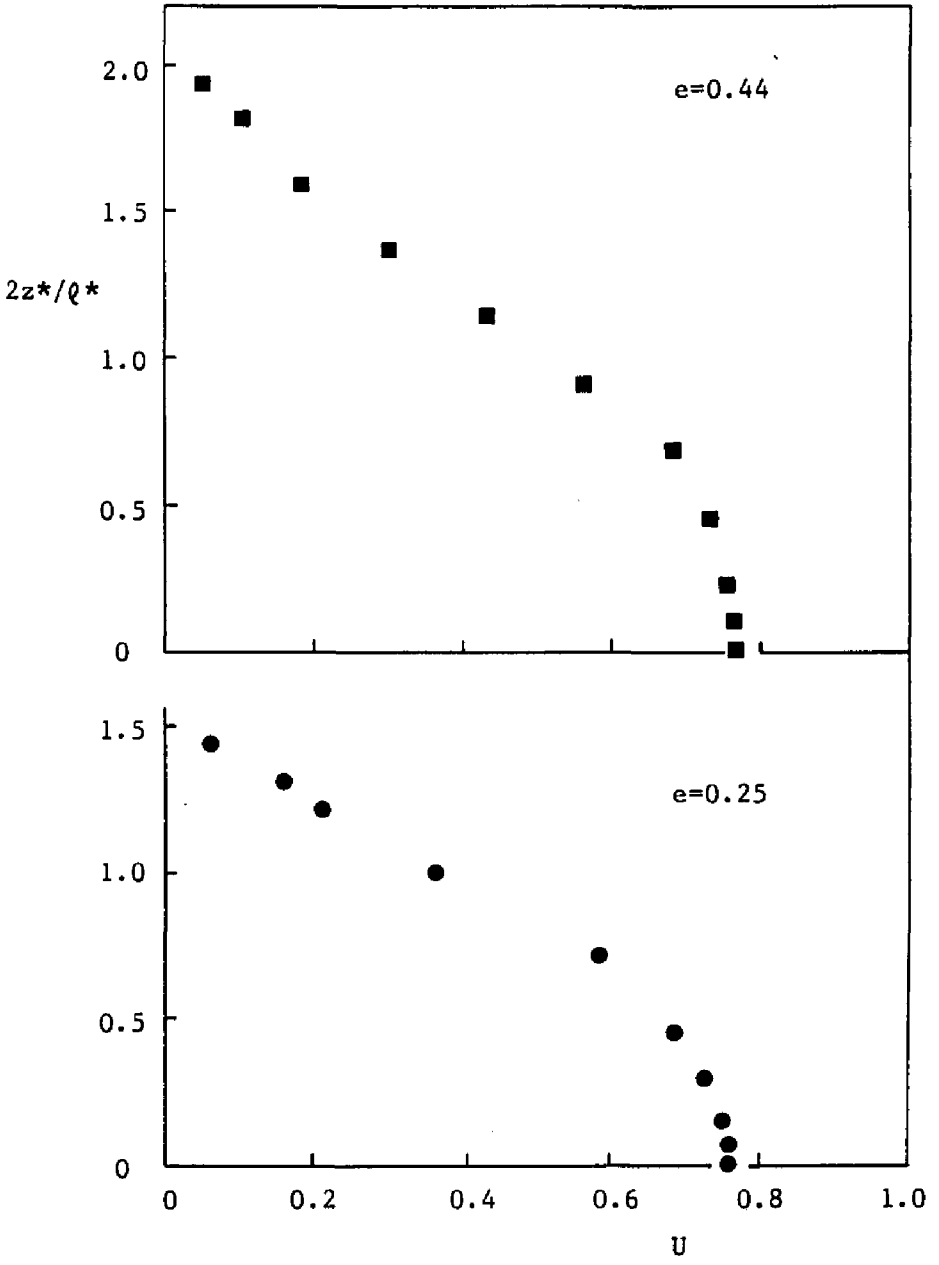

Figure 43. Spanwise profiles of velocity (h=1.07 , x=10 , y=1.57) (Table D15)

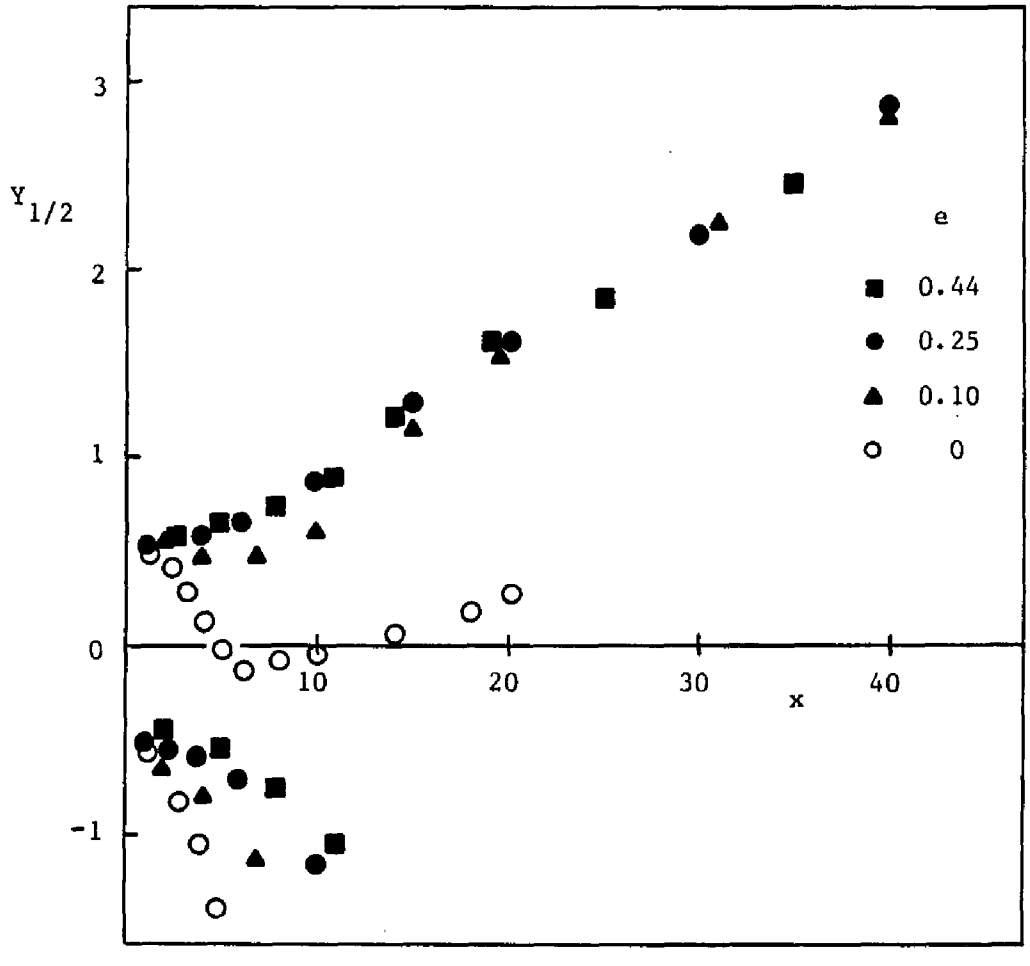

Figure 44. Vertical halfwidths of velocity (h=1.07 , z=0)
(Table D17)

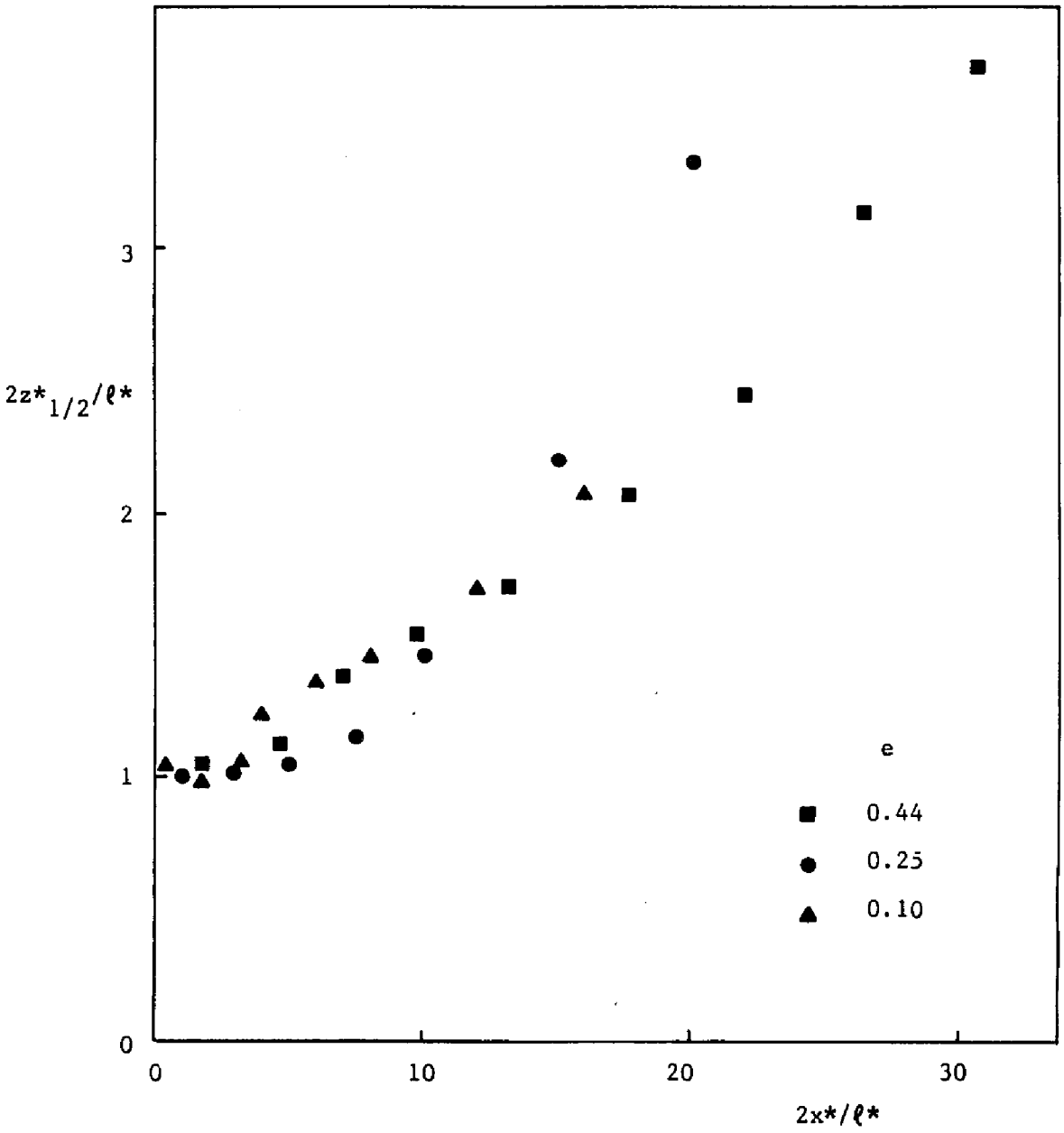

Figure 45. Spanwise halfwidths of velocity (h=1.07 , y=1.57)
(Table D18)

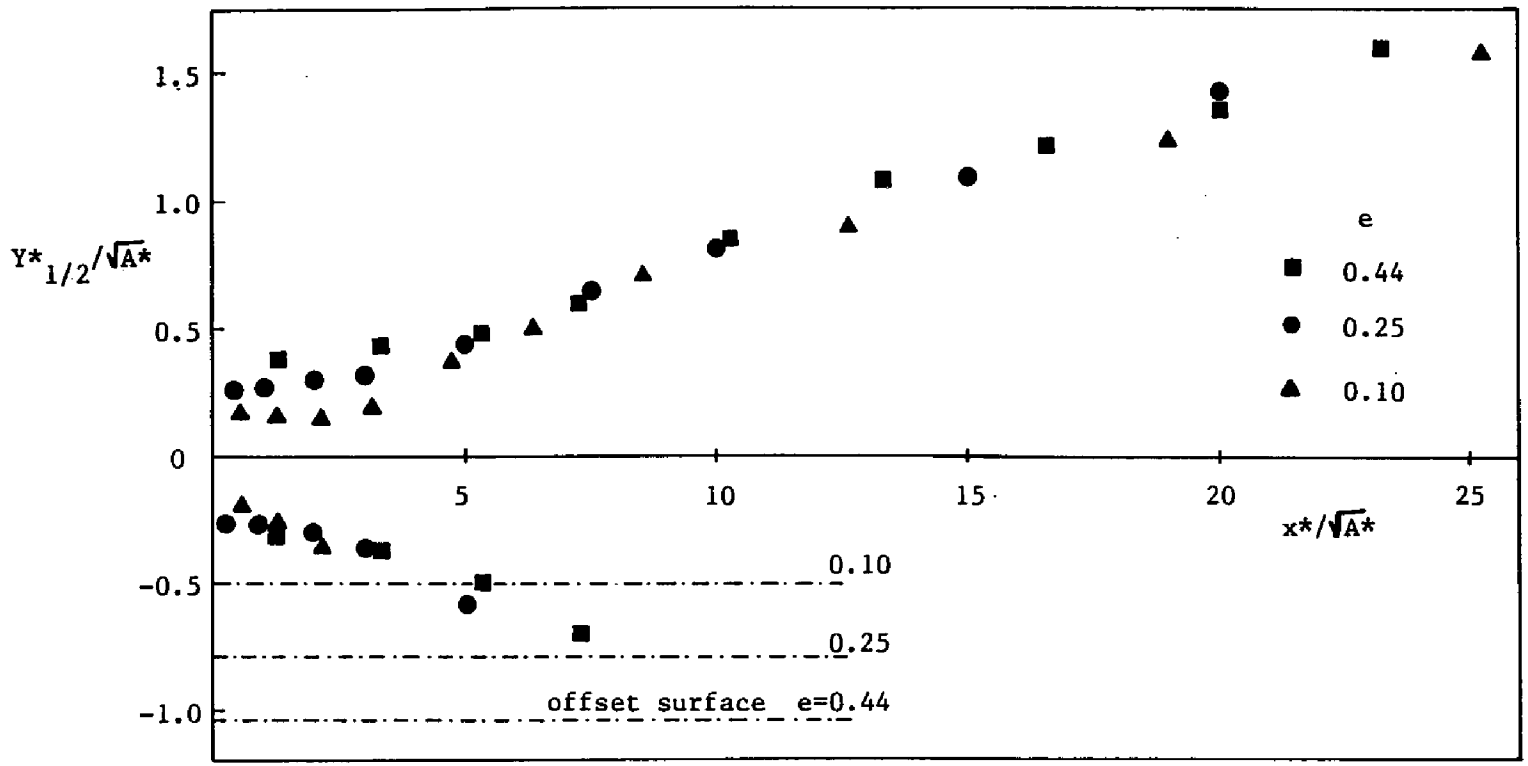

Figure 46. Normalized vertical halfwidths of velocity (h=1.07 , z=0) (Table D17)

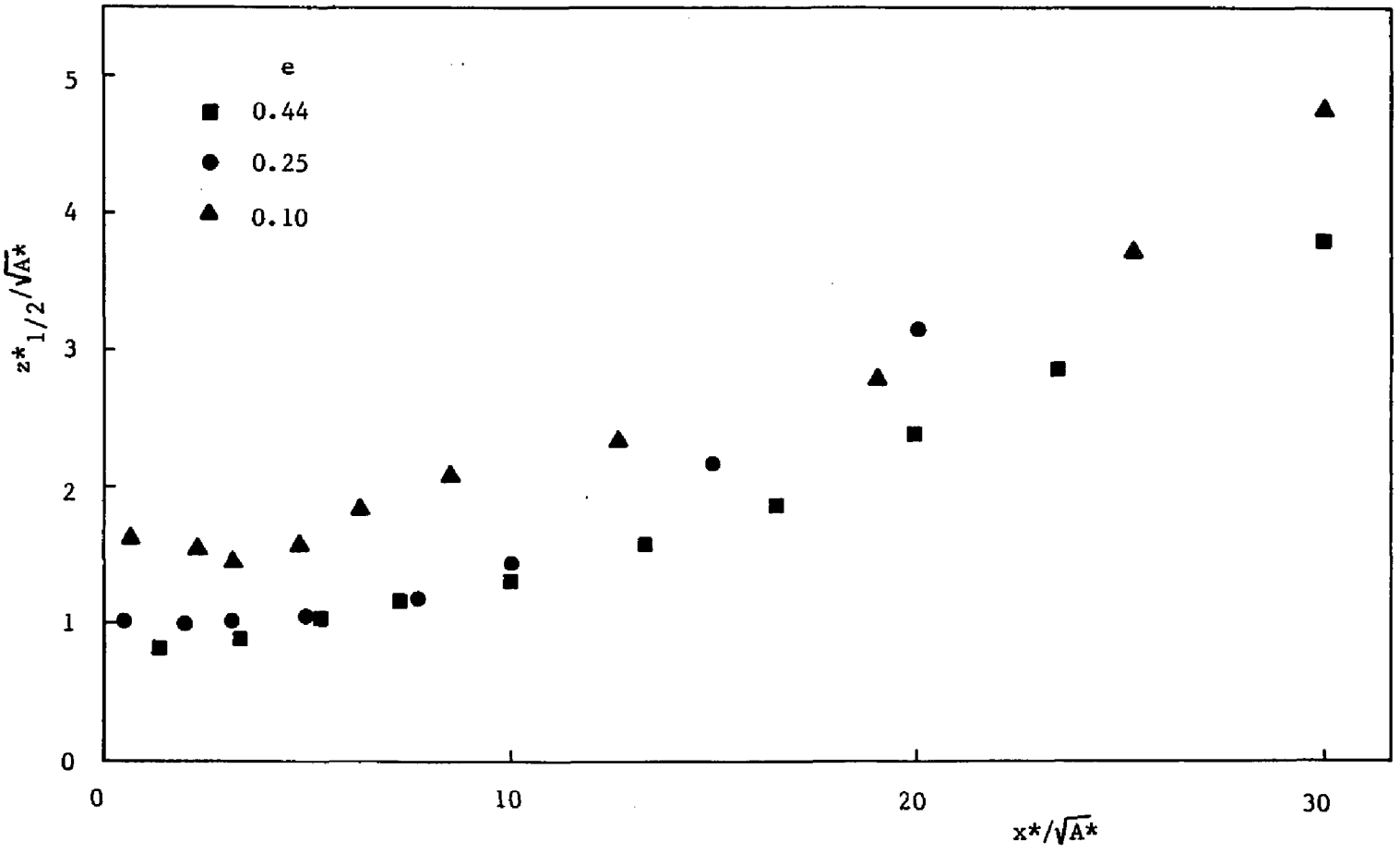

Figure 47. Normalized spanwise halfwidths of velocity (h=1.07 , y=1.57) (Table D18)

The local effectiveness of offset jets discharging from various outlets was measured by the decay of the maximum velocity along the vertical centerplane and is presented in Figure 48. It is shown that the decays corresponding to larger aspect ratios are accompanied by lower values of U_{cmax}. Nondimensionalization of x* with division by $\sqrt{A^*}$, Figure 49, results in a convergence of all decays into a single curve, which can be approximated by the equation:

$$U_{cmax} = 1.83\,(x^*/\sqrt{A^*})^{-0.521} \qquad (\text{for } x^*/\sqrt{A^*} \geq 3)$$

Trajectories along the vertical centerplane of offset jets discharging from various outlets (with constant h = 1.07) are examined in Figure 50. It is shown that trajectories of three-dimensional jets differ significantly from that of two-dimensional jets. However as e is decreased from 0.25 to 0.1, trajectory pattern moves towards that of two-dimensional jet.

All experimental data on velocity field that so far have been discussed were based on measurements taken with a Pitot-static pressure probe. According to the probe's specifications, velocity readings are accurate to 2% up to angles of attack (yaw and pitch) of 30° (Figure 51). Verification of the data accuracy was achieved by measuring the angles of attack with a three-dimensional directional probe (for details, see Appendix A). In addition to angles of attack, three-dimensional directional probes are capable of measuring total and static pressures. Thus, the velocity vectors as well as the three velocity components can be calculated.

A detailed investigation of the velocity field characteristics (i.e., yaw and pitch angles, velocity vectors and the three velocity components) for a typical

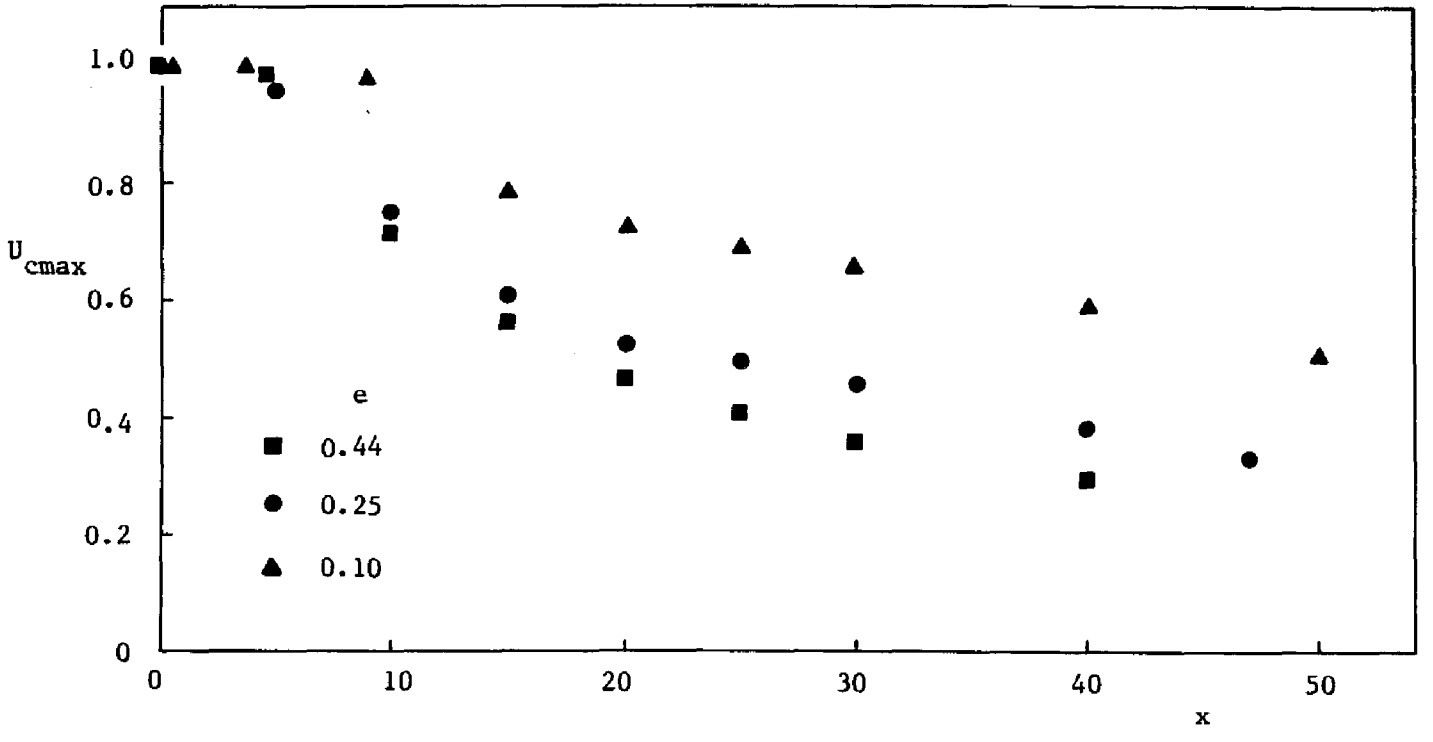

Figure 48. Maximum velocity decay (h=1.07 , z=0) (Table D19)

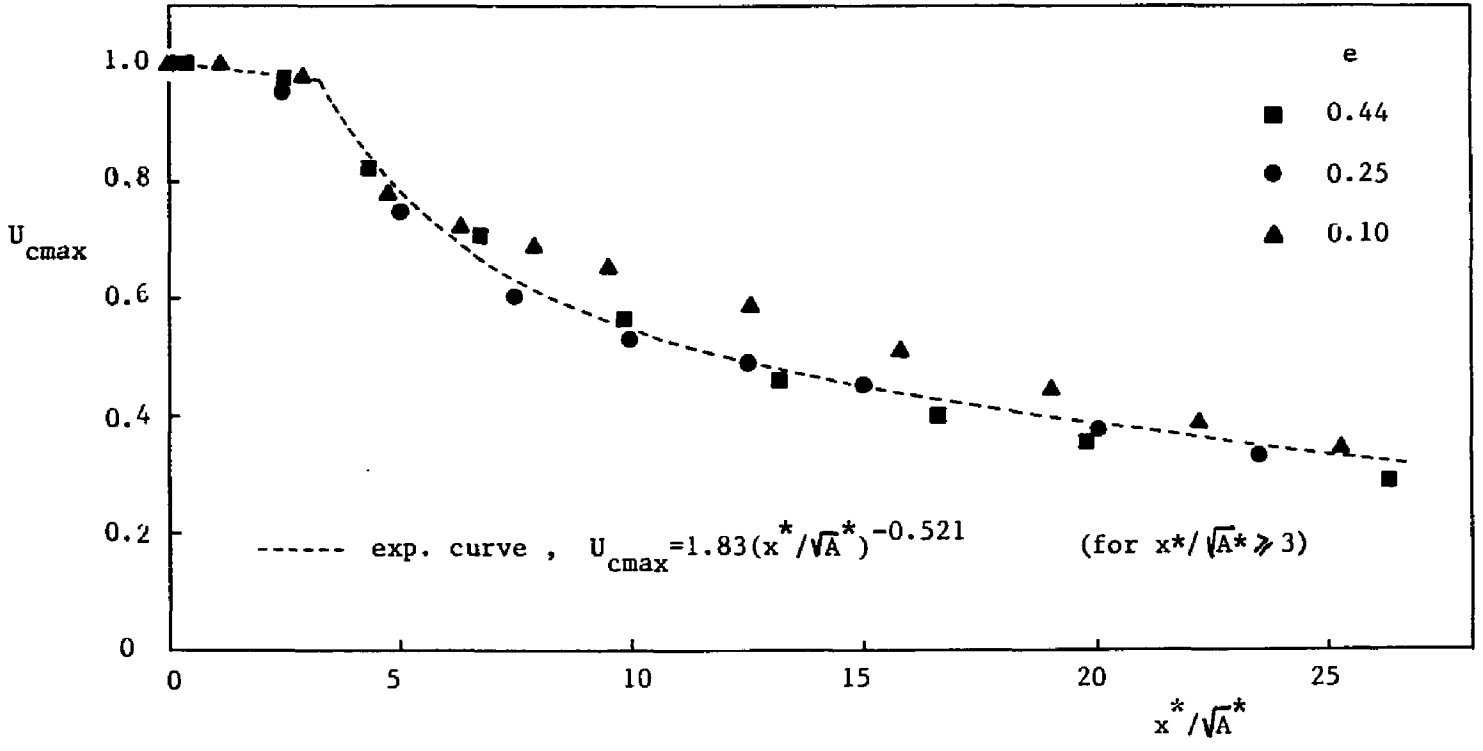

Figure 49. Normalized maximum velocity decay (h=1.07 , z=0) (Table D19)

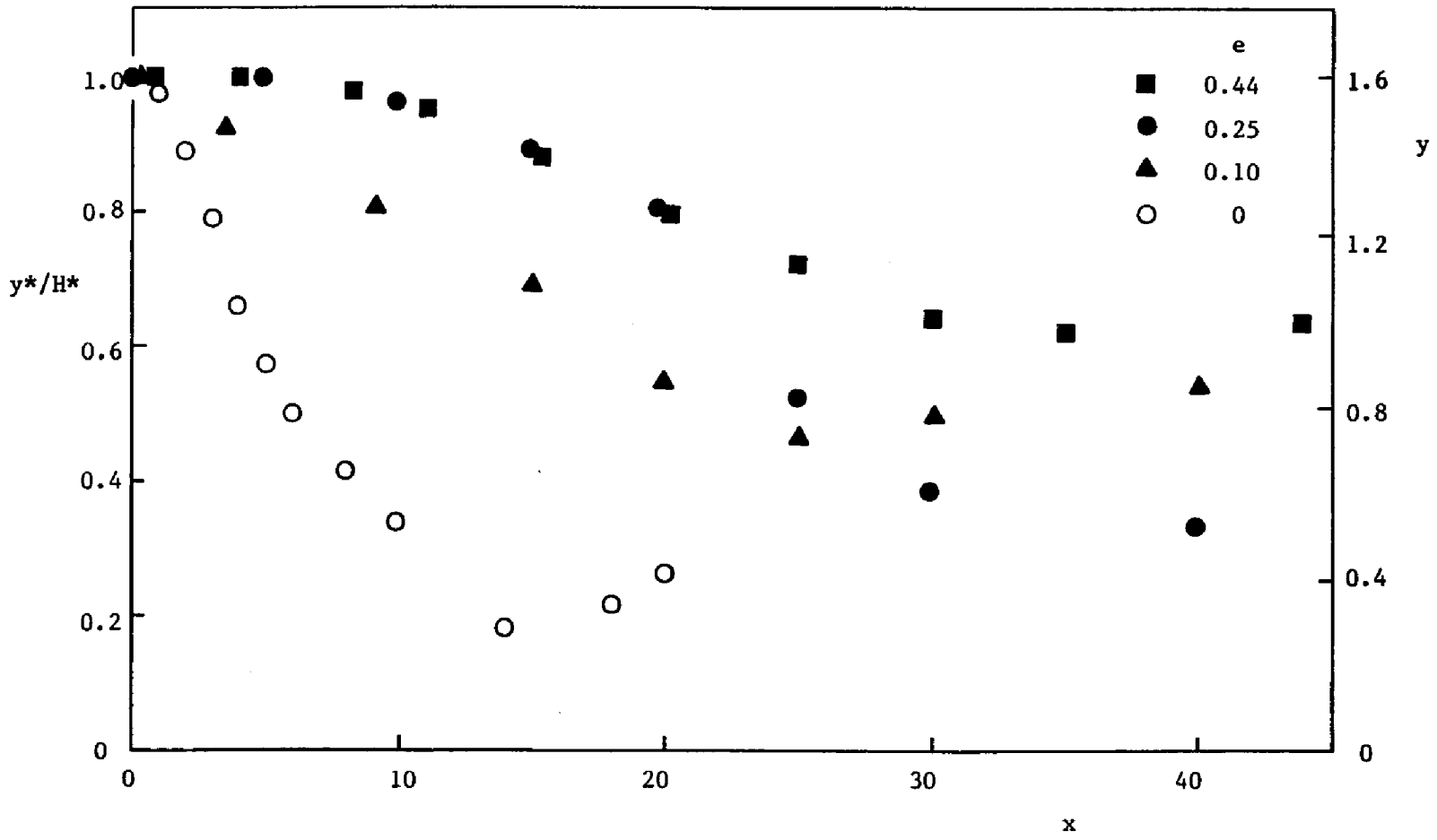

Figure 50. Jet trajectories (h=1.07 , z=0) (Table D19)

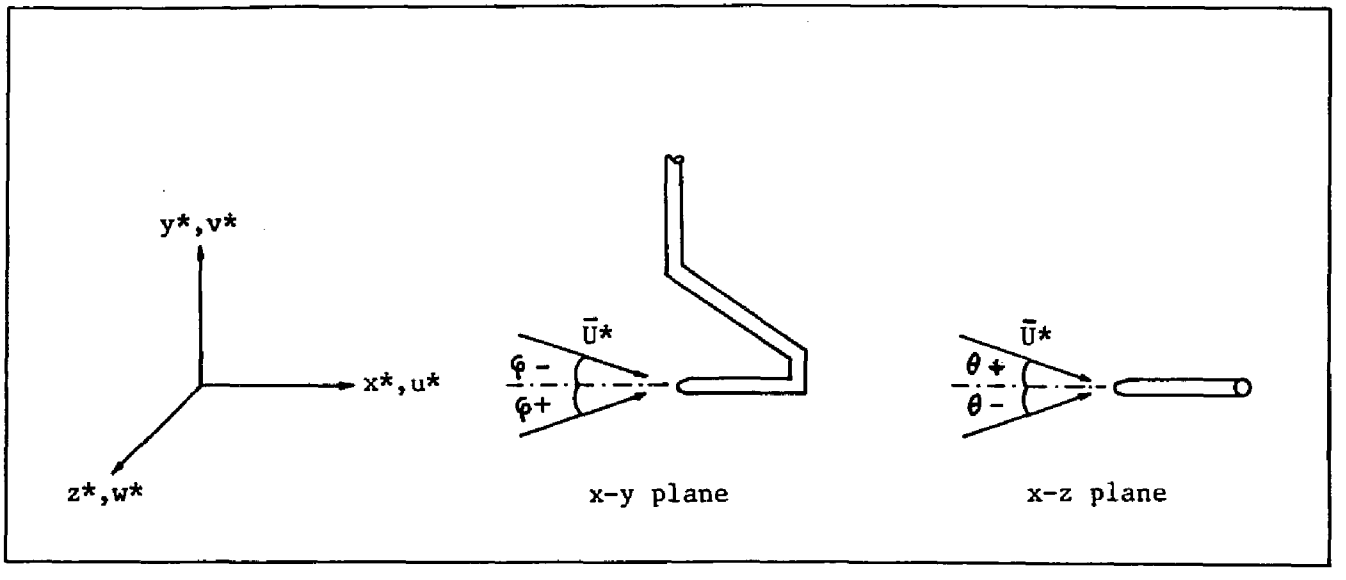

Figure 51. Illustration of pitch (φ) and yaw (θ) angles

case of an offset jet (e = 0.25, h = 1.86) is presented in the following part of this section.

The vertical profiles of the velocity vectors at various axial stations along the vertical centerplane (z = 0) are shown in Figure 52. This format of presentation gives a descriptive picture of the flow pattern as the jet attaches to the offset surface. It may be noted that the present velocity data are in agreement with those taken by the Pitot-static pressure probe. In addition, these data confirm the location of jet reattachment which was previously estimated by measuring the surface pressure on the offset surface.

The vertical profiles corresponding to x-y projections of the velocity vectors at various lateral stations ($z^* = 0$, $z^* = 0.5\ell^*$, $z^* = 0.7\ell^*$) across the x = 15 plane are presented in Figure 53. These profiles may also furnish quantitative information regarding the axial (u) and vertical (v) components of velocity.

The lateral profiles corresponding to x-z projections of the velocity vectors were examined at three vertical stations (Y = -1.18, Y = 0, Y = 1.18) along the x = 15 plane and are presented in Figure 54. In addition to quantitative information regarding the axial (u) and lateral (w) components of velocity, this figure confirms the asymmtery between the upper and lower station profiles, which have been first observed and discussed in Figure 30.

A detailed description of the u, v and w velocity components along the y- (at x = 15, $z^* = 0.5\ell^*$) and z- (at x = 15, y = 1.18) directions is given in Figures 55 and 56, respectively. The existence of a three-dimensional flow, as well as the dominance of the u-component can be confirmed in both figures.

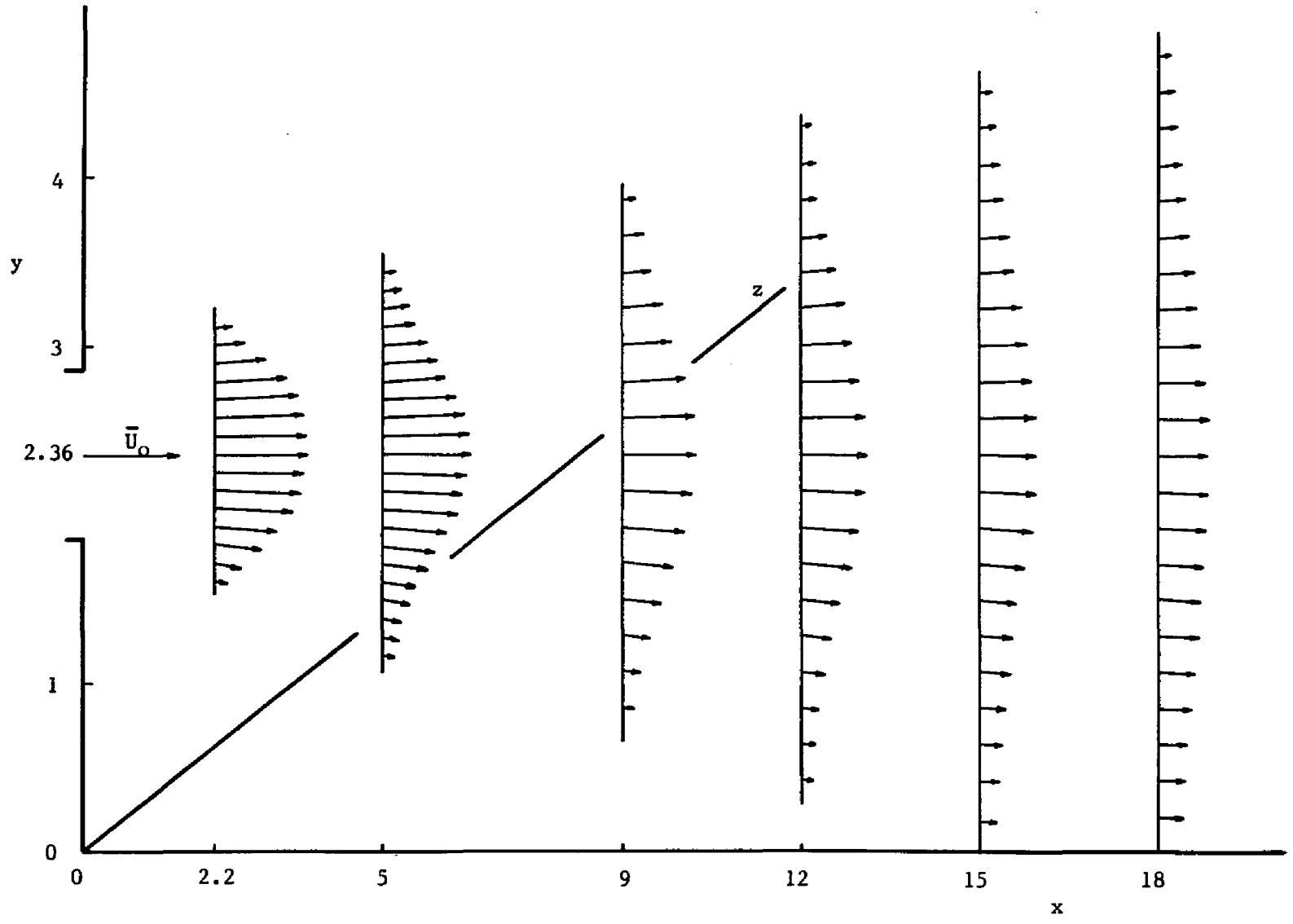

Figure 52. Vertical profiles of velocity vectors (e=0.25 , h=1.86 , z=0) (Table E1)

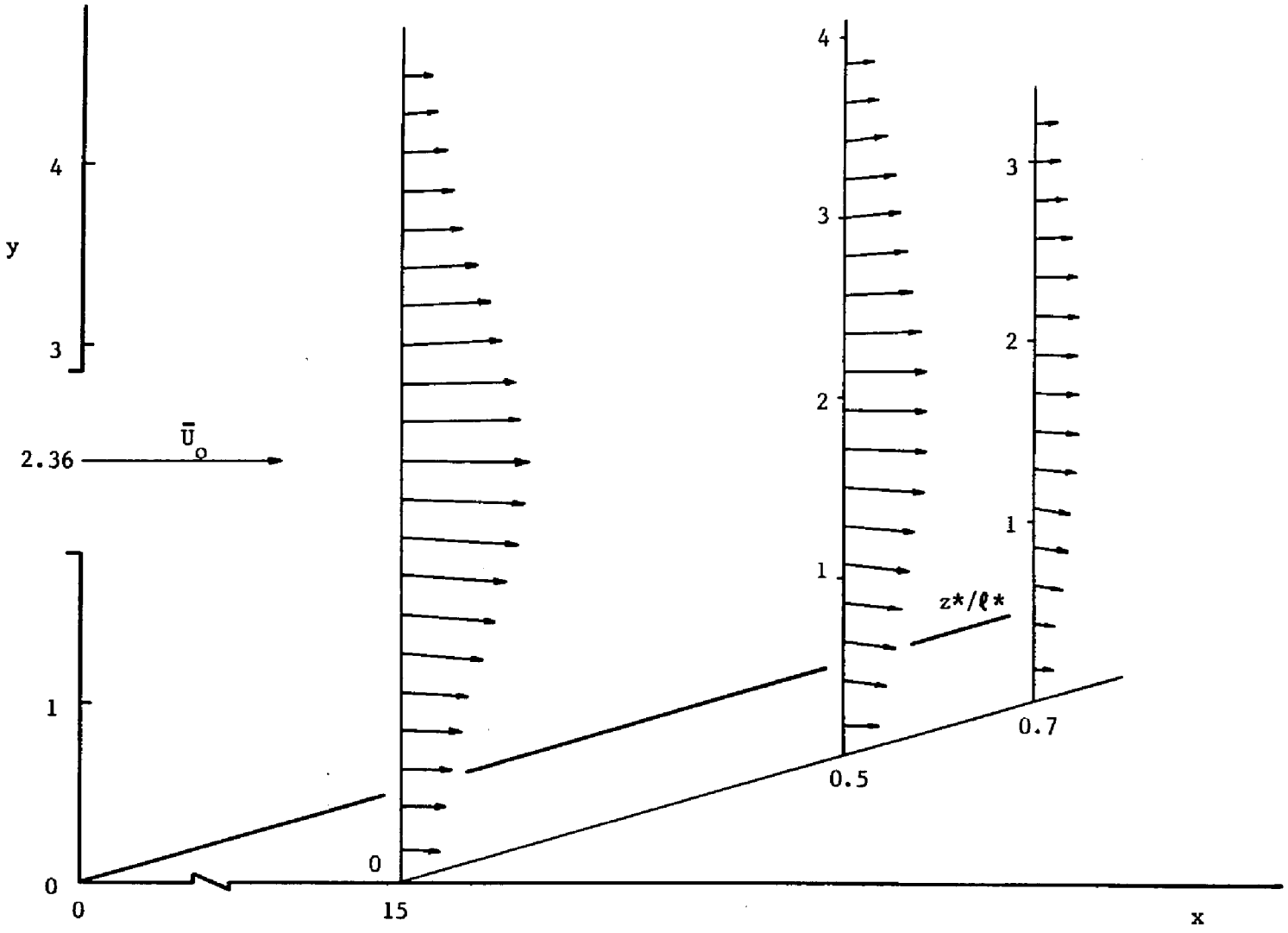

Figure 53. Vertical profiles of the x-y projections of velocity vectors (e=0.25 , h=1.86 , x=15) (Tables E1 and E2)

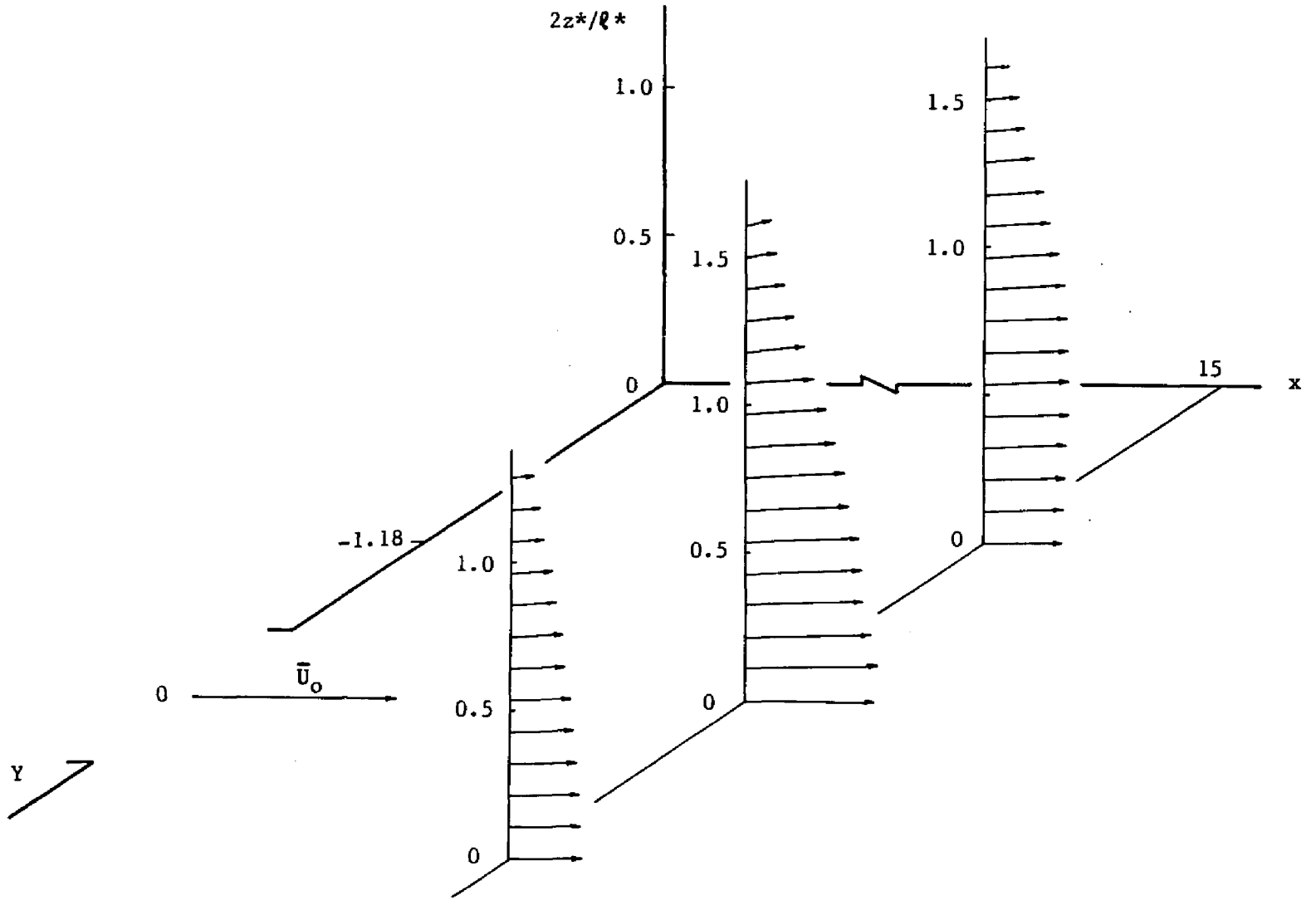

Figure 54. Lateral profiles of the x-z projections of velocity vectors (e=0.25 , h=1.86 , x=15) (Table E3)

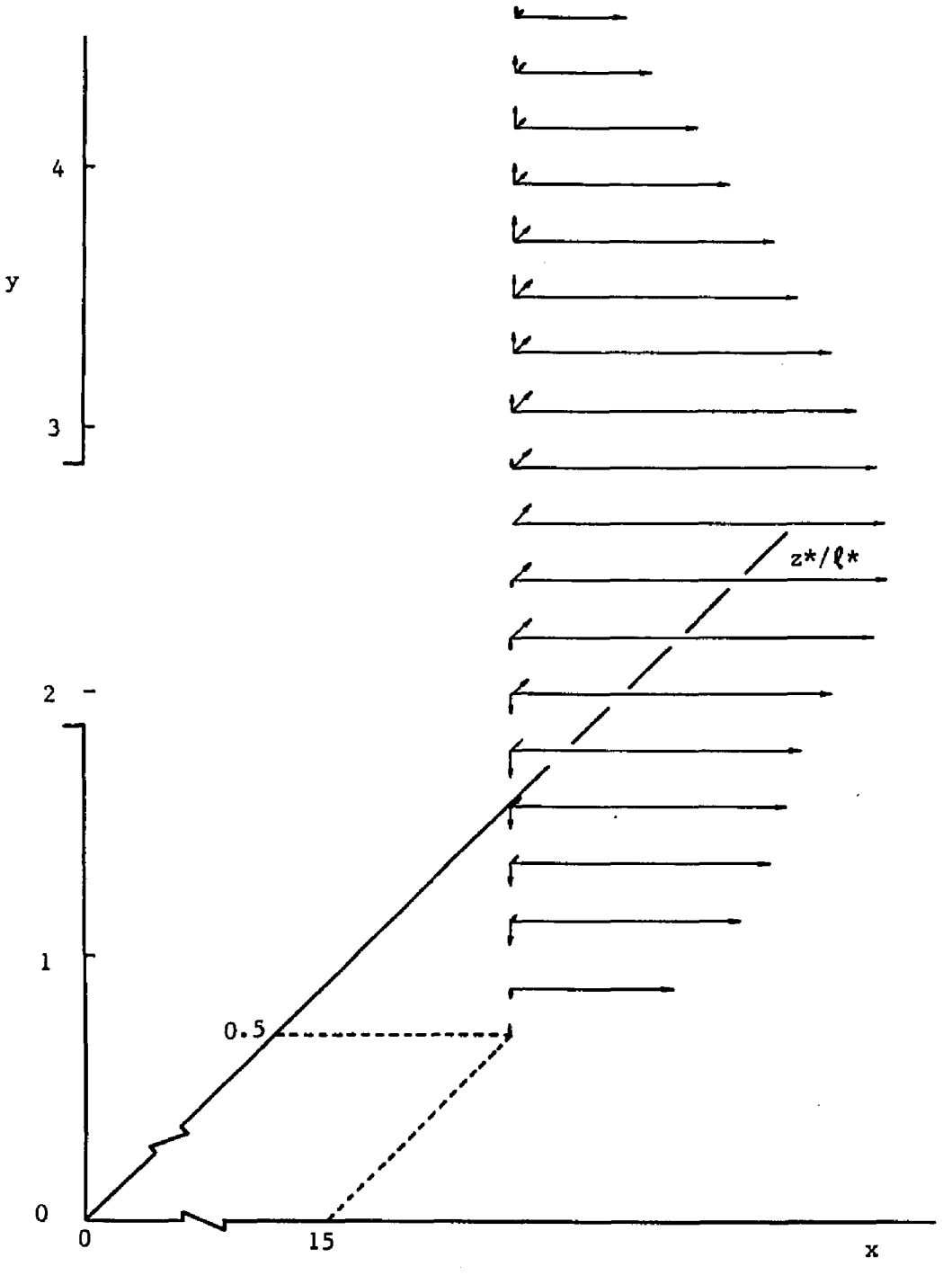

Figure 55. The three velocity components of a typical vertical profile (e=0.25 , h=1.86 , x=15 , z^*/ℓ^*=5) (Table E2)

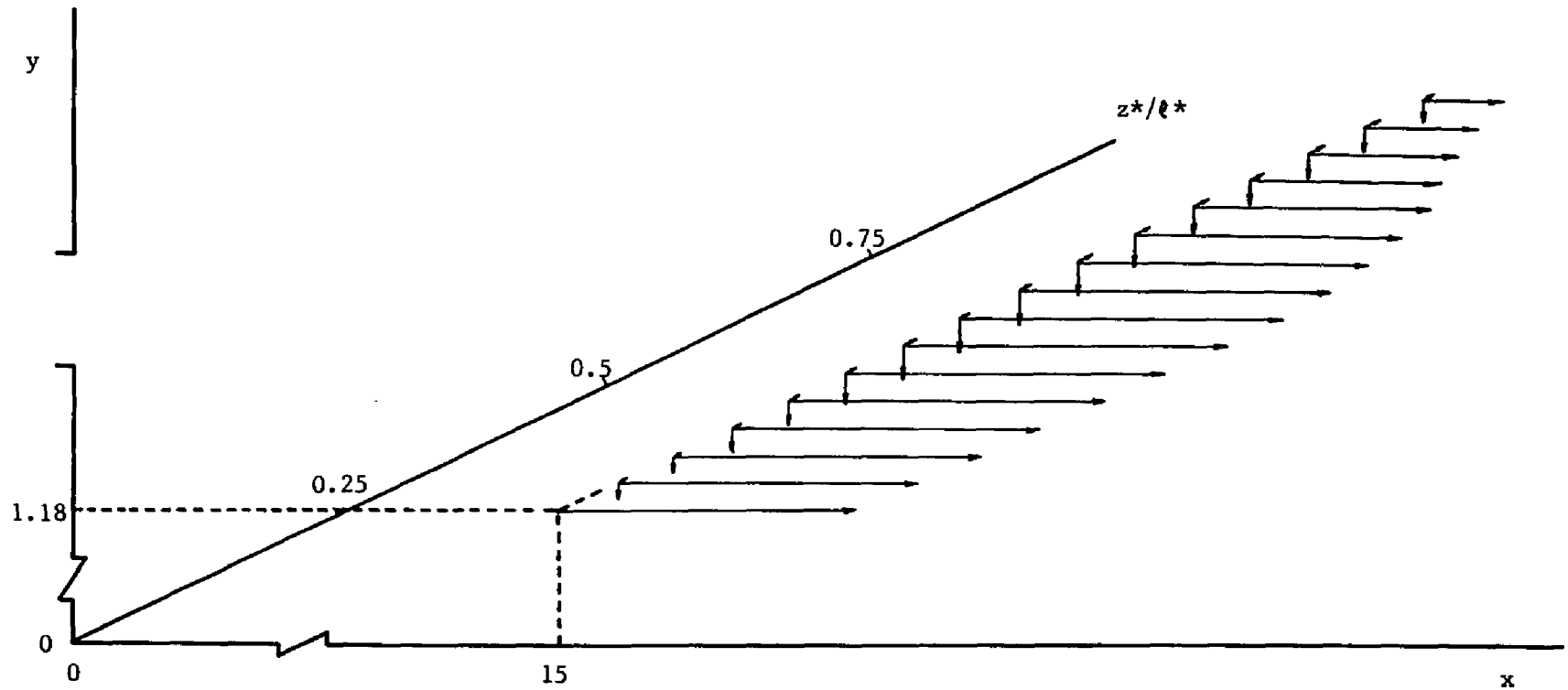

Figure 56. The three velocity components of a typical lateral profile (e=0.25 , h=1.86 , y=1.18) (Table E3)

A quantitative comparison between u and v components of velocity was examined at three axial stations (x = 2.2, x = 9, x = 15) along the vertical centerplane (z = 0) and is presented in Figures 57 and 58. An increase of $|v/u|$ can be observed in Figure 58 as the position of the corresponding components approaches the edges of the jet. However, exception to this behavior is the data in the vicinity of reattachment (i.e., lower part of data corresponding to the x = 15 station). In this area the flow streamlines become nearly parallel to the offset surface, as it was shown in Figure 52.

Variations of the angles of attack in the three-dimensions are presented in Figures 59 through 62. The pitch angle, φ, variation along the y-direction was examined at various central axial stations and is shown in Figure 59. The offset surface influence on direction of the jet flow can be verified by the different behavior of $|\varphi|$ in upper and lower halfs of the graph. As it was expected, φ was found to be approximately zero in the vicinity of the offset surface for cases corresponding to positions downstream of reattachment (i.e., x = 18).

The yaw angle, θ, variation along the y-direction was examined at two lateral positions across the x = 15 station and is presented in Figure 60. The behavior of θ in the vicinity of the offset surface was found to be strongly dependent on lateral position. For example, at $z^* = 0.5\ell^*$, θ starts with 0° and increases up to 4° as y is increased, while at $z^* = 0.7\ell^*$, θ starts with 7° and decreases up to 3.6° further up.

The φ and θ variations along the z-direction were examined at x = 15 station and are given in Figures 61 and 62, respectively. These variations correspond to the horizontal centerplane (Y = 0) and to two other symmetrical

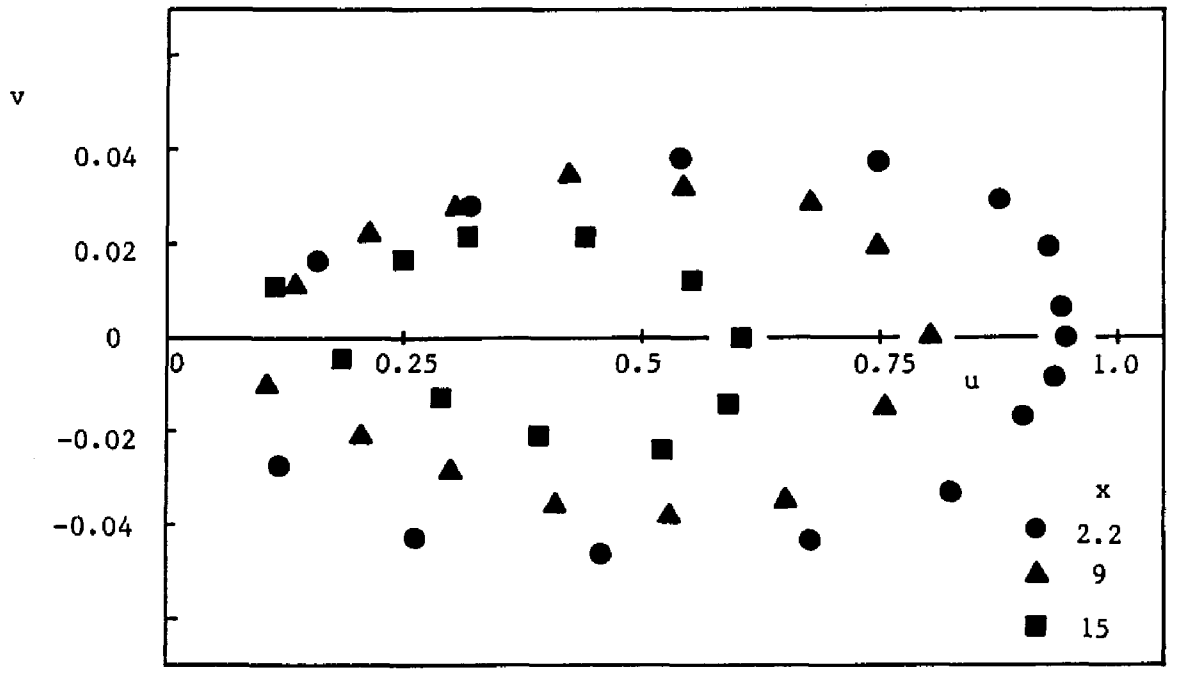

Figure 57. Comparison between u and v components of velocity
(e=0.25 , h=1.86 , z=0) (Table E1)

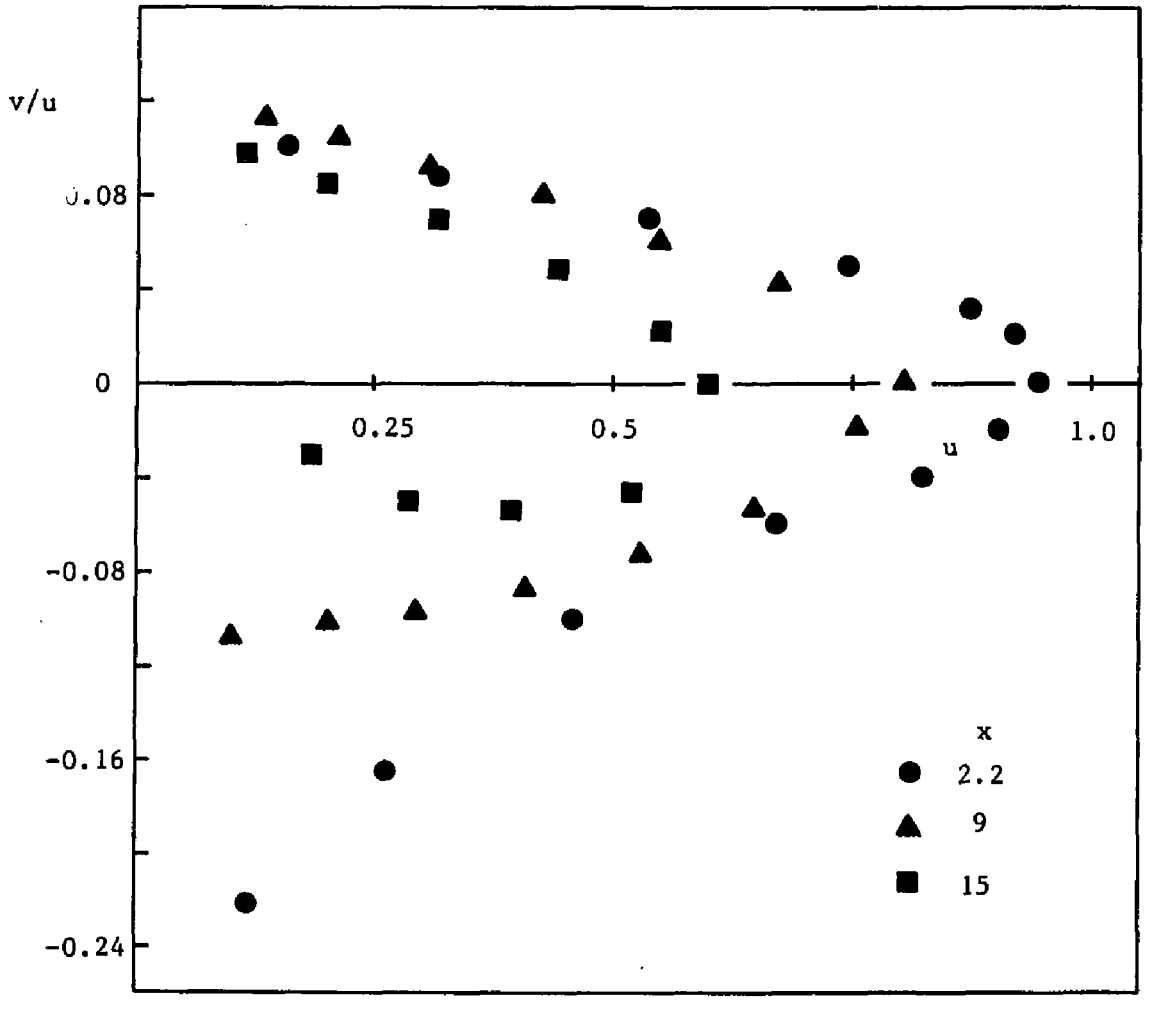

Figure 58. Comparison between u and v velocity components (e=0.25 , h=1.86 , z=0) (Table E1)

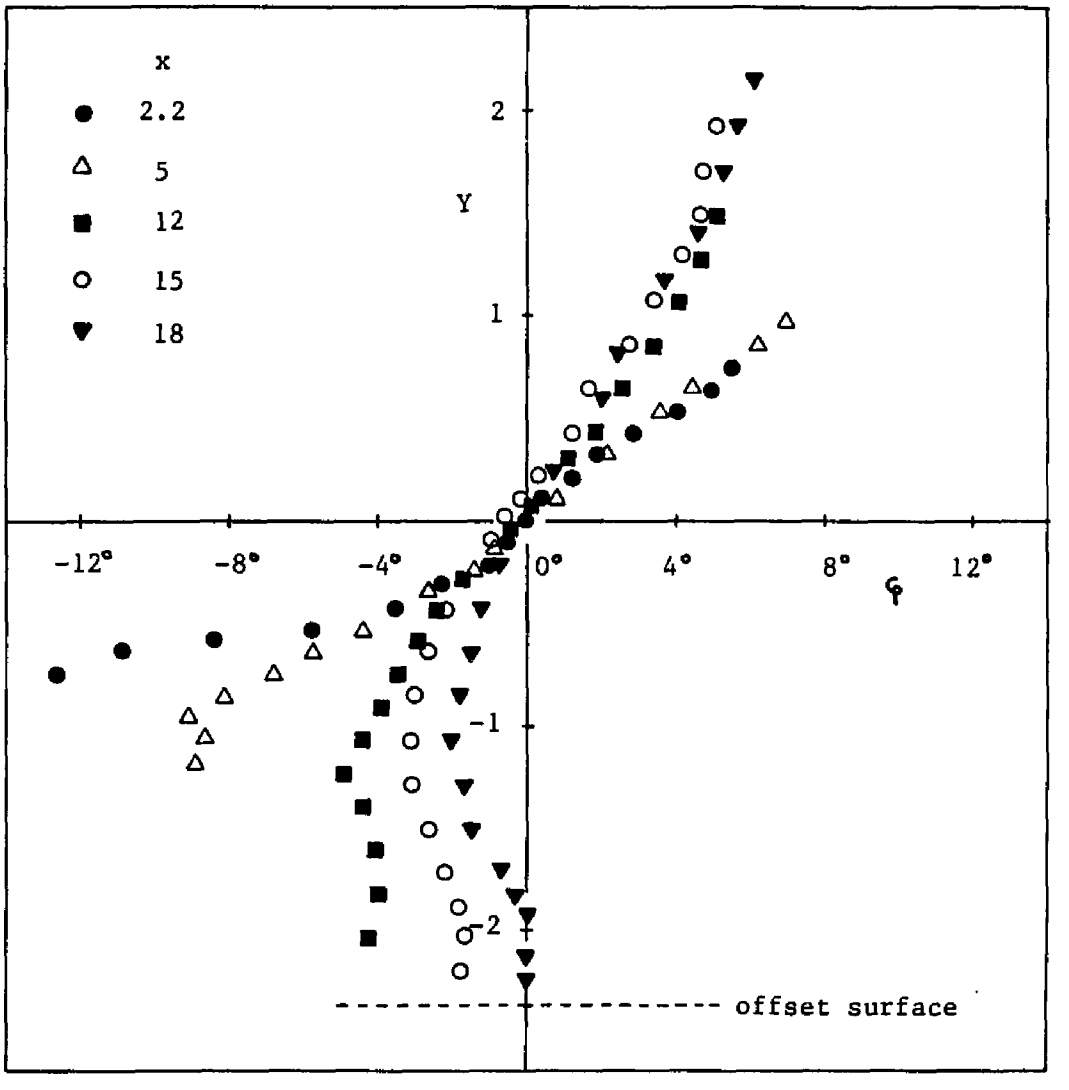

Figure 59. Variation of pitch angle along the y-direction (e=0.25 , h=1.86 , z=0) (Table E1)

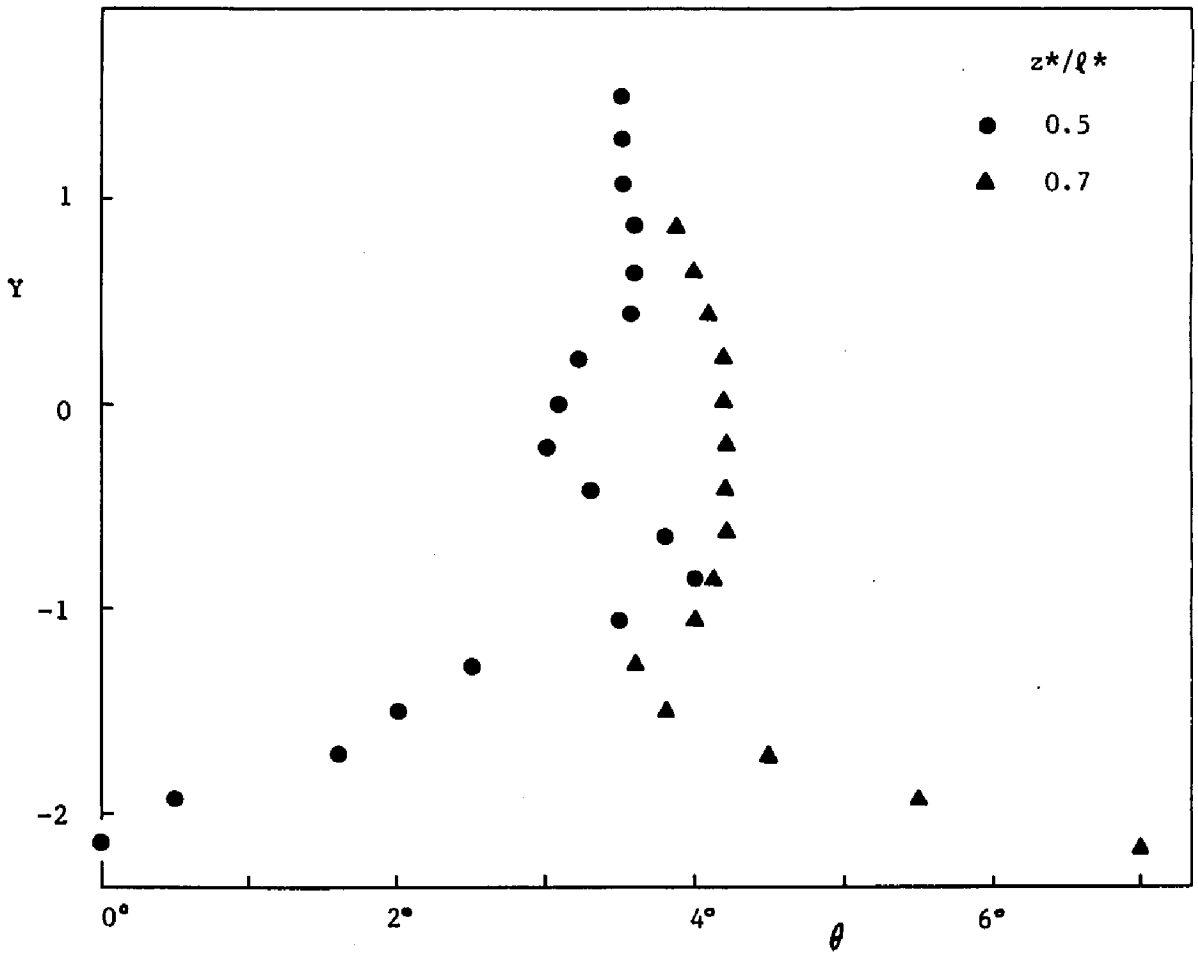

Figure 60. Variation of yaw angle along the y-direction (e=0.25 , h=1.86 , x=15) (Table E2)

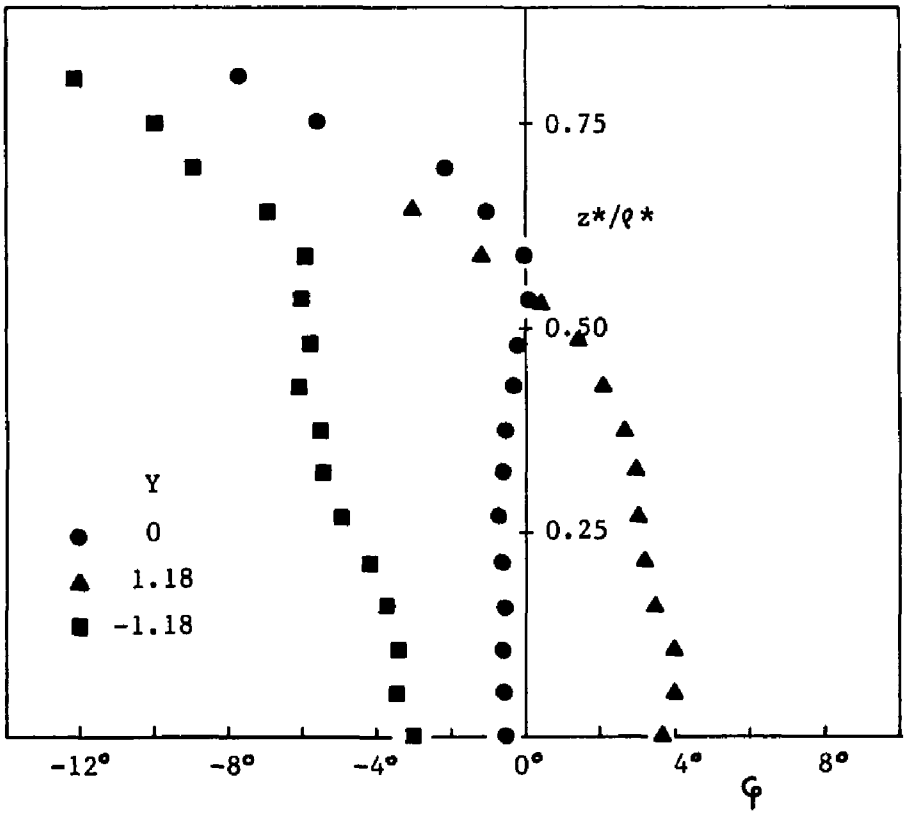

Figure 61. Variation of pitch angle along the z-direction (e=0.25 , h=1.86 , x=15) (Table E3)

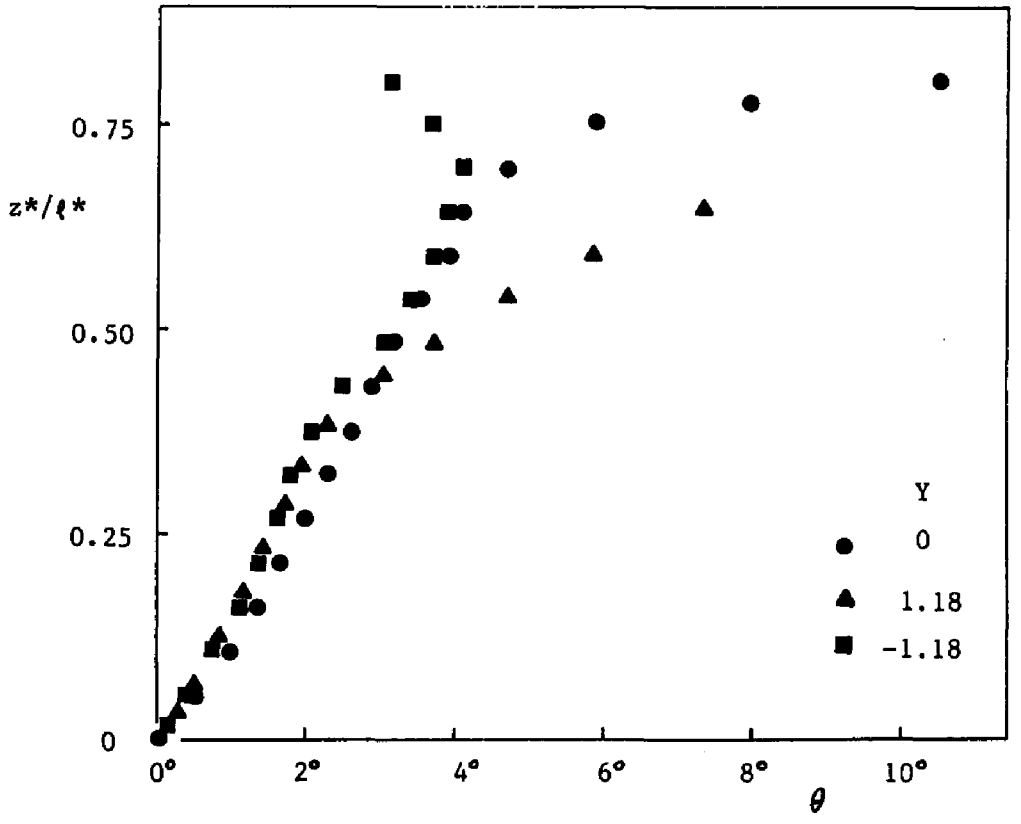

Figure 62. Variation of yaw angle along the z-direction (e=0.25 , h=1.86 , x=15) (Table E3)

planes (Y = ±1.18). The bending of the jet flow towards the offset surface can be confirmed by the general tendency of φ to reach negative values for all examined cases in Figure 61.

The θ variation, Figure 62, shows a constant rate of increase in the region $0 < z^* < 0.5\ell^*$ for all cases, and a behavior strongly dependent on Y elsewhere.

Finally, it should be emphasized that all data obtained with the three-dimensional directional probe show angles of attack up to 12°. This observation constitutes a confirmation regarding the accuracy of the data collected with the Pitot-static pressure probe and which have been used to calculate most of the velocity field characteristics.

3. Temperature Field

Extensive data on temperature characteristics were obtained for offset jets having various values of discharge aspect ratio and offset distance. Temperature measurements at the outlet of several channels under different exit conditions showed that the discharge profiles tend to depart somewhat from the top-hat shape. Figure 63 shows temperature profiles for two channels, e = 0.25 and e = 0.44, under typical flow conditions.

The development of the vertical profiles of temperature along the x-direction of the centerplane (z = 0) was examined for two aspect ratios (i.e., e = 0.44 and e = 0.25) and is presented in Figures 64 and 65, respectively. the observed asymmetry between the upper and lower parts of the profiles, which is

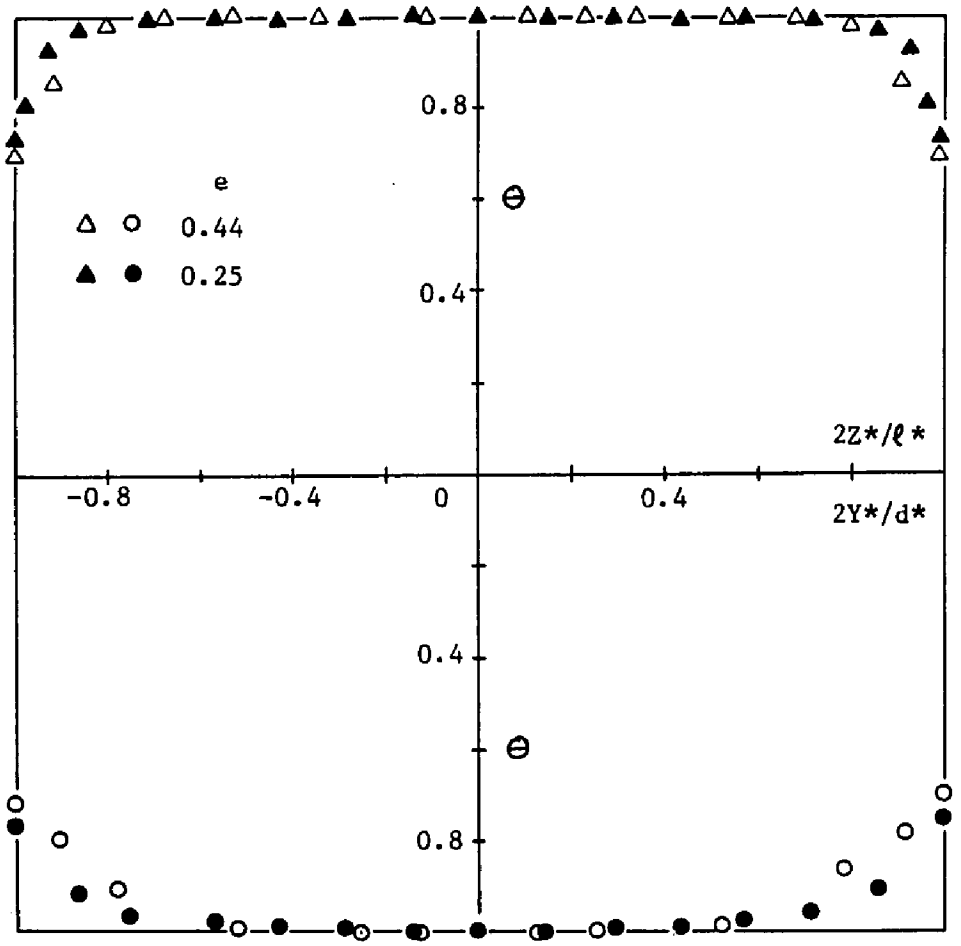

Figure 63. Discharge temperature profiles (Tables F1 and F2)

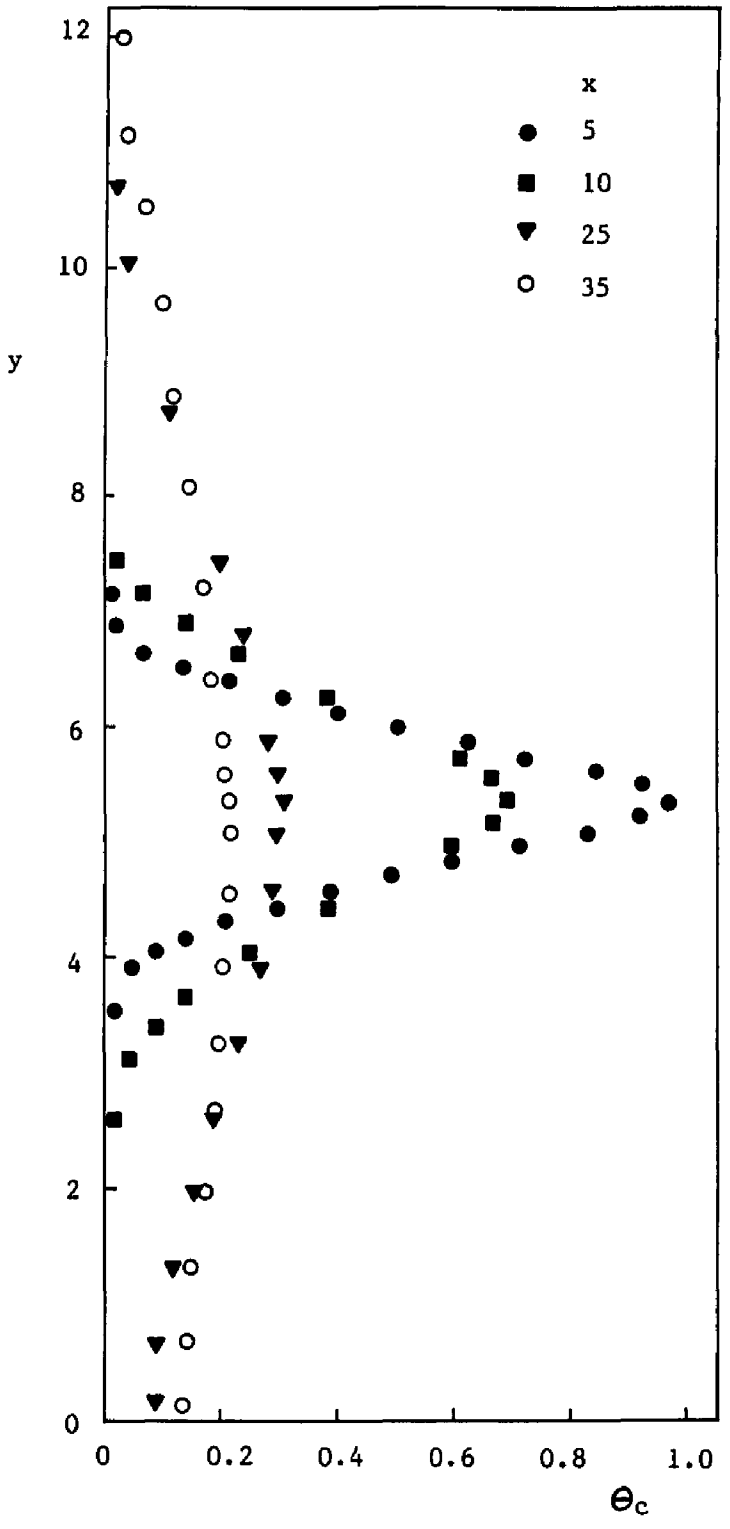

Figure 64. Vertical profiles of temperature (e=0.44 , z=0 , h=4.85) (Table F3)

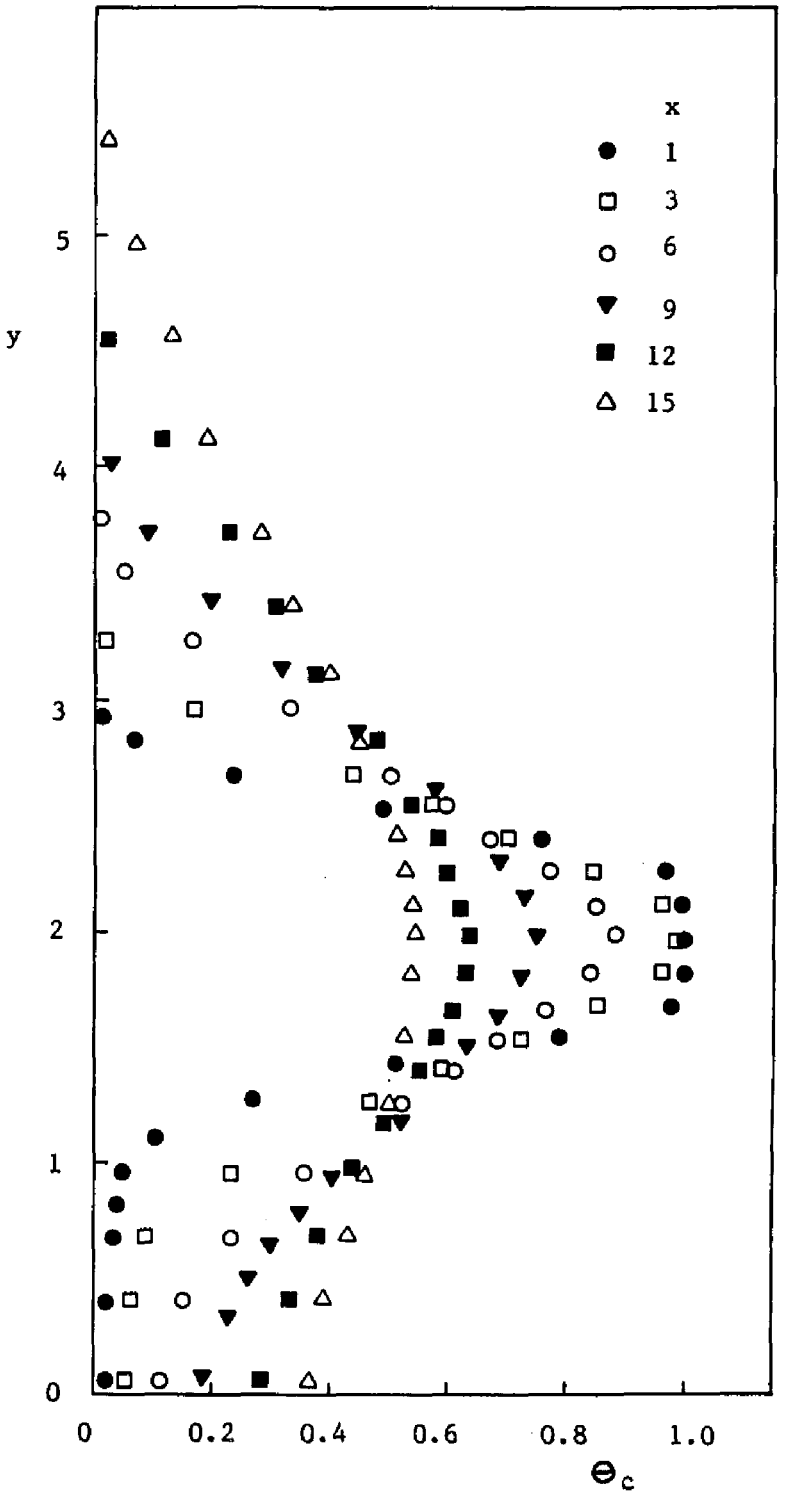

Figure 65. Vertical profiles of temperature (e=0.25 , z=0 , h=1.46) (Tables F5 and F6)

magnified as the jet proceeds further downstream, is attributed to the presence of the offset surface.

To reveal any similarity of temperature profiles an alternate form of nondimensionalization was used. Temperatures and vertical distances are nondimensionalized with divisions by the local maximum temperature difference ($T^*_{max} - T^*_\infty$) and vertical temperature halfwidth ($Y^*_{T1/2}$, distance where temperature difference has decayed to half of its maximum value), respectively. Figure 66 shows the dimensionless temperature profiles for e = 0.25. The general tendency towards a single similar profile is apparent for all data except for those corresponding to locations in the vicinity of the offset surface. This profile may be approximated by the following exponential equation:

$$\Theta_{cmax} = \exp\left[-(0.8021\ Y/Y_{T1/2})^2\right] \qquad (\text{for } Y/Y_{T1/2} \gtrsim -1.1)$$

The vertical centerplane (z = 0) temperature map, as well as the corresponding isothermal contours of a typical three-dimensional offset jet (i.e., e = 0.25, h = 1.46) are given in Figures 67 and 68, respectively. The temperature distribution differs significantly from that of two-dimensional offset jets. The approximately constant cavity temperature found in two-dimensional studies is replaced with a considerably varying temperature field. In addition, the shift of the isothermal contours shown in Figure 68 demonstrates the influence of the offset surface on temperature distribution. The development of the spanwise temperature profiles along the x-direction was examined at the horizontal centerplane (y = 5.35) and is presented in Figure 69. The profiles corresponding to the axial stations x = 5, 10, 25 appear to be still developing.

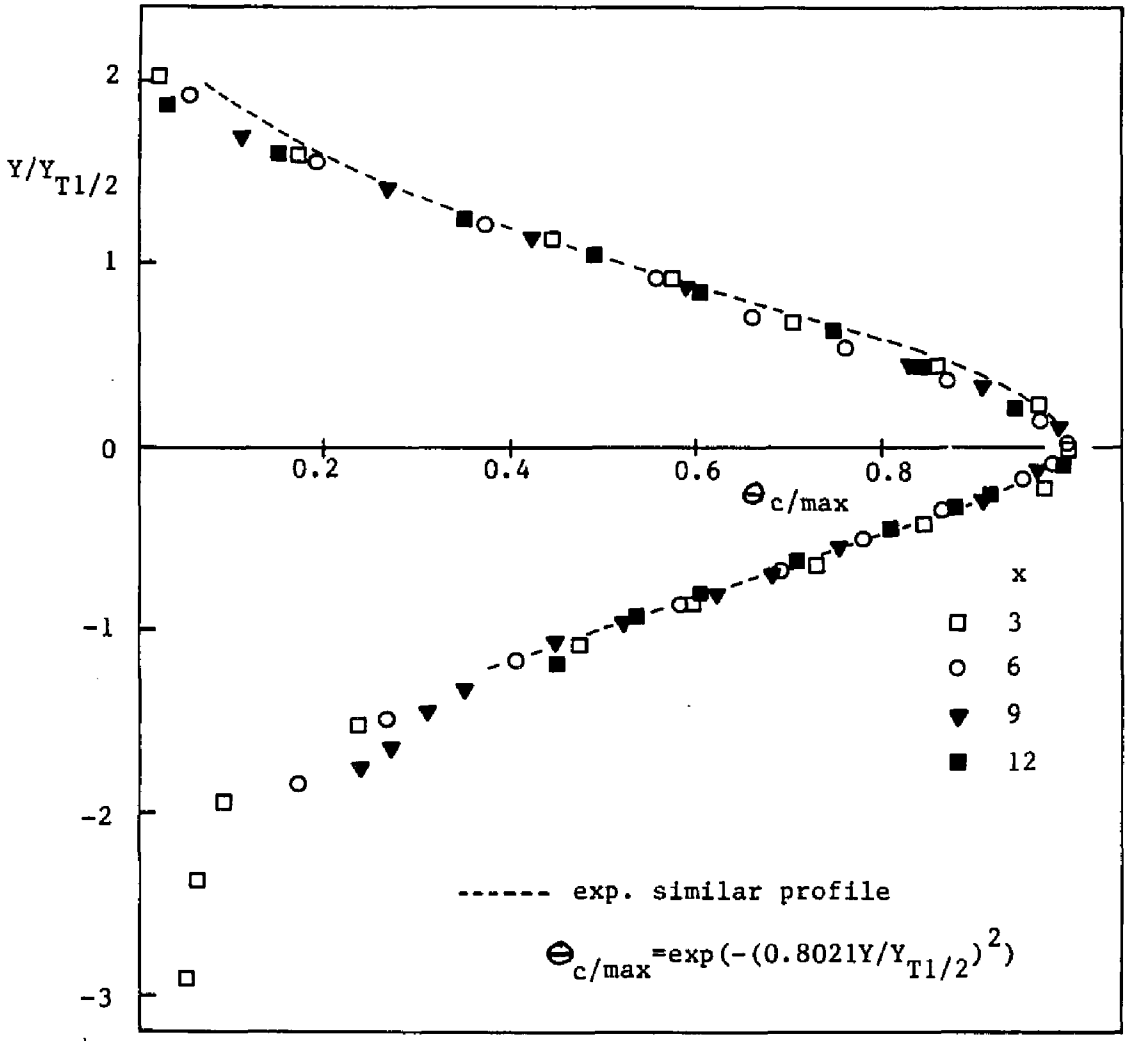

Figure 66. Vertical profiles of temperature in similarity form (e=0.25 , h=1.46 , z=0) (Tables F5 and F6)

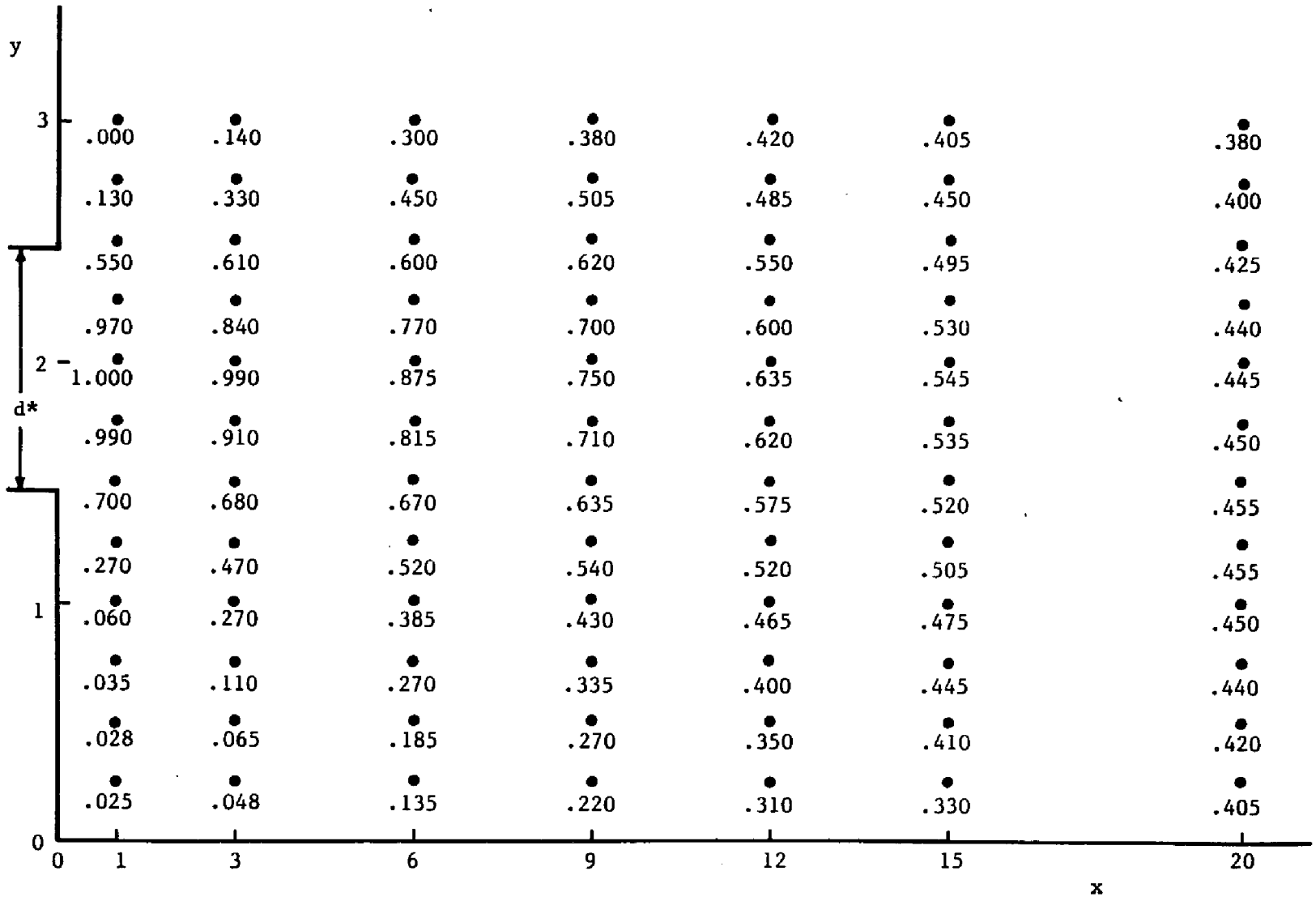

Figure 67. Vertical centerplane temperature map (e=0.25 , h=1.46 , z=0) (Tables F5 and F6)

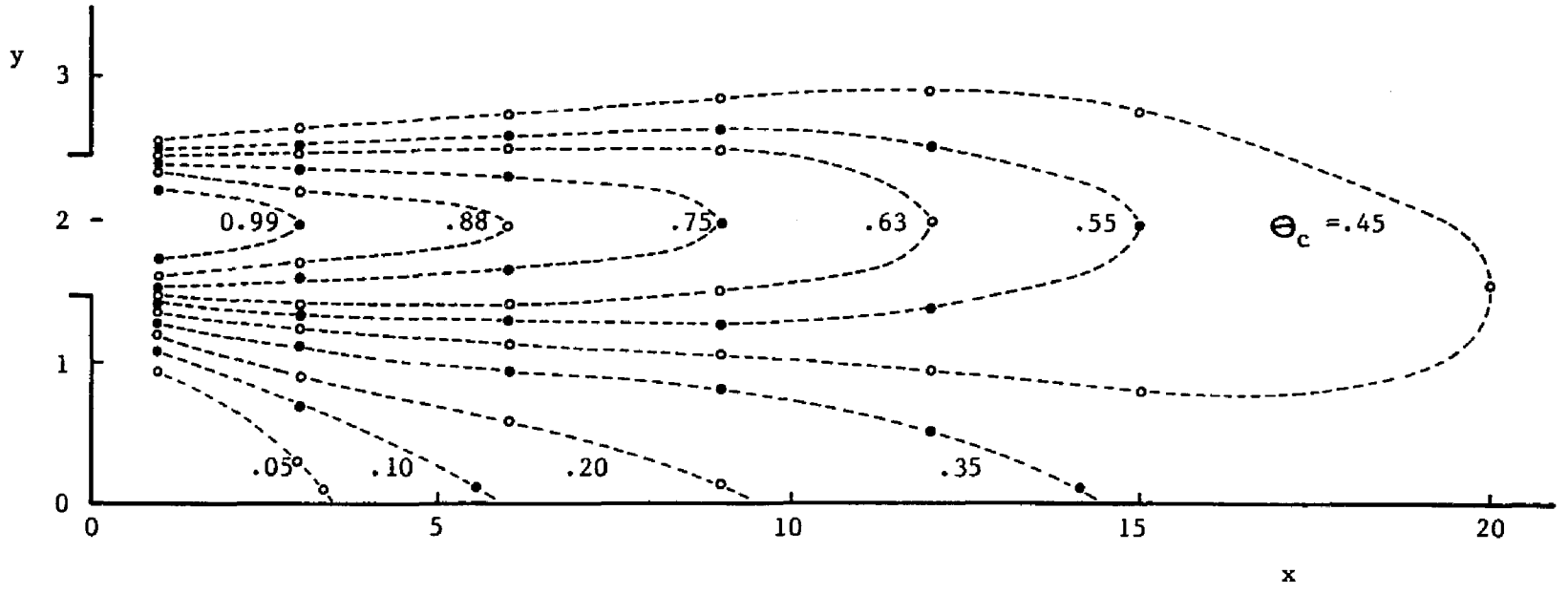

Figure 68. Vertical centerplane isothermal contours (e=0.25 , h=1.46 , z=0) (Tables F5 and F6)

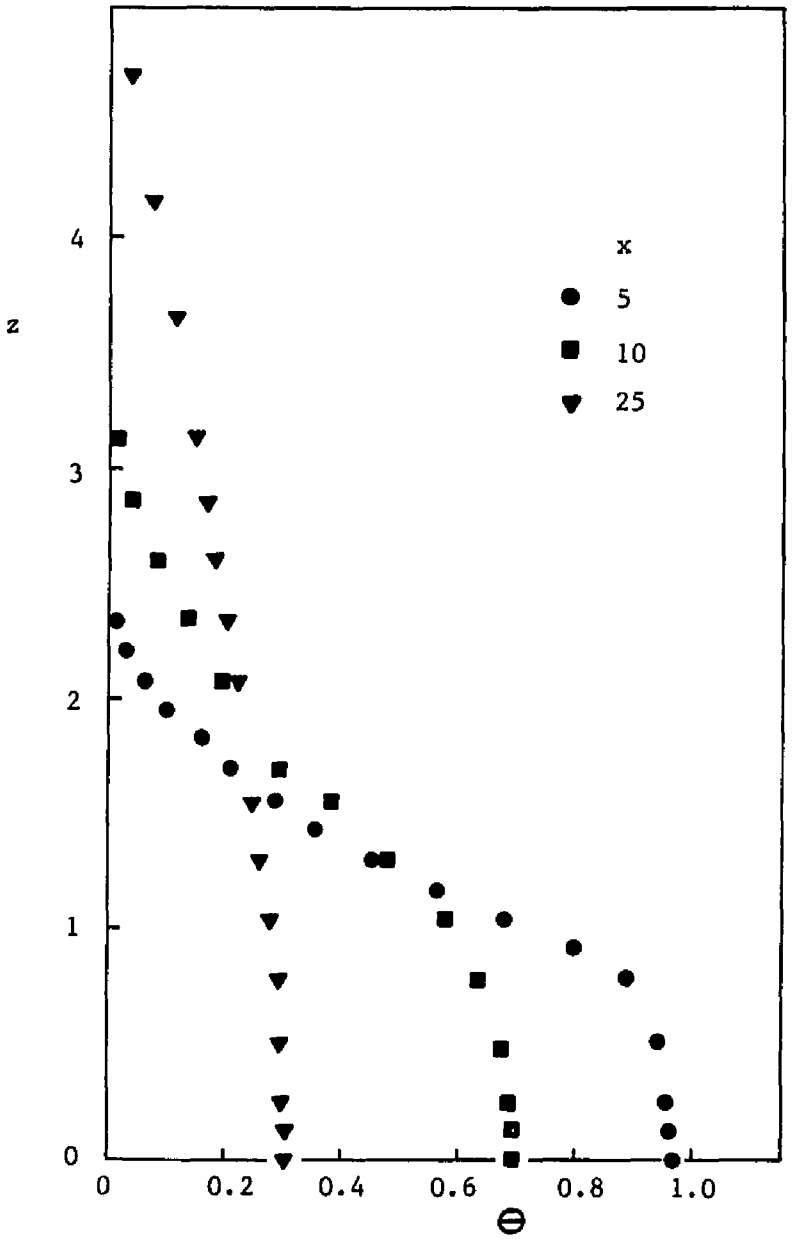

Figure 69. Spanwise profiles of temperature (e=0.44 , h=4.85 , y=5.35) (Table F4)

The effect of the offset distance parameter, h, on the temperature field was also investigated and the results are presented in Figures 70 through 74. The development of temperature profiles along the vertical centerplane (z = 0) as h is varied ($4.85 \lesssim h \lesssim 1.07$) was examined at two axial stations (x = 10, x = 25) and is shown in Figures 70 and 71, respectively. The profiles at x = 10 station are seen to be independent of h in regions away from the offset surface. Also, the tendency of offset jets to approach the behavior of wall jets as h decreases is evident in both figures.

The growths of temperature halfwidths in both directions ($Y_{T_{1/2}}$ and $2Z^*_{T_{1/2}}/\ell^*$) for various values of h are presented in Figures 72 and 73. Their behavior is qualitatively similar to that of velocity halfwidths which have been discussed earlier.

The offset jets maximum temperature decays along the vertical centerplane are compared with those of wall and free jets in Figure 74. The offset jet decays were found to be approximately similar to that of free jet in upstream regions ($x \lesssim 15$). On the other hand, they were found to approach the wall jet decay further downstream. For the case of e = 0.44 the wall and free jet decay can be approximated by the following equations:

Wall jet: $\Theta_{cmax} = 5.66\, x^{-0.783}$ (for $x \gtrsim 8$)

Free jet: $\Theta_{cmax} = 4.18\, x^{-0.831}$ (for $x \gtrsim 5$)

The effects of the discharge geometry on the temperature field were fully investigated for a typical case with h = 1.46 and the results are reported in

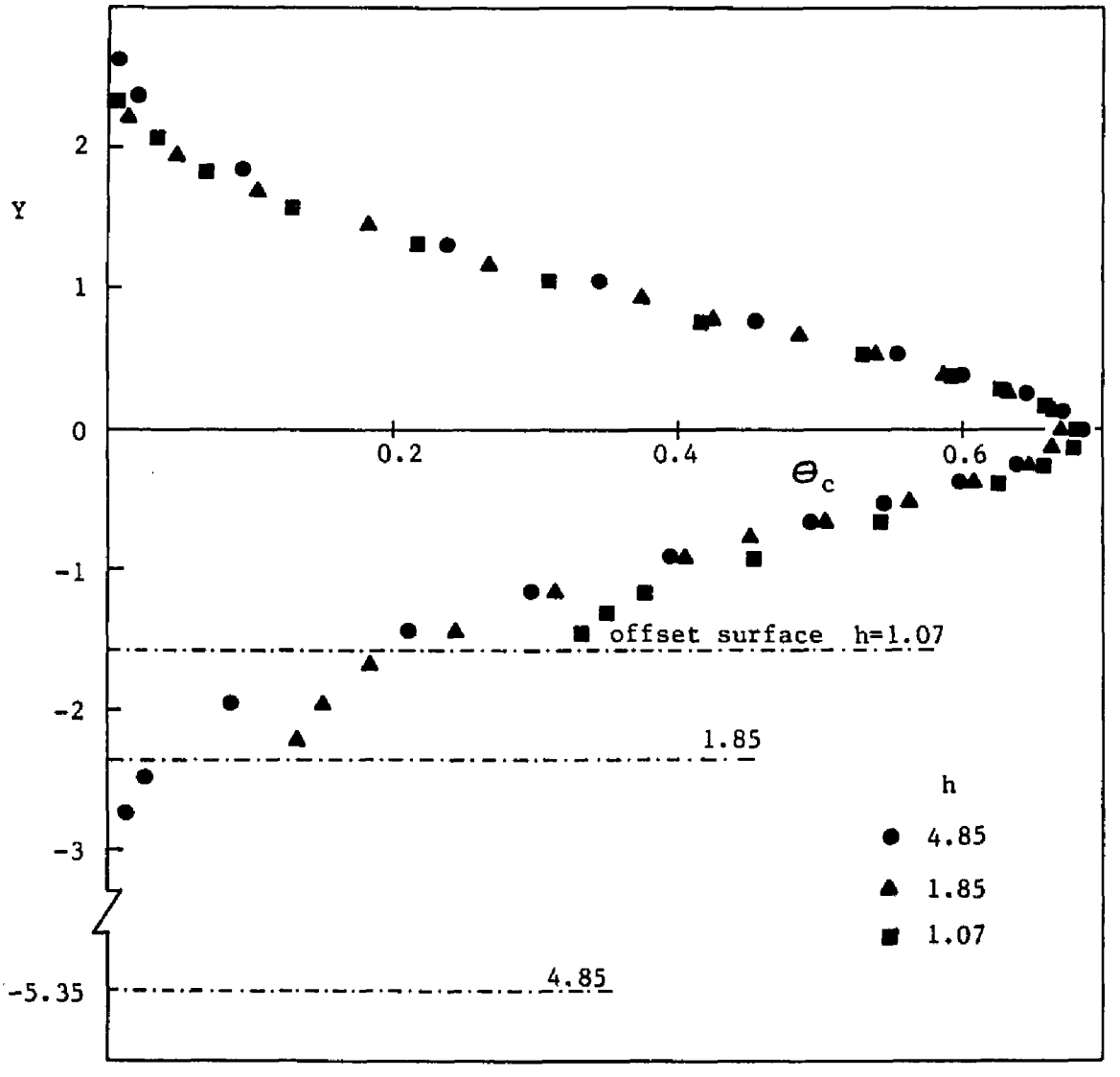

Figure 70. Vertical profiles of temperature (e=0.44 , x=10 , z=0)(Table F8)

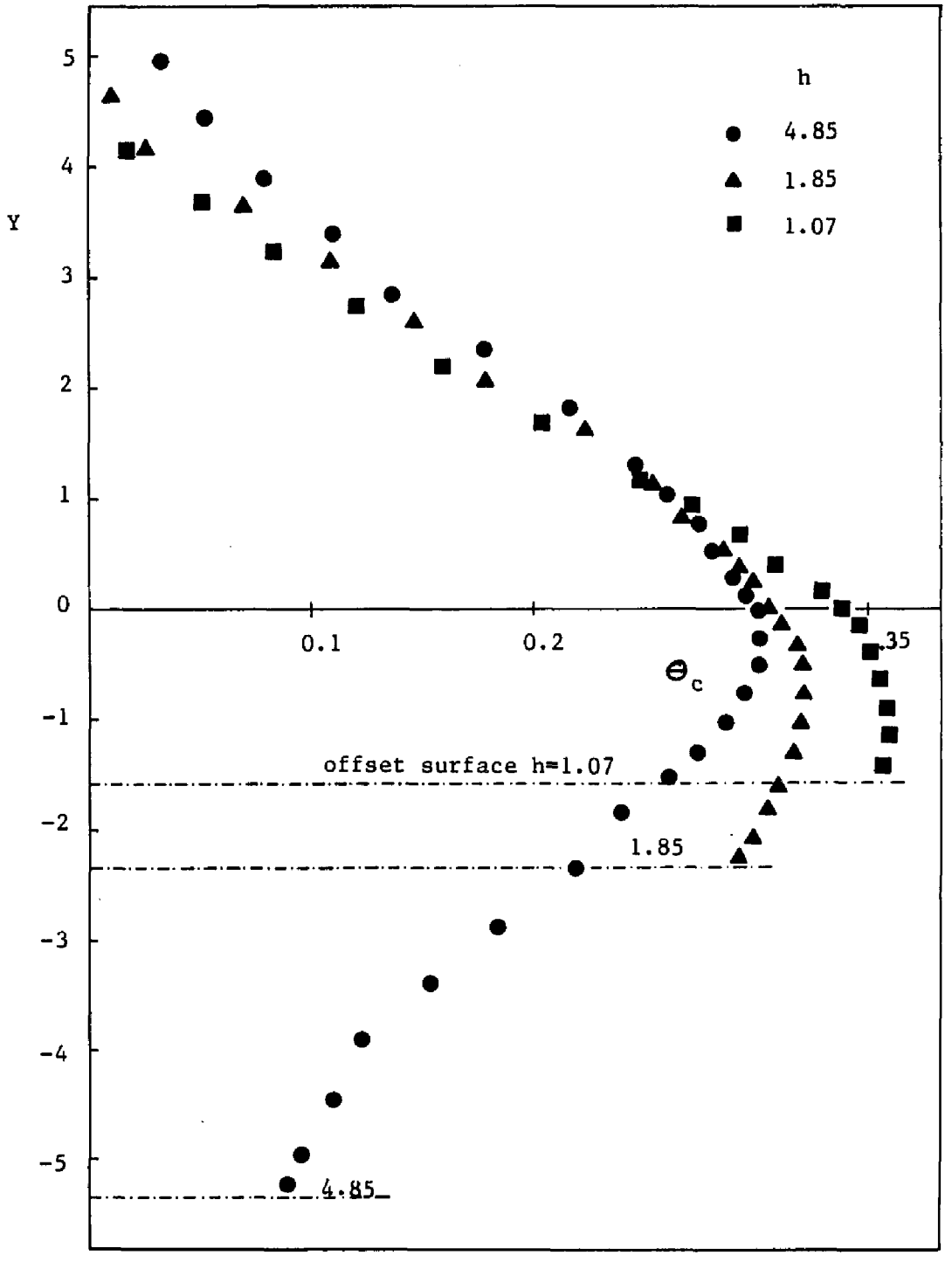

Figure 71. Vertical profiles of temperature (e=0.44 , x=25 , z=0)
(Table F9)

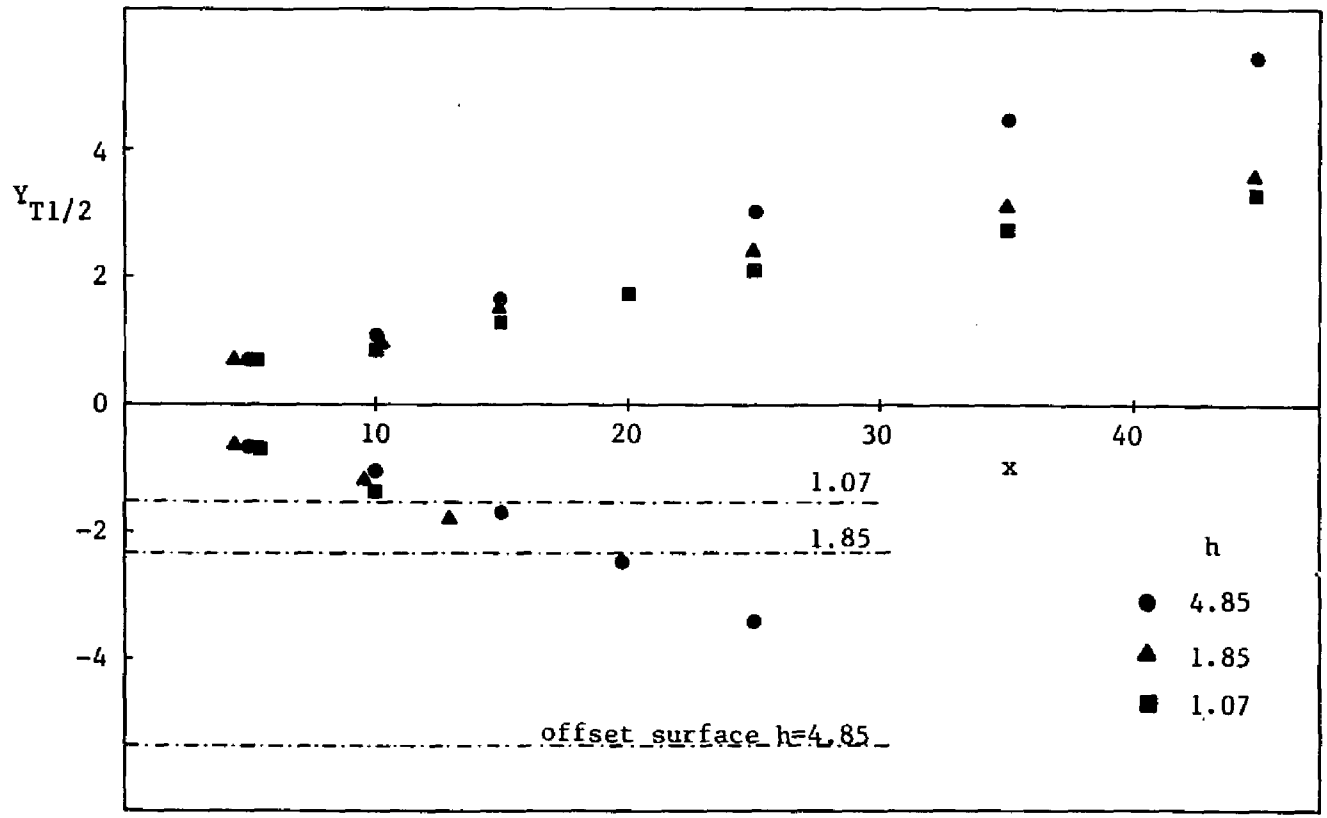

Figure 72. Vertical halfwidths of temperature (e=0.44 , z=0) (Table F10)

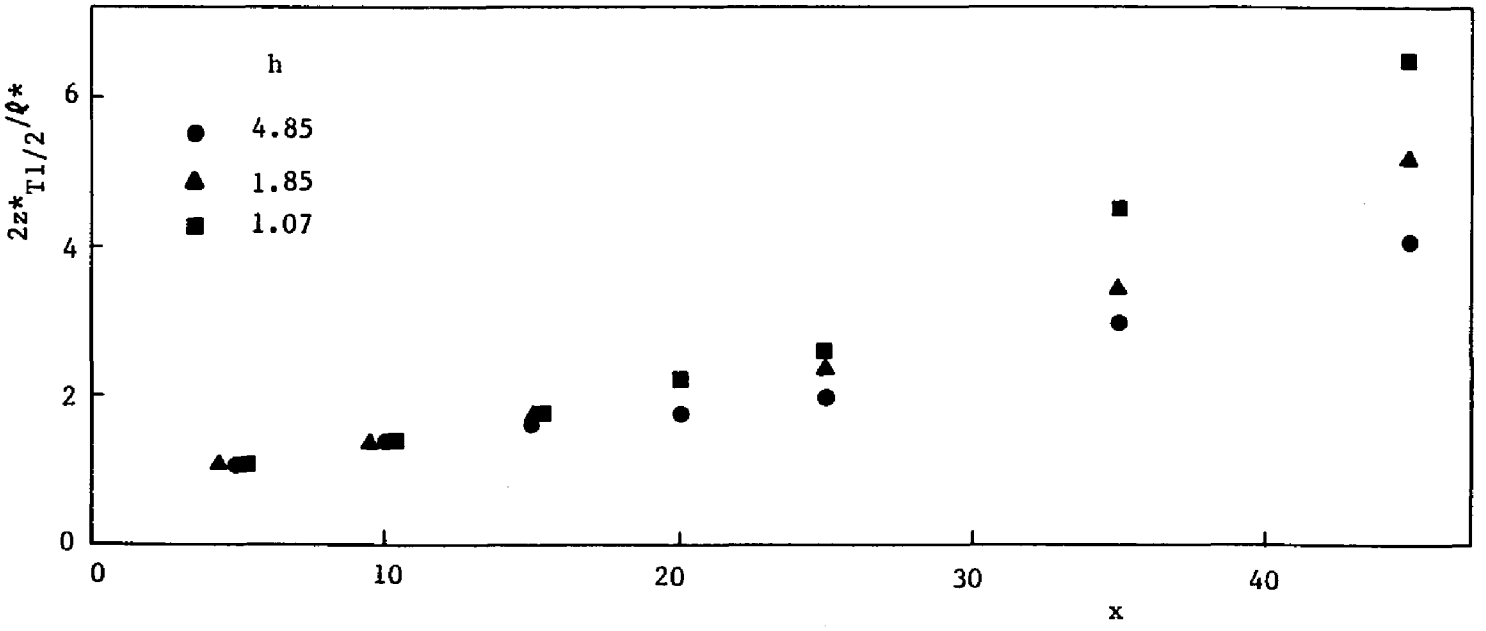

Figure 73. Spanwise halfwidths of temperature (e=0.44 , y=h+1/2) (Table F11)

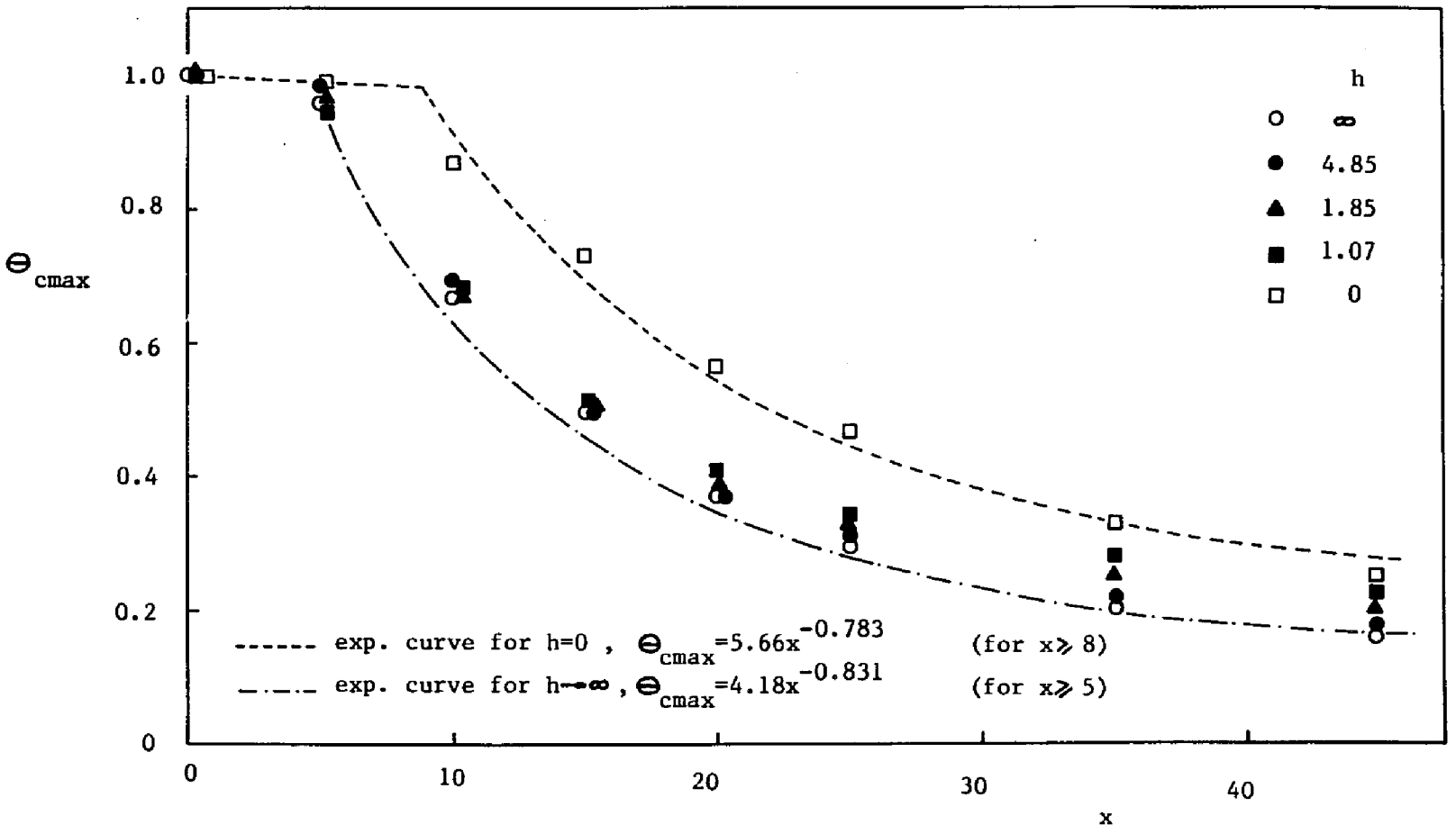

Figure 74. Maximum temperature decay (e=0.44 , z=0) (Table F12)

Figures 75 through 83. Temperature profiles along the y- and z-directions of jets discharging from various aspect ratio channels (i.e., e = 0.44, e = 0.25, e = 0.1) were examined at x = 9 and are shown in Figures 75 and 76, respectively. The vertical profiles, examined at z = 0, tend to approach the behavior of two-dimensional jets as e is decreased. The spanwise profiles, examined at y = 1.96, show an increase in their spread as e is increased. An alternate presentation of profiles, where temperature is nondimensionalized with division by the difference, $T^*_{max} - T^*_{\infty}$, is demonstrated in Figures 77 and 78. Similarity is evident only in the case of vertical profiles corresponding to e = 0.44 and e = 0.25. As e is decreased to 0.1 considerable departure from the similarity form is noted.

The growth of the temperature halfwidths in the y-direction ($Y_{T_{1/2}}$), shown in Figure 79, indicates an identical behavior for the e = 0.44 and e = 0.25 jets, which however is different from that of the e = 0.1 jet. The same result is observed in Figure 80 where the halfwidths are presented in normalized form. The temperature halfwidths in the z-direction ($2Z^*_{T_{1/2}}/\ell^*$), reported in Figure 81, show a dramatic increase of the spanwise thermal spread as e is increased.

The local thermal effectiveness of offset jets discharging from various outlets was measured by the decay of the maximum temperature along the vertical centerplane and is presented in Figure 82. It is generally observed that the decays corresponding to larger aspect ratios are accompanied by lower values of maximum temperature (Θ_{cmax}). Nondimensionalization of x* with division by $\sqrt{A^*}$, Figure 83, results in a convergence of all decays into a single curve, which can be approximated by the equation,

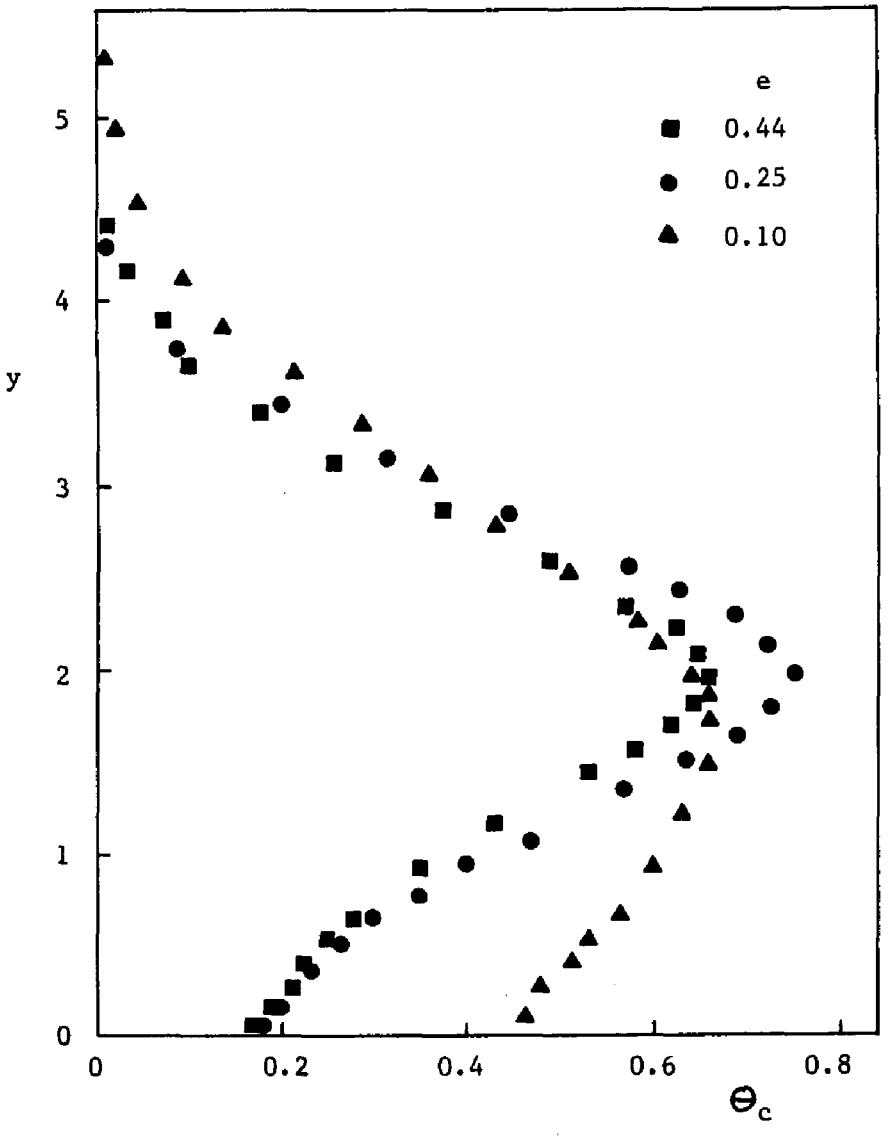

Figure 75. Vertical profiles of temperature (h=1.46 , x=9 , z=0) (Table F14)

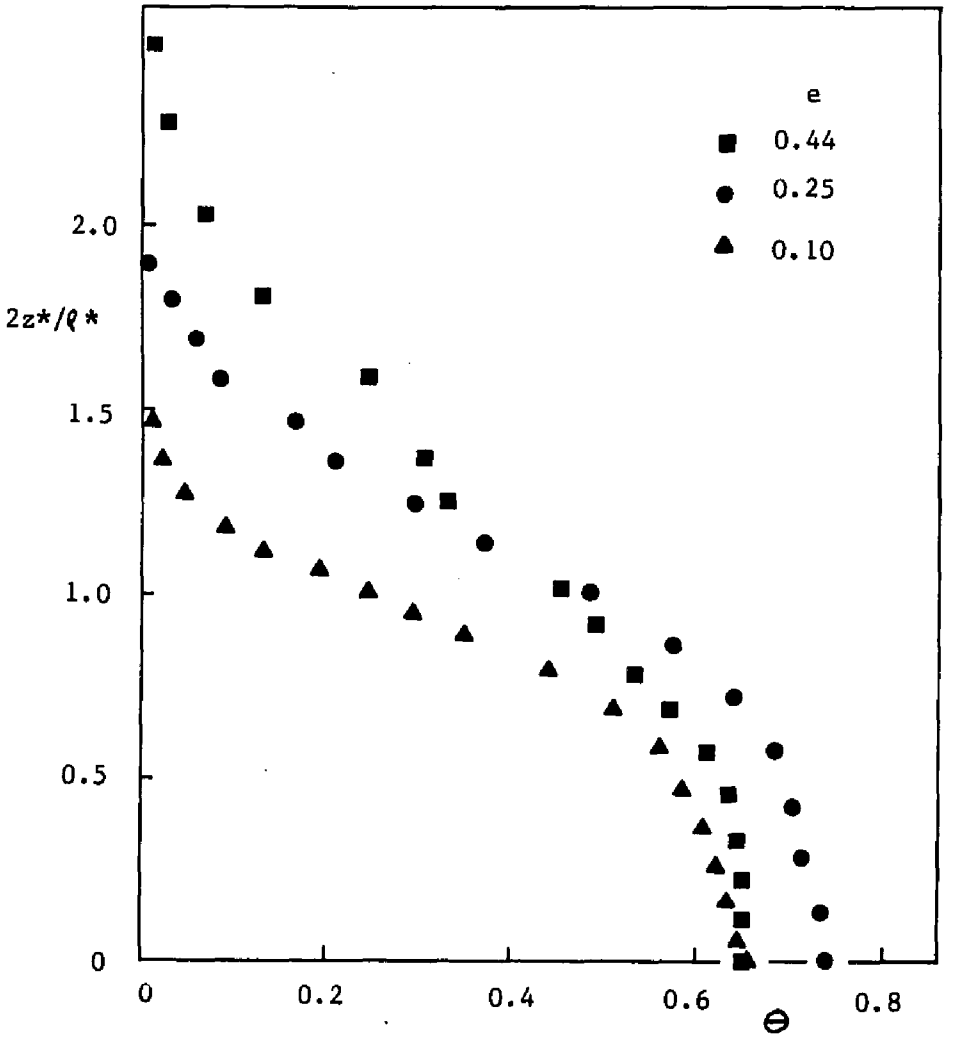

Figure 76. Spanwise profiles of temperature (h=1.46 , x=9 , y=1.96) (Table F15)

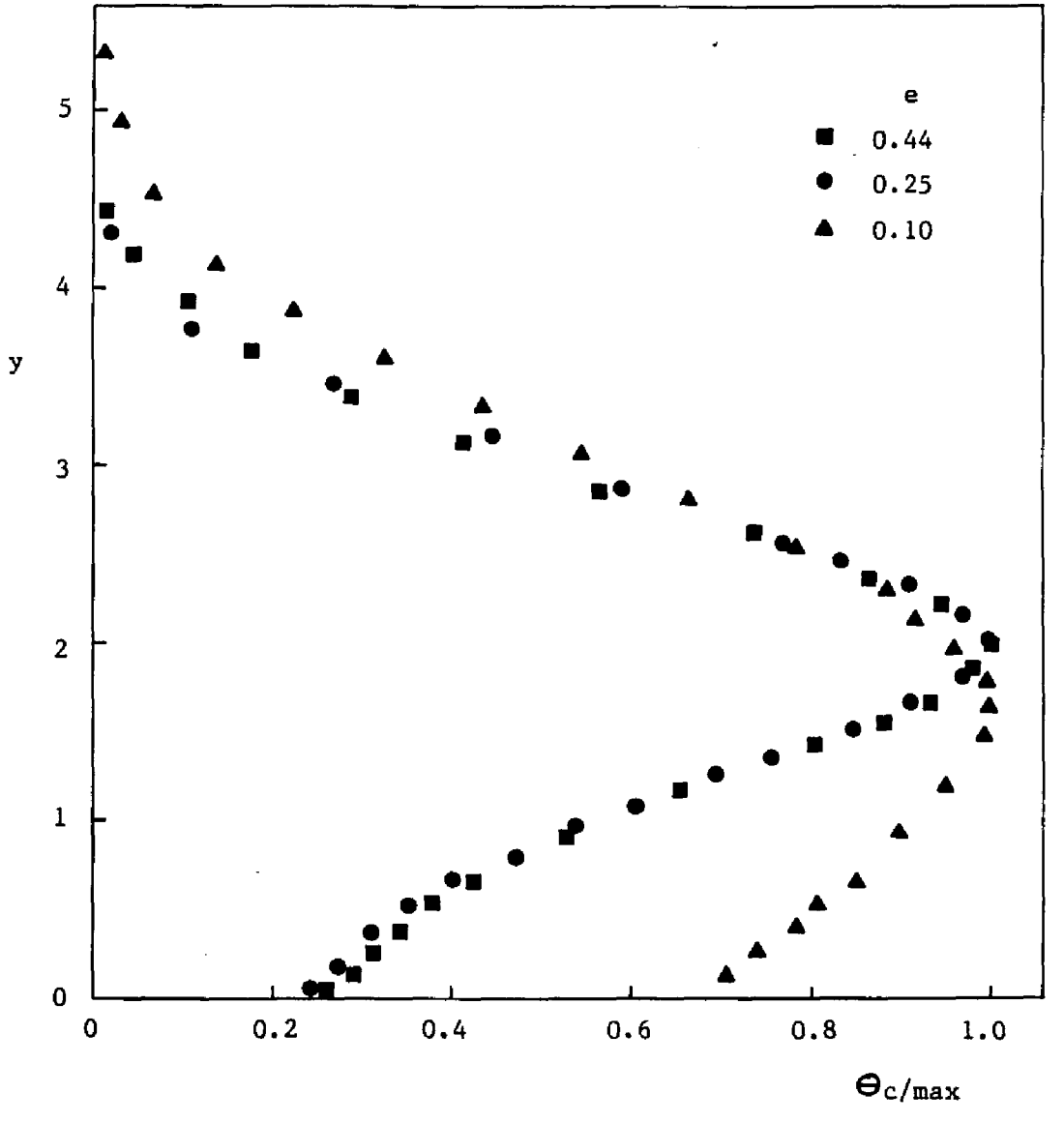

Figure 77. Vertical profiles of temperature (h=1.46 , x=9 , z=0)
(Table F14)

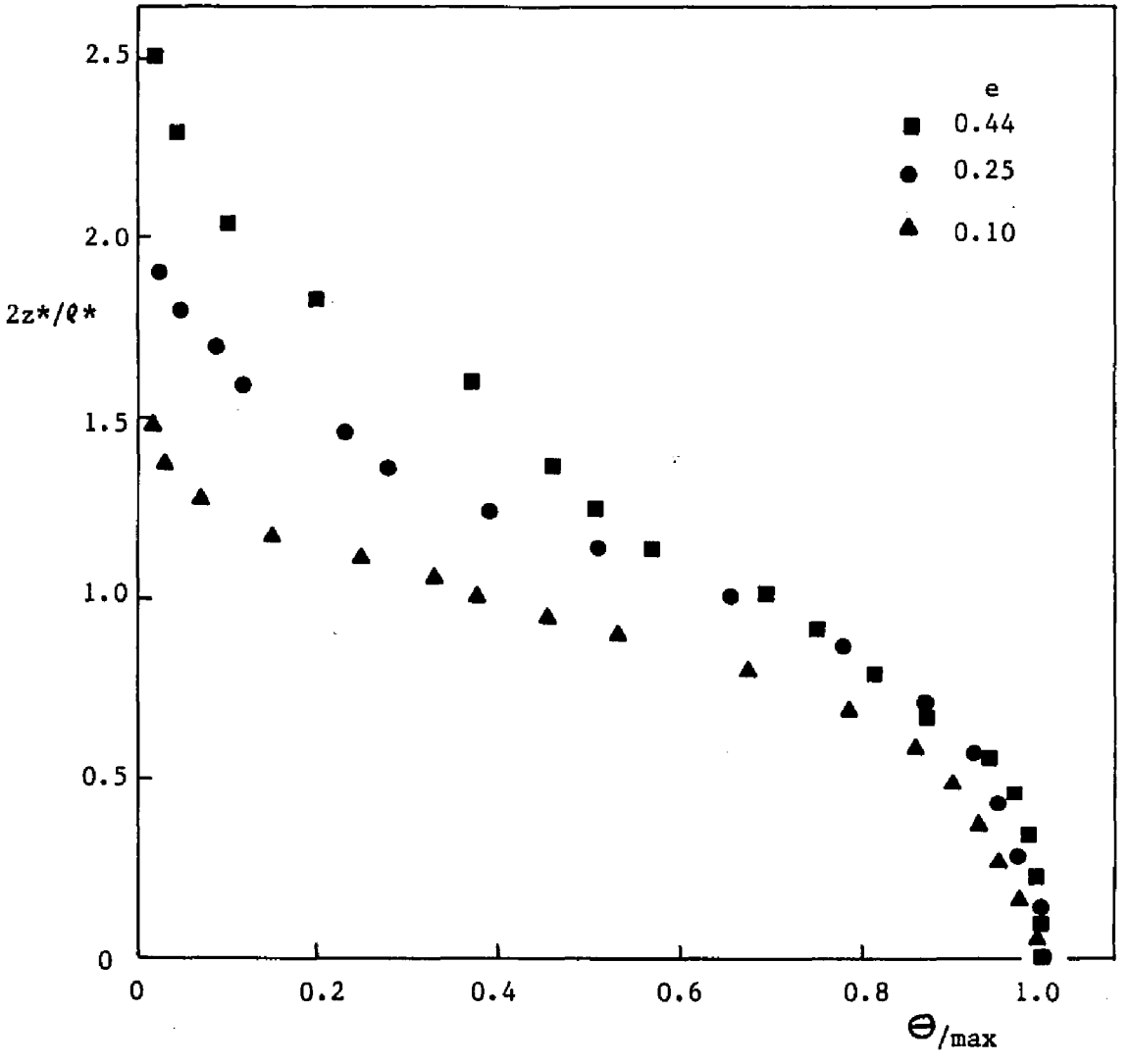

Figure 78. Spanwise profiles of temperature (h=1.46 , x=9 , y=1.96) (Table F15)

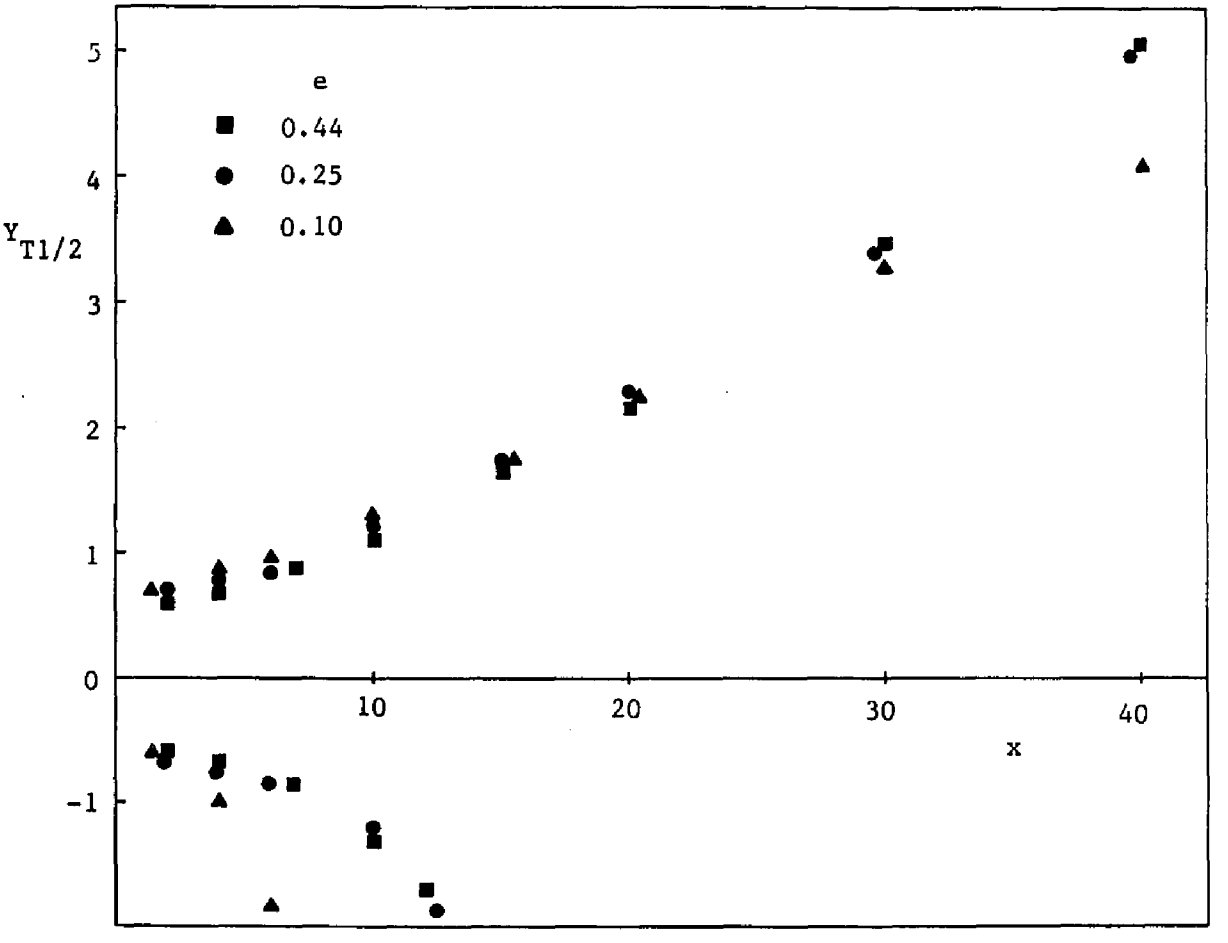

Figure 79. Vertical halfwidths of temperature (h=1.46 , z=0) (Table F16)

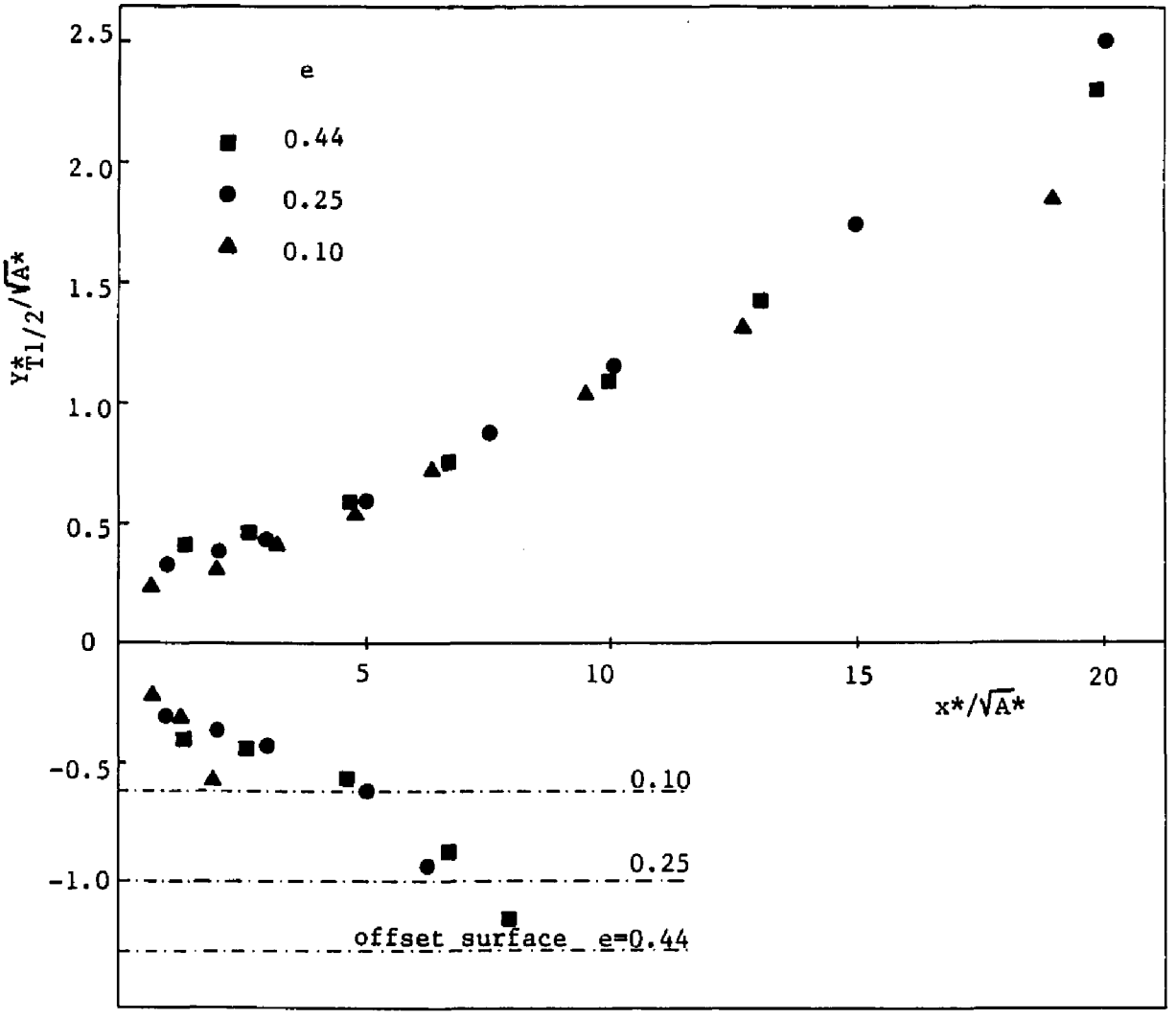

Figure 80. Normalized vertical halfwidths of temperature (h=1.46 , z=0) (Table F16)

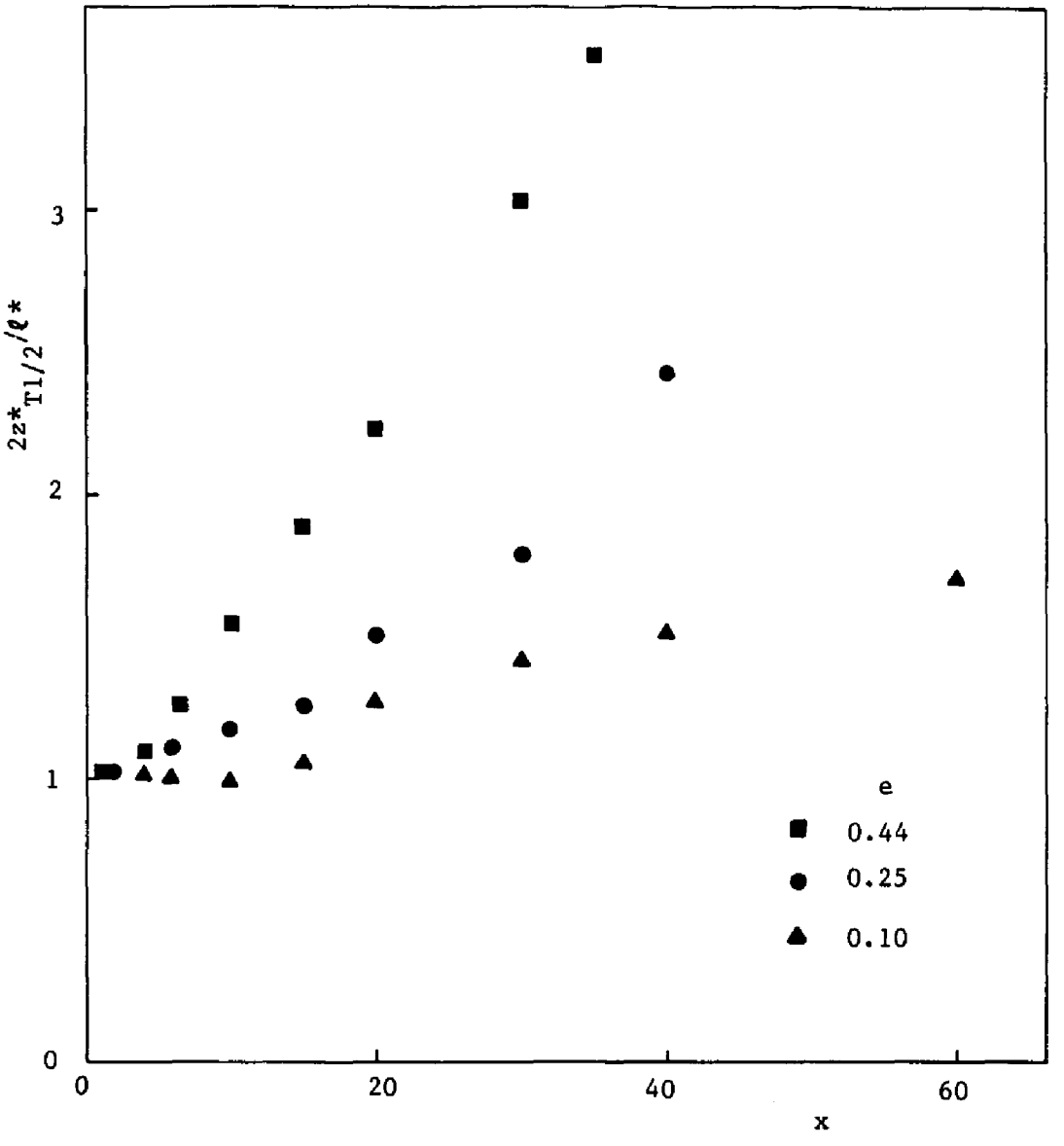

Figure 81. Spanwise halfwidths of temperature (h=1.46 , y=1.96) (Table F16)

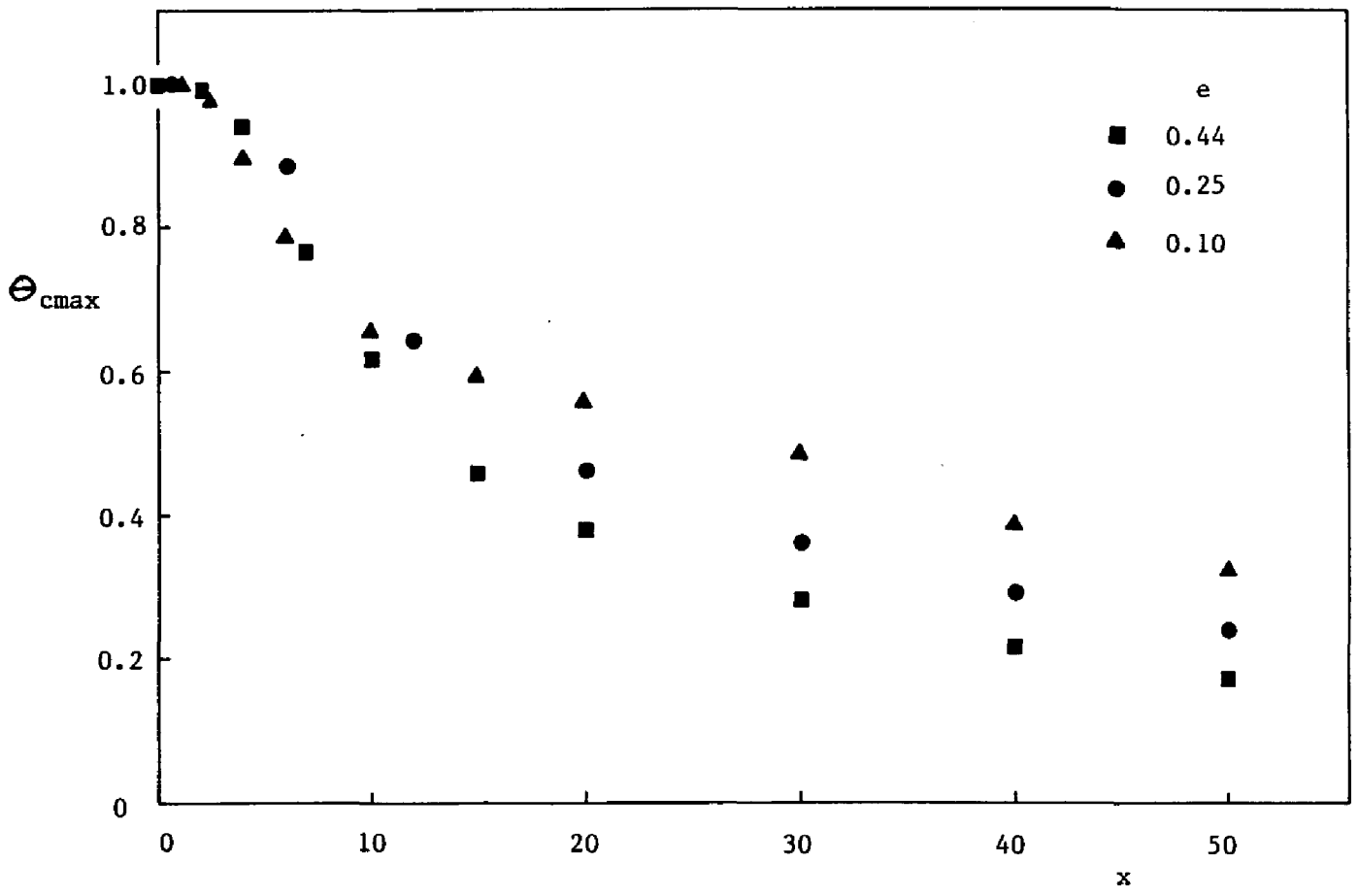

Figure 82. Maximum temperature decay (h=1.46 , z=0) (Table F17)

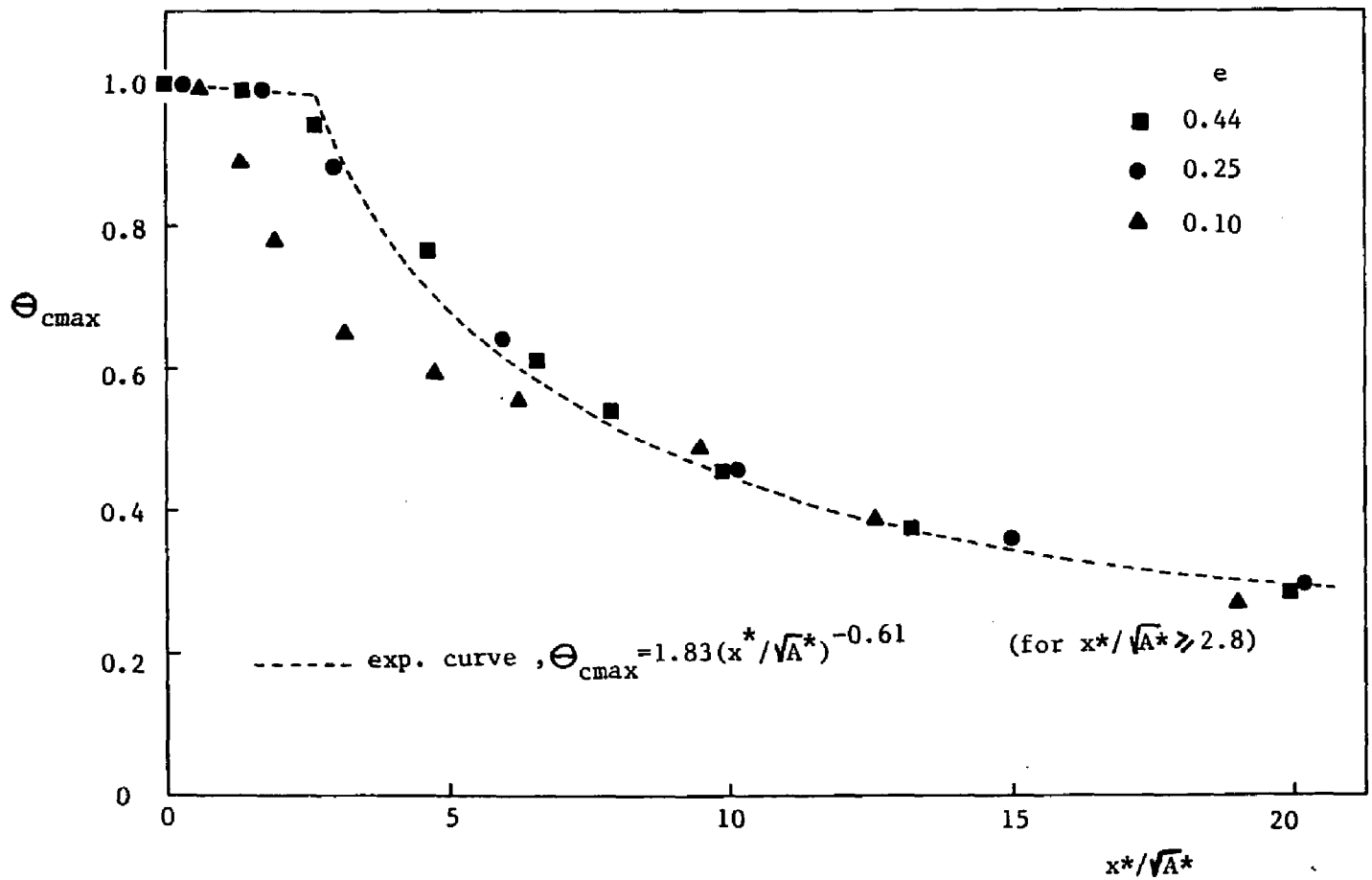

Figure 83. Normalized maximum temperature decay (h=1.46 , z=0) (Table F17)

$$\Theta_{cmax} = 1.83\,(x^*/\sqrt{A^*})^{-0.61} \qquad \text{(for } x^*/\sqrt{A^*} \geq 2.8\text{)}$$

However, exception to this normalization form are the data corresponding to e = 0.1 channel and $x^*/\sqrt{A^*} < 8$ region. This portion of the decay follows a different path than that mentioned above.

4. Comparison Between Velocity and Temperature Fields

Experimental data in dimensionless form on velocity and temperature fields for the same flow and geometric conditions are compared in this section to assess similarities and differences between them.

Comparison between the discharge velocity and temperature distributions, shown in Figure 84, indicates that the temperature profiles are flatter than those of the velocity field. The vertical and spanwise distributions of velocity and temperature at axial station x = 9 (e = 0.25, h = 1.46) are presented in Figures 85 and 86, respectively. Although the values of velocity are greater than those of temperature in the vicinity of the centerline, the opposite is observed as the jet edges are approached. In Figures 87 and 88, the previous vertical and spanwise profiles are plotted using the local halfwidth and the local maximum velocity or temperature difference. Here, the shapes exhibited in both figures are seen to converge onto a single similarity profile.

In addition, vertical and spanwise profiles of velocity and temperature for other conditions (e = 0.44, h = 4.85) were examined at two axial stations, x = 5 and x = 25, and are presented in Figures 89 and 90, respectively. The nearfield

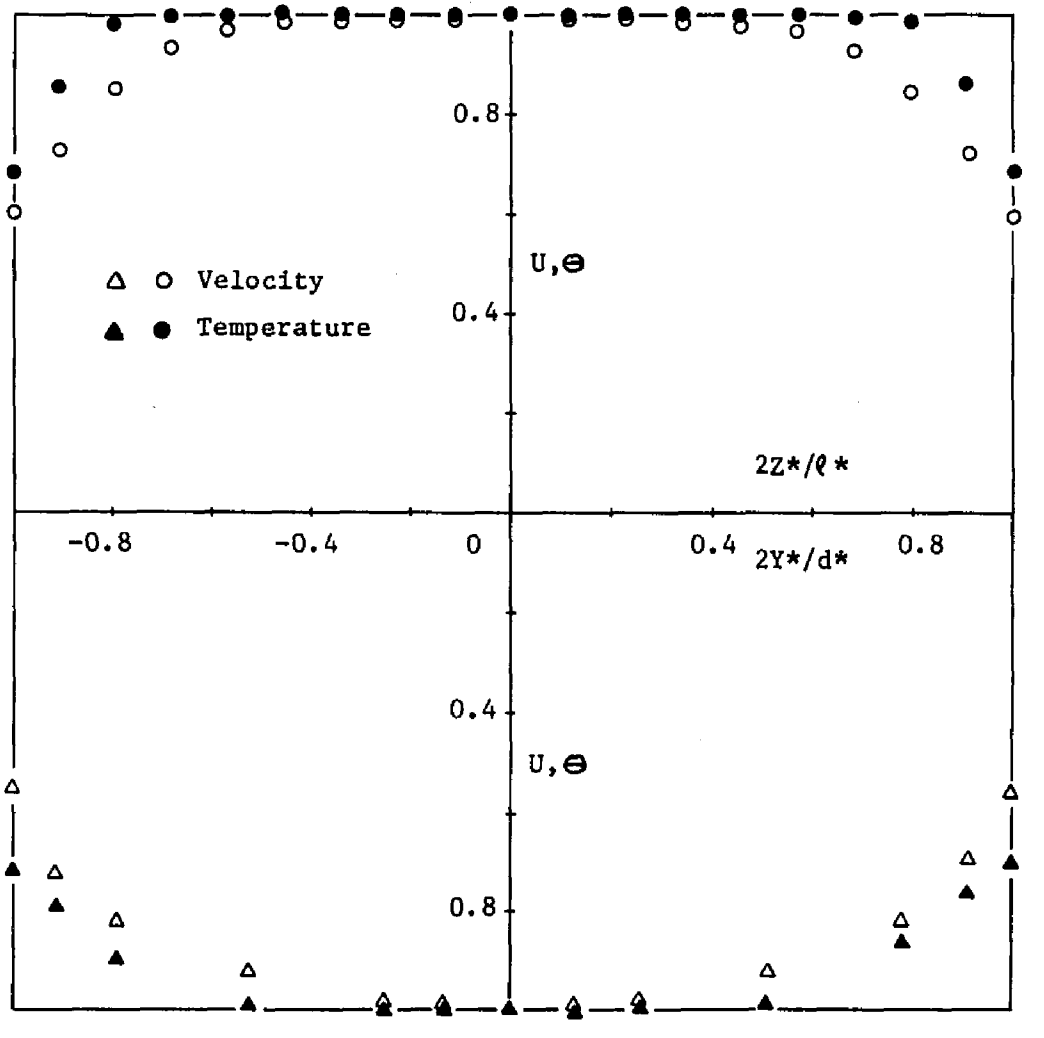

Figure 84. Discharge velocity and temperature profiles (e=0.44)

(Tables D1 , D2 , F1 and F2)

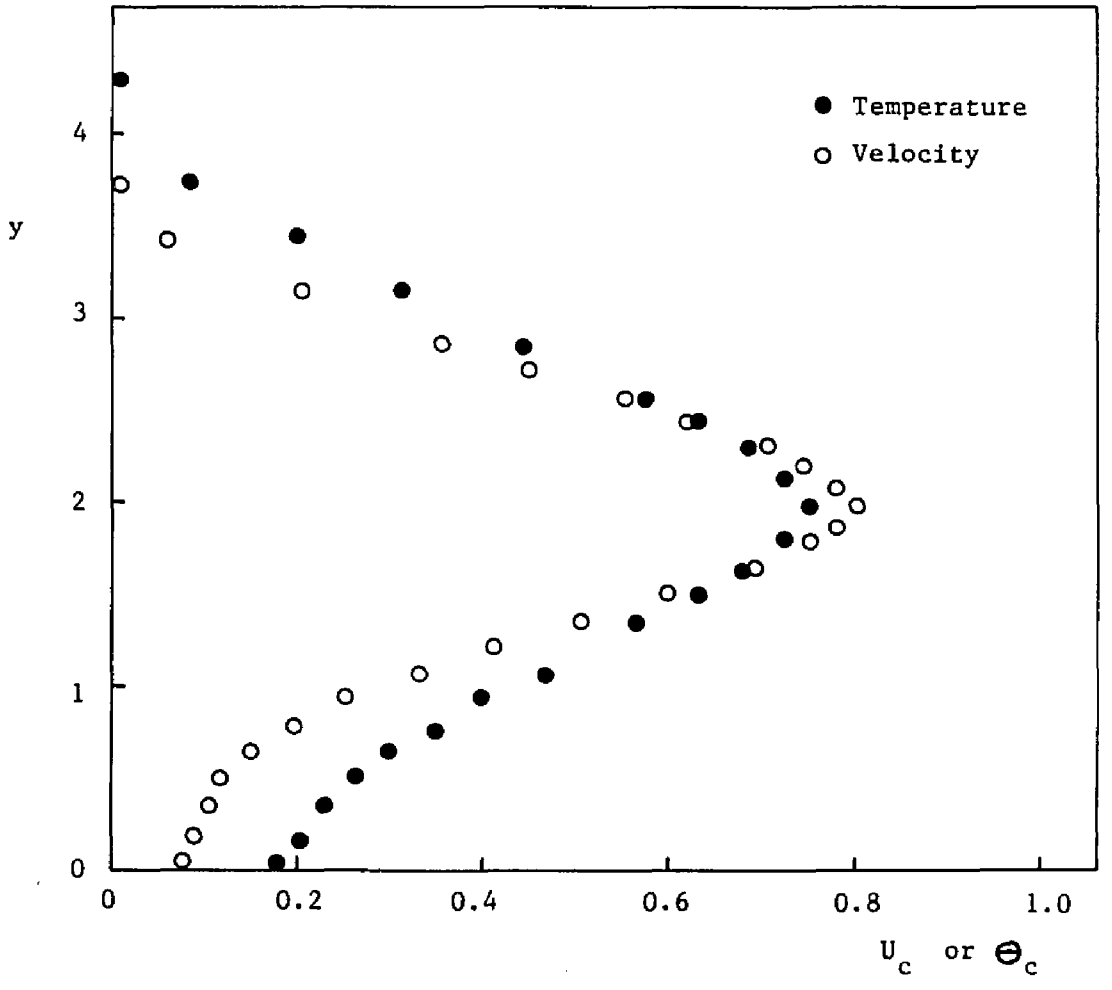

Figure 85. Vertical profiles of temperature and velocity (e=0.25 , h=1.46 , x=9 , z=0) (Table F5)

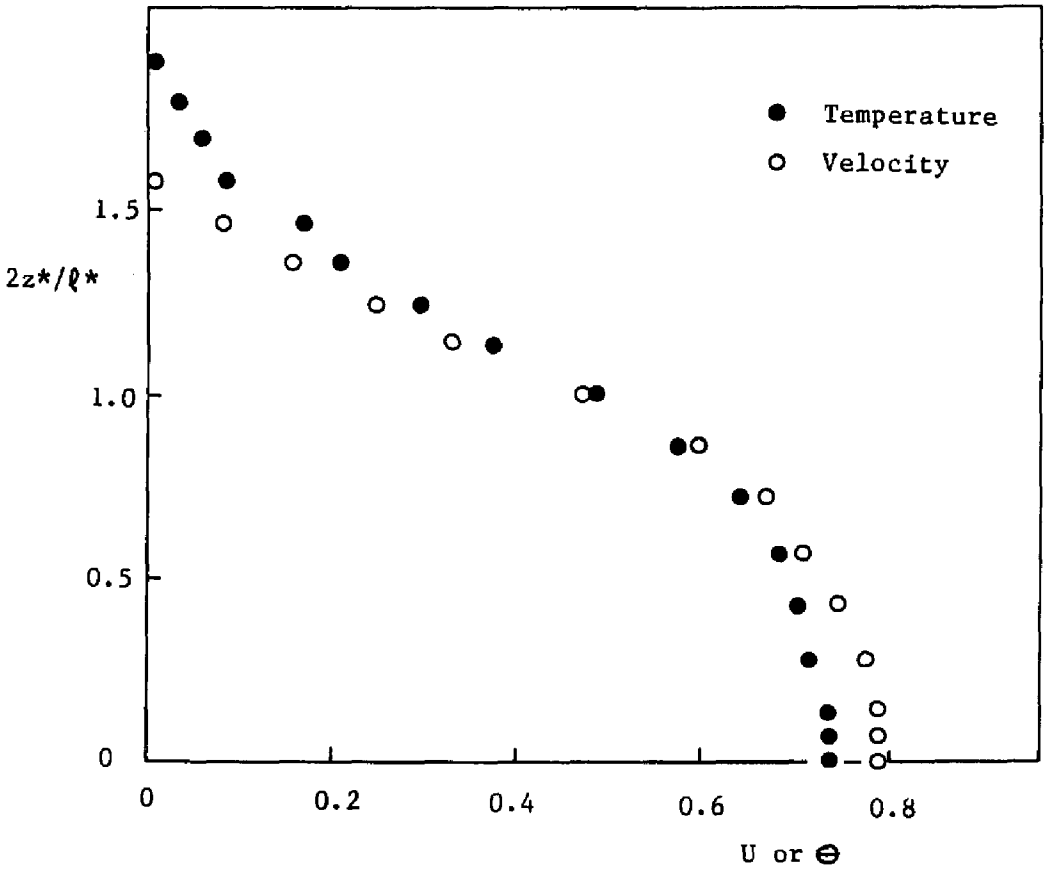

Figure 86. Spanwise profiles of temperature (e=0.25 , h=1.46 , x=9 , y=1.96) (Table F7)

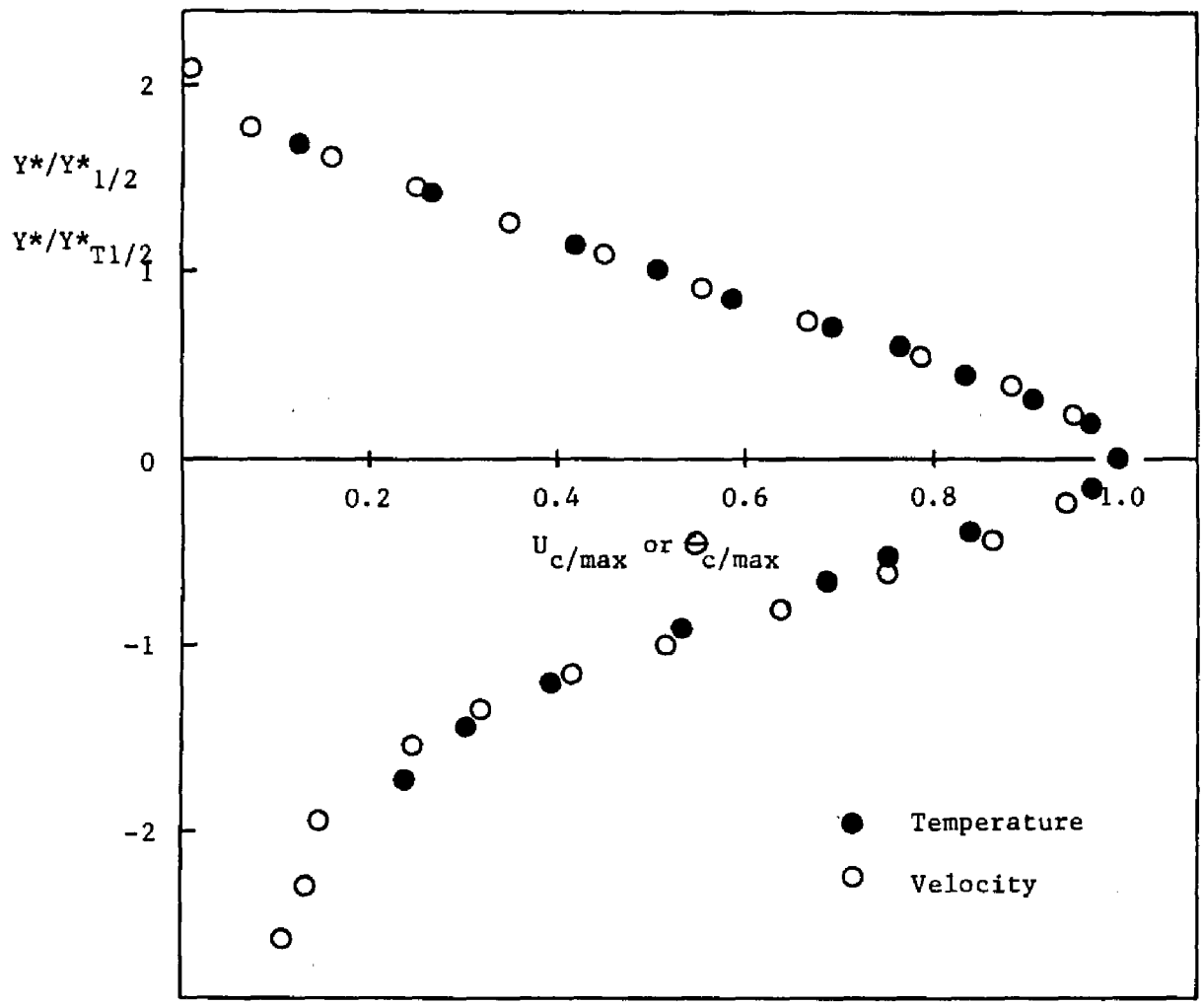

Figure 87. Vertical profiles of temperature and velocity in similarity form (e=0.25 , h=1.46 , x=9 , z=0) (Table F5)

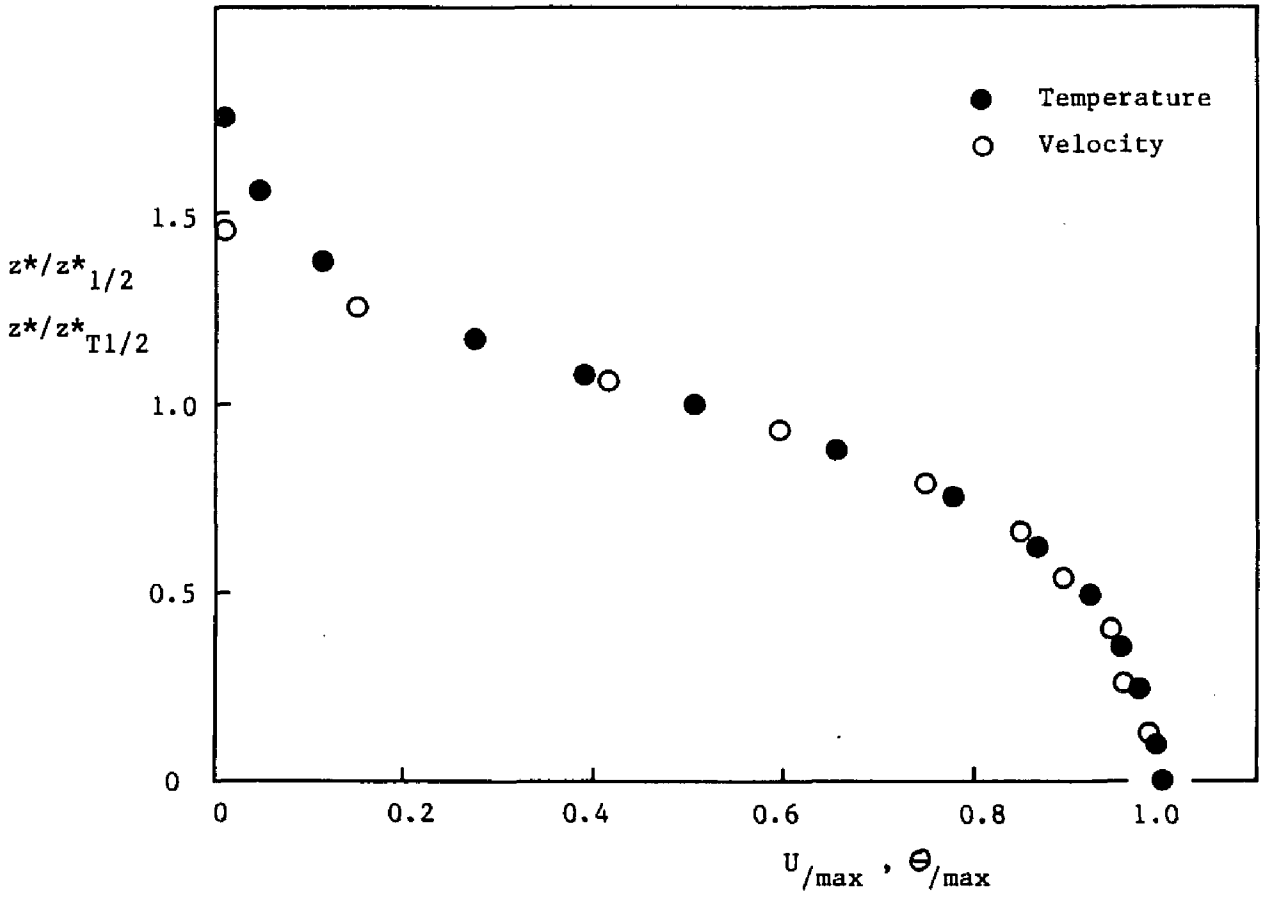

Figure 88. Spanwise profiles of temperature and velocity in similarity form (e=0.25 , h=1.46 , x=9 , y=1.96) (Table F7)

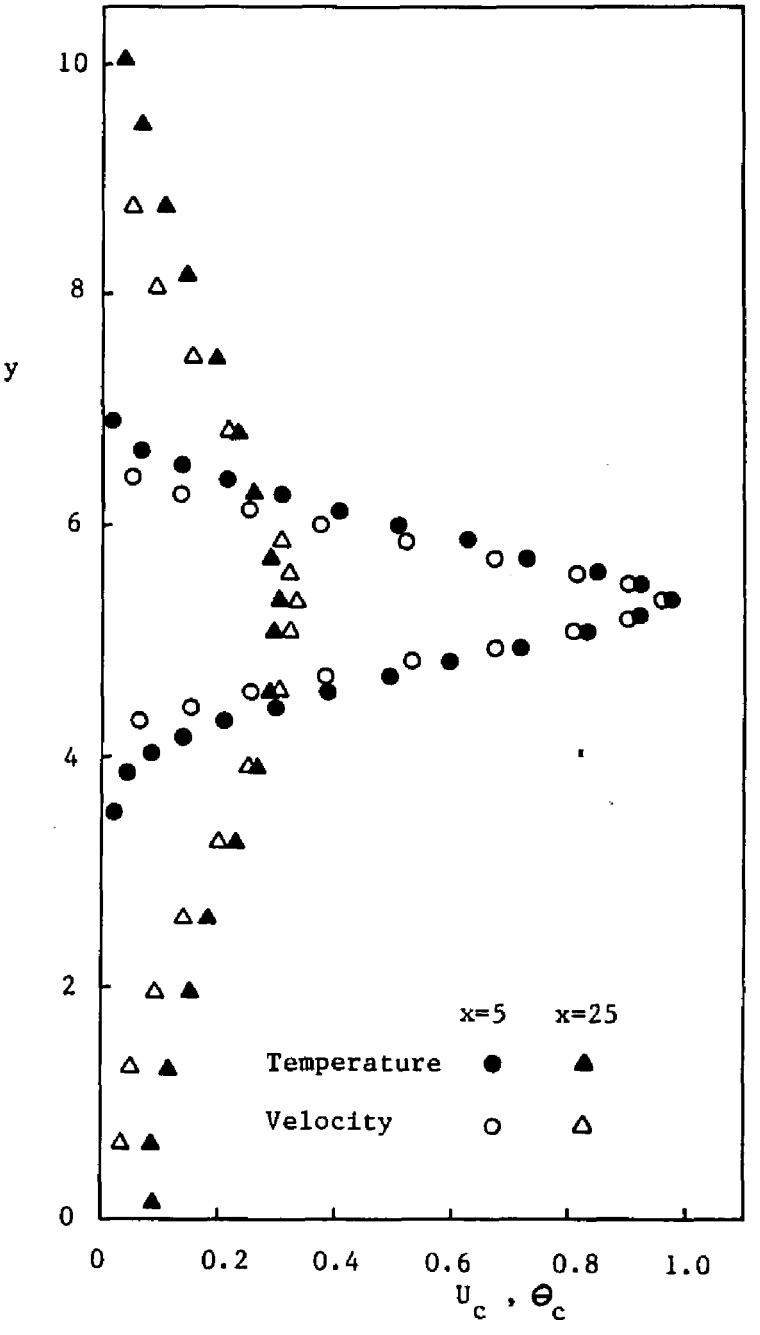

Figure 89. Vertical profiles of temperature and velocity
(e=0.44 , h=4.85 , z=0) (Table F3)

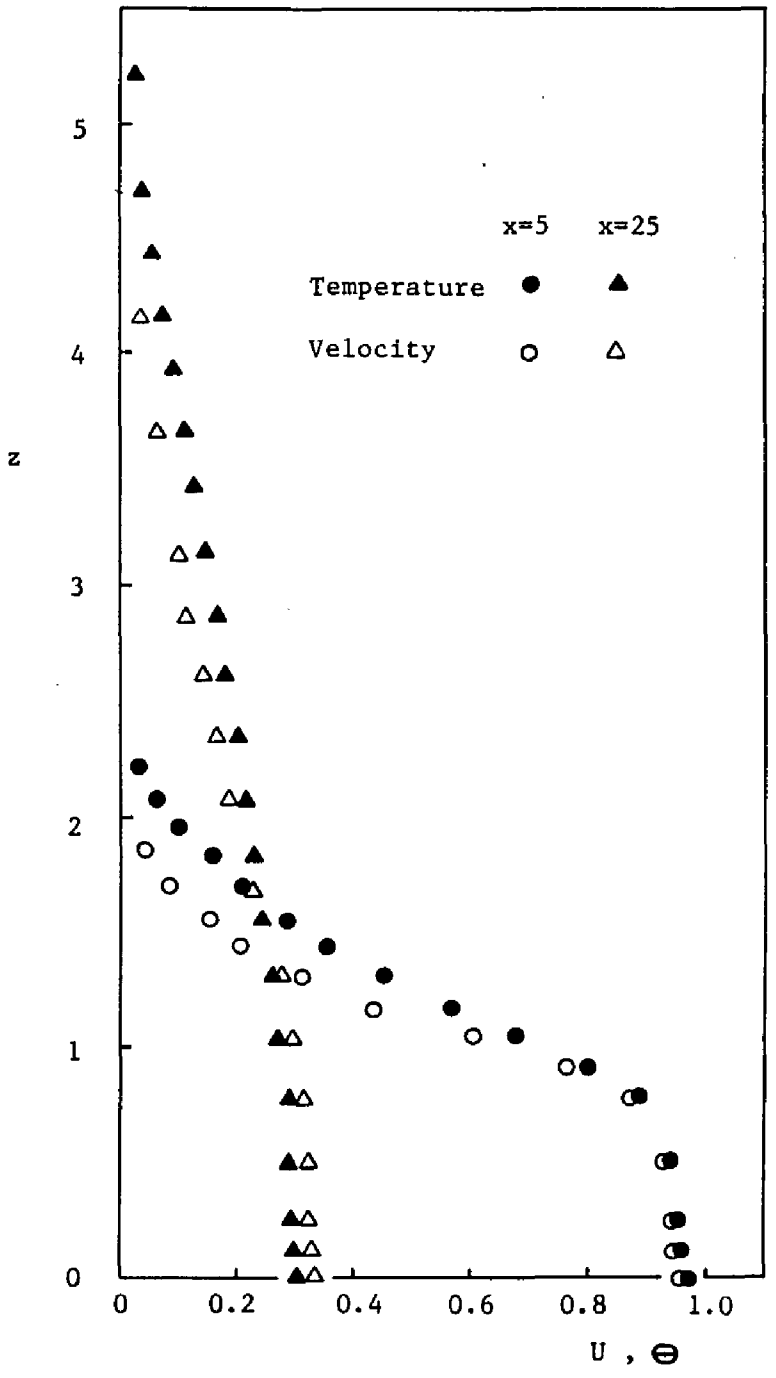

Figure 90. Spanwise profiles of temperature and velocity
(e=0.44 , h=4.85 , y=5.35) (Table F4)

profiles (x = 5) are characteristic of the discharge temperature and velocity distributions and the extent of the cores. This is verified by the different quantitative relation of velocity and temperature profiles in the two examined axial stations.

Comparison between the maximum velocity and temperature decays was made at two different cases (e = 0.44, h = 4.85 and e = 0.25, h = 1.46) and is shown in Figures 91 and 92, respectively. The decays in both cases are seen to be nearly the same with the velocity being slightly above the temperature decays. Consequently, it is stated that the experimental evidence suggests that the turbulent Prandtl number Pr_T is, in fact, near unity.

5. Visualization

Two methods are commonly employed in the experimental investigation of flow behavior: flow visualization and flow measurements. Flow visualization provides the overall picture of the entire flow field, while its information is only qualitative. On the other hand, flow measurements yield quantitative information, but the information is localized to the vicinity of the measuring probe. The two methods utilized simultaneously may serve as the basis for the theoretical modeling.

Two techniques of flow visualization have been used in the present investigation: (i) the oil/lampblack and (ii) the smoke injection (for details, see chapter III). The patterns of air flow adjacent to the offset surface for a typical case with e = 0.44 and h = 1.85 are presented in Figure 93. The location of

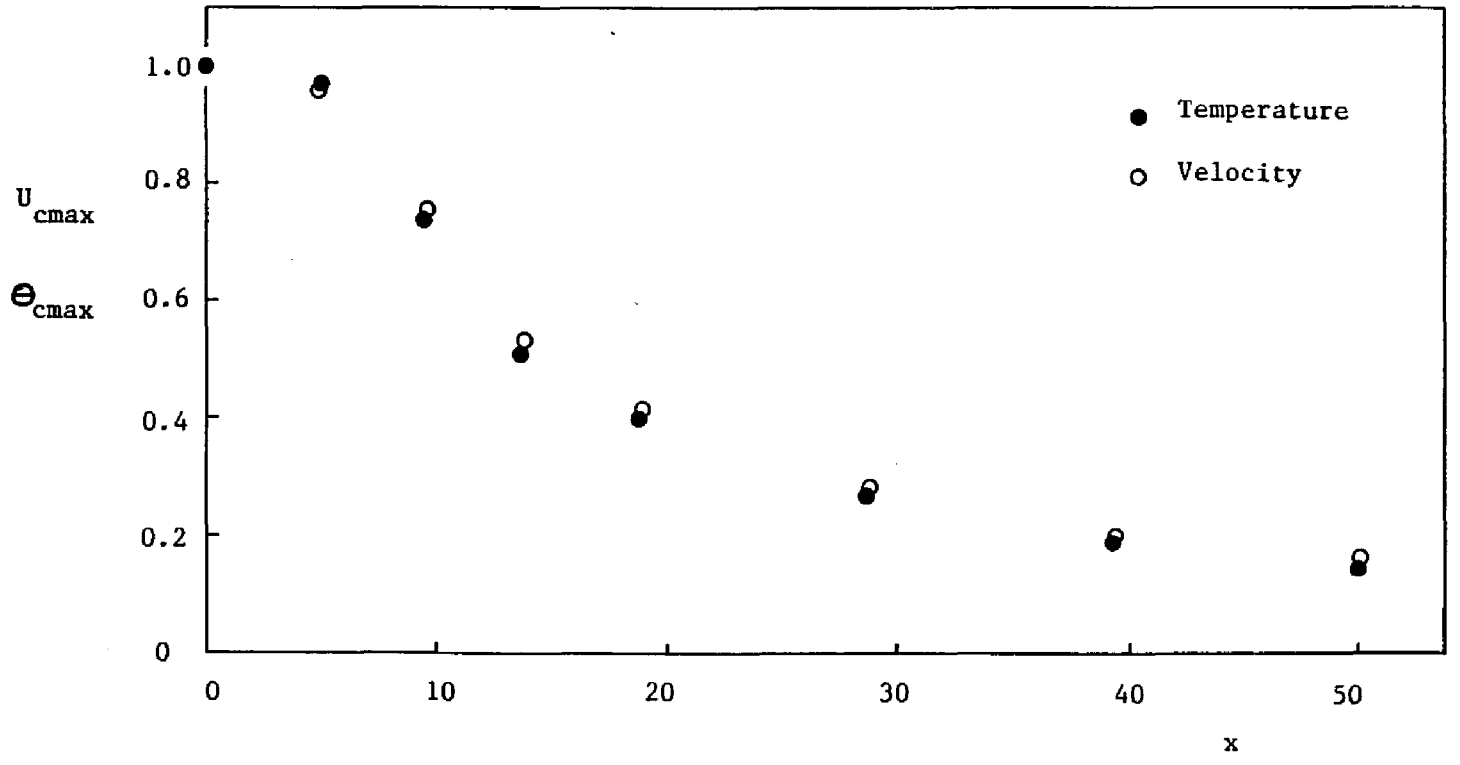

Figure 91. Maximum velocity and temperature decays (e=0.44 , h=4.85 , z=0) (Table F13)

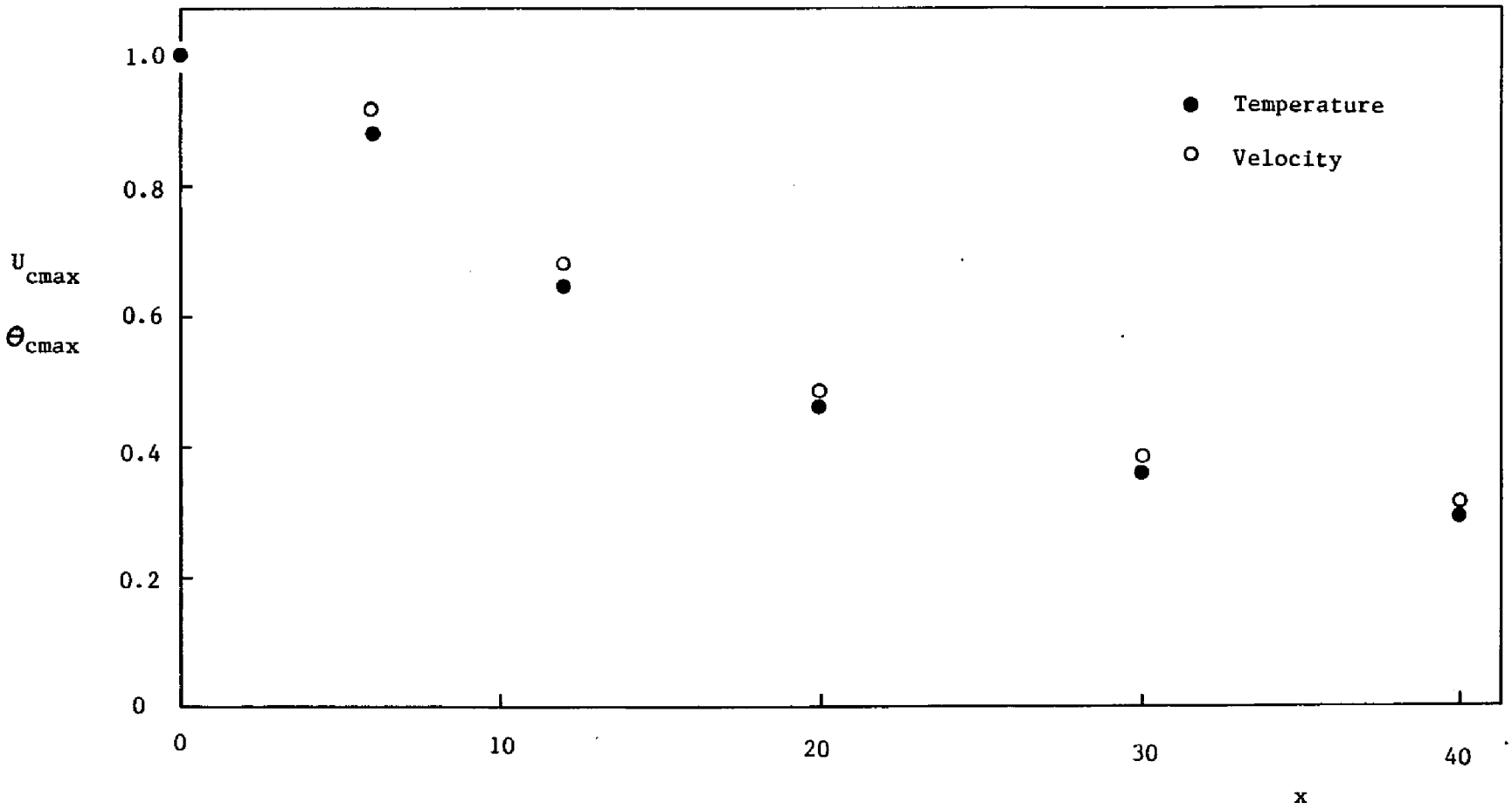

Figure 92. Maximum velocity and temperature decays (e=0.25 , h=1.46 , z=0) (Table F13)

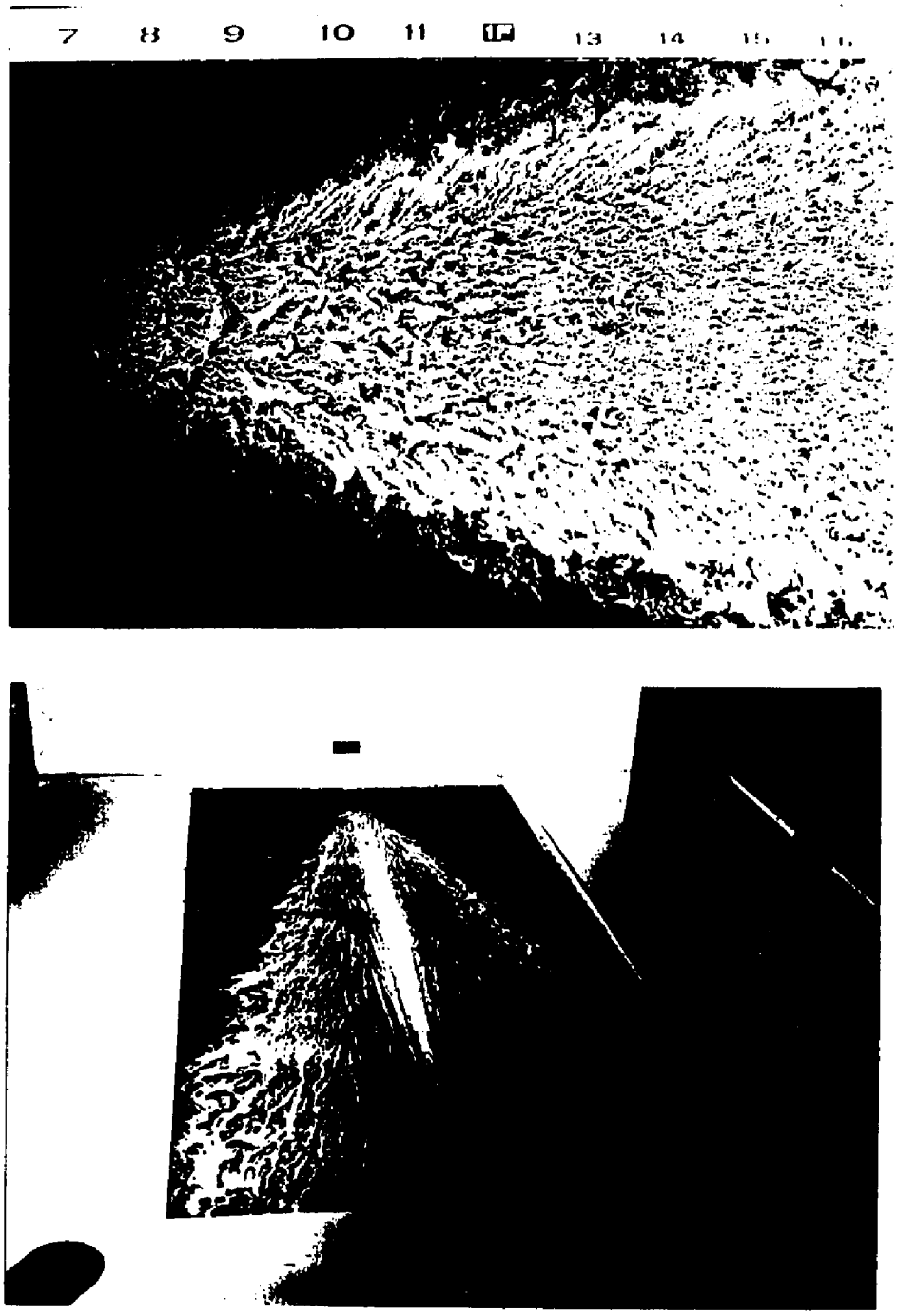

Figure 93. The patterns of air flow adjacent to the offset surface (e=0.44 , h=1.85)

reattachment, which is shown in this figure, was found to be in good agreement with that predicted earlier in this chapter by use of surface pressure measurements (Figure 19).

The overall picture of the three-dimensional offset jet flowfield (e = 0.25 and h = 1) was made visible throught the use of smoke injection and is presented in Figure 94. The recirculation pattern, which was found to characterize two-dimensional offset jet flows, does not appear in the three-dimensional flows, as it can be confirmed by this figure.

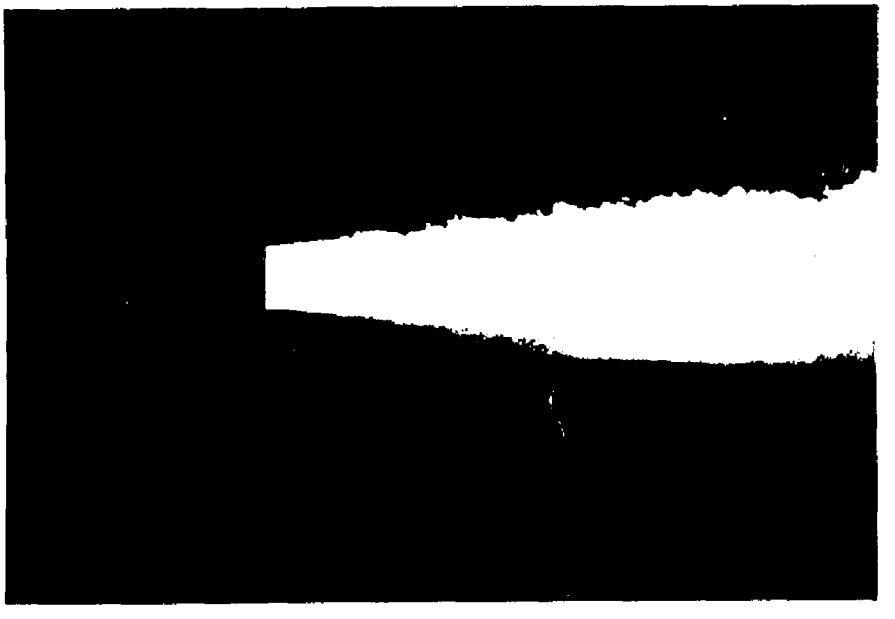

Figure 94. Overall picture of a three-dimensional offset jet flowfield (e=0.25 , h=1)

V. SUMMARY AND CONCLUSIONS

In general, surface pressure distribution for three-dimensional jets can differ significantly from two-dimensional jets. However, the centerline surface pressure distribution for three-dimensional jets approaches that of two-dimensional jets at $eh \ll 1$.

The negative/positive/negative feature of surface pressure coefficient was found to characterize three-dimensional offset jets. The negative surface pressure following reattachment is confined to lateral distances within the channel halfwidth, i.e. $z < 1/2e$. Negative pressure peaks just downstream of the discharge and the positive peaks after the reattachment points are enhanced as the aspect ratio and/or offset distance are decreased.

The reattachment to offset distance ratio, x_r/h, indicates a significantly different behavior between the two- and three-dimensional jets. In the two-dimensional case it decreases and asymptotically approaches the value of 2.4 as h is increased. However, for three-dimensional jets it increases and reaches asymptotically a value close to 6.

Jet bending towards the offset surface becomes more pronounced as h is decreased. Also, the influence of the offset surface on flow and thermal fields increases as h is decreased and is more pronounced in the central plane ($z = 0$) than elsewhere ($z > 0$).

Jet trajectory and the decay of maximum velocity were found to be approximately independent of Re_o. Furthermore, maximum velocity and temperature decays were shown to be very similar to those of the free jet in upstream regions. On the other hand, they were shown to approach the wall jet decays further downstream.

Flow visualization and the flow pattern obtained with the directional probe were found to be in agreement with the velocity data which were based on measurements taken with a Pitot-static pressure probe.

Through the use of various length scales the similarities and differences in jet behavior were noted. The use of halfwidth as the characteristic length scale was seen to produce a set of similar curves for a given aspect ratio, while the $\sqrt{A^*}$ length scale was shown to be capable to correlating the curves of various aspect ratios in a particular set.

APPENDIX A

Verification of Experimental Data

To establish confidence in the experimental setup and measuring techniques that have been used in the present study, some data are compared with those published by other investigators.

Experimental data from the present study and the experimental results of Rajaratnam and Pani[36] describing the maximum centerplane velocity decay of a wall jet are presented in Figure A1. Data from this study and the similarity curve of Sforza and Herbst[32] describing velocity profiles in the lateral direction of a wall jet (e = 0.1) are shown in Figure A2. In addition, present data as well as results of Kumada et al.,[12] Parameswaran et al.[10] and Bourque et al.[4] presenting the variation of x_r with h for two-dimensional offset jets are given in Figure A3. All sets of data collected in this study are found to be in reasonable agreement with those published by other investigators.

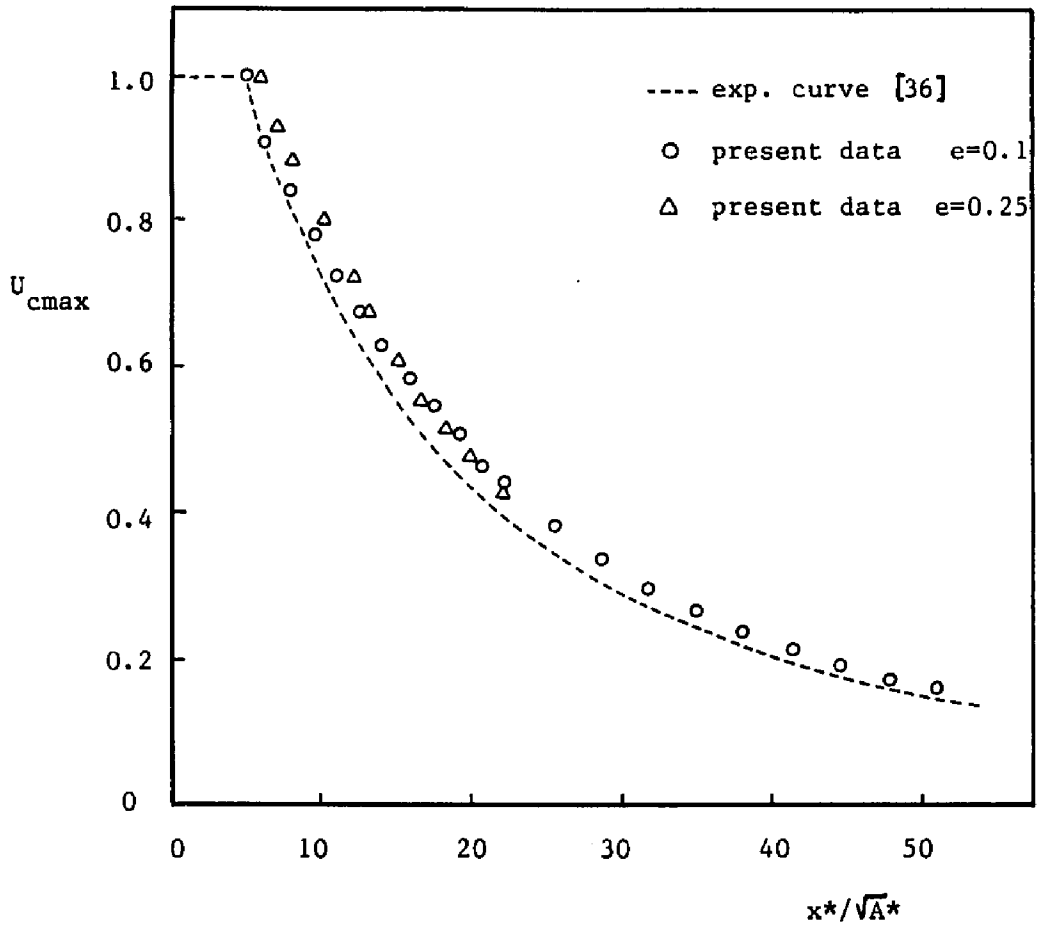

Figure A1. Maximum velocity decay for three-dimensional wall jets (Reference 38)

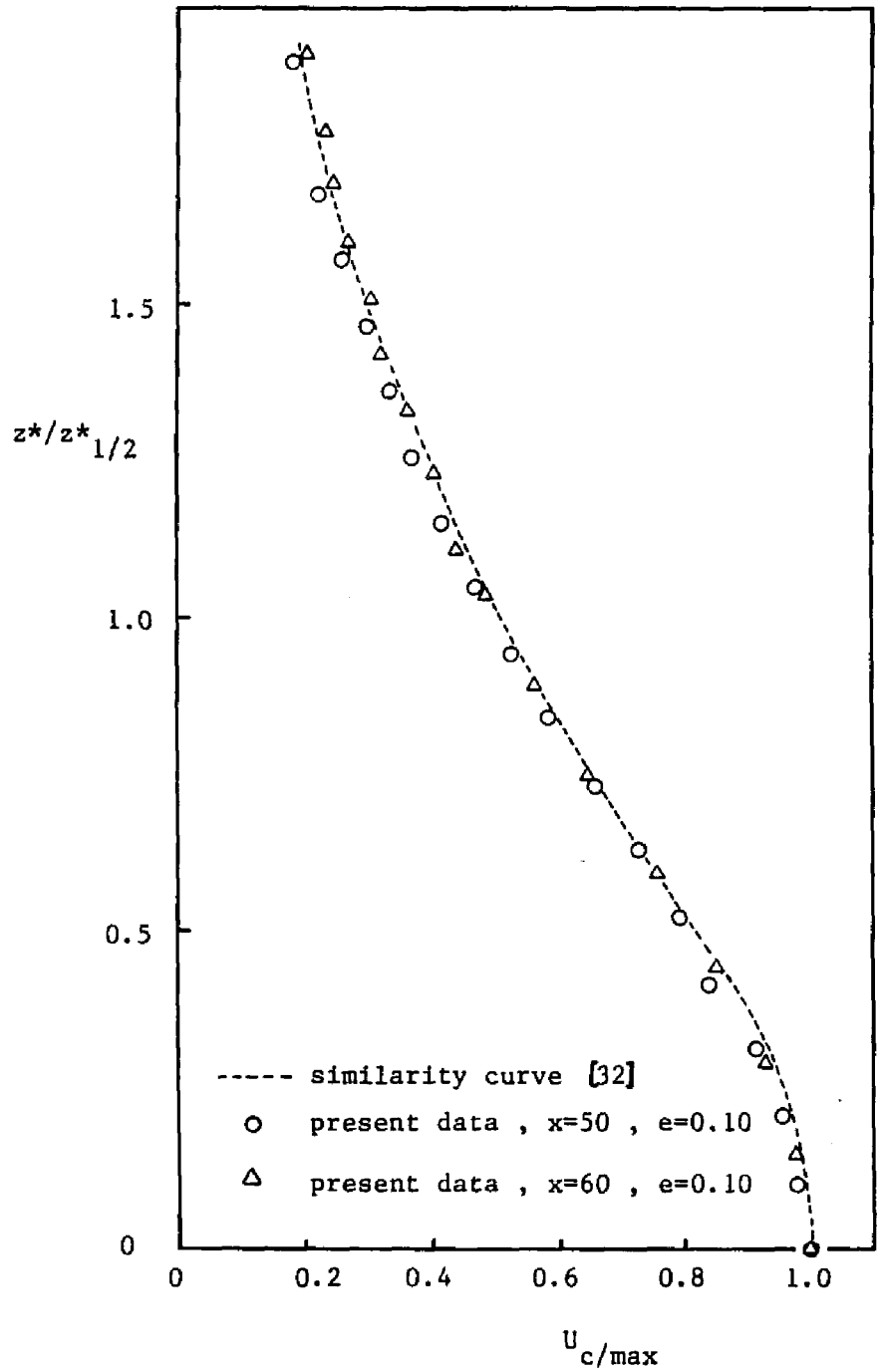

Figure A2. Spanwise velocity profiles for three-dimensional wall jets (Reference 38)

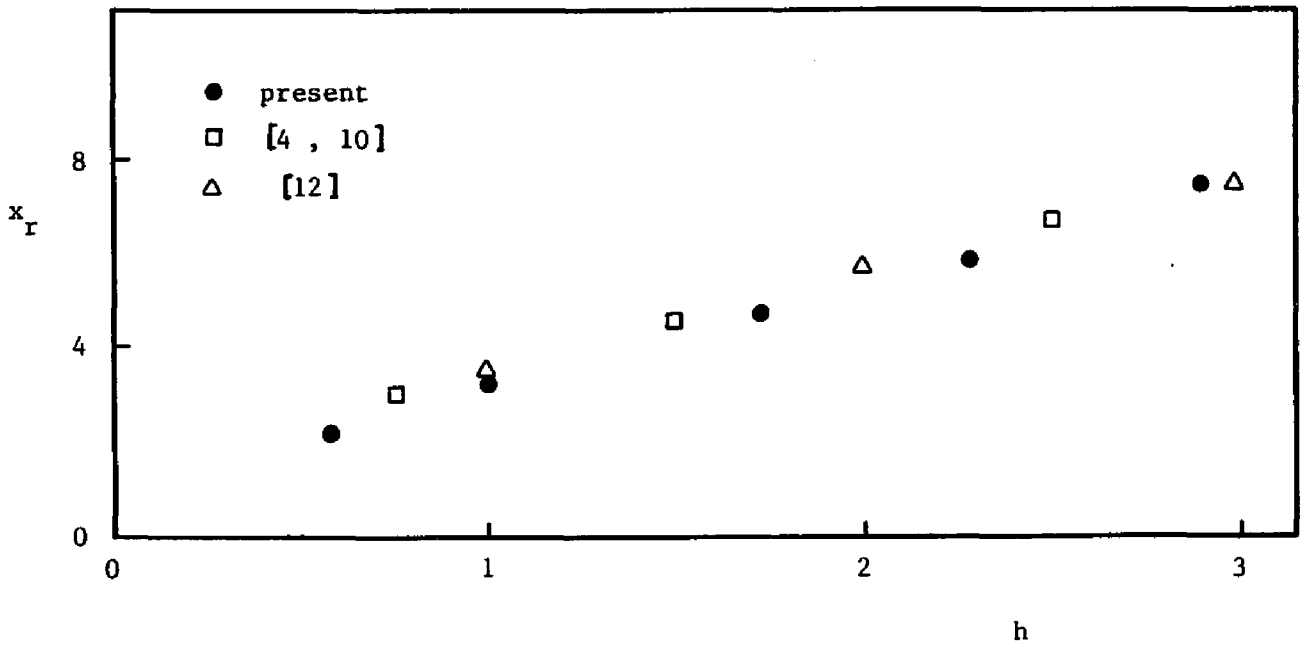

Figure A3. Variation of reattachment distance with offset distance for two-dimensional offset jets (Table B8)

APPENDIX B

Surface Pressure Disc Probe

The surface pressure disc probe was constructed at the Heat Transfer Laboratory of the City College and is shown in Figure B1. It was made out of 0.013 cm steel shims and has a diameter of 4.8 cm, leading edge thickness 0.03cm and trailing edge thickness 0.11 cm. A hole with 0.05 cm diameter was drilled at a distance 1.12 cm from the leading edge. Pressure signal at the surface hole is transmitted to the pressure sensor through a stainless steel tube, o.d. = 0.08 cm, which penetrates the disc probe.

Surface pressure data using the disc probe were compared with those using pressure taps in Figures B2 and B3. The inaccuracy of measurements taken with the disc probe is evident in both figures, particularly in the wall jet type region. These inaccurate readings may be attributed to the disc probe thickness which was found to be a significant factor in measuring very small magnitudes of surface pressure.

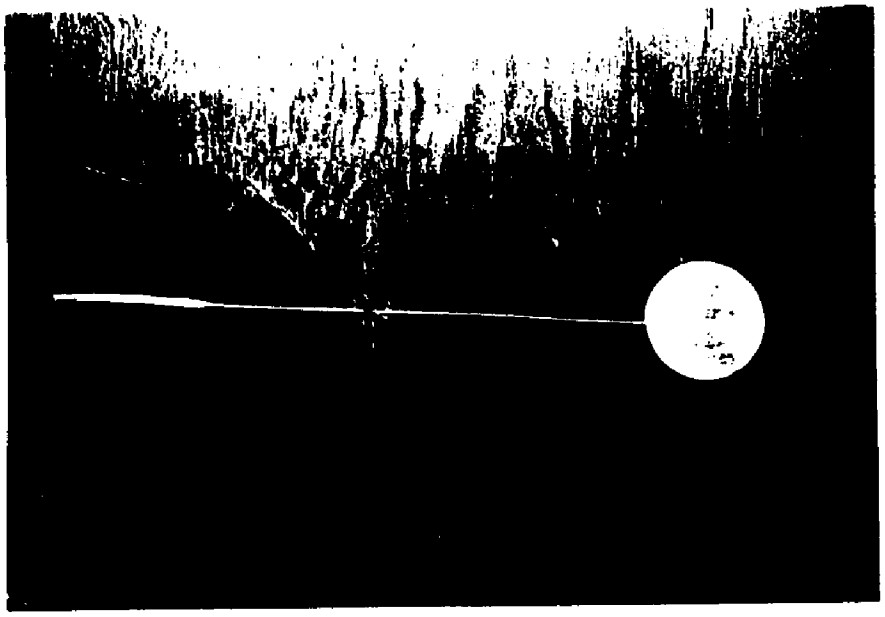

Figure B1. Surface pressure disc probe

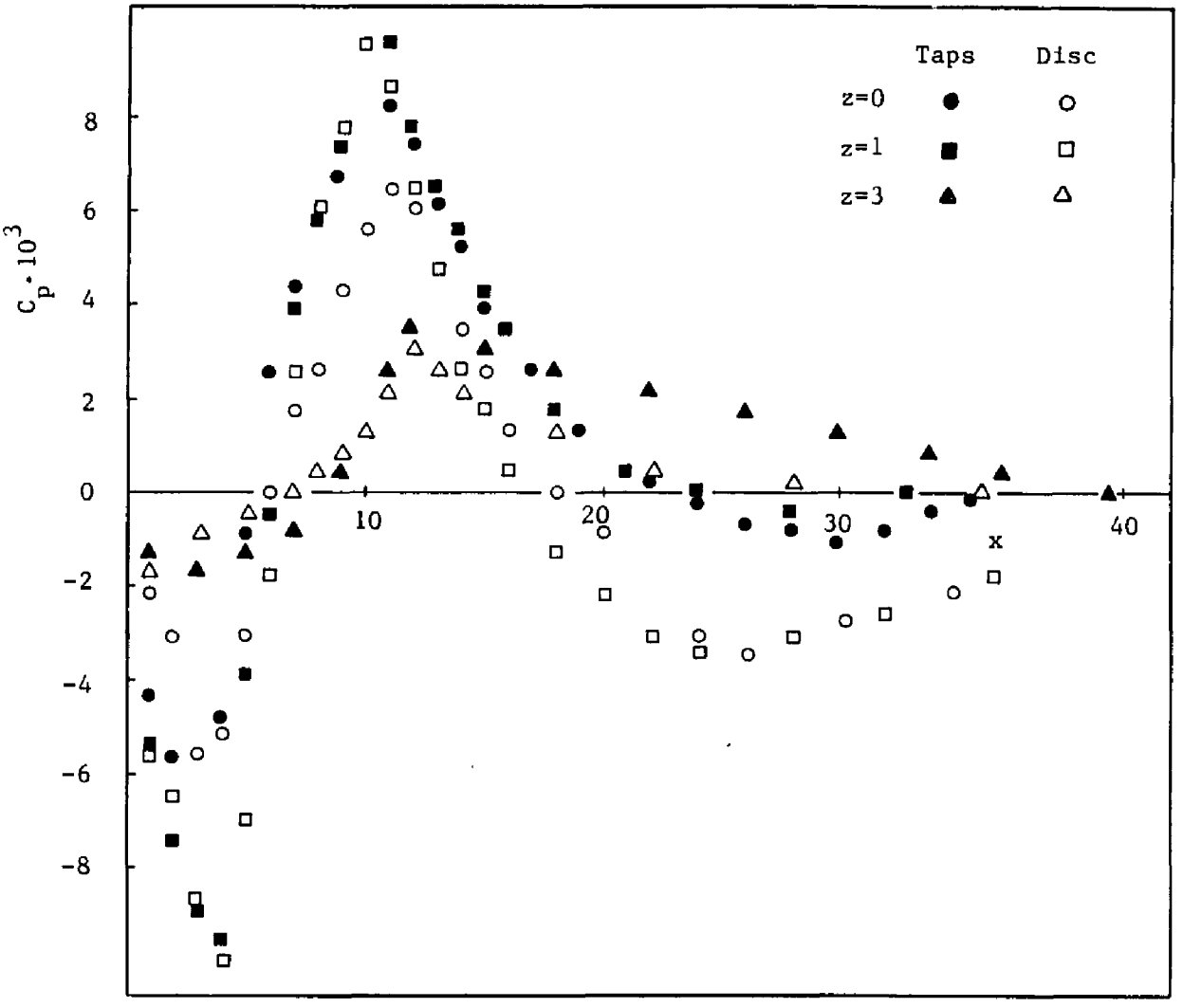

Figure B2. Axial surface pressure distributions measured with both methods (e=0.25 , h=1) (Tables B1 and C1)

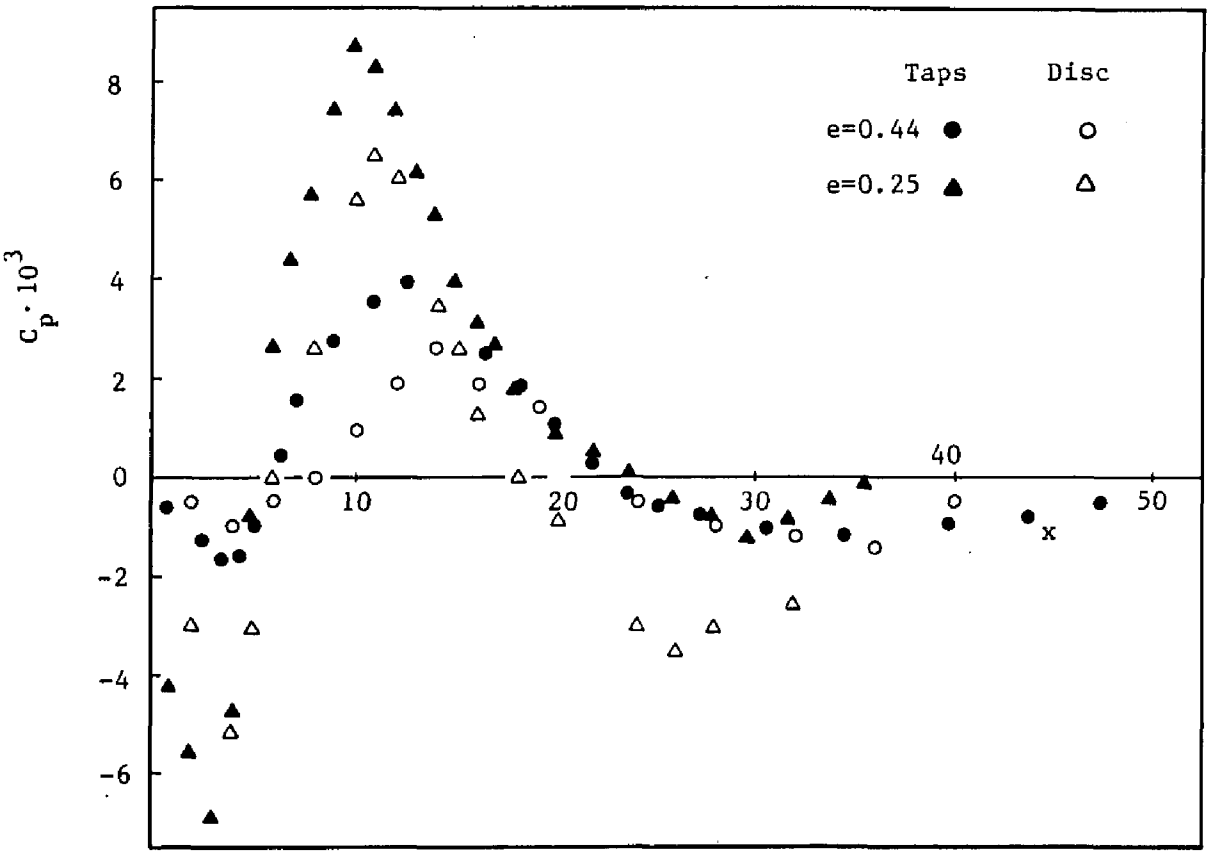

Figure B3. Axial surface pressure distributions measured with both methods (h=1 , z=0)(Tables B1 , B5 , C1 , C2)

APPENDIX C

Three-Dimensional Directional Probe

The three-dimensional directional probe (Figure C1) measures yaw and pitch angles of fluid flow, as well as total and static pressures.

A centrally located pressure hole measures pressure P_1^*, while two lateral pressure holes measure pressures P_2^* and P_3^* (Figure C2b). If the probe is rotated by a manual traverse unit (Figure C3) until $P_2^* = P_3^*$ as read out on a sensitive pressure indicator, the yaw angle of flow θ is then indicated by the traverse unit scale.

When the yaw angle has been determined an additional differential pressure $P_4^* - P_5^*$ is measured by pressure holes located above and below the total pressure P_1^* hole (Figure C2a). Pitch angle φ is determined by calculating the ratio $(P_4^* - P_5^*)/(P_1^* - P_2^*)$ and using the calibration curve for the probe on Figure C4. At any particular pitch angle, the velocity pressure coefficient $(P_t^* - P_s^*)/(P_1^* - P_2^*)$ and the total pressure coefficient $(P_1^* - P_t^*)/(P_t^* - P_s^*)$ can be read from the calibration curves for the probe on Figures C5 and C6, and $(P_t^* - P_s^*)$ and P_s^* calculated. Once $(P_t^* - P_s^*)$ has been found the total velocity vector U^* can be determined. Then, with known total velocity, yaw angle and pitch angle, the three velocity components are given by the following equations (see Figure C7):

$$u^* = U^* \cos\varphi \cos\theta$$

$$v^* = U^* \sin\varphi$$

$$w^* = U^* \cos\varphi \sin\theta$$

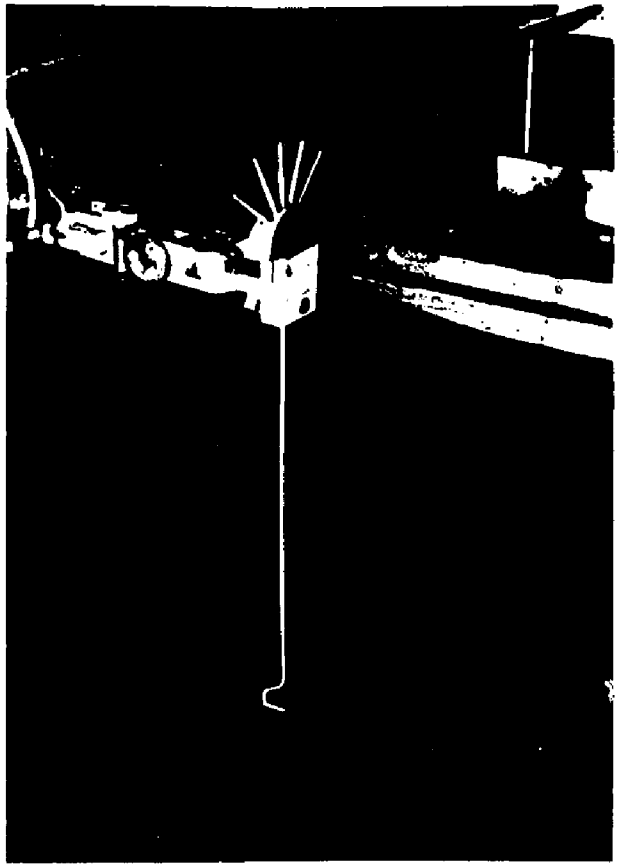

Figure C1. Three-dimensional directional probe

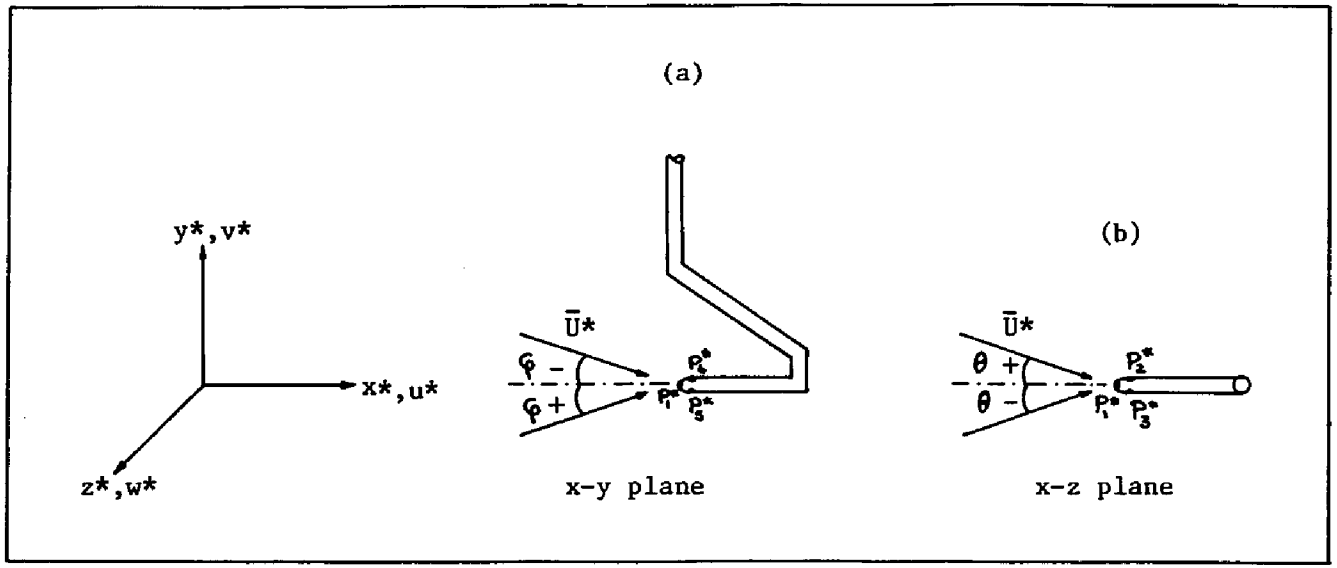

Figure C2. Illustration of pitch (φ) and yaw (θ) angles

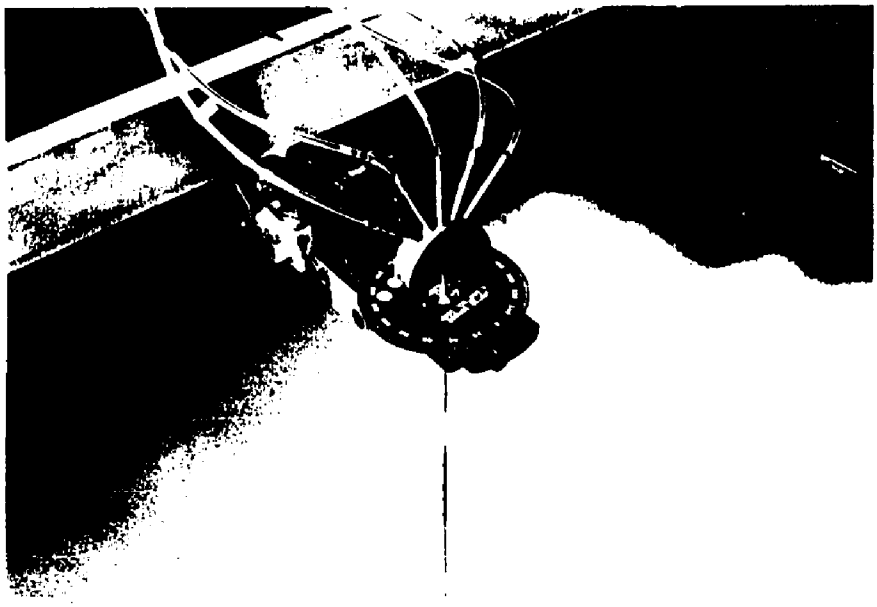

Figure C3. Manual traverse unit

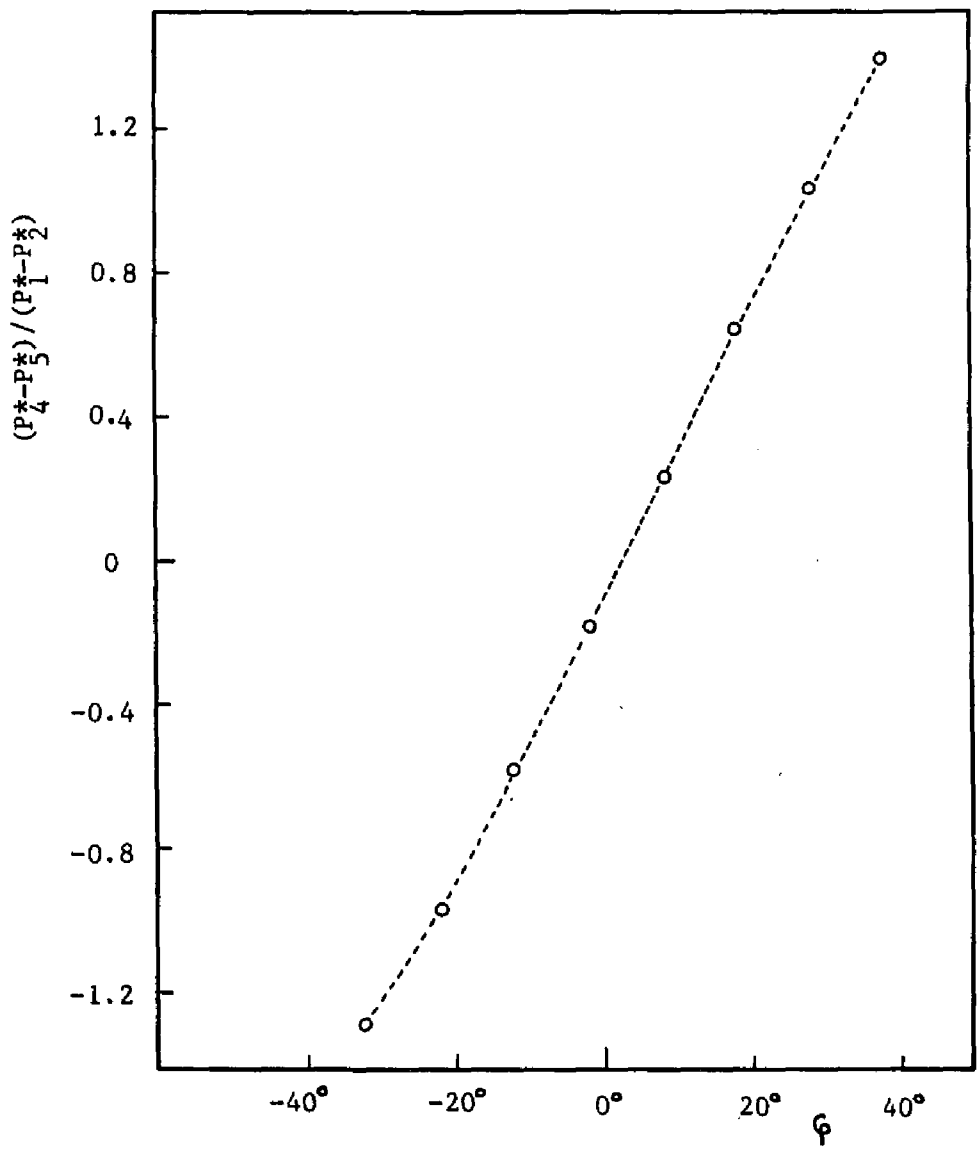

Figure C4. Pitch angle pressure coefficient vs pitch angle

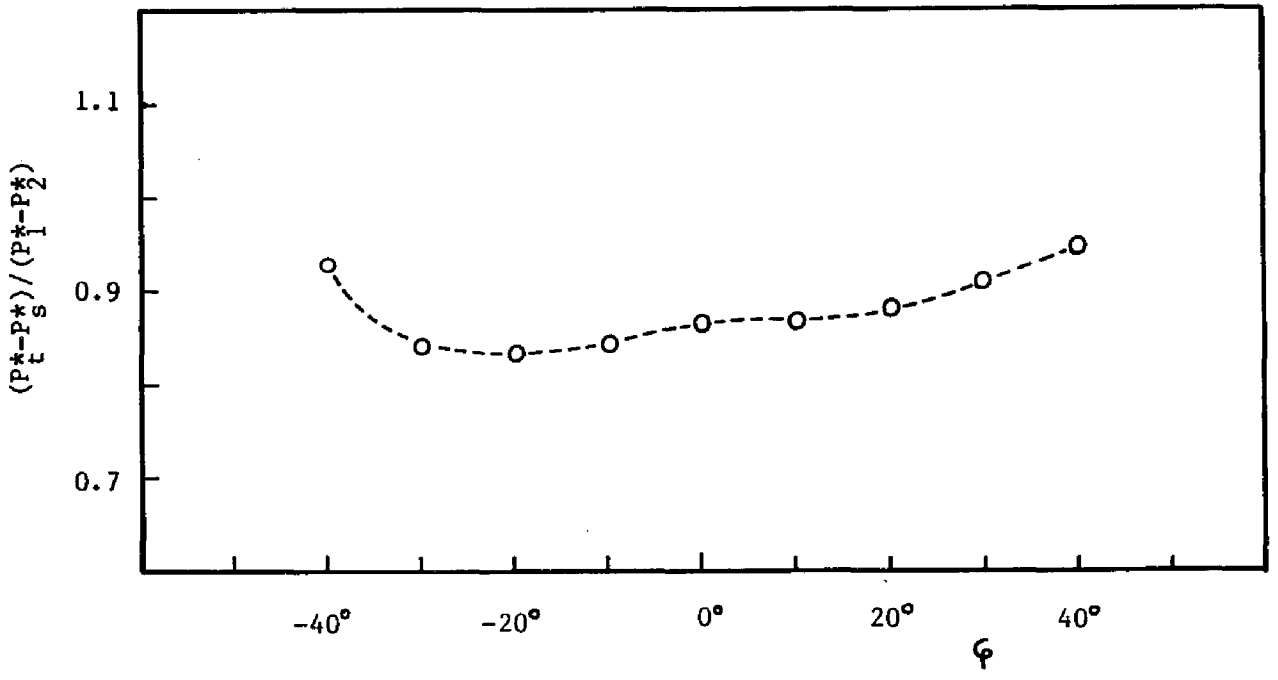

Figure C5. Velocity pressure coefficient vs pitch angle

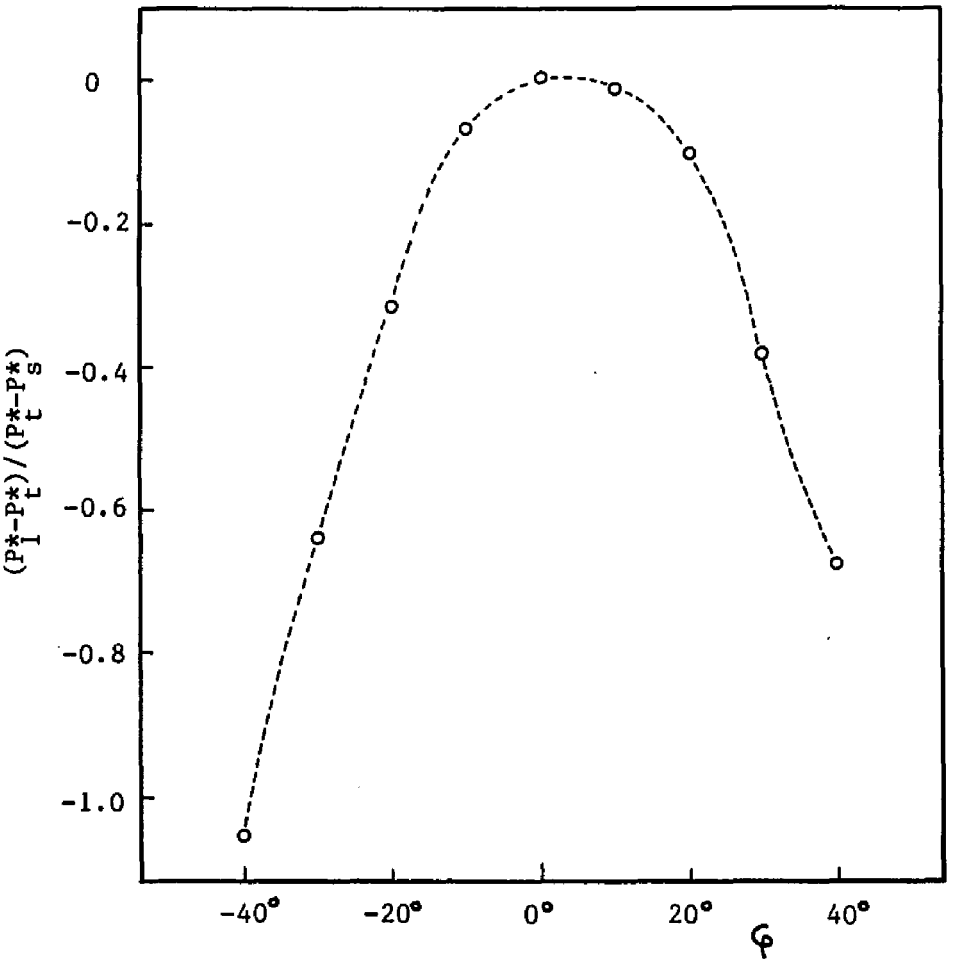

Figure C6. Total pressure coefficient vs pitch angle

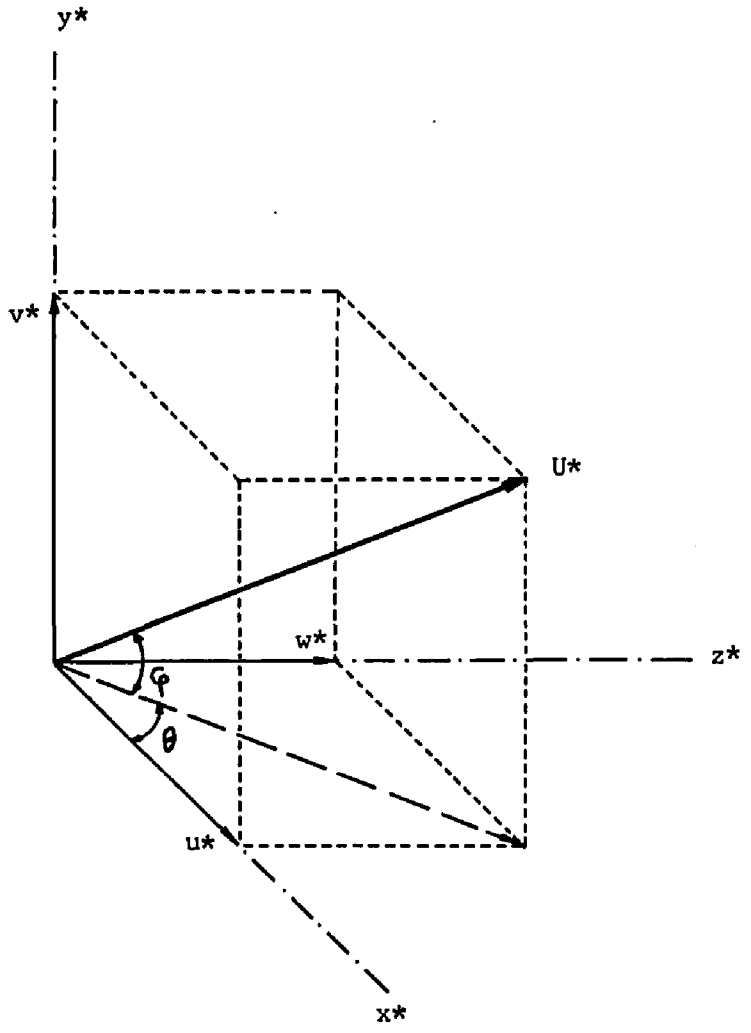

Figure C7. The three velocity components

APPENDIX D

Calibration of Pressure Transducer-Carrier Demodulator Set

The "Validyne DP15" pressure transducer - "Validyne CD15" carrier demodulator set which is used for pressure measurements, was calibrated with the help of a "Meriam" micromanometer before and after each group of experiments. The sensitivity of this micromanometer was of the order of 0.00254 cm of water. A "TSI 1125" calibrator (Figure D1), which was connected to a high pressure nitrogen tank through a pressure regulator, was used as a variable pressure source. A typical calibration curve is presented in Figure D2.

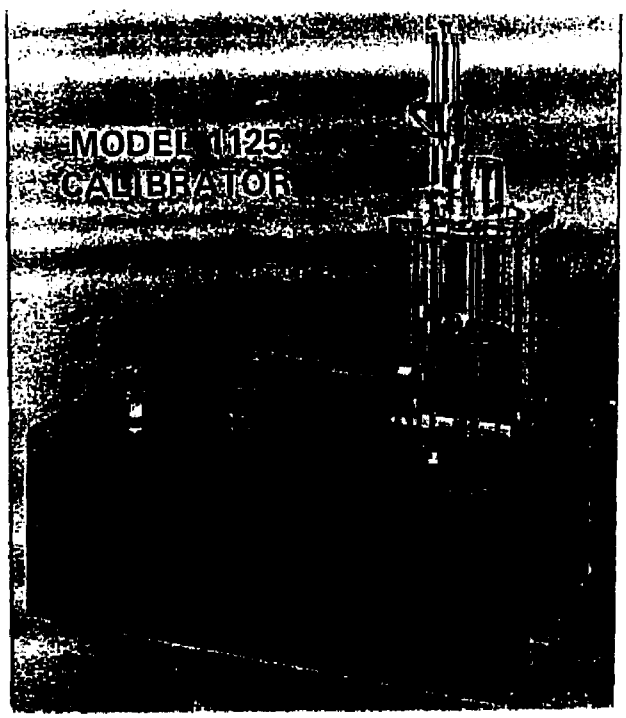

Figure D1. Calibrator

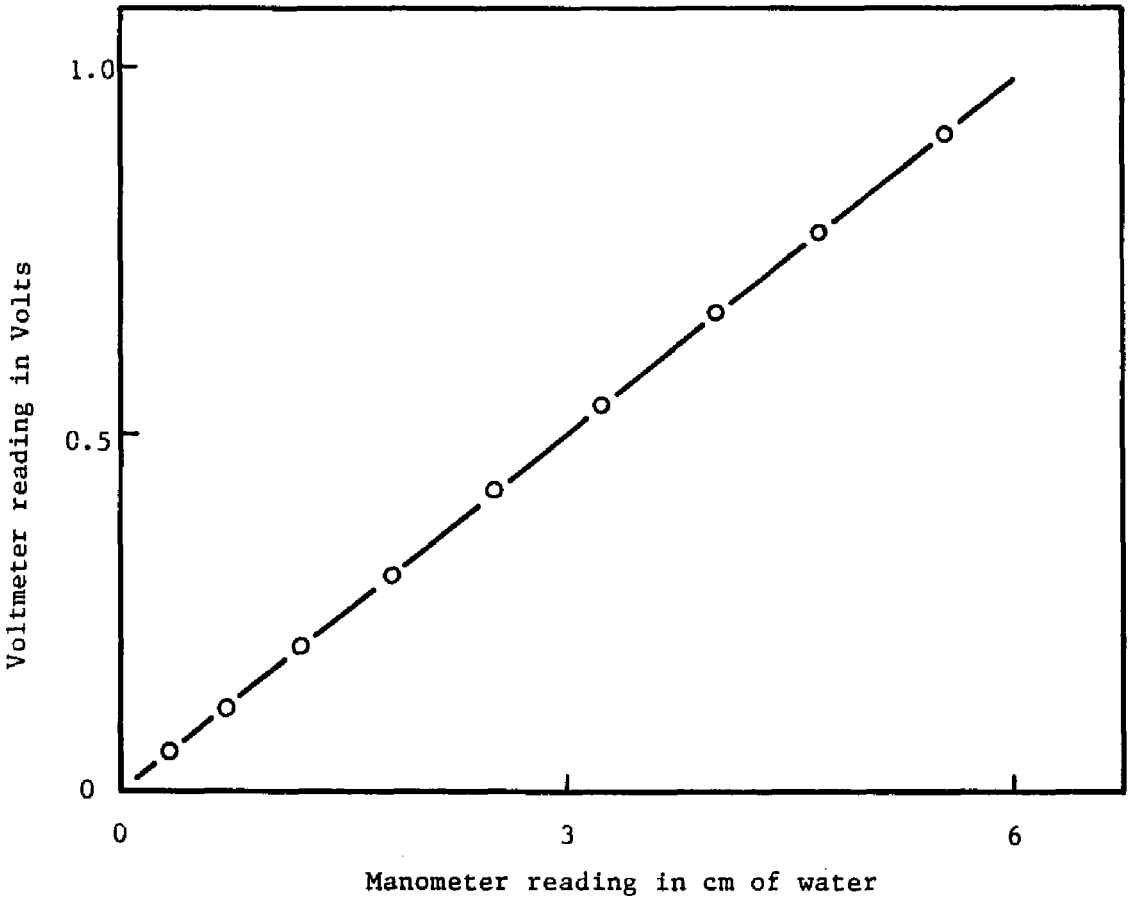

Figure D2. Transducer-Demodulator calibration curve

APPENDIX E

Error Analysis

The present investigation would be incomplete without a discussion on the experimental error of the results. This error is mainly caused by the inaccuracy of the used instruments as well as by the properties and characteristics of the probes.

A. Inaccuracy of the instruments

(a) **Transducer**

Linearity: 0.5%

Zero shift: 1% of full scale each 1,000 psig.

(b) **Demodulator**

Shift in gain: 0.01% per ^{o}C (negligible)

(c) **Digital Voltmeter**

Maximum error: 0.5%

(d) **Digital temperature indicator**

Temperature resolution: 1^{o} C

Note: The transducer-demodulator sets were calibrated before and after each series of experiments.

B. Properties and characteristics of the probes

(a) Pitot-static probes

If the fluid stream is not parallel to the probe head, errors occur in both total and static readings. These are the most important errors in this type of instrument because they cannot be corrected without taking independent readings with another type of probe.

Note that yaw and pitch angles affect the readings exactly the same. The errors in total and static pressure increase quite rapidly for angles of attack higher than 5^{o}, but they tend to compensate each other so the probe yields velocity readings accurate to 2% up to angles of attack of 30^{o}. This is the chief advantage of the Prandtl design over other types.

The static pressure indication is sensitive to distance from solid boundaries. The probe and boundary form a Ventouri passage which accelerates the flow and decreases the static pressure on one side. The calibration curve shows that static readings should not be taken closer than 5 tube diameters from a boundary for 1% accuracy.

Pitot-static probes appear to be insensitive to isotropic turbulence which is the most common type. Under some conditions of high intensity, large scale turbulence which makes the angle of attack at a probe vary over a wide range, the probe would presumably have an error corresponding to the average yaw or pitch angle caused by the turbulence.

(b) **Directional probe (three-dimensional)**

This five holes probe is furnished with individual calibration curves up to pitch angles of 40^{o}. It is usable up to Mach 0.7. The individual calibration curves have a 3% error approximately. The manual traverse unit scale which indicates the yaw angle of flow is accurate to $\pm 1^{o}$.

C. Total experimental error

The greatest error lies in those readings taken at the jet edges, near the wall and in the farfield of the flow. While the velocity could be measured to within approximately ±4% in the central region of the nearfield, greater inaccuracy was estimated for the farfield and outer edges of the jet with a compiled error in the order of ±10%.

The temperature measurement was found to possess a much higher error of approximately ±15% in the farfield, due to the wandering of the digital readout about the true average value, the oscillation of the heater and the fact that the heating unit's thermocouple sampled at a station significantly upstream of the channel entrance.

The surface pressure measurements are disposed to a quite high uncertainty due to their very small magnitudes and due to an intense wandering of the digital readout about the real true value. The cumulative error on the final measured surface pressure coefficient lies in the vicinity of 20%.

The measurements corresponding to the larger channels had the advantage of improved accuracy in position specification though a better

representation of the jet behavior is seen for the smaller dimension jets in which measurements at much greater diameter distances could be taken. Since the greatest uncertainty was found to lie in the values obtained in the farfield and at the outer edges of the jet, several runs were made for each set of readings with emphasis on data collection in these high variability regions, until repeatability was assured. The repeatability of data was the single most important criterion used in judging reliability.

APPENDIX F

Tabulation of Data

Table A

Dimensions of discharges

e	d* (in)	ℓ* (in)
0.44	0.77	1.76
0.25	1.40	5.60
0.10	0.38	3.80

TABLE B1

$C_p \times 10^3$ (e = 0.25, h = 1, Re_o = 39,000)

x \ z	0	0.5	1	2	2.5	3	3.5	4
1	-4.35	-4.79	-5.23	-3.92		-1.31		-0.87
2	-5.66	-5.23	-7.40	-4.35	-3.05			
3	-6.97	-7.40	-8.93	-4.79		-1.74		
4	-4.79	-5.66	-9.58	-4.35	-2.61		-0.87	
5	-0.87	-4.35	-3.92	-3.48	-2.18	-1.31		
6	2.61	-0.87	-0.44	-2.61	-1.74			
7	4.35	2.18	3.92	0.44	-0.87	-0.87		-0.44
8	5.66	3.92	6.10	2.61	2.61	-0.44		
9	7.40	6.10	7.40	5.23	5.66	0.44		
10	8.71	7.84	8.71	6.97	6.10	1.31	-0.43	
11	8.27	8.71	9.58	7.84	6.53	2.61	0	
12	7.40	7.40	7.84	6.53	6.10	3.48	0.43	
13	6.10	5.23	6.53	5.23	5.23		0.87	
14	5.23	4.79	5.66	4.35	4.35		1.31	0
15	3.92	4.35	4.35	3.48		3.05	1.74	
16	3.05	3.92	3.48	3.05	3.48		2.18	0.43
17	2.61						2.61	
18	1.74	1.74	1.74	2.18	2.18	2.61		0.87
19	1.31						2.18	
20	0.87	0.87		1.31	1.74			1.31
21			0.44					
22	0.22			0.87	1.31	2.18	1.74	
23		0.44						
24	-0.22		0		0.87			
25				0.44				
26	-0.66	0			0.43	1.74		
28	-0.87		-0.44	0				
29		-0.44						1.74
30	-1.09				0	1.31	1.31	
32	-0.87	0	0					
34	-0.44					0.87		
36	0							
37						0.44		1.31
38							0.87	
42						0	0.43	0.87
46								0.43
48							0	
50								0

TABLE B2

$C_p \times 10^3$ (e = 0.25, h = 1, Re_o = 39,000)

x / z	3	10	20
0	-6.97	8.71	0.87
0.5	-7.40	7.84	0.87
1	-8.71	8.71	1.08
2	-4.79	6.97	1.31
2.5	-2.83	6.10	1.74
3	-1.74	1.31	2.40
3.5	-0.87	-0.43	1.96
4	-0.66	-0.22	1.31

TABLE B3

$C_{pc} \times 10^3$ (e = 0.44, h = 0.61)

Re_o / x	26,300	39,100	55,400
0.46	-3.71	-3.50	-5.53
0.91	-4.29	-3.76	-5.98
1.37	-5.43	-4.80	-7.71
1.83	-5.14	-4.93	-10.16
2.74	-1.43	-2.34	-6.43
3.65	0.86	0.52	0.90
4.56	2.00	2.34	6.43
5.48	2.29	2.99	7.39
6.39	2.57	3.11	
7.30	2.72	3.24	7.52
9.13	3.14	3.37	7.58
10.95	3.43	3.63	7.91
12.78	2.29	2.34	4.56
14.60	1.43	1.43	2.18
16.43	0.43	0.39	0.19
18.25	0	0	-0.32
20.08	-0.57	-0.26	-0.90
21.90	-1.14	-0.52	-1.93
23.73	-1.72	-1.56	-2.44
25.55	-1.43	-1.17	-2.96
27.38	-1.14	-1.04	-2.83
29.21	-1.00	-0.91	-2.51
32.86	-0.86	-0.84	-2.19
36.51	-0.57	-0.78	-2.12
40.16	-0.29	-0.52	-1.61
43.81	-0.14	-0.26	-0.90
47.46	0	0	-0.51

TABLE B4

$C_{p_c} \times 10^3$ (e = 0.25, Re_o = 39,000)

x \ h	0.35	0.48	1.00	1.47	2.21	2.90
0.5	-39.15	-29.58				
1	-28.71	-26.54	-4.35	-1.74		
1.5	5.66					
2	26.97	13.05	-5.66		-0.44	0
2.5	30.02					
3	26.10	22.19	-6.97	-2.18		
4	16.01	16.53	-4.79	-3.05	-0.87	
5	10.44	11.31	-0.87	-3.48		
6	7.84	8.27	2.61	-3.05		-0.44
7	6.53	7.84	4.35	-2.18		
7.5					-1.31	
8	6.10	7.40	5.66	-0.87		
9	5.66	6.97	7.40	0		
10	5.23	6.53	8.71	2.61		-0.87
11		6.10	8.27	4.79	-0.44	
12	3.92	5.23	7.40	6.53	0.87	
13		3.05	6.10	6.97	2.18	-1.31
14	2.40	2.61	5.23	6.75	3.48	-0.87
15		2.18	3.92	6.53	4.35	-0.22
16	0.87	1.74	3.05	5.23	5.23	0.22
17	0	1.09	2.61	4.35	4.79	1.31
18	-0.44	0.44	1.74	3.92	4.35	1.74
19	-0.87	0	1.31	3.05	3.92	2.18
20	-2.18	-0.87	0.87	2.18	3.48	2.61
21	-2.61	-1.74				2.83
22	-1.31	-1.31	0.44	1.31	2.61	3.48
23						2.83
24	-0.87	-1.09	0	0.87	2.18	2.61
25						2.40
26	-0.44		-0.44	0.44	1.31	
27						2.18
28		-0.44	-0.87	-0.44	0.87	
29	0					
30			-1.31		0.44	1.74
32		0	-0.87	-0.66	0	1.31
34			-0.44			
35						0.87
36			0			
37				0		
38					-0.44	0.44
40						
42					0	
43						-0.22
48						0

TABLE B5

$C_{p_c} \times 10^3$ (h = 1)

x \ e	0.44
0.913	-0.65
1.369	-0.78
1.825	-0.91
2.738	-1.30
3.651	-1.68
4.563	-1.68
5.476	-1.04
6.389	0.39
7.301	1.55
9.127	2.72
10.952	3.50
12.777	3.89
14.602	3.50
16.428	2.46
18.253	1.81
20.078	1.04
21.904	0.39
23.729	-0.39
25.554	-0.58
27.380	-0.78
29.205	-0.91
31.030	-1.04
32.855	-1.17
34.681	-1.17
36.506	-1.17
38.331	-1.04
40.157	-0.97
41.982	-0.91
43.807	-0.78
45.632	-0.65
47.458	-0.52
51.108	-0.39
54.759	-0.26

x \ e	0.10
0.933	-69.81
1.867	-60.84
2.8	-55.08
3.733	-11.53
5.6	62.12
7.467	49.96
9.333	36.51
11.2	20.49
13.067	12.81
17.933	9.61
18.667	9.61
22.4	6.73
26.133	-0.26
33.6	-1.47
41.067	-0.64

TABLE B6

C_p (e = 0, Re_o = 39,000)

x \ h	0.57	1	1.72	2.28
0.25	-0.096	-0.086	-0.081	-0.076
0.5	-0.096	-0.090	-0.083	-0.077
0.75	-0.100	-0.093	-0.085	-0.080
1	-0.107	-0.095	-0.087	-0.083
1.5	-0.108	-0.102	-0.090	-0.084
2	-0.036	-0.111	-0.093	-0.086
2.5	0.066	-0.098	-0.099	-0.090
3	-0.111	-0.042	-0.109	-0.095
3.5	0.102	0.044	-0.111	-0.107
4	0.074	0.109	-0.084	-0.115
4.5		0.139		
5	0.033	0.116	0.047	-0.081
6	0.015	0.063	0.144	0.036
7	0.007	0.028	0.129	0.144
8	0.005	0.014	0.072	0.154
9	0.003	0.008	0.037	0.098
10	0.002	0.006	0.019	0.052
11	0.001	0.004	0.010	0.027
12	0.001	0.003	0.007	0.015
13		0.002	0.004	0.007
14	0	0.001	0.002	0.005
15		0.001		
16		0.001	0.001	0.003
17		0		

TABLE B7

$C_{Pcmax} \times 10^3$ (Re_o = 39,000)

h \ e	0	0.1	0.25	0.44
0.14			67.4	
0.20				29.1
0.35			30	
0.47				13
0.48			22.2	
0.54		93		
0.57	115			
0.61				8.4
1.00		66		3.9
1.07	140		8.7	
1.47			7	
1.72	160			
1.79				3
1.83		37		
1.85				2.9
2.21			5.2	
2.28	174			
2.85				2.2
2.90			3.5	
3.00		24		

TABLE B8

x_r (Re_o = 39,000)

h \ e	0	0.25	0.44
0.48		1.5	
0.57	2.2		
0.61			3.2
1.00			6.0
1.07	3.3	5.2	
1.47		8.0	
1.72	4.6		
1.85			12.0
2.21		11.6	
2.28	5.8		
2.85			18.0
2.90	7.4	15.8	

TABLE B9

x_a (Re_D = 39,000)

h \ e	0	0.1	0.25	0.44
0.47				2.2
0.48			3	
0.54		3.2		
0.57	3.2			
1.00		4.5		12.8
1.07	4.5		10	
1.47			13	
1.72	6.2			
1.79				18.3
1.83		1.31		
2.21			16	
2.28	7.5			
2.85				21.9
2.90	9.4		21	
3.00		20.2		

TABLE C1
(Disc Probe Data)

$C_p \times 10^3$ (e = 0.25, h = 1.00, Re_o = 39,000)

x \ z	0	1	2	3
1	-2.16	-5.62	-5.19	
2	-3.03	-6.48	-4.76	
3	-5.62	-8.65	-4.32	-0.86
4	-5.19	-9.94	-3.89	
5	-3.03	-6.92	-3.46	-0.43
6	0	-1.73	-2.16	
7	1.73	2.59	1.30	0
8	2.59	6.05	4.76	0.43
9	4.32	7.78	6.92	0.86
10	5.62	9.51	8.21	1.30
11	6.48	8.21	7.35	2.16
12	6.05	6.48	6.05	3.03
13	4.76	4.76	4.76	2.59
14	3.46	2.59	3.46	2.16
15	2.59	1.73	2.59	
16	1.30	0.43	1.73	1.73
18	0	-1.30	0.43	1.30
20	-0.86	-2.16	0	0.86
22		-3.03	-0.43	0.43
24	-3.03	-3.46	-0.86	
26	-3.46		-1.30	
28	-3.03	-3.03	-1.73	0.21
32	-2.59	-2.59	-2.16	
36			-1.73	0

TABLE C2
(Disc Probe Data)

$C_{pc} \times 10^3$ (e = 0.44, h = 1.00, Re_o = 39,000)

x \ z	0
2	-0.48
4	-0.96
6	-0.48
8	0
10	0.96
12	1.91
14	2.63
16	1.91
18	1.43
20	0
24	-0.48
28	-0.96
32	-1.19
36	-1.43
40	-0.48

TABLE D1

Discharge Velocity Profiles

(x = 0, z = 0)

(U_o^* = 32.93 m/sec, e = 0.44)		(U_o^* = 39.18 m/sec, e = 0.10)	
2Y*/d*	U	2Y*/d*	U
-1	.524	-.975	.575
-.934	.690	-.925	.675
-.870	.768	-.8	.800
-.740	.841	-.675	.850
-.608	.892	-.4	.925
-.478	.927	-.25	.970
-.348	.96	0	1
-.218	.981	.25	.975
-.088	.997	.4	.930
0	1.000	.675	.850
.088	.998	.8	.796
.218	.983	.925	.675
.348	.960	.975	.575
.478	.930		
.608	.894		
.740	.843		
.870	.767		
.934	.692		
1	.519		

TABLE D2

Discharge Velocity Profiles

(x = 0, Y = 0)

(U_o^* = 32.93 m/sec, e = 0.44)		(U_o^* = 39.18 m/sec, e = 0.10)	
2z*/ℓ*	U	2z*/ℓ*	U
-1	.601	-1	.550
-.967	.677	-.970	.653
-.910	.745	-.945	.762
-.853	.802	-.880	.913
-.796	.854	-.750	.968
-.739	.899	-.550	.988
-.683	.930	-.300	.999
-.626	.958	-.150	1
-.569	.970	0	1
-.455	.979	.150	1
-.341	.985	.275	.998
-.228	.991	.438	.996
-.114	.997	.625	.981
0	1	.750	.963
.228	.989	.880	.921
.455	.977	.965	.750
.683	.928	.988	.663
.796	.853	1	.550
.910	.743		
.967	.678		
1	.596		

TABLE D3

(e = 0.44, h = 4.85, z = 0, $U_o^* = 32.93^m$/sec)

x = 5		x = 10		x = 25		x = 35		x = 45	
y	U_c	y	U_c	y	U_c	y	U_c	y	U_c
4.172	0	3.846	.074	0.196	0	0.065	.097	0.065	.116
4.237	.036	4.237	.188	0.652	.037	0.326	.103	0.326	.127
4.302	.051	4.563	.347	0.913	.037	0.652	.110	0.652	.132
4.368	.103	4.889	.555	1.108	.052	0.978	.116	1.304	.142
4.498	.205	5.020	.643	1.304	.063	1.304	.121	1.956	.155
4.628	.327	5.150	.711	1.956	.103	1.630	.137	2.608	.167
4.759	.472	5.215	.745	2.608	.142	1.956	.146	3.259	.179
4.889	.614	5.280	.765	3.259	.200	2.282	.163	3.585	.186
5.020	.771	5.346	.777	3.911	.271	2.608	.175	3.911	.193
5.085	.832	5.411	.776	4.563	.337	2.934	.190	4.237	.193
5.150	.888	5.541	.749	4.889	.358	3.259	.207	4.433	.193
5.215	.933	5.737	.642	5.020	.364	3.585	.222	4.563	.197
5.280	.957	5.997	.469	5.085	.365	3.911	.234	4.694	.200
5.313	.963	6.128	.389	5.150	.367	4.237	.248	4.824	.197
5.346	.967	6.258	.313	5.215	.371	4.433	.250	4.954	.193
5.378	.967	6.389	.242	5.280	.369	4.563	.256	5.085	.193
5.411	.964	6.519	.181	5.345	.368	4.694	.258	5.378	.193
5.476	.942	6.649	.128	5.411	.367	4.824	.261	5.215	.193
5.541	.907	6.780	.090	5.541	.364	4.954	.258	5.541	.190
5.606	.857	6.91	.052	5.867	.345	5.085	.261	5.867	.186
5.671	.804			6.519	.281	5.215	.261	7.171	.155
5.737	.729			7.171	.201	5.378	.258	8.475	.116
5.802	.665			7.823	.142	5.541	.253	9.778	.063
5.932	.512			8.475	.082	5.867	.245	10.430	.037
6.063	.359			8.996	.037	6.519	.222	11.343	0
6.193	.235			9.126	0	7.171	.186		
6.323	.120					7.823	.155		
6.454	0					8.475	.116		
						9.126	.082		
						9.778	.052		
						10.430	.037		
						10.561	0		

TABLE D4

(e = 0.44, h = 4.85, $z^* = 0.4\ell^*$, $U_o^* = 32.93$ m/sec)

x = 5		x = 10		x = 25		x = 35	
y	U	y	U	y	U	y	U
4.172	0	3.846	.083	1.108	0	0.065	.090
4.237	.051	4.237	.185	1.304	.037	0.326	.097
4.302	.081	4.563	.345	1.956	.082	0.652	.103
4.368	.131	4.889	.512	2.608	.127	1.304	.121
4.498	.215	5.020	.585	3.259	.193	1.956	.146
4.628	.319	5.150	.638	3.911	.253	2.608	.175
4.759	.465	5.215	.651	4.563	.312	3.259	.207
4.889	.608	5.280	.669	4.889	.333	3.911	.231
5.020	.701	5.346	.672	5.020	.337	4.237	.242
5.085	.747	5.411	.667	5.085	.337	4.433	.245
5.150	.767	5.541	.640	5.150	.337	4.563	.250
5.215	.775	5.737	.554	5.215	.339	4.694	.250
5.280	.772	5.997	.418	5.280	.339	4.824	.253
5.313	.773	6.128	.339	5.378	.337	4.954	.250
5.346	.769	6.258	.267	5.411	.335	5.085	.253
5.378	.771	6.389	.209	5.541	.331	5.215	.253
5.411	.773	6.519	.161	5.867	.312	5.378	.250
5.476	.773	6.649	.111	6.519	.216	5.541	.245
5.541	.763	6.780	.074	7.171	.183	5.867	.237
5.606	.744	6.910	.037	7.823	.121	6.519	.213
5.672	.709			8.475	.052	7.171	.186
5.802	.585			8.670	.037	7.823	.146
5.932	.445			8.801	0	8.475	.116
6.063	.308					9.126	.082
6.193	.202					9.778	.063
6.323	.103					10.430	.037
6.454	0					10.691	0

TABLE D5

(e = 0.44, h = 4.85, y = 5.35, U_o^* = 32.93 m/sec)

x = 5		x = 10		x = 25		x = 35		x = 45	
$2z^*/\ell^*$	U	$2z^*/\ell^*$	U	$2z^*/\ell^*$	U	$2z^*/\ell^*$	U	$2z^*/\ell^*$	U
0	.964	0	.779	0	.367	0	.258	0	.190
.057	.963	.057	.778	.057	.366	.057	.258	.057	.190
.114	.961	.114	.777	.114	.364	.114	.261	.114	.190
.228	.953	.228	.769	.228	.362	.228	.261	.228	.193
.341	.945	.341	.760	.341	.360	.341	.261	.341	.193
.455	.940	.455	.751	.455	.352	.455	.258	.455	.197
.569	.930	.569	.733	.569	.347	.569	.256	.569	.193
.683	.885	.683	.711	.683	.343	.683	.256	.683	.193
.796	.749	.910	.610	.769	.331	.910	.248	.910	.193
.910	.603	1.138	.463	.910	.323	1.138	.240	1.138	.190
1.024	.462	1.365	.339	1.024	.312	1.365	.222	1.365	.183
1.138	.306	1.593	.215	1.138	.292	1.593	.203	1.593	.175
1.251	.192	1.820	.128	1.365	.273	1.820	.193	1.820	.167
1.479	.063	2.048	.037	1.593	.240	2.048	.179	2.048	.155
1.593	.036			1.820	.216	2.275	.163	2.503	.137
1.706	0			2.048	.179	2.503	.146	2.958	.121
				2.275	.146	2.730	.132	3.413	.103
				2.503	.121	2.958	.116	3.868	.090
				2.730	.090	3.185	.097	4.323	.063
				2.958	.052	3.413	.082	4.778	.052
				3.185	.037	3.641	.073	5.233	.037
				3.299	0	3.868	.063	5.575	0
						4.096	.052		
						4.323	.037		
						4.664	0		

TABLE D6

U (e = 0.44, h = 4.85, y = 4.7, U_o^* = 32.93 m/sec)

$2z^*/\ell^*$ \ x	10	25	35
0	.429	.345	.263
.057	.426	.345	.263
.114	.423	.345	.263
.171			.261
.228	.421	.345	.261
.341	.426		.261
.455	.432	.339	.258
.569	.435		.258
.683	.434	.325	.256
.910	.391	.304	.245
1.138	.326	.285	.237
1.365	.242	.263	.225
1.593	.152	.234	.210
1.820	.083	.203	
1.991	.037		
2.048		.175	.179
2.275		.146	
2.503		.116	.151
2.730		.082	
2.958		.052	.116
3.072		.037	
3.185		0	
3.413			.090
3.868			.063
4.096			.052
4.323			.037
4.664			0

TABLE D7

U (e = 0.44, h = 4.85, x = 10, $U_o^* = 32.93$ m/sec)

$2z^*/\ell^*$ \ y	10	25	35
0	.779	.429	.467
.057	.778	.426	.467
.114	.777	.423	.467
.228	.769	.421	.461
.341	.760	.426	.452
.455	.751	.432	.440
.569	.733	.435	.426
.683	.711	.434	.413
.910	.610	.391	.389
1.138	.463	.326	.328
1.365	.339	.242	.245
1.593	.215	.152	.157
1.820	.128	.083	.074
1.991		.037	0
2.048	.037		

TABLE D8

Max. Velocity Decay - Trajectory

(e = 0.44, h = 1.85, z = 0)

x	Re_o = 26,000		Re_o = 38,000		Re_o = 50,000	
	$U_{c\,max}$	y	$U_{c\,max}$	y	$U_{c\,max}$	y
0	1.000	2.35	1.000	2.35	1.000	2.35
2	.986	2.35			.990	2.35
3.65			.980	2.35		
5	.956	2.35			.967	2.35
9.13			.806	2.28		
10	.751	2.31			.760	2.35
14			.621	2.25		
15	.557	2.25			.564	2.28
18.25			.499	2.22		
20	.447	2.15			.454	2.22
23			.408	2.09		
28			.344	1.92		
30	.323	1.70			.328	1.70
34			.295	1.56		
40	.258	1.24			.266	1.30
44			.242	1.17		

TABLE D9

(e = 0.44, x = 10, z = 0, $U_0^* = 32.93$ m/sec)

h = 4.85		h = 1.85		h = 1.07	
y	U_c	y	U_c	y	U_c
3.85	.074	0.78	.073	.13	.187
4.24	.188	1.04	.132	.26	.201
4.56	.347	1.30	.223	.39	.214
4.89	.555				
5.02	.643	1.56	.348	.65	.291
5.15	.711	1.69	.431	.91	.437
5.22	.745	1.83	.512	1.17	.611
5.28	.765	1.96	.602	1.43	.741
5.35	.777	2.09	.679	1.57	.760
5.41	.776	2.22	.743	1.69	.736
5.54	.749	2.35	.766	1.96	.602
5.74	.642	2.48	.757	2.22	.418
6.00	.469	2.61	.706	2.48	.279
6.13	.389	2.74	.632	2.74	.151
6.26	.313	2.87	.556	3.00	.037
6.39	.242	3.00	.459		
6.52	.181	3.13	.376		
6.65	.128	3.39	.232		
6.78	.090	3.65	.116		
6.91	.052	3.78	.064		

TABLE D10

(e = 0.44, x = 25, z = 0, $U_0^* = 32.93$ m/sec)

h = 4.85		h = 1.85		h = 1.07	
y	U_c	y	U_c	y	U_c
.20	0	.13	.235	.13	.320
.65	.037	.52	.279	.26	.350
.91	.037	.91	.313	.39	.368
1.11	.052	1.30	.346	.65	.388
1.30	.063	1.56	.363	.91	.400
1.96	.103	1.83	.372	1.04	.402
2.61	.142	2.09	.376	1.17	.398
3.26	.200	2.22	.370	1.43	.393
3.91	.271	2.35	.368	1.56	.383
4.56	.337	2.48	.361	1.69	.372
4.89	.358	2.61	.354	1.96	.346
5.02	.364	2.87	.332	2.22	.311
5.09	.365	3.13	.300	2.48	.282
5.15	.367	3.39	.272	2.74	.251
5.22	.371	3.78	.223	3.00	.217
5.28	.369	4.17	.183	3.26	.180
5.35	.368	4.69	.122	3.52	.147
5.41	.367	5.22	.073	3.78	.122
5.54	.364	5.48	.037	4.04	.090
5.87	.345			4.30	.052
6.52	.281			4.43	.037
7.17	.201				
7.82	.142				
8.48	.082				
9.00	.037				
9.13	0				

TABLE D11

$Y_{\frac{1}{2}}$ (e = 0.44, z = 0, $U_o^* = 32.93$ m/sec)

x \ h	0	1.07	1.85	4.85	∞
2	.59	.59 -.46		0.55 -0.51	0.56
3.65			0.58 -0.55		
5	.65	.67 -.56		.63 -.53	0.61
8		.71 -.75			
9.13			0.72 -0.83		
10	.72			.78 -.74	0.75
11		.89 -1.06			
14			1.12 -1.24		
15	.93	1.23		1.17 -1.21	1.16
18.25			1.44 -1.76		
20	1.23	1.62		1.58 -1.74	1.64
23			1.81		
25		1.82		2.08 -2.48	
28			2.15		
30	1.71	2.08		2.45 -3.03	2.74
34			2.38		
35		2.41		2.80 -4.31	
40	2.17			3.32 -4.95	4.10
44			2.73		
45		2.60		3.52	

TABLE D12

$2Z^{R}_{h}/\ell^{*}$ (e = 0.44, y = h +½, U^{*}_{0} = 32.93 m/sec)

x \ h	0	1.07	1.85	4.85	∞
2	.99	1.06			.98
3.65			.98		
5	1.02	1.14		.98	.99
8		1.38			
9.13			1.23		
10	1.19			1.19	1.23
11		1.54			
14			1.45		
15	1.54	1.71		1.55	1.49
18.25			1.60		
20	1.99	2.06			1.76
23			1.79		
25		2.45		1.99	
28			2.15		
30	3.24	3.13			2.36
34			2.53		
35		3.75		2.56	
40	4.78				3.02
44			3.66		
45		5.06		3.23	

TABLE D13

Max. Vel. Decay - Trajectory

(ϵ = 0.44, z = 0, U_o^* = 32.93 m/sec)

x	h = 0		h = 1.07		h = 1.85		h = 4.85		h → ∞	
	U_{cmax}	y	U_{cmax}	y	U_{cmax}	y	U_{cmax}	y	U_{cmax}	Y
0	1.000	.50	1.000	1.57	1.000	2.35	1.000	5.35	1.000	0
2	.989	.57	.989	1.57					.987	0
3.65					.980					
5	.974	.60	.961	1.57			.964	5.35	.962	0
8			.859	1.53						
9.13					.806	2.28				
10	.919	.55					.768	5.35	.765	0
11			.726	1.5						
14					.621	2.25				
15	.738	.54	.584	1.37			.559	5.28	.558	0
18.25					.499	2.22				
20	.606	.52	.468	1.24					.449	0
23					.408	2.09				
25			.402	1.16			.368	5.22		
28					.344	1.92				
30	.424	.50	.357	.98					.307	- .033
34					.295	1.56				
35			.320	.99			.276	5.02		
40	.310	.46							.223	- .065
44					.242	1.17				
45			.260	1.00			.207	4.63		

TABLE D14

(h = 1.07, x = 10, z = 0)

e = 0.10 (U_o^* = 47.97 m/sec)		e = 0.25 (U_o^* = 18.29 m/sec)	
y	U_c	y	U_c
.13	.57	.07	.270
.26	.59	.14	.286
.39	.62	.21	.300
.52	.65	.36	.334
.65	.69	.50	.371
.79	.75	.64	.435
.92	.83	.93	.567
1.05	.90	1.21	.693
1.18	.94	1.35	.735
1.31	.92	1.50	.753
1.44	.88	1.57	.753
1.57	.80	1.64	.747
1.70	.67	1.79	.709
1.83	.60	1.93	.649
2.09	.46	2.21	.499
2.36	.34	2.50	.365
2.62	.23	2.79	.217
2.89	.16	3.07	.126

TABLE D15

(h = 1.07, x = 10, y = 1.57)

e = 0.44 (U_o^* = 32.93 m/sec)		e = 0.25 (U_o^* = 18.29 m/sec)	
z/δ*	U	z/δ*	U
0	.76	0	.756
.06	.76	.07	.756
.11	.76	.11	.753
.23	.75	.14	.750
.46	.73	.22	.741
.68	.68	.29	.724
.91	.56	.36	.706
1.14	.43	.43	.687
1.37	.30	.57	.642
1.59	.18	.72	.586
1.82	.10	.86	.477
1.93	.05	1.00	.359
		1.14	.270
		1.22	.207
		1.30	.160
		1.44	.066

TABLE D16

(ϵ = 0.1, h = 1.07, x = 3.55, z = 0)
(U_0^* = 47.87 m/sec)

y	U_c
.13	~ -.060
.26	~ -.121
.39	~ -.051
.52	.167
.65	.330
.79	.530
.92	.732
1.05	.947
1.18	.992
1.31	.998
1.44	.999
1.57	.996
1.70	.984
1.83	.853
1.95	.621
2.09	.435
2.22	.250
2.36	.102
2.46	.024

TABLE D17

(h = 1.07, z = 0)

(U_0^* = 32.93 m/sec) ϵ = 0.44		(18.29 m/sec) ϵ = 0.25		(47.87 m/sec) ϵ = 0.10		(18.29 m/sec) ϵ = 0	
x	$Y_{½}$	x	$Y_{½}$	x	$Y_{½}$	x	$Y_{½}$
2	.59 -.46	2	.54 -.53	2	.53 -.64	.5	.49 -.50
5	.67 -.56	4	.57 -.59	4	.48 -.81	1	.49 -.53
8	.71 -.75	6	.64 -.71	7	.44 -1.15	2	.41 -.63
11	.89 -1.06	10	.86 -1.15	10	.56	3	.27 -.81
15	1.23	15	1.29	15	1.13	4	.11 -1.08
20	1.62	20	1.61	20	1.57	5	-0.34 -1.51
25	1.82	30	2.18	30	2.21	6	-.11
30	2.08	40	2.86	40	2.80	8	-.09
35	2.41			60	3.87	10	-.05
				80	4.93	14	.04
				100	5.73	18	.18
						20	.25

TABLE D18

($h = 1.07$, $y = 1.57$)

($U_o^* = 32.93$ m/sec) e = 0.44		(18.29 m/sec) e = 0.25		(47.87 m/sec) e = 0.10	
$2x^*/\ell^*$	$2Z^*_{½}/\ell^*$	$2x^*/\ell^*$	$2Z^*_{½}/\ell^*$	$2x^*/\ell^*$	$2Z^*_{½}/\ell^*$
1.75	1.06	1.00	1.00	.40	1.05
4.36	1.14	2.01	.99	.79	1.04
6.98	1.38	3.01	1.02	1.38	.97
9.60	1.54	5.02	1.04	1.98	.90
13.09	1.71	7.53	1.15	2.96	1.00
17.45	2.06	10.04	1.46	3.95	1.23
21.82	2.45	15.05	2.20	5.93	1.37
26.18	3.13	20.07	3.32	7.90	1.45
30.54	3.75			11.85	1.71
39.27	5.06			15.80	2.32
				19.75	2.98

TABLE D19

Max. Centerplane Vel. Decay & Trajectory

($h = 1.07$, $z = 0$)

($U_o^* = 32.93$ m/sec) e = 0.44			(18.29 m/sec) e = 0.25			(47.87 m/sec) e = 0.10		
x	$U_{c\,max}$	y	x	$U_{c\,max}$	y	x	$U_{c\,max}$	y
0	1.000	1.57	0	1.000	1.57	0	1.000	1.57
2	.989	1.57	5	.954	1.57	3.55	.999	1.47
5	.961	1.57	10	.750	1.50	8.95	.977	1.27
8	.859	1.53	15	.604	1.39	15	.778	1.10
11	.726	1.50	20	.533	1.25	20	.719	.87
15	.584	1.37	25	.494	.82	25	.686	.73
20	.468	1.24	30	.455	.61	30	.651	.80
25	.402	1.16	40	.380	.54	40	.583	.87
30	.357	.98	47	.329		50	.510	.93
35	.320	.99				60	.446	1.07
45	.260	1.00				80	.343	1.07

TABLE E1

(e = 0.25, h = 1.86, z = 0, (θ = 0), $U_o^* = 18.9$ m/sec)

x = 2.2			x = 5			x = 9			x = 12			x = 15			x = 18		
y	φ°	U	y	φ°	U	y	φ°	U	y	φ°	U	y	φ°	U	y	φ°	U
1.61	-12.6	.124	1.18	-8.9	.096	0.75	-5.9	.104	.32	-4.2	.117	.18	-1.7	.187	.11	-.1	.236
1.71	-10.5	.269	1.29	-8.4	.143	0.86	-5.8	.132	.43	-4	.130	.32	-1.6	.207	.21	0	.255
1.82	-5.8	.460	1.39	-9.1	.194	0.96	-5.9	.162	.54	-4	.153	.43	-1.6	.216	.32	-.1	.268
1.93	-3.5	.675	1.5	-8.1	.270	1.07	-5.7	.208	.64	-4.2	.166	.54	-2	.235	.43	0	.307
2.04	-2.3	.827	1.61	-6.8	.344	1.18	-5.7	.249	.75	-4.1	.191	.64	-2.2	.253	.54	-.4	.298
2.14	-1	.900	1.71	-5.7	.448	1.29	-5.7	.296	.86	-4.4	.219	.86	-2.6	.289	.64	-.7	.313
2.25	-0.5	.933	1.82	-4.3	.547	1.39	-5.6	.352	.96	-4.4	.251	1.07	-3.1	.338	.86	-1.6	.346
2.36	0	.947	1.93	-3.2	.653	1.5	-5	.412	1.07	-4.9	.290	1.29	-3.1	.395	1.07	-1.7	.378
2.46	0.4	.945	2.04	-2.5	.754	1.61	-4.7	.473	1.18	-4.9	.331	1.5	-3	.460	1.29	-2	.424
2.57	1.2	.928	2.14	-1.2	.843	1.71	-4.1	.53	1.29	-4.4	.363	1.71	-2.6	.522	1.5	-1.8	.464
2.68	1.9	.875	2.25	-0.6	.901	1.82	-3.4	.589	1.39	-4.1	.404	1.93	-2.2	.565	1.71	-1.5	.497
2.79	2.8	.748	2.36	0	.929	1.93	-3.1	.650	1.5	-3.7	.446	2.14	-1.2	.606	1.03	-1.2	.527
									1.61								
2.89	4	.539	2.46	0.8	.921	2.04	-2.1	.709	1.71	-3.4	.500	2.25	-0.9	.605	2.03	-.8	.535
									1.82	-3.1	.537	2.36	-0.6	.604	2.14	-.7	.561
3	5	.320	2.57	1.4	.874	2.14	-1.1	.755	1.93	-2.6	.576	2.36	-0.6	.604	2.14	-.7	.561
									2.04	-2.4	.617						
3.11	5.5	.162	2.68	2	.789	2.25	-0.7	.788	2.14	-1.6	.653	2.46	-0.1	.602	2.25	-.3	.539
									2.25	-1.2	.680						
			2.79	2.9	.685	2.36	-0.1	.802	2.36	-0.7	.696	2.57	0.3	.6	2.36	-.1	.537
									2.46	-0.2	.700						
			2.89	3.6	.577	2.46	0.8	.797	2.57	-0.3	.695	2.79	1.2	.55	2.57	.6	.525
									2.68	0.8	.680	3	1.7	.5			
			3	4.5	.464	2.57	1.4	.768	2.79	1.2	.652	3.21	2.8	.44	2.78	1.3	.492
									2.89	1.8	.624	3.42	3.4	.369	3	2.1	.455
			3.11	5.6	.362	2.68	1.7	.723	3	2.5	.542	3.64	4.1	.314	3.21	2.6	.413
									3.21	3.4	.459	3.86	4.7	.253	3.42	3.5	.371
			3.21	6.2	.287	2.79	2.4	.674	3.42	4	.366						
						2.89	2.9	.607	3.64	4.7	.281	4.07	4.7	.2	3.86	4.9	.287
			3.32	6.9	.208	3	3.3	.547	3.86	5.1	.212	4.29	5.5	.16	4.07	5.3	.238
						3.21	4.6	.425									
			3.43	6.8	.145	3.42	5.1	.311	4.07	4.5	.148	4.5	5.4	.116	4.29	5.7	.205
						3.64	5.9	.214							4.5	6.1	.169
						3.86	6.2	.127							4.71	5.7	.138

TABLE E2

(e = 0.25, h = 1.86, x = 15, $U_0^* = 18.9$ m/sec)

	$z^*/\theta^* = 0.5$			$z^*/\theta^* = 0.7$		
y	φ°	θ°	U	φ°	θ°	U
.18	-2.1	0	.180			
.32	-3.6	0	.241	-3	7	.118
.43	-4.7	0.5	.255	-6	5.5	.120
.64	-4.6	1.6	.288	-7	4.5	.136
.86	-4.1	2	.303	-7	3.8	.176
1.07	-4.6	2.5	.325	-7	3.6	.185
1.29	-3.6	3.5	.356	-3.5	4	.217
1.5	-2	4	.403	-2.2	4.1	.232
1.71	-0.7	3.8	.417	-1.2	4.2	.220
1.93	0.2	3.3	.413	-.4	4.2	.211
2.14	1	3	.405	0	4.2	.210
2.36	2	3.1	.386	0	4.2	.194
2.57	3	3.2	.353	1.2	4.2	.178
2.78	4	3.6	.315	2.7	4.1	.150
3	5.1	3.6	.291	3.8	4	.121
3.21	5.5	3.6	.243	4.5	3.9	.099
3.42	7.4	3.5	.204			
3.64	6.8	3.5	.152			
3.86	5.2	3.5	.123			

TABLE E3

(e = 0.25, h = 1.86, x = 15, $U_0^* = 18.9$ m/sec)

	Y = 0			Y = -1.18			Y = 1.18		
$2z^*/\theta^*$	φ°	θ°	U	φ°	θ°	U	φ°	θ°	U
0	-.5	0	.604	-3.1	0	.374	3.7	0	.353
.11	-.5	.5	.611	-3.5	.4	.378	3.9	.4	.349
.21	-.5	1	.6	-3.4	.8	.380	4	.7	.340
.32	-.6	1.3	.582	-3.7	1.2	.388	3.4	1.1	.329
.43	-.7	1.7	.569	-4.2	1.4	.398	3.1	1.3	.321
.54	-.8	2	.55	-5	1.6	.402	3	1.6	.301
.64	-.6	2.3	.518	-5.5	1.8	.406	2.9	1.9	.271
.75	-.5	2.6	.481	-5.6	2.1	.403	2.5	2.3	.251
.86	-.3	2.9	.44	-6.1	2.5	.394	1.9	2.9	.224
.96	-.1	3.2	.4	-5.8	3	.361	1.3	3.7	.194
1.07	0	3.5	.346	-6.1	3.4	.330	0	4.7	.170
1.18	-.1	3.8	.295	-6	3.7	.293	-1.3	5.8	.139
1.29	-1.1	4.1	.24	-7	3.9	.239	-3.1	7.3	.107
1.39	-2.2	4.7	.189	-9	4.1	.191			
1.5	-6	5.9	.134	-10.1	3.7	.152			
1.61	-7.5	10.5	.109	-12.2	3.1	.124			

TABLE F1

Discharge Temperature Profiles
($x = 0$, $z = 0$)

($U_0^* = 32.93$ m/sec, $T_0^* = 103^o$ C, $T_\infty^* = 28.3^o$ C), e = 0.44		($U_0^* = 9.97$ m/sec, $T_0^* = 87.8^o$ C, $T_\infty^* = 21.7^o$ C), e = 0.25	
$2Y^*/d^*$	Θ	$2Y^*/d^*$	Θ
-1	.716	-1	.765
-.91	.791	-.86	.916
-.78	.896	-.71	.962
-.52	.992	-.57	.979
-.26	1	-.43	.992
-.13	1	-.29	.992
0	1	-.14	1
.13	1	0	1
.26	.992	.14	1
.52	.985	.29	.992
.78	.858	.43	.992
.91	.769	.57	.975
1	.702	.71	.958
		.86	.908
		1	.756

TABLE F2

Discharge Temperature Profiles
($x = 0$, $Y = 0$)

($U_0^* = 32.93$ m/sec, $T_0^* = 103^o$ C, $T_\infty^* = 28.3^o$ C), e = 0.44		($U_0^* = 9.97$ m/sec, $T_0^* = 87.8^o$ C, $T_\infty^* = 21.7^o$ C), e = 0.25	
$2z^*/\ell^*$	Θ	$2z^*/\ell^*$	Θ
-1	.687	-.97	.798
-.909	.858	-.93	.924
-.796	.985	-.86	.966
-.682	.993	-.72	.987
-.568	1	-.57	.992
-.455	1	-.43	.992
-.341	1	-.29	.996
-.227	1	-.14	1
-.113	1	-.07	1
0	1	0	1
.113	1	.07	1
.227	1	.14	1
.341	1	.29	.996
.455	1	.43	.992
.568	1	.57	.992
.682	.993	.72	.987
.796	.985	.86	.966
.909	.851	.93	.924
1	.679	.97	.798

TABLE F3

(e = 0.44, h = 4.85, z = 0
U_o^* = 32.93 m/sec
T_o^* = 103° C
T_∞^* = 28.3° C)

x = 5			x = 10			x = 25			x = 35		
y	Θ_c	U_c	y	Θ_c	U_c	y	Θ_c	U_c	y	Θ_c	U_c
3.52	.022		2.61	.015		.13	.089	0	.13	.133	.082
3.91	.052		3.13	.044		.65	.089	.037	.65	.141	.104
4.04	.09		3.39	.089		1.30	.119	.052	1.30	.148	.116
4.17	.142	0	3.65	.141		1.96	.156	.097	1.96	.163	.143
4.30	.209	.064	3.78	.170	0	2.61	.185	.138	2.61	.178	.165
4.43	.299	.155	3.91	.207	.074	3.26	.230	.2	3.26	.193	.192
4.56	.388	.257	4.04	.252	.112	3.91	.267	.256	3.91	.207	.219
4.69	.493	.387	4.17	.289	.159	4.56	.289	.302	4.56	.215	.235
4.82	.597	.530	4.43	.385	.273	4.82	.296	.320	4.82	.215	.235
4.95	.716	.672	4.69	.496	.414	5.09	.296	.327	5.09	.215	.235
5.09	.828	.811	4.95	.593	.579	5.22	.304	.331	5.22	.215	.235
5.22	.918	.916	5.09	.644	.656	5.35	.304	.333	5.35	.215	.235
5.28	.955	.947	5.22	.681	.705	5.48	.304	.329	5.48	.207	.228
			5.28	.689	.725						
5.35	.970	.956	5.35	.696	.733	5.61	.296	.320	5.61	.207	.228
			5.41	.696	.729						
5.41	.955	.947	5.48	.689	.715	5.87	.281	.306	5.87	.204	.222
			5.61	.659	.663						
5.48	.925	.919	5.74	.607	.591	6.13	.274	.282	6.13	.2	.213
5.61	.843	.813	6.00	.511	.420						
5.74	.724	.668	6.26	.385	.265	6.78	.237	.220	6.78	.185	.185
			6.52	.289	.154						
5.87	.627	.519	6.65	.230	.098	7.43	.200	.161	7.43	.170	.152
6	.507	.374							8.08	.148	.122
6.13	.403	.249	6.78	.185	.052	8.08	.148	.097	8.74	.122	.082
6.26	.306	.135							9.39	.096	.052
6.39	.216	.052	6.91	.141	0	8.74	.111	.052	10.04	.074	0
6.52	.134	0									
6.65	.067		7.17	.067		9.39	.074	0	11.34	.033	
6.91	.015					10.04	.037		12.00	.022	
7.17	.007		7.43	.022		10.69	.015		13.30	.007	
						11.34	0				

TABLE F8

(e = 0.44, h = 4.85, y = 5.35
$U_o^* = 32.93$ m/sec)
$T_o^* = 103^o$ C
$T_\infty^* = 28.3^o$ C)

	x = 5		x = 10		x = 25	
z	Θ	U	Θ	U	Θ	U
0	.970	.956	.694	.732	.304	.333
.07	.970	.955	.694	.732	.304	.333
.13	.962	.953	.694	.732	.304	.333
.26	.955	.946	.687	.728	.296	.329
.52	.940	.930	.679	.709	.296	.324
.78	.887	.869	.634	.673	.296	.313
.91	.797	.759				
1.04	.677	.6	.575	.585	.274	.294
1.17	.564	.435				
1.30	.451	.312	.478	.454	.259	.274
1.43	.353	.207				
1.56	.286	.154	.381	.330	.244	.252
1.70	.211	.083				
1.83	.158	.052	.291	.215	.230	.223
1.96	.098	0				
2.09	.060		.201	.117	.215	.196
2.22	.030					
2.35	.008		.134	.052	.200	.170
2.61			.082	0	.178	.148
2.87			.037		.163	.117
3.13			.015		.148	.104
3.39			0			
3.65					.111	.063
4.17					.074	.036
4.69					.037	0
5.22					.022	

TABLE F5

(e = 0.25, h = 1.46, z = 0,
$U_o^* = 9.97$ m/sec
x = 9, $T_o^* = 93.3^o$ C
$T_\infty^* = 25^o$ C)

y	Θ_c	U_c
.04	.179	.073
.07	.192	.089
.14	.204	.094
.21	.213	.103
.36	.233	.111
.5	.263	.119
.64	.3	.152
.79	.35	.198
.93	.4	.254
1.07	.467	.332
1.21	.517	.413
1.36	.567	.502
1.5	.633	.598
1.64	.683	.688
1.79	.725	.750
1.86	.742	.778
1.93	.75	.794
1.96	.75	.798
2	.75	.791
2.07	.742	.783
2.14	.725	.756
2.29	.683	.702
2.43	.625	.620
2.57	.575	.533
2.86	.442	.355
3.14	.317	.202
3.43	.2	.060
3.71	.083	0
4	.008	

TABLE F6

Θ_c (e = 0.25, h = 1.46, z = 0, $U_0^* = 9.97$ m/sec
$T_0^* = 93.3^o$ C
$T_\infty^* = 25^o$ C)

x / y	1	3	6	12	15	20
.04	.024	.049		.287	.368	.393
.39	.024	.057	.154	.336	.393	.413
.68	.033	.089	.236	.385	.433	.433
.82	.041					
.96	.049	.236	.358	.449	.466	.449
1.11	.102					
1.25	.276	.472	.520	.514	.506	.457
1.39	.512	.593	.610	.555		
1.54	.789	.724	.691	.579	.530	.457
1.68	.976	.854	.764	.611	.534	.457
1.82	1	.967	.864	.628	.538	.457
1.89		.992	.874	.636	.547	.457
1.96	1	.992	.886	.636	.547	.449
2.04		.976	.878	.628	.543	.449
2.11	1	.959	.854	.619	.538	.449
2.25	.967	.846	.772	.599	.530	.441
2.39	.756	.699	.675	.579	.514	.433
2.54	.488	.569	.585	.538	.490	.425
2.68	.236	.439	.504			
2.82	.057			.474	.441	.393
2.96	0	.171	.333			
3.11				.377	.401	.368
3.25		.016	.163			
3.39				.312	.336	.328
3.54			.049			
3.68				.223	.287	.300
3.89			0			
4.11				.109	.190	.247
4.54				.020	.130	.198
4.96					.069	.150
5.39					.020	.101
5.82						.069

TABLE F7

(e = 0.25, h = 1.46, y = 1.96,
$U_0^* = 9.97$ m/sec
x = 9, $T_0^* = 93.3^o$ C
$T_\infty^* = 25^o$ C)

zz^*/ℓ^*	Θ	U
0	.74	.79
.07	.74	.794
.14	.74	.788
.22	.724	.772
.29	.715	.767
.36	.711	.753
.43	.707	.748
.50	.691	.728
.57	.683	.708
.65	.675	.706
.72	.642	.67
.79	.618	.638
.86	.577	.594
.93	.537	.54
1.00	.484	.472
1.08	.415	.395
1.15	.374	.33
1.25	.301	.244
1.36	.203	.118
1.47	.17	.084
1.58	.085	0
1.69	.061	
1.80	.033	
1.90	.008	
2.01	0	

TABLE F9

(e . 0.44, x = 25, z = 0
$U_0^* = 32.93$ m/sec
$T_0^* = 103^o$ C
$T_\infty^* = 28.30$ C)

h = 4.85		h = 1.85		h = 1.07	
Y	Θ_c	Y	Θ_c	Y	Θ_c
-5.22	.089	-2.22	.293	-1.44	.363
-4.96	.096	-2.09	.299	-1.18	.369
-4.44	.110	-1.83	.306	-.92	.366
-3.92	.123	-1.57	.312	-.66	.363
-3.39	.154	-1.31	.316	-.53	.360
-2.87	.185	-1.05	.319	-.40	.357
-2.35	.219	-.79	.319	-.27	.350
-1.83	.240	-.66	.319	-.14	.344
-1.57	.260	-.52	.322	0	.338
-1.31	.274	-.39	.319	.13	.331
-1.04	.281	-.26	.312	.26	.319
-0.78	.295	-.13	.312	.39	.309
-.52	.301	0	.306	.65	.293
-.26	.301	.13	.306	.91	.271
0	.301	.26	.299	1.17	.248
.13	.295	.39	.293	1.69	.204
.26	.291	.52	.287	2.21	.159
.52	.281	.79	.268	2.73	.121
.78	.274				
1.04	.260	1.05	.255	3.25	.083
1.30	.247				
1.83	.216	1.56	.223	3.78	.051
2.37	.178	2.08	.178		
2.86	.137	2.60	.147	4.30	.019
3.39	.110	3.13	.108		
3.91	.079	3.65	.070		
4.43	.051	4.17	.025		
4.95	.034	4.69	.012		
5.47	.014				

TABLE F8

(e = 0.44, x = 10, z = 0
$U_0^* = 32.93$ m/sec
$T_0^* = 103^o$ C
$T_\infty^* = 28.30$ C)

h = 4.85		h = 1.85		h = 1.07	
Y	Θ_c	Y	Θ_c	Y	Θ_c
-2.74	.013	-2.22	.131	-1.44	.331
-2.48	.026	-1.96	.150	-1.31	.350
-1.96	.086	-1.70	.183	-1.18	.376
-1.44	.211	-1.44	.242	-.92	.452
-1.18	.296	-1.18	.314	-.66	.541
-0.92	.395	-.92	.405	-.39	.624
-.66	.493	-.79	.451	-.26	.656
-.52	.546	-.66	.503	-.13	.682
-.39	.599	-.52	.562	0	.688
-.26	.638	-.39	.608	.13	.669
-.13	.671	-.26	.647	.26	.631
0	.684	-.13	.667	.39	.592
.13	.671	0	.673	.52	.529
.26	.645	.13	.667	.79	.420
.39	.599	.26	.634	1.04	.309
.52	.553	.39	.588	1.30	.217
.79	.454	.52	.536	1.56	.127
1.04	.342	.66	.484	1.82	.067
1.30	.237	.79	.425	2.08	.032
1.82	.092	.92	.373	2.34	.006
2.37	.020	1.17	.268		
2.61	.007	1.43	.183		
		1.69	.105		
		1.95	.046		
		2.21	.013		

TABLE F10

$Y_{\frac{1}{2}}$ (e = 0.44, z = 0, $U_0^* = 32.93$ m/sec
$T_0^* = 103^o$ C
$T_\infty^* = 28.3^o$ C)

x \ h	4.85	1.85	1.07
5	-.66 .67	-.67 .70	-.68 .68
10	-1.05 1.04	-1.11 1.01	-1.37 .92
15	-1.73 1.63	1.50	1.33
20			1.76
25	-3.39 2.99	2.39	2.08
35	4.43	3.06	2.73
45	5.41	3.56	3.32

TABLE F11

$2Z^*_{T\frac{1}{2}}/\ell^*$ (e = 0.44, z = 0, $U_0^* = 32.93$ m/sec
($T_0^* = 103^o$ C, $T_\infty^* = 28.3^o$ C)

x \ h	4.85	1.85	1.07
5	1.07	1.08	1.08
10	1.37	1.32	1.31
15	1.6	1.68	1.72
20			2.22
25	1.96	2.39	2.62
35	2.96	3.41	4.55
45	4.04	5.15	6.54

TABLE F12

Θ_{cmax} (e = 0.44, z = 0, U_0^* = 32.93 m/se-, T_0^* = 103° C, T_∞^* = 28.3° C)

x \ h	∞	4.85	1.85	1.07	0
0	1.000	1.000	1.000	1.000	1.000
5	.959	.987	.961	.948	.980
10	.671	.691	.673	.684	.870
15	.486	.493	.490	.510	.726
20	.370			.407	.562
25	.295	.309	.314	.342	.466
35	.212	.211	.248	.284	.329
45	.158	.173	.209	.226	.247

TABLE F13

e = 0.25, h = 1.46
z = 0, U_0^* = 9.97 m/sec
T_0^* = 94° C, T_∞^* = 25° C

x	Θ_c	U_c
0	1.000	1.000
6	.880	.917
12	.637	.683
20	.460	.490
30	.363	.386
40	.291	.319

e = 0.44, h = 4.85
z = 0, U_0^* = 32.93 m/sec
T_0^* = 103° C, T_∞^* = 28.3° C

x	Θ_c	U_c
0	1.000	1.000
5	.977	.956
9.6	.737	.751
13.8	.511	.535
19	.406	.417
28.6	.271	.277
39.1	.203	.200
50	.150	.156

TABLE F14

(h = 1.46, x = 9, z = 0)

$U_0^* = 9.6$ m/sec, $T_0^* = 122.7^o$ C, $T_\infty^* = 28.9^o$ C, e = 0.44		$U_0^* = 9.94$ m/sec, $T_0^* = 95.6^o$ C, $T_\infty^* = 29.2^o$ C, e = 0.25		$U_0^* = 6.7$ m/sec, $T_0^* = 108^o$ C, $T_\infty^* = 32.7^o$ C, e = 0.10	
y	Θ_c	y	Θ_c	y	Θ_c
.07	.172	.04	.179	.13	.467
.13	.189	.07	.192	.27	.489
.20	.201	.14	.204	.4	.519
.26	.207	.21	.213	.53	.533
.39	.225	.36	.233	.67	.563
.52	.249	.5	.263	.93	.593
.65	.278	.64	.3	1.2	.63
.91	.349	.79	.35	1.47	.659
1.17	.432	.93	.4	1.73	.659
1.43	.527	1.07	.467	1.87	.659
1.56	.580	1.21	.517	1.96	.644
1.69	.615	1.36	.567	2.05	.622
1.83	.645	1.5	.633	2.13	.607
		1.64	.683		
		1.79	.725		
1.96	.657	1.86	.742	2.27	.585
2.09	.651	1.93	.750	2.53	.511
2.22	.621	2	.750	2.8	.437
2.35	.568	2.07	.742	3.07	.359
2.61	.485	2.14	.725	3.33	.289
2.87	.373				
3.13	.272	2.29	.683	3.6	.215
3.39	.178	2.43	.625	3.87	.148
3.65	.118	2.57	.575	4.13	.093
3.91	.071	2.86	.442	4.53	.044
4.17	.030	3.14	.317	4.93	.022
4.43	.012	3.43	.200	5.33	.007
		3.71	.083		
		4.29	.008		

TABLE F15

(h = 1.46, x = 9, y = 1.96)

$U_0^* = 9.6$ m/sec, $T_0^* = 122.7^o$ C, $T_\infty^* = 28.9^o$ C, e = 0.44		$U_0^* = 9.94$ m/sec, $T_0^* = 95.6^o$ C, $T_\infty^* = 29.2^o$ C, e = 0.25		$U_0^* = 6.7$ m/sec, $T_0^* = 108^o$ C, $T_\infty^* = 32.7^o$ C, e = 0.10	
$2z^*/t^*$	Θ	$2z^*/t^*$	Θ	$2z^*/t^*$	Θ
0	.657	0	.74	0	.650
.11	.654	.07	.74	.05	.644
.23	.651	.14	.74	.16	.637
.34	.645	1.22	.724	.26	.622
.46	.636	.29	.715	.37	.607
.57	.612	.36	.711	.47	.585
.68	.574	.43	.707	.58	.559
.8	.536	.5	.691	.69	.511
.91	.491	.57	.683	.79	.441
1.02	.456	.65	.675	.90	.348
1.14	.373	.72	.642	.95	.296
1.25	.331	.79	.618	1.00	.244
1.37	.302	.86	.577	1.05	.215
1.59	.243	.93	.537	1.11	.133
1.82	.130	1	.484	1.16	.096
2.04	.065	1.07	.415	1.26	.044
2.28	.027	1.15	.374	1.37	.019
2.50	.009	1.25	.301	1.48	.011
		1.36	.203		
		1.47	.170		
		1.58	.085		
		1.69	.061		
		1.79	.033		
		1.9	.008		
		2	0		

TABLE F16

(h = 1.46)

$U_o^* = 9.6$ m/sec, $T_o^* = 122.7°$ C, $T_\infty^* = 28.9°$ C, e = 0.44			$U_o^* = 9.94$ m/sec, $T_o^* = 95.6°$ C, $T_\infty^* = 29.2°$ C, e = 0.25			$U_o^* = 6.7$ m/sec, $T_o^* = 108°$ C, $T_\infty^* = 32.7°$ C, e = 0.10		
x	$2Z^*_{T½}/\ell^*$	$Y_{T½}$	x	$2Z^*_{T½}/\ell^*$	$Y_{T½}$	x	$2Z^*_{T½}/\ell^*$	$Y_{T½}$
2	1.02	-.6 .6	2	1.03	-.64 .64	2	1.01	-.68 .68
4	1.09	-.66 .68	4	1.06	-.71 .75	4	1.01	-.99 .85
7	1.26	-.85 .87	6	1.11	-.86 .82	6	1.00	-1.83 .95
10	1.54	-1.31 1.13	10	1.17	-1.21 1.18	10	.99	1.28
12		-1.70	12.5		-1.86	15	1.05	1.68
15	1.88	1.63	15	1.25	1.75	20	1.26	2.28
20	2.22	2.15	20	1.49	2.29	30	1.40	3.28
30	3.01	3.45	30	1.77	3.46	40	1.50	4.08
40	4.10	5.08	40	2.42	5	60	1.69	5.68
50	6.26	6.32						
60	7.11	7.82						

TABLE F17

(h = 1.46, z = 0)

$U_o^* = 9.6$ m/sec, $T_o^* = 122.7°$ C, $T_\infty^* = 28.9°$ C, e = 0.44		$U_o^* = 9.97$ m/sec, $T_o^* = 95.6°$ C, $T_\infty^* = 29.2°$ C, e = 0.25		$U_o^* = 6.7$ m/sec, $T_o^* = 108°$ C, $T_\infty^* = 32.7°$ C, e = 0.10	
x	$\Theta_{c\,max}$	x	$\Theta_{c\,max}$	x	$\Theta_{c\,max}$
0	1.000	0	1.000	0	1.000
2	.988	6	.880	2	.985
4	.940	12	.637	4	.885
7	.762	20	.460	6	.779
10	.613	30	.363	10	.649
12	.54	40	.291	15	.595
15	.458			20	.557
20	.375			30	.481
30	.280			40	.382
40	.214			60	.267
50	.173				
60	.143				

REFERENCES

1. Sacks, S., John, J.E.A., and Marks, C.H., "Interaction of a Three-Dimensional Fluid Jet with a Nearby Wall Boundary," Proceedings of Thermal Pollution Analysis Conference, Virginia Polytechnic Institute and State University, Blacksburg, 1974, pp. 96-117.

2. Sawyer, R.A., "The Flow due to a Two-Dimensional Jet Issuing Parallel to a Flat Plate," Journal of Fluid Mechanics, Vol. 9, 1960, pp. 543-560.

3. Sawyer, R.A., "Two-Dimensional Reattaching Jet Flows Including the Effects of Curvature on Entrainment," Journal of Fluid Mechanics, Vol. 17, 1963, pp. 481-498.

4. Bourque, C. and Newman, B.G., "Reattachment of a Two-Dimensional Incompressible Jet to an Adjacent Flat Plate," Aeronautical Quarterly, Vol. 11, 1960, pp. 201-232.

5. Bourque, C., "Reattachment of Two-Dimensional Jet to Adjacent Flat Plate," ASME Advances in Fluidics, 1967, Fluidics Symposium, pp. 192-204.

6. Rajaratnam, N. and Subramanya, K., "Plane Turbulent Reattached Wall-Jets," Proceedings of ASCE, Journal of Hydraulics Division, Vol. 94, 1968, pp. 95-112.

7. Hoch, J. and Jiji, L.M., "Two-Dimensional Turbulent Offset Jet-Boundary Interaction," ASME Transactions Journal of Fluids Engineering, Vol. 103, 1981, pp. 154-161.

8. Hoch, J. and Jiji, L.M., "Theoretical and Experimental Temperature Distribution in Two-Dimensional Jet-Boundary Interaction," ASME Transactions, Journal of Heat Transfer, Vol. 103, 1981, pp. 331-336.

9. Daggett, L.L., "Plane Turbulent Reattached Wall Jet," Proceedings of ASCE, Journal of Hydraulics Division, Vol. 94, 1968, pp. 1590-1595.

10. Parameswaran, V. and Alpay, S.A., "Studies on Re-attaching Wall Jets," Transactions of the CSME, Vol. 3, 1975, pp. 83-89.

11. Tanaka, T. and Tanaka, E., "Experimental Studies of a Radial Turbulent Jet (Flow before an Attachment Point of Attaching Jet Flow)," Bulletin of JSME, Vol. 21, 1978, pp. 665-672.

12. Kumada, M., Mabuchi, I. and Oyakawa, K., "Studies on Heat Transfer to Turbulent Jets with Adjacent Boundaries," Bulletin of JSME, Vol. 16, 1973, pp. 1712-1720.

13. Murai, K., Taga, M., Akagawa, K. and Origane, T., "Flow Characteristics of a Jet Adjacent to a Plane Wall," Bulletin of JSME, Vol. 24, 1981, pp. 684-690.

14. Marsters, G.F., "The Attachment of a Plane Ventilated Jet to a Plane Parallet Wall," Transactions of CSME, Vol. 4, 1976-77, pp. 197-203.

15. El-Taher, R.M., "Experimental Investigation of Curvature Effects of Ventilated Wall Jets," AIAA Journal, Vol. 21, 1983, pp. 1505-1512.

16. Shibl, A. and Shaalan, M., "Turbulent Jet Attachment over a Circular Wall," ASME Paper No. 80-C2/Aero-2, 1980.

17. Marsters, G.F., Howkins, B. and Kortschak, E., "Heat Transfer to a Plane Wall from a Heated, Ventilated Plane Jet," International Journal of Heat Mass Transfer, Vol. 23, 1980, pp. 301-309.

18. Vogel, J.C., Eaton, J.K. and Adams, E.W., "Combined Heat Transfer Fluid Dynamic Measurements Behind a Backward Facing Step," ASME Paper No. 83-WA/HT-11, 1983.

19. Sforza, P.M., Steiger, M.H. and Trentacoste, N., "Studies on Three-Dimensional Viscous Jets," AIAA Journal, Vol. 4, 1966, pp. 800-806.

20. Trentacoste, N. and Sforza, P., "Further Experimental Results for Three-Dimensional Free Jets," AIAA Journal, Vol. 5, 1967, pp. 885-891.

21. Quinn, W.R., Pollard, A. and Marsters, G.F., "Measurements in a Turbulent Rectangular Free Jet," Fourth Symposium on Turbulent Shear Flows, University of Karlsruhe, West Germany, 1983.

22. Quinn, W.R., Pollard, A. and Marsters, G.F., "On Saddle-Backed Velocity Distributions in a Three-Dimensional Turbulent Free Jet, "AIAA Fournal (accepted), 1983.

23. Marsters, G.F. and Fotheringham, J., "The Influence of Aspect Ratio on Incompressible, Turbulent Flows from Rectangular Slots," Aeronautical Quarterly, Vol. 31, 1980, pp. 285-305.

24. Trentacoste, N. and Sforza, P., "Some Remarks on Three-Dimensional Wakes and Jets," AIAA Journal, Vol. 6, 1968, pp. 2454-2456.

25. Marsters, G.F., "Spanwise Velocity Distribution in Jets from Rectangular Slots," AIAA Journal, Vol. 19, 1981, pp. 148-152.

26. McGuirk, J.J. and Rodi, W., "The Calculation of Three-Dimensional Turbulent Free Jets," Symposium of Turbulent Shear FLows, Penn. State University, 1977.

27. Sfeir, A.A., "Investigation of Three-Dimensional Turbulent Rectangular Jets," AIAA Journal, Vol. 17, 1979, pp. 1055-1060.

28. Sforza, P.M. and Stasi, W., "Heated Three-Dimensional Turbulent Jets," ASME Paper No. 77-WA/HT-27, 1977.

29. Sfeir, A.A., "The Velocity and Temperature Fields of Rectangular Jets," International Journal of Heat and Mass Transfer, Vol. 19, 1976, pp. 1289-1297.

30. Jiji, L.M. and Moghadam, S.M., "Theoretical and Experimental Investigation of Three-Dimensional Buoyant Turbulent Jets," Proceedings of the Seventh International Heat Transfer Conference, Munchen, West Germany, Vol. 2, 1982, pp. 425-430.

31. Sforza, P.M., "The Surface Layer in Three-Dimensional Wall Jets," (ASME Publication) Turbulent Boundary Layers: Forced, Incompressible, Non-Reacting, H.E. Webber - Editor, 1979.

32. Sforza, P.M. and Herbst, G., "A Study of Three-Dimensional Incompressible Turbulent Wall Jets," AIAA Journal, Vol. 8, 1970, pp. 276-283.

33. Catalano, G.D., Morton, J.B. and Humphris, R.R., "An Experimental Investigation of a Three-Dimensional Wall Jet," AIAA Journal, Vol. 15, 1977, pp. 1146-1151.

34. Catalano, G.D., Morton, J.B. and Humphris, R.R., "Pressure and Velocity Measurements in a Three-Dimensional Wall Jet," AIAA Journal, Vol. 17, 1979, pp. 332-333.

35. Morton, J.B., Catalano, G.D. and Humphris, R.R., "Some Two-Point Statistical Properties of a Three-Dimensional Wall Jet," AIAA Journal, Vol. 16, 1978, pp. 693-698.

36. Rajaratram, N. and Pani. B.S., "Three-Dimensional Turbulent Wall Jets," Technical Report, Department of Civil Engineering, University of Alberta, Edmonton, 1970.

37. Rajaratnam, N. and Pani, B.S., "Three-Dimensional Turbulent Wall Jets," Proceedings of ASCE, Journal of Hydraulics Division, Vol. 100, 1974, pp. 69-83.

38. Butterman, H.C., Jiji, L.M. and Hoch, J., "Theoretical and Experimental Studies of Velocity and Temperature Distribution in Three-Dimensional Turbulent Wall Jets," ASME Paper, No. 83-WA/HT-4, 1983.

39. Townsend, A.A., "Entrainment and the Structure of Turbulent Flow," Journal of Fluid Mechanics, Vol. 41, 1970, pp. 13-46.

40. Paizis, S.T. and Schwarz, W.H., "Entrainment Rates in Turbulent Shear Flows," Journal of Fluid Mechanics, Vol. 68, 1975, pp. 297-308.

41. Bevilaqua, P.M. and Lykoudis, P.S., "Some Observations on the Mechanism of Entrainment," AIAA Journal, Vol. 15, 1977, pp. 1194-1196.

42. Corrsin, S. and Kistler, A.L., "Free Stream Boundaries of Turbulent Flows," NACA Report 1244, 1955.

43. Bremhorst, K. and Harch, W.H., "The Mechanism of jet Entrainment," AIAA Journal, Vol. 16, 1978, pp. 1004-1106.

44. Newman, B.G., "The Deflection of Plane Jets by Adjacent Boundaries-Coada Effect," Boundary Layer and Flow Control, Pergamon Press, London, 1961, p. 232.

45. Sparrow, E.M., Ramsey, J.W. and Mass, E.A., "Effects of Finite Width on Heat Transfer Flow About an Inclined Rectangular Plate," ASME Transactions, Journal of Heat Transfer, Vol. 101, 1979, pp. 199-204.

46. Hoch, J., "Two-Dimensional Jet-Boundary Interaction for a Submerged Thermal Discharge," PhD. dissertation, Mechanical Engineering Department, The City University of New York, 1979.

47. Butterman, H.C., "Studies of Buoyant Rectangular Three-Dimensional Wall Jets," Masters Thesis, Mechanical Engineering Department, The City College of the City University of New York, 1983.